

University of Windsor

Scholarship at UWindor

Electronic Theses and Dissertations

Theses, Dissertations, and Major Papers

4-25-2018

BUBBLE-PUMP-DRIVEN SOLAR ABSORPTION AIR CONDITIONING FOR RESIDENTIAL APPLICATIONS

Julia Aman
University of Windsor

Follow this and additional works at: <https://scholar.uwindsor.ca/etd>

Recommended Citation

Aman, Julia, "BUBBLE-PUMP-DRIVEN SOLAR ABSORPTION AIR CONDITIONING FOR RESIDENTIAL APPLICATIONS" (2018). *Electronic Theses and Dissertations*. 7424.
<https://scholar.uwindsor.ca/etd/7424>

This online database contains the full-text of PhD dissertations and Masters' theses of University of Windsor students from 1954 forward. These documents are made available for personal study and research purposes only, in accordance with the Canadian Copyright Act and the Creative Commons license—CC BY-NC-ND (Attribution, Non-Commercial, No Derivative Works). Under this license, works must always be attributed to the copyright holder (original author), cannot be used for any commercial purposes, and may not be altered. Any other use would require the permission of the copyright holder. Students may inquire about withdrawing their dissertation and/or thesis from this database. For additional inquiries, please contact the repository administrator via email (scholarship@uwindsor.ca) or by telephone at 519-253-3000ext. 3208.

**BUBBLE-PUMP-DRIVEN SOLAR ABSORPTION AIR CONDITIONING
FOR RESIDENTIAL APPLICATIONS**

by

Julia Aman

A Dissertation

Submitted to the Faculty of Graduate Studies
through the Department of Mechanical, Automotive & Materials Engineering
in Partial Fulfillment of the Requirements for
the Degree of Doctor of Philosophy
at the University of Windsor
Windsor, Ontario, Canada

Windsor, Ontario, Canada

2018

©2018 Julia Aman

Bubble-Pump-Driven Solar Absorption Air Conditioning for Residential Applications
by

Julia Aman

APPROVED BY:

I. Beausoleil-Morrison, External Examiner
Carleton University

R. Carriveau,
Department of Civil and Environmental Engineering

A. Sobiesiak
Department of Mechanical, Automotive & Materials Engineering

B. Zhou
Department of Mechanical, Automotive & Materials Engineering

P. Henshaw, Co-Advisor
Department of Civil and Environmental Engineering

D. S.-K. Ting, Co-Advisor
Department of Mechanical, Automotive & Materials Engineering

April 4, 2018

DECLARATION OF PREVIOUS PUBLICATION

I. Previous Publication

This thesis includes seven original papers that have been previously published/submitted for publication in peer reviewed journals, as follows:

| Thesis Chapter | Publication title/full citation | Publication status* |
|------------------|---|---------------------|
| <i>Chapter 2</i> | Aman, J., Henshaw, P. Ting, D. S-K., Solar sorption cooling for residential air-conditioning applications, <i>International Journal of Renewable Energy Technologies</i> , 9 (1/2) (2018) 136-157. | <i>Published</i> |
| <i>Chapter 3</i> | Aman, J., Ting, D. S-K., Henshaw, P., Residential solar air conditioning: energy and exergy analyses of an ammonia-water absorption cooling system, <i>Applied Thermal Engineering</i> , 62 (2014) 424-432. | <i>Published</i> |
| <i>Chapter 4</i> | Aman, J., Henshaw, P. Ting, D. S-K., Modelling and Analysis of Bubble Pump Parameters for Vapor Absorption Refrigeration Systems, <i>Proceedings of ASHRAE Annual conference 2016</i> , St. Louis, MO, June 25-29, 2016. | <i>Published</i> |
| <i>Chapter 5</i> | Aman, J., Henshaw, P. Ting, D. S-K., Performance characterization of a bubble pump for vapor absorption refrigeration systems, <i>International Journal of Refrigeration</i> , 85 (2018) 58–69. | <i>Published</i> |
| <i>Chapter 6</i> | Aman, J., Henshaw, P. Ting, D. S-K., Bubble-pump-driven LiBr-H ₂ O and LiCl-H ₂ O absorption air-conditioning systems, <i>Thermal Science and Engineering Progress</i> , https://doi.org/10.1016/j.tsep.2017.10.022 . | <i>Published</i> |

| | | |
|-------------------|---|---------------------|
| <i>Chapter 7</i> | Aman, J., Henshaw, P. Ting, D. S-K., Advanced exergy analysis of a bubble-pump-driven LiCl-H ₂ O absorption air-conditioning system, International Journal of Exergy. | <i>Under review</i> |
| <i>APPENDIX A</i> | Aman, J., Henshaw, P. Ting, D. S-K., Energy efficiency and economic feasibility of an absorption air-conditioning system using wet, dry and hybrid heat rejection methods, International Journal of Environmental Studies, 75 (1) (2018) 68-85. | <i>Published</i> |

I certify that I have obtained a written permission from the copyright owner(s) to include the above published material(s) in my thesis. I certify that the above material describes work completed during my registration as a graduate student at the University of Windsor.

II. General

I declare that, to the best of my knowledge, my thesis does not infringe upon anyone's copyright nor violate any proprietary rights and that any ideas, techniques, quotations, or any other material from the work of other people included in my thesis, published or otherwise, are fully acknowledged in accordance with the standard referencing practices. Furthermore, to the extent that I have included copyrighted material that surpasses the bounds of fair dealing within the meaning of the Canada Copyright Act, I certify that I have obtained a written permission from the copyright owner(s) to include such material(s) in my thesis.

I declare that this is a true copy of my thesis, including any final revisions, as approved by my thesis committee and the Graduate Studies office, and that this thesis has not been submitted for a higher degree to any other University or Institution.

ABSTRACT

Large-scale heat-driven absorption cooling systems are currently available in the marketplace for industrial applications. The high temperature is required in the generator for driving this absorption chiller. For this reason, this type of chiller was originally designed to use direct-fired gas. However, the low efficiency of this cooling cycle restricts its use in small-scale applications. The concept of a solar-driven absorption chiller can satisfy the increasing demand for air conditioning without contributing greenhouse gases to the global environment. This research contributes to providing an efficient air conditioning driven by low temperature solar heat and independent of grid electricity, which may be useful in remote residential communities. The performance of 10 kW absorption and adsorption cooling systems were compared for the selection of a suitable cooling technology that can be driven by low temperature heat source such as a flat plate solar collector. Analysis revealed that under any operating conditions, the coefficient of performance (COP) of the absorption cooling system is higher. However, absorption chillers have a lower efficiency than traditional compression refrigeration systems, when used for small scale applications. Hence, energy and exergy analyses were conducted to evaluate the performance of a solar-driven air-cooled ammonia-water absorption chiller for residential air conditioning. Low driving temperature heat sources were optimized (70~80°C) and the efficiencies (COP=0.6, exergetic efficiency=32%) of the system were evaluated. The highest exergy losses were identified in the absorption process (63%) followed by the generator (13%) and the condenser (11%).

In order to replace the only electrical component (pump) in an absorption chiller and make it independent of grid electricity, a solar-thermal-driven bubble pump was introduced in a vapor absorption refrigeration (VAR) cycle. This solar-thermal-driven pump can circulate the solution to the absorber and the generator to create the necessary refrigerant vapor for cooling. An analytical model of a bubble pump was developed and experimental work was conducted. Furthermore, a dimensional analysis was performed, considering bubble pump geometry and the solution properties. The bubble pump performance was defined in terms of non-dimensional parameters which can be used in all bubble-pump-driven absorption refrigeration systems. Experimental and theoretical results for a new refrigerant-absorbent solution (LiCl-H₂O) were compared, and the flow regime (slug flow) was determined for the highest pump efficiency. Moreover, in order to employ the advantages of high performance, the bubble pump was incorporated into a simulation of a water-based vapor absorption refrigeration cycle. A new absorbent-refrigerant pair (LiCl-H₂O) for a bubble-pump-operated VARS was proposed and a thermodynamic comparison was made between LiBr-H₂O and LiCl-H₂O systems.

Finally, energy, exergy and advanced exergy analyses were performed on this proposed refrigeration cycle, and the exergy losses due to the internal irreversibilities of each component and the effect of the irreversibilities of the other components were determined. The avoidable exergy destruction was identified pertaining to the potential improvement of the overall system structure. The highest avoidable endogenous exergy losses occurred in the generator.

DEDICATION

To my parents, my husband, my children and family.

ACKNOWLEDGEMENTS

Completing this PhD and becoming a Doctor is the blessing of Almighty for me. Words cannot express how He guided me in this journey and led me to meet these great people at the University of Windsor. Through my father's encouragement and my husband's dedication and enthusiasm, I embarked on my journey to complete my PhD 8 years after finishing my Master's degree. When Dr. David Ting and Dr. Paul Henshaw accepted me to be their graduate student, I could not fathom how incredible their leadership would be. Through the tremendous efforts of the people I am grateful to have in my life, the Almighty granted me success.

When the frustration plagued my mind, my advisor, Dr. Ting, told me, "Remember, a dead fish can float downstream, but it takes a live one to swim upstream". With the support of their research expertise, encouragement, and patience, I propelled myself against the current throughout this quest. I am extremely fortunate to be able to work with advisors who are both intelligent researchers and excellent advisors. Despite their busy schedule, I am honoured by the time and effort they dedicated to my success, even if it meant commenting on every line of my manuscript. Words fail to describe my eternal gratefulness for their guidance academically and professionally. Without their dedication and support, I would not be successful.

I am also indebted to my committee members Dr. Andrzej Sobiesiak, Dr. Biao Zhou, and Dr. Rupp Carriveau, for their effort, time, encouragement, and insight. Their suggestions and feedback for my PhD dissertation are appreciated immensely. I would like to express my sincere gratitude to my external Dr. Ian Beausoleil-Morrison of Carleton University for his time and invaluable suggestions in spite of his busy schedule. I am also grateful to Dr. Nihar Biswas for chairing my PhD defense. My thanks and appreciation also go to Mr. Andy Jenner, Mr. Matt St. Louis, Mr. Patrick Seguin, and Mr. Bill Middleton for their technical support for my experimental set-up. I also would like to thank Mr. Terry Patrick, Maintenance Manager for International Nutrient Technologies for the donation of Kathene

solution for my experiment. I am thankful to our finance and graduate secretary Angela Haskell for her kind support throughout my PhD studies.

I gratefully acknowledge the Natural Sciences and Engineering Research Council (NSERC) of Canada for providing the research funding, the Ontario Ministry of Training, Colleges and Universities for providing me the Ontario Graduate Scholarship (OGS) and Queen Elizabeth II Graduate Scholarship in Science and Technology, and the University of Windsor for selecting me for Sustainable Engineering Faculty Scholarship (Doctoral) to carry out my PhD research.

Finally, my family's relentless support allowed me to complete my PhD degree. The countless sacrifices from my mom and dad, my husband and my kids to see me successful are invaluable. My parents gave me endless love and raised me to believe in the importance of education. The inspiration, support, encouragement, advice and motivation by my husband always gave me the strength to move forward, even during the hardest time during my PhD study. The unconditional support by my kids motivated me to be successful. I am forever grateful to be blessed with my family.

TABLE OF CONTENTS

| | |
|--|-----|
| DECLARATION OF PREVIOUS PUBLICATION..... | ii |
| ABSTRACT..... | iv |
| DEDICATION..... | vi |
| ACKNOWLEDGEMENTS..... | vii |
| LIST OF TABLES..... | xiv |
| LIST OF FIGURES..... | xvi |
| LIST OF APPENDICES..... | xx |
| CHAPTER 1..... | 1 |
| INTRODUCTION..... | 1 |
| 1.1. Overview..... | 1 |
| 1.1.1. Solar Thermal Cooling..... | 2 |
| 1.1.2. Bubble-Pump-Driven Vapor Absorption Refrigeration Systems (VARs)..... | 3 |
| 1.1.3. Diffusion absorption refrigeration (DAR) systems..... | 5 |
| 1.1.4. Water based refrigerant VARs..... | 6 |
| 1.2. Objective and Scope of Work of this Study..... | 7 |
| 1.3. Thesis Organization..... | 8 |
| REFERENCES..... | 11 |
| CHAPTER 2..... | 14 |
| SOLAR SORPTION COOLING FOR RESIDENTIAL AIR-CONDITIONING APPLICATIONS..... | 14 |
| 2.1. Introduction..... | 14 |
| 2.2. Cycle operation principles..... | 18 |
| 2.3. Thermodynamic model..... | 22 |

| | |
|--|--------|
| 2.4. Results and discussion..... | 27 |
| 2.5. Conclusions | 35 |
| Nomenclature | 36 |
| REFERENCES..... | 37 |
| CHAPTER 3 | 41 |
| RESIDENTIAL SOLAR AIR CONDITIONING: ENERGY AND EXERGY ANALYSES OF AN AMMONIA-WATER ABSORPTION COOLING SYSTEM | 41 |
| 3.1. Introduction | 41 |
| 3.2. Cycle Operation Principles..... | 43 |
| 3.3. Thermodynamic Model | 46 |
| 3.3.1. First Law Analysis (Energy Method) | 46 |
| 3.3.2. Second Law Analysis (Exergy Method)..... | 48 |
| 3.3.3. Thermodynamic properties | 50 |
| 3.3.4. Theoretical Considerations | 50 |
| 3.4. Results and analysis | 51 |
| 3.5. Conclusions | 60 |
| Nomenclature | 61 |
| REFERENCES..... | 62 |
| CHAPTER 4 | 65 |
| MODELLING AND ANALYSIS OF BUBBLE PUMP PARAMETERS FOR VAPOR ABSORPTION REFRIGERATION SYSTEMS | 65 |
| 4.1. Introduction | 65 |
| 4.2. System Analysis | 68 |
| 4.2.1. Bubble Pump Modeling | 68 |
| 4.3. Experimental Set-up and Procedure..... | 71 |

| | | |
|--|--|-----|
| 4.3.1. | Measuring Instruments..... | 71 |
| 4.3.2. | Experimental Procedure..... | 72 |
| 4.4. | Results and Discussions | 72 |
| 4.4.1. | Effects of Submergence Ratio and Input Heat..... | 73 |
| 4.4.2. | Effects of Tube Diameter and Input Heat | 73 |
| 4.5. | Conclusions | 75 |
| | Nomenclature | 76 |
| | REFERENCES..... | 76 |
| CHAPTER 5 | | 79 |
| PERFORMANCE CHARACTERIZATION OF A BUBBLE PUMP FOR VAPOR ABSORPTION REFRIGERATION SYSTEMS..... | | 79 |
| 5.1. | Introduction..... | 79 |
| 5.2. | Analytical models..... | 84 |
| 5.3. | Theoretical Results..... | 94 |
| 5.4. | Experimental Technique | 97 |
| 5.3. | Measuring Instrument | 98 |
| 5.4.1. | Experimental procedure | 98 |
| 5.4.2. | Experimental Results and Model Validation | 99 |
| 5.4. | Conclusions | 100 |
| | Nomenclature | 102 |
| | REFERENCES..... | 103 |
| CHAPTER 6 | | 107 |
| BUBBLE-PUMP-DRIVEN LiBr-H ₂ O AND LiCl-H ₂ O ABSORPTION AIR- CONDITIONING SYSTEMS | | 107 |
| 6.1. | Introduction | 107 |
| 6.2. | System Description | 111 |

| | | |
|--|---|-----|
| 6.3. | Thermodynamic and Simulation Model..... | 112 |
| 6.3.1. | Thermodynamic properties | 117 |
| 6.4. | Results and Analysis | 117 |
| 6.5. | Conclusions | 123 |
| | Nomenclature | 124 |
| | REFERENCES..... | 124 |
| CHAPTER 7 | | 127 |
| ADVANCED EXERGY ANALYSIS OF A BUBBLE-PUMP-DRIVEN LiCl-H ₂ O ABSORPTION AIR-CONDITIONING SYSTEM | | 127 |
| 7.1. | Introduction | 127 |
| 7.2. | System Description | 128 |
| 7.3. | Thermodynamic Analysis | 129 |
| 7.3.1. | Conventional Exergy Analysis | 130 |
| 7.3.2. | Advanced Exergy Analysis..... | 132 |
| 7.4. | Theoretical Considerations..... | 135 |
| 7.5. | Results and Analysis | 136 |
| 7.6. | Conclusions | 145 |
| | Nomenclature | 147 |
| | REFERENCES..... | 147 |
| CHAPTER 8 | | 151 |
| DISCUSSION AND CONCLUSIONS | | 151 |
| 8.1. | Research Outcomes | 151 |
| 8.2. | Recommendations for Future Research | 156 |
| APPENDICES | | 159 |
| Appendix A..... | | 159 |

| | |
|--|-----|
| ENERGY EFFICIENCY AND ECONOMIC FEASIBILITY OF AN ABSORPTION AIR-CONDITIONING SYSTEM USING WET, DRY AND HYBRID HEAT REJECTION METHODS | 159 |
| A.1. Introduction | 159 |
| A.2. System Analysis | 162 |
| A.2.1. Thermodynamic analysis | 164 |
| A.2.2. Economic analysis..... | 165 |
| A.3. Simulation Procedure | 167 |
| A.4. Results and Analysis | 171 |
| A.4.1. Thermodynamic performance | 171 |
| A.4.2. Energy and Economic Performance..... | 175 |
| A.5. Conclusion..... | 178 |
| Nomenclature | 179 |
| REFERENCES..... | 179 |
| Appendix B | 184 |
| AIR LIFT PUMP AND TWO-PHASE FLOW..... | 184 |
| B.1. Two-Phase Flow..... | 184 |
| B.2. Methods of Analysis for Gas-Liquid Flow | 187 |
| B.3. Flow Pattern in Upward Vertical Two-Phase Flow | 189 |
| B.4. Mechanism for the breakdown of the bubbly flow pattern | 190 |
| B.5. Mechanism for the slug to churn flow transition | 191 |
| B.6. Air Lift Pump | 191 |
| REFERENCES..... | 193 |
| Appendix C | 195 |
| PERMISSIONS FOR PREVIOUSLY PUBLISHED WORKS | 195 |
| VITA AUCTORIS | 197 |

LIST OF TABLES

| | |
|---|-----|
| <i>Table 2.1: Temperature distribution for absorption and adsorption cooling system</i> | 28 |
| <i>Table 2.2: Different states thermodynamic properties of an ammonia-water absorption cycle at operating conditions $T_{gen} = 80^{\circ}\text{C}$, $T_{con} = 30^{\circ}\text{C}$, $T_{abs} = 30^{\circ}\text{C}$, $T_{eva} = 2^{\circ}\text{C}$, $\eta_{HEX} = 80\%$ and a cooling load of 10 kW</i> | 28 |
| <i>Table 2.3: Properties of activated carbon and ammonia for 10kW adsorption chiller at $T_{gen/des} = 80^{\circ}\text{C}$, $T_{cond} = 30^{\circ}\text{C}$, $T_{abs/ads} = 30^{\circ}\text{C}$, $T_{eva} = 2^{\circ}\text{C}$, for 2 hours cycle period.</i> | 28 |
| <i>Table 2.4: Energy flow for different component in absorption and adsorption system for 10 kW cooling capacity</i> | 29 |
| <i>Table 3.1: Thermodynamic properties at different states in ammonia-water absorption cycle at operating conditions $T_{gen} = 80^{\circ}\text{C}$, $T_{cond} = 30^{\circ}\text{C}$, $T_{abs} = 30^{\circ}\text{C}$, $T_{eva} = 2^{\circ}\text{C}$, $\eta_{HEX} = 80\%$ and a cooling load of 10 kW</i> | 52 |
| <i>Table 3.2: Energy flow for different components in ammonia-water absorption cycle</i> | 52 |
| <i>Table 5.1: Variables used in the bubble pump performance analysis and their dimensions</i> | 84 |
| <i>Table 5.2: Dimensional matrix with all independent variables for bubble pump performance</i> | 86 |
| <i>Table 5.3: Dimensional set for possible dimensional variables for bubble pump performance</i> | 86 |
| <i>Table 5.4: Dimensionless numbers and their physical interpretations</i> | 87 |
| <i>Table 6.1: Thermodynamic properties at different states in LiBr-H₂O and LiCl-H₂O absorption cycles at operating conditions $T_{gen} = 70^{\circ}\text{C}$, $T_{cond} = 35^{\circ}\text{C}$, $T_{abs} = 35^{\circ}\text{C}$, $T_{eva} = 7^{\circ}\text{C}$, $\eta_{HEX} = 80$, $D=10$ mm, $H=0.28$ m, and $L=0.47$ m.</i> | 119 |
| <i>Table 6.2: Thermodynamic analysis of bubble pump operated LiBr-H₂O and LiCl-H₂O absorption air-conditioning systems</i> | 119 |
| <i>Table 7.1: Energy and the exergy balance equations of the LiCl-H₂O absorption refrigeration cycle</i> | 132 |
| <i>Table 7.2: The algorithm and the assumption of parameters considering for different operating conditions of a LiCl-H₂O absorption refrigeration cycle</i> | 133 |

| | |
|---|-----|
| <i>Table 7.3: Thermodynamic properties at different states in LiCl-H₂O absorption cycles under ideal operating conditions $T_{gen} = 75^{\circ}\text{C}$, $T_{cond} = 35^{\circ}\text{C}$, $T_{abs} = 35^{\circ}\text{C}$, $T_{eva} = 7^{\circ}\text{C}$, $\eta_{HEX} = 90$, $D=10\text{ mm}$, $H=0.3\text{ m}$, $L=0.5\text{ m}$ and $Q_{BP} = 85\text{ W}$.</i> | 137 |
| <i>Table 7.4: Thermodynamic properties at different states in LiCl-H₂O absorption cycles under real operating conditions $T_{gen} = 70^{\circ}\text{C}$, $T_{cond} = 40^{\circ}\text{C}$, $T_{abs} = 40^{\circ}\text{C}$, $T_{eva} = 9^{\circ}\text{C}$, $\eta_{HEX} = 80\%$, $D=10\text{ mm}$, $H=0.3\text{ m}$, $L=0.5\text{ m}$ and $Q_{BP} = 80\text{ W}$.</i> | 137 |
| <i>Table 7.5: Thermodynamic properties at different states in LiCl-H₂O absorption cycles under unavoidable operating conditions $T_{gen} = 74.5^{\circ}\text{C}$, $T_{cond} = 35.5^{\circ}\text{C}$, $T_{abs} = 35.5^{\circ}\text{C}$, $T_{eva} = 7.2^{\circ}\text{C}$, $\eta_{HEX} = 88\%$, $D=10\text{ mm}$, $H=0.3\text{ m}$, $L=0.5\text{ m}$ and $Q_{BP} = 84\text{ W}$.</i> | 138 |
| <i>Table 7.6: Results of conventional exergy analysis of a LiCl-H₂O absorption refrigeration cycle under different operating conditions.</i> | 139 |
| <i>Table 7.7: Results of advanced exergy analysis of a LiCl-H₂O absorption refrigeration cycle.</i> | 140 |
| <i>Table A.1: Electrical energy consumption by pumps of a 15 kW absorption cooling system [Shafiullah, 2016].</i> | 168 |
| <i>Table A.2: Variation of dry-bulb and wet-bulb temperature with respect to absorber temperature</i> | 168 |
| <i>Table A.3: Type51b: Input variables for cooling tower</i> | 170 |
| <i>Table A.4: Type511: Input variables for cooling tower</i> | 170 |
| <i>Table A.5: Energy flow rate of each component of 15 kW NH₃-H₂O absorption air-conditioning system.</i> | 171 |
| <i>Table A.6: Energy and economic performance of different cooling methods of absorption chiller at operating condition of at $T_{gen}=80^{\circ}\text{C}$, $T_{eva}=6^{\circ}\text{C}$, $T_{abs}=35^{\circ}\text{C}$, $T_{cond}=40^{\circ}\text{C}$</i> | 177 |
| <i>Table B.1: Classification of two-phase flow [Ishii & Hibiki, 2013].</i> | 185 |

LIST OF FIGURES

| | |
|---|----|
| <i>Figure 1.1: Vapor Absorption Refrigeration System (VARS).....</i> | 4 |
| <i>Figure 1.2: Schematic of DAR System.....</i> | 6 |
| <i>Figure 1.3: Schematic of bubble-pump-driven LiBr-H₂O VARS.....</i> | 7 |
| <i>Figure 2.1: Schematic diagram of the solar ammonia-water absorption cooling cycle</i> | 19 |
| <i>Figure 2.2: Schematic of Solar Adsorption Cooling System.</i> | 21 |
| <i>Figure 2.3: Clapeyron diagram for thermodynamic cycle of adsorption cooling system.....</i> | 21 |
| <i>Figure 2.4: Performance comparison of absorption & adsorption cooling systems at different cooling load with ammonia concentration in/on absorbent/adsorbent same as 10 kW system, operating at $T_{gen} = 80^{\circ}\text{C}$ $T_{cond} = 30^{\circ}\text{C}$, $T_{eva} = 2^{\circ}\text{C}$, $T_{abs/ads} = 30^{\circ}\text{C}$.....</i> | 30 |
| <i>Figure 2.5: Effect of generator or desorber temperature on the COP for 10 kW absorption & adsorption cooling systems at $T_{cond} = 30^{\circ}\text{C}$, $T_{eva} = 2^{\circ}\text{C}$, $T_{abs/ads} = 30^{\circ}\text{C}$.</i> | 32 |
| <i>Figure 2.6: Effect of desorber temperature on the COP and carbon content for 10kW adsorption cooling system at $T_{cond} = 30^{\circ}\text{C}$, $T_{eva} = 2^{\circ}\text{C}$, $T_{ads} = 30^{\circ}\text{C}$.</i> | 33 |
| <i>Figure 2.7: Cooling capacity variation with increasing generator or desorber temperature for a constant temperature of 2°C in the evaporator at $T_{cond} = 30^{\circ}\text{C}$, $T_{abs/ads} = 30^{\circ}\text{C}$.</i> | 33 |
| <i>Figure 2.8: Effect of absorber or adsorber temperature on the COP for 10kW Absorption & Adsorption cooling system at $T_{cond} = 30^{\circ}\text{C}$, $T_{eva} = 2^{\circ}\text{C}$, $T_{gen/des} = 80^{\circ}\text{C}$.</i> | 34 |
| <i>Figure 3.1: Schematic diagram of the solar ammonia-water absorption cooling cycle</i> | 44 |
| <i>Figure 3.2: Pressure, concentration and temperature diagram of ammonia - water mixture.</i> | 45 |
| <i>Figure 3.3: Non-dimensional exergy loss of different components of a 10kW system at $T_{gen} = 80^{\circ}\text{C}$, $T_{cond} = 30^{\circ}\text{C}$, $T_{abs} = 30^{\circ}\text{C}$, $T_{eva} = 2^{\circ}\text{C}$, $\eta_{HEX} = 80\%$.....</i> | 53 |
| <i>Figure 3.4: Effect of generator temperature on the COP, reversible COPE and exergetic efficiency at $T_{cond} = 30^{\circ}\text{C}$, $T_{abs} = 30^{\circ}\text{C}$, $T_{eva} = 2^{\circ}\text{C}$, $\eta_{HEX} = 80\%$.....</i> | 54 |

| | |
|---|------------|
| <i>Figure 3.6: Effect of generator temperature on the circulation ratio (CR) at $T_{cond} = 30^{\circ}\text{C}$, $T_{abs} = 30^{\circ}\text{C}$, $T_{eva} = 2^{\circ}\text{C}$, $\eta_{HEX} = 80\%$.....</i> | <i>55</i> |
| <i>Figure 3.7: Effect of evaporator temperature on the COP, reversible COP_E and exergetic efficiency of 10kW system at $T_{gen} = 80^{\circ}\text{C}$, $T_{cond} = 30^{\circ}\text{C}$, $T_{abs} = 30^{\circ}\text{C}$, $\eta_{HEX} = 80\%$</i> | <i>56</i> |
| <i>Figure 3.8: Effect of evaporator temperature on the total exergy loss of 10kW system at $T_{gen} = 80^{\circ}\text{C}$, $T_{cond} = 30^{\circ}\text{C}$, $T_{abs} = 30^{\circ}\text{C}$, $\eta_{HEX} = 80\%$.....</i> | <i>56</i> |
| <i>Figure 3.9: Effect of condenser temperature on the COP, reversible COP_E and exergetic efficiency of 10kW system at $T_{gen} = 80^{\circ}\text{C}$, $T_{abs} = 30^{\circ}\text{C}$, $T_{eva} = 2^{\circ}\text{C}$, $\eta_{HEX} = 80\%$.....</i> | <i>57</i> |
| <i>Figure 3.10: Effect of condenser temperature on the total exergy loss of 10kW system at $T_{gen} = 80^{\circ}\text{C}$, $T_{abs} = 30^{\circ}\text{C}$, $T_{eva} = 2^{\circ}\text{C}$, $\eta_{HEX} = 80\%$.....</i> | <i>58</i> |
| <i>Figure 3.11: Effect of absorber temperature on the COP, reversible COP_E and exergetic efficiency of 10kW system at $T_{gen} = 80^{\circ}\text{C}$, $T_{cond} = 30^{\circ}\text{C}$, $T_{eva} = 2^{\circ}\text{C}$, $\eta_{HEX} = 80\%$.....</i> | <i>59</i> |
| <i>Figure 3.12: Effect of absorber temperature on the total exergy loss of 10kW system at $T_{gen} = 80^{\circ}\text{C}$, $T_{cond} = 30^{\circ}\text{C}$, $T_{eva} = 2^{\circ}\text{C}$, $\eta_{HEX} = 80\%$.....</i> | <i>59</i> |
| <i>Figure 4.1: Flow regimes in a bubble pump.....</i> | <i>66</i> |
| <i>Figure 4.2: Bubble pump schematic and experimental set-up</i> | <i>71</i> |
| <i>Figure 4.3: Bubble pump performance for different SR ratio at $D=8\text{ mm}$.....</i> | <i>74</i> |
| <i>Figure 4.4: Bubble pump performance for different diameter at submergence ratio, $SR=0.8$.</i> | <i>75</i> |
| <i>Figure 5.1: Vapor Absorption Refrigeration System.....</i> | <i>80</i> |
| <i>Figure 5.2: Bubble Pump in Vapor Absorption Refrigeration System.....</i> | <i>80</i> |
| <i>Figure 5.3: Bubble Pump Apparatus used.....</i> | <i>89</i> |
| <i>Figure 5.4: Performance characteristics of a bubble pump at $vb'=0.145$.....</i> | <i>96</i> |
| <i>Figure 5.5: Flow regime of a bubble pump.</i> | <i>98</i> |
| <i>Figure 5.6: Comparison between theoretical and experimental results of a bubble pump at different P' for $\text{LiCl-H}_2\text{O}$ ($vb'=0.145$) and pure water ($vb'=0.038$) working fluids.....</i> | <i>100</i> |
| <i>Figure 6.1: Flow diagram of solar absorption air-conditioning system.....</i> | <i>112</i> |

| | |
|---|------------|
| <i>Figure 6.2: Bubble Pump Generator Control Volume</i> | <i>113</i> |
| <i>Figure 6.3: Solution Heat Exchanger Control Volume</i> | <i>116</i> |
| <i>Figure 6.4: Absorber Control Volume.....</i> | <i>116</i> |
| <i>Figure 6.5: Evaporator Control Volume</i> | <i>116</i> |
| <i>Figure 6.6: Condenser Control Volume</i> | <i>117</i> |
| <i>Figure 6.7: Performance comparison of a bubble pump operated LiBr-H₂O VARS between the proposed model and the experimental results of Saravanan & Maiya [2003].</i> | <i>118</i> |
| <i>Figure 6.8: Lifting ratio of LiBr-H₂O and LiCl-H₂O VARS at different bubble pump heat input at T_{gen} = 70°C.....</i> | <i>121</i> |
| <i>Figure 6.9: Strong solution and refrigerant flow rate by the bubble pump at different heat input at T_{gen} = 70°C for LiBr-H₂O and LiCl-H₂O.....</i> | <i>121</i> |
| <i>Figure 6.10: Coefficient of performance of LiBr-H₂O and LiCl-H₂O VARS at different bubble pump heat input at T_{gen} = 70°C, T_{cond} = 35°C, T_{abs} = 35°C, T_{eva} = 7°C, η_{HEX} = 80.....</i> | <i>122</i> |
| <i>Figure 7.1: Flow diagram of a bubble pump operated vapor absorption air-conditioning system.....</i> | <i>129</i> |
| <i>Figure 7.2: The total exergy destruction split into the endogenous, exogenous, unavoidable, avoidable, endogenous-unavoidable, exogenous-unavoidable, endogenous-avoidable, and exogenous-avoidable divisions for each component.</i> | <i>144</i> |
| <i>Figure 7.3: Exergy destruction ratio of the overall system based on advanced exergy analysis.</i> | <i>144</i> |
| <i>Figure 7.4: Exergy destruction rate of each component of a bubble-pump-driven LiCl-H₂O absorption refrigeration cycle based on conventional exergy and advanced exergy analyses.....</i> | <i>145</i> |
| <i>Figure A.1: Schematic of a wet/dry cooled single-effect NH₃-H₂O absorption cooling system.....</i> | <i>163</i> |
| <i>Figure A.2: Schematic of a hybrid-cooled single-effect NH₃-H₂O absorption cooling system.....</i> | <i>163</i> |
| <i>Figure A.3: Simulation procedure for the analysis of a 15 kW NH₃-H₂O absorption cooling system with different heat rejection methods.....</i> | <i>169</i> |

| | |
|---|-----|
| <i>Figure A.4: Electrical COP of 15kW NH₃-H₂O absorption cooling system with different heat rejection methods at T_{gen}=80°C, T_{eva}=6°C.</i> | 173 |
| <i>Figure A.5: Primary Energy Ratio (PER) of 15 kW NH₃-H₂O absorption cooling system with different heat rejection methods at T_{gen}=80°C, T_{eva}=6°C.</i> | 174 |
| <i>Figure A.6: Electrical energy consumption and water flow rate of 15 kW NH₃-H₂O absorption cooling system with different heat rejection methods at T_{gen}=80°C, T_{eva}=6°C.</i> | 175 |
| <i>Figure A.7: Electricity consumption per year in Canada and UAE for 15 kW NH₃-H₂O absorption cooling system with different heat rejection methods.</i> | 176 |
| <i>Figure A.8: Water consumption per year in Canada and UAE for 15 kW NH₃-H₂O absorption cooling system with wet and hybrid heat rejection methods.</i> | 177 |
| <i>Figure B.1: Schematic of Air-Lift pump</i> | 184 |
| <i>Figure B.2: Operation curve for a 9.53 mm in diameter air-water lift pump at H/L=0.8.</i> | 193 |

LIST OF APPENDICES

Appendix A: Energy efficiency and economic feasibility of an absorption air-conditioning system using wet, dry and hybrid heat rejection methods.

Appendix B: Air-lift pump and two-phase flow.

Appendix C: Permissions for previously published works.

CHAPTER 1

INTRODUCTION

1.1. Overview

According to the International Energy Agency, present energy sources and use are economically, environmentally and socially unsustainable [OECD/IEA, 2012]. The increasing energy demand and the price of traditional energy resources is stimulating the practice of energy conservation, and the search for alternative energy sources. Due to climate change, population growth, and increasing standard of living conditions, residential and small commercial air-conditioning demands are increasing significantly. Building heating and cooling systems account for 50% of the total global energy consumption [Kharseh *et al.*, 2011]. In tropical countries, 70% of the total household energy is being used by air-conditioning systems [Prasartkaew & Kumar, 2013]. The International Institute of Refrigeration reported that refrigeration and air conditioning systems consume approximately 15% of the total world electricity generation [Kalkan *et al.*, 2012]. This percentage is predicted to increase with the rise in world summer temperature of 2 ~ 4°C by the end of the century [IPCC, 2007]. Climate change and an increase in the standard of living will continue to increase the demand for air-conditioning, which will further increase electricity consumption. This is especially poignant in developing countries, where the rapid growth of the economy and consequent prosperity has caused a rapid rise in conventional air conditioning system installation and use [Hassan, 2013]. The growth of the air conditioning market worldwide has been significantly elevated in recent years, accelerating the consumption of electricity. Approximately 80% of the world's electricity is being generated from fossil fuels, which contribute significantly to greenhouse gas emissions [Fong, *et al.*, 2010]. Therefore, it is crucial to reduce the consumption of unsustainable fossil fuels, and at the same time, it is imperative to promote sustainable energy technology to meet the increasing energy demand in an environmentally friendly manner. Solar technologies are a sustainable means to meet this increasing energy demand. The abundant amount of solar radiation in most tropical and developing countries is a renewable energy source, which is available most of the year [Ashhab *et al.*, 2013]. This

abundant solar power makes solar cooling technology a suitable alternative, particularly for people who live in remote areas and suffer from a shortage of electricity.

1.1.1. Solar Thermal Cooling

Thermally-driven cooling systems have already been proven for their technical feasibility. The traditional vapor compression machine used for air-conditioning operates on electrically driven compressor chillers. Their operation causes a high energy demand during the peak load period in the summer, which triggers the start-up of fossil fuel power plants in some jurisdictions, such as Ontario, where the base load is met by nuclear power. Solar thermal cooling could reduce electricity needs during the peak periods in summer by replacing electrically driven compressor chillers with thermally driven chillers. In addition, the peak electrical energy demand in the summer occurs a few hours after the highest solar irradiation. This offset between energy supply and cooling demand can be met by incorporating heat storage into the solar collector loop of the system. Furthermore, this heat storage will also provide cooling comfort beyond sunset during the night.

The most common method for producing thermally activated cooling is sorption cooling. Sorption includes both absorption and adsorption: “absorption is the process in which a substance in one phase is incorporated into another substance of a different phase (e.g. gas being absorbed by a liquid); whereas adsorption refers to the use of a solid for adhering or bonding ions and molecules of another substance onto its surface” [Deng *et al.*, 2011]. The adsorption process creates a film of a gas or liquid substance (adsorbate) on a solid surface (adsorbent). This is a surface-based process whereas absorption utilizes the whole volume of the material [Choudhury *et al.*, 2013].

In sorption cooling systems, thermal compression of the refrigerant is employed instead of mechanical compression. The absorption and adsorption cooling technologies are mostly used in central air conditioning systems with decentralized fan coils or cooled ceilings [Treberspurg *et al.*, 2011]. The development and use of sorption cooling technologies are increasing of interest because of their simple construction, long life time, low operating costs and low temperature heat source benefits.

Currently, different cooling technologies driven by waste heat are available, but they are mostly sized for 50 kW capacities, whereas small scale technology is still emerging and

requires low-cost systems with minimal maintenance requirements. Recently, some companies have taken initiatives to improve absorption chillers in the power range from 50 kW down to 5 kW [Kalkan *et al.*, 2012]. For residential buildings, the required cooling capacity should be within the range of 3 to 10 kW [Wang *et al.*, 2009]. However, very few chillers are available for small scale cooling applications (less than 10kW), and they are not optimized for solar thermal power applications [Boudehenn *et al.*, 2012]. According to the International Energy Agency, small-scale system design requires R&D effort in order to develop low-cost systems, integrate them with existing equipment and optimize operation in new developments. Small-scale technology development should focus on compact machines with higher coefficients of performance (COPs) at low driving heat temperatures [OECD, 2012].

In a sorption cycle, a refrigerant and a sorbent are a pair of substances that work together. Lithium bromide-water and water-ammonia are the most common working pairs in refrigeration and air conditioning absorption refrigeration systems. Lithium bromide-water absorption systems have been used widely and are the most common and efficient for large scale air conditioning applications, as products in the range of 20 to 11,630 kW are available on the market [Deng *et al.*, 2011]. Water-ammonia machines are most commonly used for small size residential or large capacity industrial refrigeration applications [Abdulateef *et al.*, 2008]. Silica gel-water adsorption chillers are currently used for commercial applications. Adsorption cooling systems with carbon adsorbent and ammonia, ethanol, and methanol as the refrigerant are now being examined for the development of small scale applications [Askalany *et al.*, 2012].

1.1.2. Bubble-Pump-Driven Vapor Absorption Refrigeration Systems (VARS)

A vapor absorption refrigeration system (VARS) can be driven by waste heat or solar thermal energy. LiBr-H₂O and NH₃-H₂O are the most common refrigerant-absorbent working pairs for a VARS. The LiBr-H₂O absorption system has the advantage of higher efficiency, but due to its crystallization and corrosion problems, NH₃-H₂O is more preferable for small scale commercial or residential applications. The core components of absorption cooling systems are the absorber, generator, condenser and evaporator as shown in Figure 1.1. In this system, the solution is heated in the generator by solar or waste heat.

The high-pressure refrigerant vapor from the generator is condensed in the condenser, its pressure is lowered through the throttle valve, and becomes low pressure liquid refrigerant. This low pressure and low temperature liquid refrigerant enters the evaporator where the cooling effect occurs. The low pressure evaporated refrigerant vapor from the evaporator is absorbed by the liquid solution in the absorber, which is then pumped to the generator by the solution pump. After evaporating the refrigerant in the generator, the remaining liquid solution passes through the pressure reducing throttle valve and flows back to the absorber at low pressure.

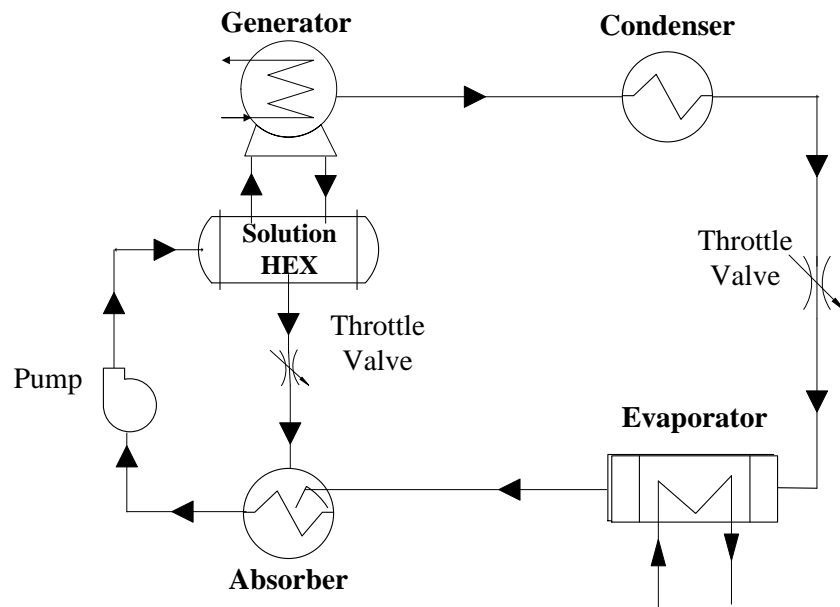


Figure 1.1: Vapor Absorption Refrigeration System (VARs)

A pump is a critical component of the absorption system to circulate the refrigerant–absorbent solution from the low-pressure absorber to the high-pressure generator. High quality mechanical/electrical energy is used to run this pump. Furthermore, the pump must handle high temperature corrosive solutions. A thermally-driven-bubble-pump, which can be powered by waste heat or solar thermal energy, can be employed to circulate the liquid solution and generate the necessary refrigerant for the required cooling effect. In a bubble pump, the vapor created (via heating) increases the buoyancy of the fluid, causing it to ascend through a vertical tube under two-phase flow conditions. For small scale applications like residential air-conditioning, this system will be more reliable than an electrical pump and independent of the availability of electricity. But for larger scale

applications of bubble-pump-operated VARS, multiple parallel pumps may be explored [Saravanan & Maiya, 2003].

1.1.3. Diffusion absorption refrigeration (DAR) systems

The conventional absorption refrigeration cycle works at two pressure levels to achieve the saturation temperature difference between the condenser and the evaporator. But in a diffusion absorption refrigeration system where the circulation of the solution is carried out by a bubble pump, there is essentially a single pressure throughout the entire cycle. Although it is called a 'single pressure' system, there are still minor pressure variations due to the flow friction and gravity. A heat-driven-bubble-pump is a mechanism to move the fluid through the cycle against this flow friction and gravity.

The single pressure absorption system cycle works on two thermodynamic cycles: the ammonia-water-hydrogen cycle and the Einstein cycle. The most familiar is the ammonia-water-hydrogen cycle which is known as the diffusion absorption refrigeration (DAR) cycle, shown in Figure 1.2, patented by Swedish engineers Platen and Munter in 1920 [Platen & Munter, 1928]. This cycle uses at least three working fluids to achieve a low evaporation temperature and high condensation temperature at a single pressure level. The third, (inert) fluid is introduced to the working fluid to lower the partial pressure of the refrigerant in the evaporator and maintain pressure equalization throughout the system. Thus, the refrigerant can evaporate at a lower temperature in the evaporator. The most common working fluids for this cycle are ammonia-water-hydrogen/helium where ammonia is the refrigerant, water is the absorbent and hydrogen or helium is the inert gas which provides the pressure equalization of the system. In the Platen and Munter cycle, the refrigerant ammonia is absorbed by the water and its partial pressure is lowered by the inert gas hydrogen or helium. The water separates the ammonia from the inert gas. In 1930, Albert Einstein and Szilard Leo disclosed another single pressure refrigeration cycle which uses butane, ammonia, and water [Delano, 1998]. Unlike the Platen and Munter cycle, the Einstein cycle utilizes absorbate fluid for pressure equalization instead of an inert gas. In this cycle, butane works as the refrigerant, ammonia is used to lower the partial pressure of the refrigerant, and water is used to absorb the ammonia and separate the butane.

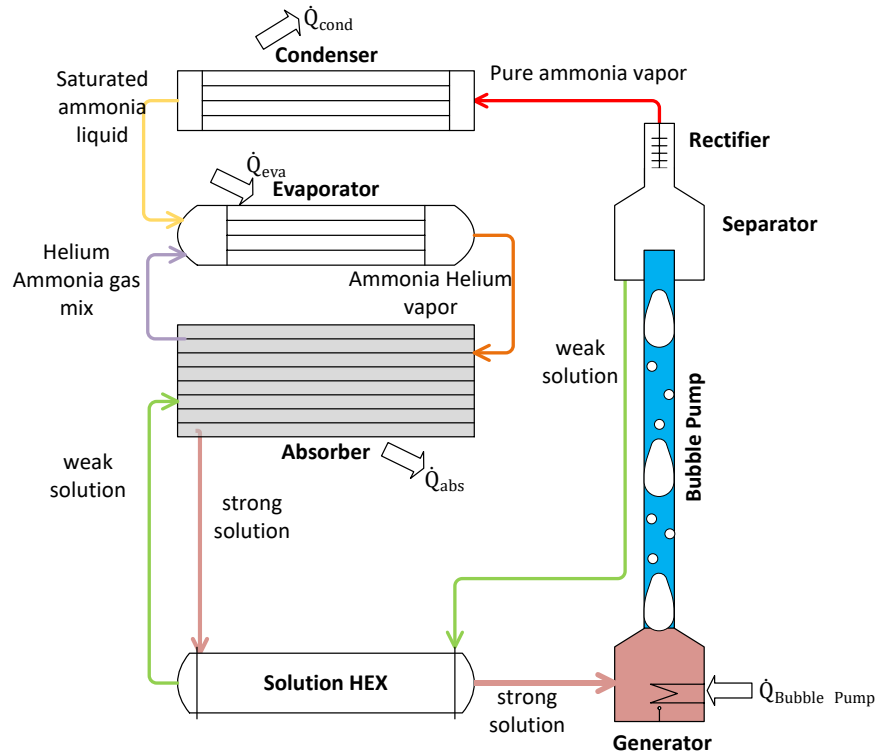


Figure 1.2: Schematic of DAR System.

1.1.4. Water-based refrigerant VARS

The pressure difference between the evaporator and the condenser should be low so that it can operate using a bubble pump in a water-based refrigeration system [Saravanan & Maiya, 2003], as shown in Figure 1.3. The water vapor pressure difference between the condenser and the evaporator of a water-salt refrigeration system is low enough to employ the bubble pump to circulate the solution and refrigerant in the system. However, the pressure-drop in the connecting tubes and in the system components is a major concern for this system because it operates under vacuum pressure. For a conventional large-scale LiBr-H₂O VARS, pressure equalizers are used to minimize the pressure loss [Saravanan & Maiya, 2003]. In bubble-pump-operated, water-based refrigerant VARS, the condenser pressure depends on the water vapor pressure from the bubble pump generator. Hence, the pressure difference between the condenser and the evaporator is lower than the conventional VARS. Therefore, the pressure drop in the system may affect the ability to

achieve this pressure difference. Hence, little research has been carried out in the use of bubble pumps in LiBr-H₂O VARS and commercial applications are not yet practicable.

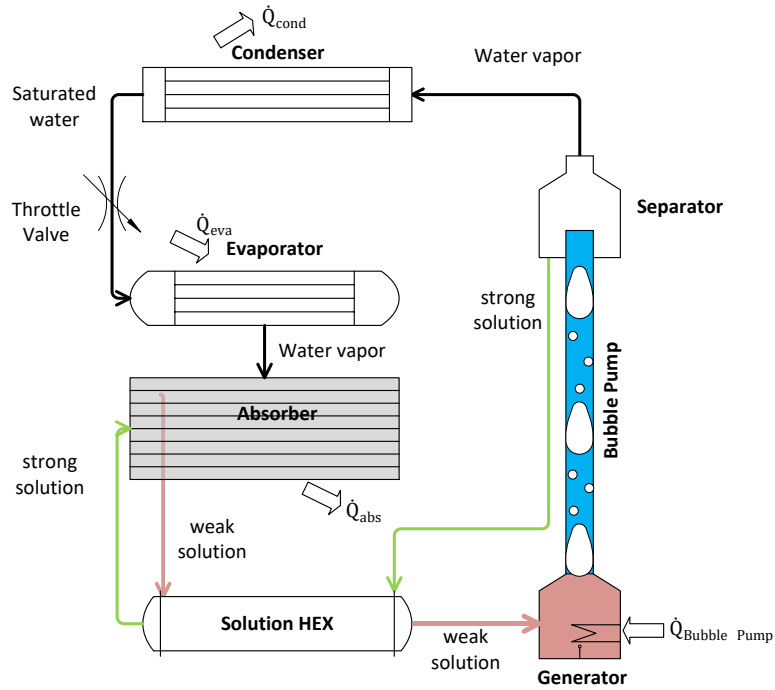


Figure 1.3: Schematic of bubble-pump-driven LiBr-H₂O VARS.

1.2. Objective and Scope of Work of this Study

The overall objective of this research is to identify an efficient air-conditioning system for residential applications that can be driven by a low temperature heat source such as flat-plate solar collectors and by using an environment friendly refrigerant. Targeting the systems to provide air conditioning in remote households, reliably and independent of the availability of electricity necessitates the use of a bubble pump VARS.

The following describes the scope of work:

- 1 Identify an appropriate thermal cooling system that can be compatible for using solar thermal energy in order to provide air conditioning in small scale applications such as in a residential home.
- 2 Optimize the operating conditions so that the systems can be driven by low temperature heat from flat-plate solar collectors and by using an environment friendly refrigerant.

- 3 Analyze the energy conversion and exergy destruction rate of an absorption cooling system in order to identify the components that need to be improvement for increasing the system performance.
- 4 Design, build and operate an experimental apparatus to quantify the inputs/outputs of a bubble pump to be used in a solar absorption cooling system.
- 5 Develop an analytical model that will contain a group of non-dimensional numbers accounting for the influence of all thermodynamic properties of the working fluid and geometric parameters of a bubble pump on the system performance.
- 6 Select a suitable environment-friendly refrigerant for higher system performance.
- 7 Analyze the advanced exergy in a bubble-pump-driven VARS for improving system performance and identifying system components which may play a major role in this improvement.

1.3. Thesis Organization

For the accomplishment of this research, the thesis has been organized as follows:

Chapter 1

The high temperature requirement and low efficiency are the downsides of an absorption chiller for small-scale air conditioning applications. Providing efficient air conditioning in residential communities that can be driven by solar thermal energy is the objective of this research. The overview, and scope of work is described in the current chapter.

Chapter 2

Absorption and adsorption cooling are the best alternatives to vapor compression cooling in residential air-conditioning applications. So, it is very important to compare these two cooling systems and their compatibility for residential applications. Though analysis of these two systems individually has been reported in the literature, component-by-component comparison of these sorption technologies has not been reported. Simplified thermodynamic models for absorption and adsorption were developed and used

in this chapter. Due to the benefits of ammonia as a refrigerant for small scale applications and the good absorbent properties of activated carbon, ammonia-water absorption and activated carbon-ammonia adsorption systems were compared in this chapter.

Chapter 3

Lithium bromide-water and ammonia-water are the most common working pairs in refrigeration and air conditioning absorption refrigeration systems. For low evaporator temperatures, the lithium bromide-water pair is not suitable, so research to improve the thermal performance of the ammonia-water absorption cycle has been increased. A complete thermodynamic analysis (energy and exergy methods) was performed to determine the losses occurring in an ammonia-water system due to the irreversibilities. The analysis identified the least efficient component in the system.

Chapter 4

In this study, an analytical model of a bubble pump was developed and experimental work was conducted in order to evaluate the efficiency of a bubble pump. In the simulation model, two-phase turbulent flow with heat loss, friction, surface tension effects and other thermophysical properties was considered. The model was validated by operating the bubble pump with water at atmospheric conditions.

Chapter 5

In a bubble-pump-operated single-pressure absorption refrigeration system, the cycle performance totally depends on the refrigerant-absorbent solution properties and the bubble pump parameters. The thermodynamic properties of a solution include viscosity, heat capacity, surface tension, thermal conductivity of single- and two-phase fluids, and the bubble pump parameters include the diameter of the tube, the height of the tube, surface roughness and gas-liquid two-phase flow patterns. To generalize these variables, it is essential to perform a dimensional analysis that will yield a group of dimensionless numbers describing the influence of important thermodynamic properties and geometric parameters of a bubble pump on the system performance. In this chapter, a dimensional analysis was performed to represent the performance characteristics of a bubble pump,

considering the thermophysical properties of the solution and the geometric parameters of the bubble pump. The non-dimensional parameters should be valid for all fluids and geometries. In this work, the experimentation was performed using pure water and LiCl-H₂O to validate the suggested model for the bubble pump performance.

Chapter 6

Since low efficiency is the main downside of bubble-pump-operated absorption refrigeration systems and the cycle efficiency depends on the amount of refrigerant desorbed from the generator, so a detailed analysis of the bubble pump generator is needed before one can improve the system efficiency. A new absorbent-refrigerant pair (LiCl-H₂O) is introduced in this chapter. Other research has shown that the LiCl-H₂O system has advantages over LiBr-H₂O system in terms of high system performance, high vapor pressure as well as low energy consumption [Saravanan & Maiya, 1998, Flores *et al.*, 2014, She *et al.*, 2015, Gogoi & Konwar, 2016, Bellos *et al.*, 2017]. In this study, the thermophysical properties of LiBr-H₂O and LiCl-H₂O were incorporated in the bubble pump modelling. This chapter also focused on the development of a mathematical simulation model for the bubble pump generator by using a two-phase flow model that can determine the cooling effect of the refrigeration cycle and a thermodynamic model of every component of this cycle in order to achieve the maximum system efficiency.

Chapter 7

For identifying the magnitude, location, and the source of thermodynamic inefficiencies in a bubble-pump-driven LiCl-H₂O vapor absorption refrigeration system, conventional exergy and advanced exergy analyses are presented in this chapter. The conventional exergy analysis was performed for each component and the total exergy destruction of each component was divided into endogenous, exogenous, unavoidable, and avoidable sub-divisions in order to identify where to focus in order to reduce exergy destruction for the improvement of the overall system performance.

Chapter 8

This chapter summarizes the findings and conclusions of each chapter, and the final conclusions of this research. Suggestions for future work are also included.

Appendix A

The effect of different heat rejection methods for the absorber and the condenser were simulated and the results were discussed in this appendix.

Appendix B

The analysis of two phase flow in an air-lift pump is discussed in this section.

REFERENCES

- Abdulateef J.M., Sopian K., Alghoul M.A., Optimum design for solar absorption refrigeration systems and comparison of the performances using ammonia-water, ammonia-lithium nitrate and ammonia-sodium thiocyanate solutions. *International Journal of Mechanical and Materials Engineering*, 3 (2008) 17-24.
- Ashhab M. S. S., Kaylani H., Abdallah A., PV solar system feasibility study. *Energy Conversion and Management*, 65 (2013) 777–782.
- Askalany A., Salem A., Ismail I.M., Hamza A., Ali H., Morsy M.G, A review on adsorption cooling systems with adsorbent carbon. *Renewable and Sustainable Energy Reviews*, 16 (2012) 493– 500.
- Bellos E., Tzivanidis C., Pavlovic S., Stefanovic V., Thermodynamic investigation of LiCl-H₂O working pair in a double effect absorption chiller driven by parabolic trough collectors. *Thermal Science and Engineering Progress*, 3 (2017) 75–87.
- Boudéhenn F., Demasles H., Wytttenbach J., Jobard X., Chèze D., Papillon P., Development of a 5 kW cooling capacity ammonia-water absorption chiller for solar cooling applications. *Energy Procedia*, 30 (2012) 35 – 43.
- Choudhury B., Chatterjee P.K., Sarkar J.P., Review paper on solar-powered air-conditioning through adsorption route. *Renewable and Sustainable Energy Reviews*, 14 (2010) 2189- 2195.

- Delano A. Design Analysis of the Einstein Refrigeration Cycle, Ph.D. Thesis, Georgia Institute of Technology, 1998, http://www.me.gatech.edu/energy/andy_phd.
- Deng J., Wang R.Z., Han G.Y., A review of thermally activated cooling technologies for combined cooling, heating and power systems. *Progress in Energy and Combustion Science*, 37 (2011) 172-203.
- Flores V. H. F., Román J.C., Alpírez G.M., Performance analysis of different working fluids for an absorption refrigeration cycle. *American Journal of Environmental Engineering*, 4(4A) (2014) 1-10, DOI: 10.5923/s.ajee.201401.01.
- Fong K. F., Chow T. T., Lee C.K., Lin Z., Chan L.S., Comparative study of different solar cooling systems for buildings in subtropical city. *Solar Energy*, 84 (2010) 227–244.
- Gogoi T.K., Konwar D., Exergy analysis of a H₂O–LiCl absorption refrigeration system with operating temperatures estimated through inverse analysis. *Energy Conversion and Management*, 110 (2016) 436–447.
- Hassan H. Z., A Solar Powered Adsorption Freezer: A Case Study for Egypt’s Climate. *International Journal of Energy Engineering*, 3 (2013) 21-29.
- IPCC, Intergovernmental Panel on Climate Change, IPCC Fourth Assessment Report: Climate Change 2007.
- Kalkan N., Young, E.A., Celiktas, A., Solar thermal air conditioning technology reducing the footprint of solar thermal air conditioning. *Renewable and Sustainable Energy Reviews*, 16 (2012) 6352–6383.
- Kharseh M., Altorkmany L., Nordell B., Global warming’s impact on the performance of GSHP. *Renewable Energy*, 36 (2011) 1485–1491.
- OECD/IEA, Technology Roadmap Solar Heating and Cooling. International Energy Agency, 2012.
- Platen, B.C. Munters, C.G., 1928. Refrigerator. U.S. Patent 1,685,764.
- Prasartkaew B., Kumar S., Experimental study on the performance of a solar-biomass hybrid air-conditioning system. *Renewable Energy*, 57 (2013) 86-93.
- Saravanan R., Maiya M.P., Experimental analysis of a bubble pump operated H₂O–LiBr vapor absorption cooler. *Applied Thermal Engineering*, 23 (2003) 2383–2397.

- Saravanan R., Maiya M.P., Thermodynamic comparison of water-based working fluid combinations for a vapour absorption refrigeration system. *Applied Thermal Engineering*, 18(7) (1998) 553-568.
- She X., Yin Y., Mengfei Xu M., Zhang, X., A novel low-grade heat-driven absorption refrigeration system with LiCl-H₂O and LiBr-H₂O working pairs. *International Journal of Refrigeration*, 58 (2015) 219-234.
- Treberspurg M., Djalili M., Staller H., New technical solutions for energy efficient buildings, State of the art report: solar heating & cooling. *SCI-Network: Sustainable Construction & Innovation through Procurement*, July 2011.
- Wang R.Z., Ge T.S., Chen C.J., Ma Q., Xiong Z.Q., Solar sorption cooling systems for residential applications: Options and guidelines. *International Journal of Refrigeration*, 32 (2009) 638 – 660.
- White S.J., Bubble Pump Design and Performance. MSc Thesis. Georgia Institute of Technology, Atlanta, USA. Mechanical Engineering. 2001.

CHAPTER 2

SOLAR SORPTION COOLING FOR RESIDENTIAL AIR-CONDITIONING APPLICATIONS

This work was published as “Aman, J., Henshaw, P. Ting, D. S-K., Solar sorption cooling for residential air-conditioning applications, International Journal of Renewable Energy Technologies, in press”.

2.1. Introduction

Thermal cooling technologies are classified as sorption cooling and desiccant cooling. Sorption cooling technologies are increasingly being developed and used because of their simple construction, low operating costs, low temperature heat source and long lifetime [Zhai et al., 2008; McNeil & Letschert, 2007]. At present, most of the air-conditioning systems driven by solar energy are based on solar sorption cooling [Zhai & Wang, 2009]. It is reported that solar assisted cooling systems can save 40 – 50% of the primary energy in Europe and the Mediterranean areas Balaras *et al.* [2007].

Thermally activated sorption cooling may be further categorized into absorption and adsorption cooling. In the absorption process, two different phases of substances are incorporated with each other, whereas, molecules or ions of different substances bond or adhere on the solid surfaces in adsorption process [Deng *et al.*, 2011]. The mechanical compressor used in conventional vapor compression systems may be replaced by the thermal compressor in sorption cooling systems. In central air conditioning systems, these two technologies are mostly used with decentralized fan coils or via cooling ceilings that provide cooling to the room by radiation and convection [Treberspurg *et al.*, 2011].

Absorption cooling systems

A refrigerant and an absorbent form a working pair in an absorption refrigeration system. Water-ammonia and lithium bromide-water are the most common working pairs that are usually used in absorption refrigeration and air conditioning systems. Currently, lithium bromide-water absorption chillers are mostly used for large scale applications. But in small scale applications, the lithium bromide-water absorption chillers are limited

because of their crystallization problem, high initial cost, and high absorber temperature [Aman et al., 2014]. For small size (<30 kW) cooling or residential air conditioning (3 to 10 kW) applications, the ammonia-water pair is widely used [Abdulateef *et al.*, 2008; Wang *et al.*, 2009]. Furthermore, the physical properties of ammonia (refrigerant with low specific volume and high pressure) enable the ammonia-water chiller to be compact [Aman *et al.*, 2014, Pons *et al.*, 1999].

The water-ammonia chiller for air conditioning was first introduced in 1964 [Ryan, 2002] and was driven by direct-fire. But it lost popularity because of its lower efficiency, compared to electrically-driven vapor compression systems. Recently, high efficiency water-ammonia chillers have been developed for light commercial and residential applications. The addition of a high efficiency heat exchanger between the generator and absorber, named as GAX, made this chiller more effective. But the high temperature required to drive this chiller limits its wide application [Wang *et al.*, 2009]. The German company, SolarNext, introduced a low-temperature driven 10 kW ammonia-water absorption chiller for commercial and residential air conditioning applications. With a driving temperature of 78~85°C, this chiller produces 16~19°C chilled water with a COP of 0.63 [Jacob & Pink, 2007]. Different research organizations and universities have built many prototypes of ammonia-water absorption chillers but none of these are commercially available. In Turkey, a solar-powered ammonia-water absorption heat pump was built as a prototype by Gazi University. The maximum COP of 0.8 was achieved at 55°C driving temperature by providing a 10°C evaporator temperature for this heat pump [Sozen *et al.*, 2002]. Stuttgart University in Germany built a prototype 2.5 kW water-ammonia diffusion absorption chiller which provided 1.5 kW of cooling load with a driving temperature of 150 to 170°C and a COP of 0.3 [Jacob & Eicker, 2002]. In Stuttgart Germany, for air-conditioning applications, ITW developed a 10 kW prototype ammonia-water absorption chiller. This chiller produced 15°C chilled water in the evaporator with a 90°C driving temperature and a COP 0.66 [Luo *et al.*, 2010]. The French National Institute developed a prototype 4.2 kW ammonia-water absorption chiller for Solar Energy. This chiller was operated at 80°C driving temperature while providing an evaporator temperature of 18°C. The best COP achieved for this chiller was of 0.65 [Boudéhenn *et al.*, 2012].

Adsorption cooling systems

The practical difference between an adsorption cooling system and an absorption system is that neither a pump nor a rectifier are needed for an adsorption system. In an adsorption cooling system, solid adsorbent and the refrigerant form a working pair. The selection of adsorbent-adsorbate (refrigerant) depends on their physical, chemical and thermodynamic properties as well as their availability and cost [Askalany *et al.*, 2012]. Silica gel, zeolites, and activated carbon are usually used as the solid adsorbent with the selection of a suitable adsorbate (refrigerant) for adsorption cooling systems [Zhai *et al.*, 2008]. The specific heat capacity and large internal pore structures of activated carbon results in a high capacity to adsorb the adsorbate [Askalany *et al.*, 2012]. Ammonia, ethanol and methanol are common adsorbates for activated carbon.

In 1848, the first adsorption cooling system was developed by Michael Faraday with the working pair of ammonia and silver chloride (AgCl) [Critoph & Zhong, 2005]. In the 1930s, commercial applications of silica gel/sulphur dioxide refrigerators existed, and in 1960, activated carbon–methanol refrigerators were commercialized. The latter two used fossil fuel burning as their heat source and were unsuccessful because of their high price compared to conventional systems [Choudhury *et al.*, 2010]. A 3.2 kW waste heat/ solar powered four-bed, double-stage, non-regenerative (hot water flow arrangements are parallel) adsorption chiller was tested by Saha *et al.* [2001]. The driving temperature for this system was 70°C and the best COP achieved was 0.36 while providing 10°C chilled water in the evaporator. Wang *et al.*, [2001] developed an adsorption air-conditioning system with a heat source temperature of 100°C. In this system, two carbon adsorbent beds and methanol refrigerant were used with a cycle time of 60 minutes for providing 3 kW cooling power with a COP of 0.21. A 10 kW silica gel–water adsorption chiller has been developed by Wang *et al.*, [2005, Part I, II]. The investigation of its operation revealed that this chiller can be driven by 85°C hot water while providing a COP of 0.4 and a 10°C chilled water temperature.

Kuczyńska & Szaflik [2010] compared the 10 kW LiBr-H₂O absorption and Silica gel-Carbon adsorption systems for air-conditioning applications. The absorption system had the higher COP (= 0.67) compared to the adsorption system (COP = 0.39) in their study. The recent scenario of absorption and adsorption cooling systems was studied by

Ghafoor & Munir [2015]. According to their study, the chiller cost for LiBr-H₂O absorption system is 300-350 Euro/kW whereas the adsorption chiller cost is 400-450 Euro/kW.

For sustainable development, small-scale absorption and adsorption cooling are the greatest alternatives to vapor compression cooling in residential air-conditioning applications. So, it is very important to compare these two cooling systems and their compatibility for residential applications. Though analysis of these two systems individually has been reported in the literature, component-by-component comparison of these sorption technologies has not been reported. In order to accomplish this task, a simplified thermodynamic model for adsorption was developed in this paper and compared with the thermodynamic model of absorption previously published by these authors [Aman, *et al.*, 2014]. Due to the benefit of ammonia as a refrigerant for small scale applications and good absorbent properties of activated carbon, ammonia-water and activated carbon-ammonia pairs have been considered in this paper to compare these two cooling systems. The analysis was conducted for a residential cooling load (10 kW) using low-temperature heat source which would be appropriate from a solar driven cooling system. This study presents the system performance of absorption and adsorption cycles as determined by the proposed thermodynamic models and the maximum system performance will be compared under different operating conditions.

A review of the mathematical modeling of the adsorption system has been described by Yong & Sumathy [2002]. Three different models were described in this literature, classified as: mass and heat transfer model, lumped parameters model and thermodynamic model. In the thermodynamic model, a detailed heat transfer process is not considered. Whereas the lumped parameter model considered only the heat transfer process, but did not reflect surface temperature variation with respect to time, which is incorporated in the heat and mass transfer process [Wang *et al.*, 2005, Part I]. For the evaluation of the best performance of a refrigeration cycle, the thermodynamic model is adequate. Almost all models have been applied to silica gel-water, zeolites-water, and activated carbon-methanol adsorbate-adsorbent pairs. The model proposed here is a thermodynamic model developed for the activated carbon-ammonia working pair in which activated carbon is directly embedded in the solar collector to work as an adsorption bed.

2.2. Cycle operation principles

Absorption cooling systems

An illustration of a single effect water-ammonia solar absorption cooling system is shown in Figure 2.1. In this system, the absorption chiller is connected to a solar thermal collector, a controller, a heat storage tank and an auxiliary heater backup system. The chiller is also connected to the indoor air cooling system to provide air-conditioning in the building. The basic components of an absorption chiller are the generator, the condenser, the absorber and the evaporator. A solution pump, heat exchanger, expansion valves and a rectifier are the ‘auxiliary’ components of this system. In the analysis that follows, the solar collector and heat storage are assumed to provide thermal energy to the refrigeration system on a continuous basis.

In this thermal-driven cooling system, ammonia is the refrigerant, which is the solute, and water is the absorbent. The heat is provided to the strong solution (high ammonia concentration) in the generator by the solar collector. Ammonia starts evaporating and passes through the rectifier while leaving the hot weak solution (lower ammonia concentration) in the generator [Aphornratana & Eames, 1995]. In condenser, the high pressure pure ammonia vapor from the generator-rectifier (State 1) is condensed, becoming high pressure ammonia liquid (State 2). After passing through the expansion valve, the ammonia vapor becomes a low-pressure ammonia liquid-vapor mixture (State 3). This low temperature and low-pressure ammonia evaporates in the evaporator and becomes ammonia vapor, which is absorbed by the cold weak solution in the absorber (State 4). The surroundings of the evaporator feel the cooling effect while surrendering its heat to vaporize the liquid ammonia in the evaporator. After leaving the evaporator, the low-pressure ammonia vapor enters the absorber and is absorbed by the weak solution, turning it into a saturated strong ammonia-water solution. This strong solution is pumped through the heat exchanger between the absorber and the generator by a solution pump (State 5-7). After losing its ammonia vapor in the generator-rectifier, the leftover hot, and now weak, solution in the generator flows back to the absorber via the heat exchanger (States 8-9) and an expansion valve (State 10). The weak solution reduces its pressure and enters the absorber at the absorber pressure and temperature.

As water and ammonia both are volatile, a rectifier is needed in this system so that there will be no moisture content in the ammonia vapor when it enters the condenser. The moisture or water vapor could freeze in the condenser or pipeline or block the expansion valve [Raghuvansh & Maheshwari, 2011] and might lower the cooling effect in the evaporator (Deng *et al.*, 2011). The COP value of the system would be lower without the heat recovery by the heat exchanger in this cycle [Adewusi & Zubair, 2004; Sun, 1998]. The solution pump in this system is the only component that needs electric power as work input.

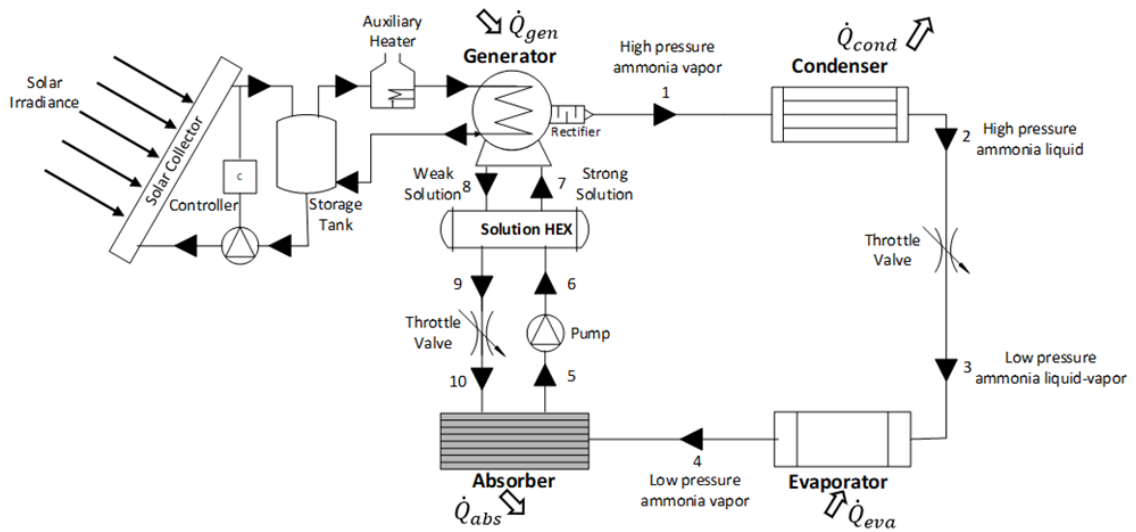


Figure 2.1: Schematic diagram of the solar ammonia-water absorption cooling cycle

Adsorption cooling systems

The main components of an adsorption cooling system are the adsorption bed, the condenser, the refrigerant storage tank and the evaporator as shown in Figure 2.2. The adsorption bed contains the adsorbent (activated carbon) that can adsorb the refrigerant (ammonia). Figure 2.2 describes the working principle of a basic adsorption chiller where the adsorption bed alternates between adsorption and desorption processes during the cycle. Two valves are necessary for the basic operation of this adsorption chiller. When solar heat is available, the adsorption bed, which begins saturated with refrigerant, is initially isolated from the condenser and the evaporator by Valves C and E. In this process,

when solar energy strikes the adsorption bed, its temperature and pressure increase. During the desorption process, Valve C is opened while Valve E remains closed. When the pressure of the full system rises up to the condenser pressure, the ammonia evaporates and flows towards the condenser. The desorbed vapor enters the condenser where it is condensed at the surrounding temperature and stored in the refrigerant storage tank. The amount of desorbed refrigerant from the adsorption bed increases with increasing bed temperature and the adsorbate concentration continues to decrease. When the adsorption bed has reached the desirable refrigerant concentration, Valve C between the condenser and adsorption bed is closed and the adsorption bed is cooled to its initial temperature. Practically, this means shielding it from the sun and promoting air cooling. The system pressure is reduced to the evaporator pressure. During the adsorption process, the adsorption bed connects to the evaporator through Valve E. This time Valve T is opened; the low-pressure liquid refrigerant from the refrigeration tank enters the evaporator, through the throttle valve. After creating the cooling effect at the evaporator, the low-pressure refrigerant (ammonia) vapor is adsorbed by the cooled adsorption bed. The basic adsorption refrigeration cycle has been described in this analysis to compare the thermodynamic performance with the absorption refrigeration cycle. For a continuous cooling effect from an adsorption system, two adsorption beds would be required: one working as a desorption bed while the other works as an adsorption bed alternatively to produce a continuous cooling effect. Note that desorption can only occur when solar energy is available, whereas adsorption may occur during the day and night.

The thermodynamic cycle of a basic adsorption refrigeration bed is represented in the Clapeyron diagram, Figure 2.3, which consists of four processes. During heating of the adsorption bed, process A-B is a constant volume pressurization process (isosteric heating phase), where B-C is a desorption process at constant pressure (isobaric heating phase). During cooling of the adsorption bed, C-D is a depressurization process at constant volume (isosteric cooling phase) and D-A is an adsorption process at constant pressure (isobaric cooling phase).

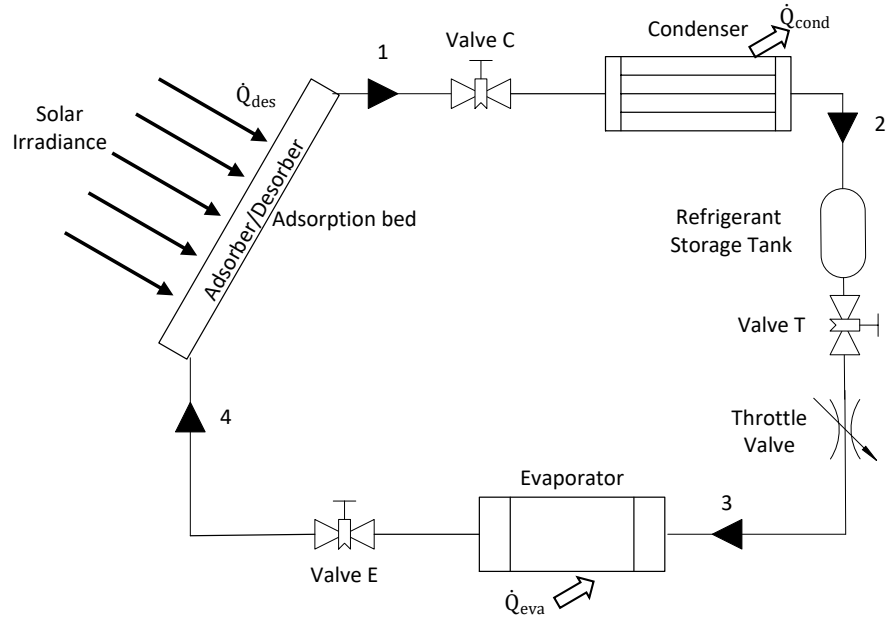


Figure 2.2: Schematic of Solar Adsorption Cooling System.

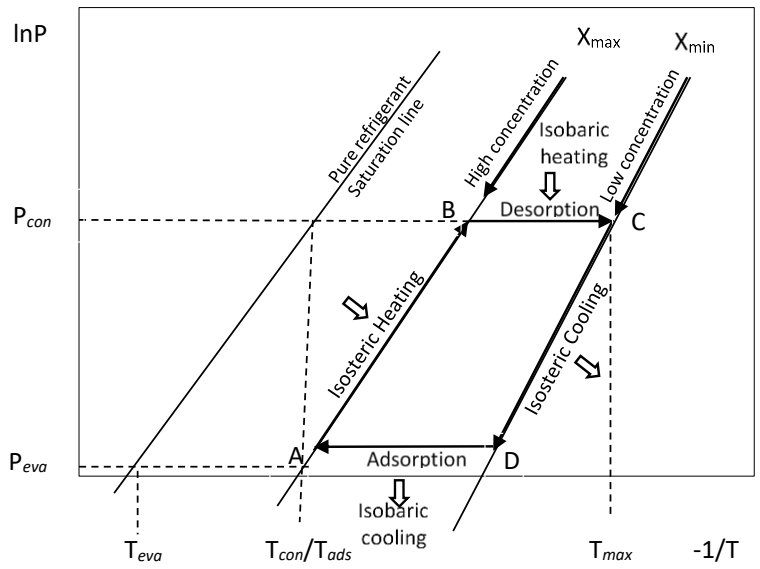


Figure 2.3: Clapeyron diagram for thermodynamic cycle of adsorption cooling system.

2.3. Thermodynamic model

Absorption system:

For the absorption system, the first law of thermodynamics was analyzed for each component by using the following mass and energy conservation equations:

$$\text{Mass Conservation: } \quad \sum \dot{m}_{in} - \sum \dot{m}_{out} = 0 \quad (1)$$

$$\text{Energy Conservation: } \quad \sum \dot{Q} = \sum \dot{m}_{out} h_{out} - \sum \dot{m}_{in} h_{in} + \dot{W} \quad (2)$$

where \dot{Q} is the heat transfer rate (kW), \dot{m} is the mass flow rate (kg/s) and h is the specific enthalpy (kJ/kg).

For this energy analysis, the following simplified assumptions have been considered (Aman *et al.*, 2014).

- The system is operating under steady state conditions.
- Ammonia-water solutions are at equilibrium condition in the absorber and the generator at their corresponding temperatures and pressures
- Unintentional pressure drops and heat losses in the pipelines and system components are negligible. So, heat transfer to and from the surroundings is negligible, other than at the condenser, evaporator and absorber.
- All throttle valves are under adiabatic conditions, which results in a constant enthalpy processes.
- The circulating pump is isentropic as its entropy generation is negligible [Aman *et al.*, 2014].
- The vapor leaving the generator/rectifier is 100% ammonia.
- The refrigerant states leaving the condenser and evaporator are saturated liquid and saturated vapor.
- The ammonia-water solution at the absorber outlet is a rich solution at the absorber temperature.
- The condenser and the absorber are air cooled at atmospheric temperature 25°C.

The heat transfer from and to the system are determined by the energy balance of each component of the system. The heat balance for generator, absorber, pump, heat exchanger, condenser and evaporator are represented by Equations (3) to (15) taken from Aman et al., [2014].

For the generator, the mass and energy balances are (numbers refer to streams in Figure 2.1):

$$\text{Total mass balance:} \quad \dot{m}_7 = \dot{m}_1 + \dot{m}_8 \quad (3)$$

$$\text{NH}_3 \text{ mass balance:} \quad X_7 \dot{m}_7 = \dot{m}_1 + X_8 \dot{m}_8 \quad (4)$$

where X is the NH_3 mass fraction in solution.

$$\text{Energy balance:} \quad \dot{Q}_{\text{gen}} = \dot{m}_1 h_1 + \dot{m}_8 h_8 - \dot{m}_7 h_7 \quad (5)$$

The mass flow rate of the strong and weak solutions are determined by Equations (3) and (4),

$$\dot{m}_7 = \frac{1-X_8}{X_7-X_8} \dot{m}_1 \quad (6)$$

$$\dot{m}_8 = \frac{1-X_7}{X_7-X_8} \dot{m}_1 \quad (7)$$

The pumping power of the solution pump could be determined by defining the circulation ratio, which is the ratio of the strong solution mass flow rate to the refrigerant mass flow rate [Hammad & Habali, 2000].

$$CR = \frac{\dot{m}_7}{\dot{m}_1} \quad (8)$$

The solution heat exchanger energy balance is represented by Equations (9) and (10).

$$T_9 = \eta_{HEX} T_6 + (1 - \eta_{HEX}) T_8 \quad (9)$$

where η_{HEX} is the heat exchanger efficiency, which is assumed to be 80%.

$$h_7 = h_6 + \frac{\dot{m}_8}{\dot{m}_6} (h_8 - h_9) \quad (10)$$

The energy balance of the pump is

$$h_6 = h_5 + (P_6 - P_5)v_6 \quad (11)$$

$$\dot{W}_p = (P_6 - P_5)v_6 \quad (12)$$

$$\text{Energy balance for condenser: } \dot{Q}_{\text{cond}} = \dot{m}_1(h_1 - h_2) \quad (13)$$

$$\text{Energy balance for evaporator: } \dot{Q}_{\text{eva}} = \dot{m}_1(h_4 - h_3) \quad (14)$$

$$\text{Energy balance for absorber: } \dot{Q}_{\text{abs}} = \dot{m}_4 h_4 + \dot{m}_{10} h_{10} - \dot{m}_5 h_5 \quad (15)$$

The coefficient of performance (COP) of the absorption cooling system can be determined by the cooling effect obtained in the evaporator and the primary energy supply to the generator. The coefficient of performance (COP) is defined as [Shahata *et al.*, 2012]:

$$\text{COP} = \frac{\text{useful energy output}}{\text{primary energy input+work done by pump}} = \frac{\dot{Q}_{\text{eva}}}{\dot{Q}_{\text{gen}} + \dot{W}_p} \quad (16)$$

Adsorption system:

The major equation that describes the thermodynamic model for an adsorption cycle is the adsorption equilibrium equation. The Dubinin-Astakhov (D-A) model is the most frequently used model to describe this phenomenon [Hassan *et al.*, 2012]. Critoph & Metcalf [2004] defined a simple version of the Dubinin–Astakhov for the modeling of carbon–ammonia adsorption as:

$$x = x_0 \exp\left[-K \left(\frac{T}{T_{\text{sat}}} - 1\right)^n\right] \quad (17)$$

where, x is the adsorbate concentration (kg/kg adsorbent), T is the test temperature, x_0 is the maximum adsorbate (adsorbate) concentration under saturation conditions, T_{sat} is the saturation temperature corresponding to the gas pressure and n is a constant. For this study, LM128 monolithic carbon has been considered, for which $x_0 = 0.3333$, $K = 3.6962$ and $n = 0.9900$ [Tamainot-Telto & Critoph, 2000]. As the specific heat changes with temperature, Tamainot-Telto and Critoph [2000] describe the correlation of the specific heat and temperature of LM128 monolithic carbon as follows:

$$(C_p)_{ac} = 775.62 + 2.826 * T_a \quad (18)$$

where, T_a = adsorbent temperature in °C.

The isosteric heat of adsorption/desorption can be determined by amount of heat required to adsorb or desorb a unit mass of the adsorbate. And this represents the enthalpy of adsorption which is a function of the amount of adsorbed refrigerant. For ammonia, the isosteric adsorption/desorption heat, q_{sh} can be determined by using Clausius-Clapeyron equation [Tamainot-Telto & Critoph, 2000].

$$q_{sh} = RA \frac{T}{T_{sat}} \quad (19)$$

where R is the gas constant (~ 488 J/kg-K), T is the sample temperature, and A is a constant ($= 2823.4$)^[38] corresponding to the slope of the saturation curve on a plot of $\ln(P)$ vs. $-1/T_{sat}$, and T_{sat} is the saturation temperature corresponding to the gas pressure P .

The following assumptions have been made to develop this thermodynamic model for an adsorption cooling system

- Pure ammonia is being adsorbed and desorbed in the adsorption and desorption cycles
- The temperature at the end of adsorption is equal to the condensing temperature.
- Constant heat source and sink temperatures.
- The specific heat of the refrigerant in the adsorbed phase is equal to the specific heat of the gas at a given pressure and temperature and is considered to be constant [Cacciola & Restuccia, 1995].
- In the adsorbent bed, the temperature is uniform.
- The refrigerant is adsorbed uniformly in the adsorption bed.
- The isosteric heat of adsorption/desorption is constant.
- Both solid and gas phases are at thermodynamic equilibrium, in which the rate of desorption is equal to the rate of adsorption.
- The full cycle was assumed to operate for two hours, meaning a one-hour desorption and a one-hour adsorption.

All thermal contributions must be considered to calculate the coefficient of performance of the adsorption chiller. The following equations have been developed in this energy analysis model.

Energy balance for desorption:

The desorption process is endothermic and is attained by the absorption of heat [Hassan *et al.*, 2012]. From the Clapeyron diagram (Figure 2.3) the heat that needs to be supplied to the adsorbent during its isosteric and isobaric heating phases has been described by the following equation:

$$\dot{Q}_{des} = \dot{Q}_{in} = [(mC_p)_{ac}(T_C - T_A) + m_{ac}x_{max}C_{pNH_3}(T_C - T_A) + m_{ac}q_{sh}\Delta x]/t_{cycle} \quad (20)$$

During this process, the heat needed to raise the temperature from T_A to T_C includes the sensible heat of the solid adsorbent and its adsorbate (refrigerant), and has been described by the first two terms on the right-hand side of the equation, while the last term is the heat of desorption for the amount of refrigerant (adsorbate) being desorbed.

Energy balance for adsorption:

The adsorption process is exothermic and develops heat [Hassan *et al.*, 2012]. During adsorption, the energy balance is given by the following equation:

$$\dot{Q}_{ads} = \dot{Q}_{out} = [(mC_p)_{ac}(T_C - T_A) + m_{ac}x_{min}C_{pNH_3}(T_C - T_A) + m_{ac}q_{sh}\Delta x + m_{ac}\Delta x C_{pNH_3}(T_{eva} - T_{ads})]/t_{cycle} \quad (21)$$

In the equation, on the right-hand side, the first two terms are the sensible heat of the solid adsorbent and its adsorbate (refrigerant) that gets released in isosteric and isobaric cooling processes from temperature T_C to T_A , the third term is the heat of adsorption for the amount of refrigerant (adsorbate) being adsorbed and the last term is the energy needed to increase the temperature of the refrigerant vapor from evaporator temperature to the adsorption temperature.

Energy balance for condenser in desorption phase (see Figure 2.2):

$$\dot{Q}_{cond} = \dot{m}_1(h_1 - h_2) \quad (22)$$

Energy balance for evaporator in adsorption phase (see Figure 2.2):

$$\dot{Q}_{eva} = \dot{m}_1(h_4 - h_3) \quad (23)$$

The coefficient of performance of the adsorption chiller can be defined as the ratio of useful energy produced to energy supplied to the chiller and is expressed as

$$COP = \frac{\text{useful energy output}}{\text{primary energy supplied}} = \frac{\dot{Q}_{eva}}{\dot{Q}_{des}} \quad (24)$$

The proposed thermodynamic models have been used to calculate the performance of the water-ammonia absorption and activated carbon-ammonia adsorption cooling systems using a spreadsheet for calculations. A 10 kW cooling capacity was considered the basis to evaluate and compare system performances for both cooling systems. A low temperature heat source was selected to supply heat to the generator / desorber of these chillers, and the absorber/adsorber cools by convection to the environment. Since ammonia is the refrigerant for both systems, a high operating pressure is obtained. The maximum and minimum pressures of both cycles have been set according to the condenser and evaporator pressures which were set at 1167 kPa and 462 kPa, respectively. The most important operating conditions for the performance of these cooling systems are the operating temperatures [Rezk & Al-Dadah, 2012]. The temperatures for both systems are shown in Table 2.1 for a cooling power of 10 kW.

Engineering Equation Solver (EES) software was used to calculate the thermodynamic properties of NH₃-H₂O for the absorption refrigeration cycle; and Excel has been used for other calculations.

2.4. Results and discussion

The thermodynamic properties of ammonia-water in a 10 kW absorption chiller are summarized in Table 2.2. Based on the analysis and the operating conditions mentioned in Table 2.1, these properties have been calculated at different states in the cycle operation.

The desorption temperature for the 10 kW adsorption cooling system was assumed to be 80°C for a constant evaporation temperature of 2°C. For this evaporator temperature and capacity, the mass flow rate of the ammonia refrigerant in this system must be a constant 0.0089 kg/s. For one adsorption/desorption cycle, the properties in Table 2.3 have

been used to achieve a 10 kW cooling load for the activated carbon-ammonia adsorption chiller.

Table 2.1: Temperature distribution for absorption and adsorption cooling system

| Absorption Chiller (ammonia-water) | | Adsorption Chiller (Activated carbon – ammonia) | |
|------------------------------------|-------|---|-------|
| Generator $T_{gen} =$ | 80 °C | Desorber $T_{des} =$ | 80 °C |
| Condenser $T_{cond} =$ | 30 °C | Condenser $T_{cond} =$ | 30 °C |
| Evaporator $T_{eva} =$ | 2 °C | Evaporator $T_{eva} =$ | 2 °C |
| Absorber $T_{abs} =$ | 30 °C | Adsorber $T_{ads} =$ | 30 °C |

Table 2.2: Different states thermodynamic properties of an ammonia-water absorption cycle at operating conditions $T_{gen} = 80^{\circ}\text{C}$, $T_{con} = 30^{\circ}\text{C}$, $T_{abs} = 30^{\circ}\text{C}$, $T_{eva} = 2^{\circ}\text{C}$, $\eta_{HEX} = 80\%$ and a cooling load of 10 kW

| Point | Temperature (°C) | Pressure (kPa) | Mass flow (kg/s) | % Concentration | Enthalpy (kJ/kg) |
|---------------------------------|------------------|----------------|------------------|-----------------|------------------|
| Generator <i>ref</i> exit (1) | 80 | 1167 | 0.0089 | 100 | 1627 |
| Condenser <i>ref</i> exit (2) | 30 | 1167 | 0.0089 | 100 | 341 |
| Evaporator <i>ref</i> inlet (3) | 2 | 462 | 0.0089 | 100 | 341 |
| Evaporator <i>ref</i> exit (4) | 2 | 462 | 0.0089 | 100 | 1466 |
| Absorber sol exit (5) | 30 | 462 | 0.0436 | 55.05 | -114 |
| Sol HEX inlet (6) | 30 | 1167 | 0.0436 | 55.05 | -114 |
| Generator sol inlet (7) | 62 | 1167 | 0.0436 | 55.05 | 35 |
| Generator sol exit (8) | 80 | 1167 | 0.0347 | 43.90 | 111 |
| Sol HEX exit (9) | 40 | 1167 | 0.0347 | 43.90 | -77 |
| Absorber sol. inlet (10) | 40 | 462 | 0.0347 | 43.90 | -77 |

Table 2.3: Properties of activated carbon and ammonia for 10kW adsorption chiller at $T_{gen/des} = 80^{\circ}\text{C}$, $T_{cond} = 30^{\circ}\text{C}$, $T_{abs/ads} = 30^{\circ}\text{C}$, $T_{eva} = 2^{\circ}\text{C}$, for 2 hours cycle period.

| | |
|------------------------------------|---------------|
| Specific Heat Capacity of carbon = | 1.002 kJ/kg-K |
| Mass of Carbon = | 675 kg |
| X max = | 23% |
| X min = | 18% |
| Heat of adsorption = | 1605 kJ/kg |

The results of the first law of thermodynamics analysis for both systems are illustrated in Table 2.4. The energy flow to or from each component of each system has been presented, as well as the COP. The result shows that, for a 10 kW cooling system, the

adsorption chiller needs more heat input than the absorption chiller to keep a constant refrigerant temperature of 2°C in the evaporator. It was also observed that the heat dissipation from the adsorber is almost double than that of the absorber. This indicates that the adsorber needs more cooling during its adsorption phase to provide the same cooling power as the absorption chiller. Both condensers have almost the same heat dissipation to achieve the same cooling effect. The heat flow pattern for both cycles is: the heat from the solar collector at high temperature goes into the generator/desorber, and the heat at low temperature goes into the evaporator from the air-conditioned area. The absorber/adsorber and the condenser reject heat to the environment at a temperature just above ambient.

Table 2.4: Energy flow for different component in absorption and adsorption system for 10 kW cooling capacity

| Absorption Chiller (water-ammonia) | | | Adsorption Chiller (activated carbon – ammonia) | | |
|------------------------------------|--------------------|-------------|---|--------------------|-------------|
| Generator | $\dot{Q}_{gen} =$ | 17 kW | Desorber | $\dot{Q}_{des} =$ | 29 kW |
| Condenser | $\dot{Q}_{cond} =$ | 11 kW | Condenser | $\dot{Q}_{cond} =$ | 12 kW |
| Evaporator | $\dot{Q}_{eva} =$ | 10 kW | Evaporator | $\dot{Q}_{eva} =$ | 10 kW |
| Absorber | $\dot{Q}_{abs} =$ | 15 kW | Adsorber | $\dot{Q}_{ads} =$ | 27 kW |
| COP | = | 0.60 | COP | = | 0.35 |

The analysis reveals that the coefficient of performance for the absorption chiller is higher than that of the adsorption chiller under the same operating conditions which is reflected in Figure 2.4. The thermophysical properties of the adsorbent in the adsorption system are the main obstacles to better system performance. The optimized thermal conductivity, permeability, porosity and specific heat of the adsorbent can increase the rate at which thermodynamic equilibrium is reached [Tamainot-Telto & Critoph, 2000], but fundamentally, there is a large mass of activated carbon that must be heated and cooled, along with the refrigerant.

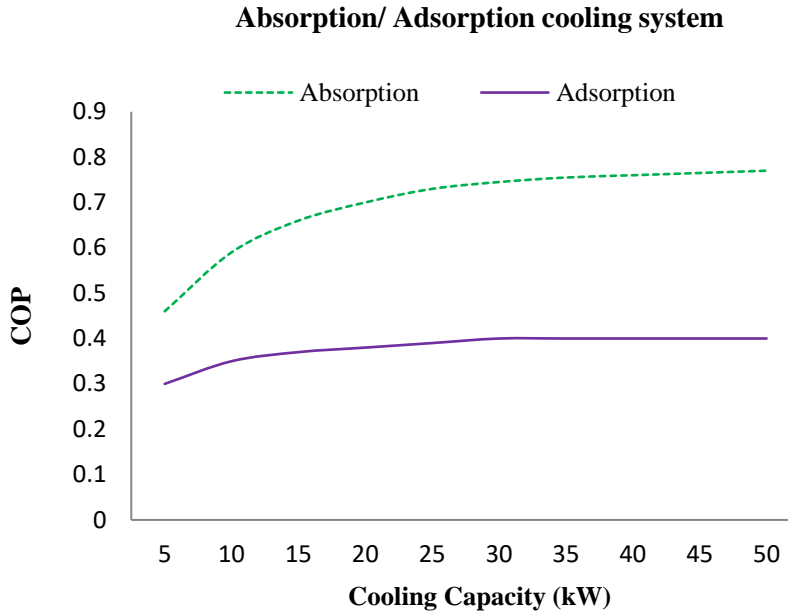


Figure 2.4: Performance comparison of absorption & adsorption cooling systems at different cooling load with ammonia concentration in/on absorbent/adsorbent same as 10 kW system, operating at $T_{gen} = 80^{\circ}\text{C}$ $T_{cond} = 30^{\circ}\text{C}$, $T_{eva} = 2^{\circ}\text{C}$, $T_{abs/ads} = 30^{\circ}\text{C}$.

Effect of generator/desorber temperature

The influence of generator and desorber temperatures on the COP of the absorption and adsorption systems is illustrated in Figure 2.5. For both devices, the condenser and absorber/adsorber temperatures were set to 30°C . In addition, the evaporator temperature has been set at 2°C because the performance strongly depends on the evaporation temperature. The results show that the COP of the absorption system is almost always higher than that of the adsorption system. At temperatures below 80°C , the COP values of both systems increase with increasing generator temperatures. But the absorption system has a generator temperature limit of 65°C and there is a sharp drop-off in COP below this temperature. In contrast, the adsorption system has a gradual decay in performance all the way down to 61°C desorber temperature. The coefficients of performance (COP) for absorption and adsorption systems pass through maxima at 80°C and 100°C , respectively. The gradients of the COP curves for the systems decrease slowly after the maximum point, because more heat is required to provide the energy embodied in the ammonia vapor. At higher desorber temperatures, less carbon is required for the adsorption system to produce

a constant cooling effect. This is because the amount of discharged ammonia vapor increases with increasing desorption temperature. To provide a constant flow rate of ammonia for a fixed cooling load, the simulated system was optimized by having less carbon. Therefore, the higher desorber temperature decreases the thermal load (the required heat energy input for a constant cooling load) of the desorber, as a result of its reduced mass. But the additional ammonia yield per kg of carbon decreases as the temperature increases, so after the maximum, the efficiency does not increase further with increasing desorber temperature. For the absorption cycle, although more ammonia vapor can be produced at the higher generator temperature, the simulation maintains the strong solution ammonia mass fraction at 55.05% and varies the ammonia-water solution mass flow rate to provide a constant ammonia vapor mass flow rate. The decrease in solution mass flow rate at higher temperatures does not completely compensate for the increase in enthalpy of the weak solution, which is at the generator temperature. This, combined with the increasing enthalpy of the ammonia vapor, means that the thermal load in the generator increases. As a result, the coefficient of performance of the absorption chiller decreases at high generator temperatures.

The adsorption bed is an important element for the performance evaluation of the adsorption cooling system. Its capacity determines the system's size as well as the capital cost. For a 10 kW adsorption cooling system, Figure 2.6 shows the variation of the coefficient of performance (COP) and the mass of carbon in the adsorption bed as a function of the desorber temperature. The mass of carbon decreases very sharply up to 90°C with a rapid increase of COP as the desorber temperature increases. Above a 90°C desorber temperature, both curves become almost flat. During the desorption process, the amount of ammonia leaving the adsorption bed depends on the difference of the concentrations (Δx) at adsorber and desorber temperatures. The ammonia concentration in the adsorption bed decreases with increasing desorber temperature because more ammonia vapor is released at higher desorber temperatures. So, the difference of ammonia concentrations increases as the desorber temperature increases. As a result, with constant adsorber temperature and cooling load, less carbon is needed to desorb the same amount of ammonia with increasing desorber temperature. This leads to a decrease of the amount

of energy needed for the desorber to provide the same cooling effect, which results in a higher COP.

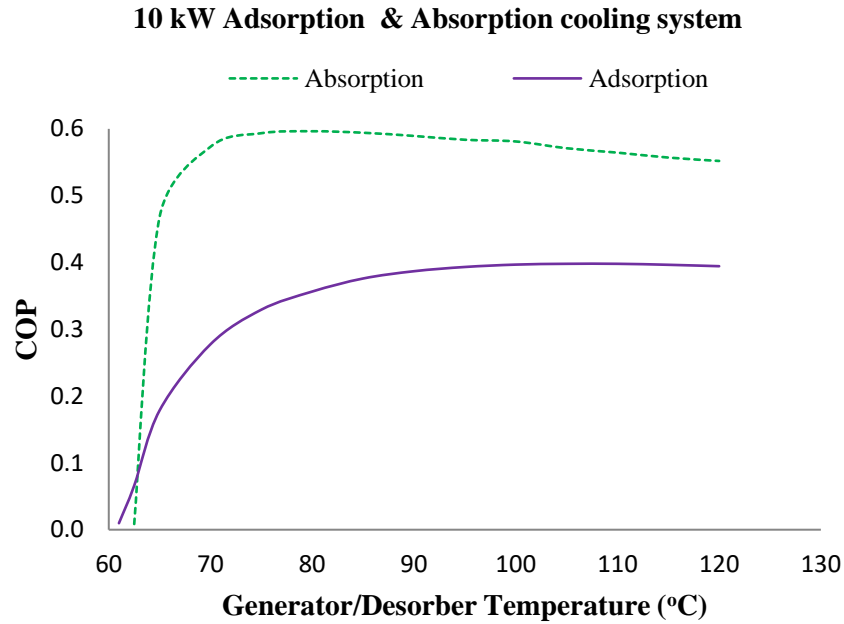


Figure 2.5: Effect of generator or desorber temperature on the COP for 10 kW absorption & adsorption cooling systems at $T_{cond} = 30^{\circ}\text{C}$, $T_{eva} = 2^{\circ}\text{C}$, $T_{abs/ads} = 30^{\circ}\text{C}$.

The effect of varying the generator or desorber temperature on the cooling capacity, with constant solution mass flow rate (absorber) or constant carbon amount (adsorber), is illustrated in Figure 2.7. Increasing the generator/desorber temperature increases the cooling capacity for both absorption and adsorption systems that supply a constant temperature (2°C) in the evaporator at constant condenser and absorber/adsorber temperatures. When the required cooling capacity is low, the adsorption system can provide the same cooling effect at a slightly lower input temperature than the absorption system. As the heat source temperature increases, the cooling capacity increases more for the adsorption cooling system as compared to the absorption system. Higher desorber temperatures for a fixed adsorption bed produce more ammonia vapor leading to the adsorption cycle having a higher cooling effect as well as a higher efficiency.

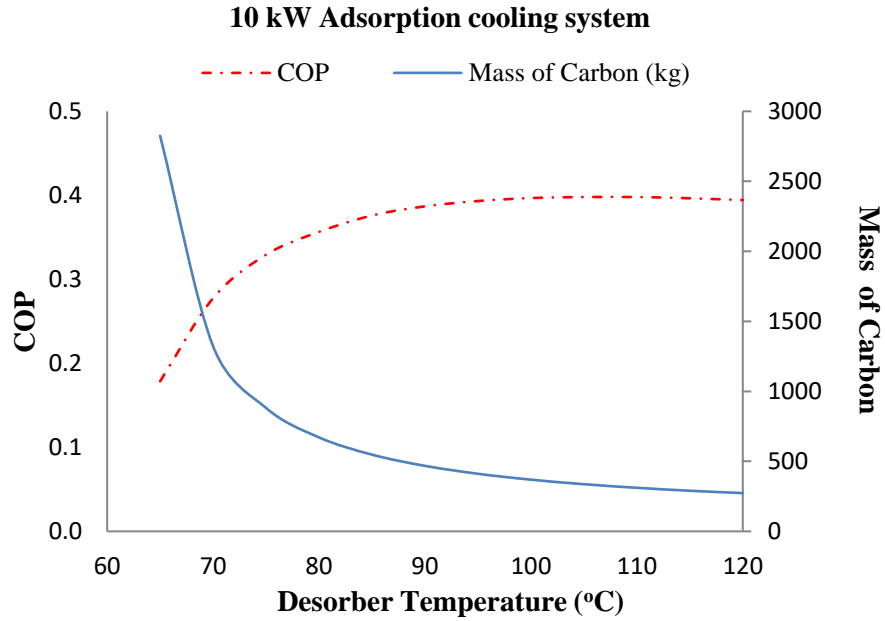


Figure 2.6: Effect of desorber temperature on the COP and carbon content for 10kW adsorption cooling system at $T_{cond} = 30^{\circ}\text{C}$, $T_{eva} = 2^{\circ}\text{C}$, $T_{ads} = 30^{\circ}\text{C}$.

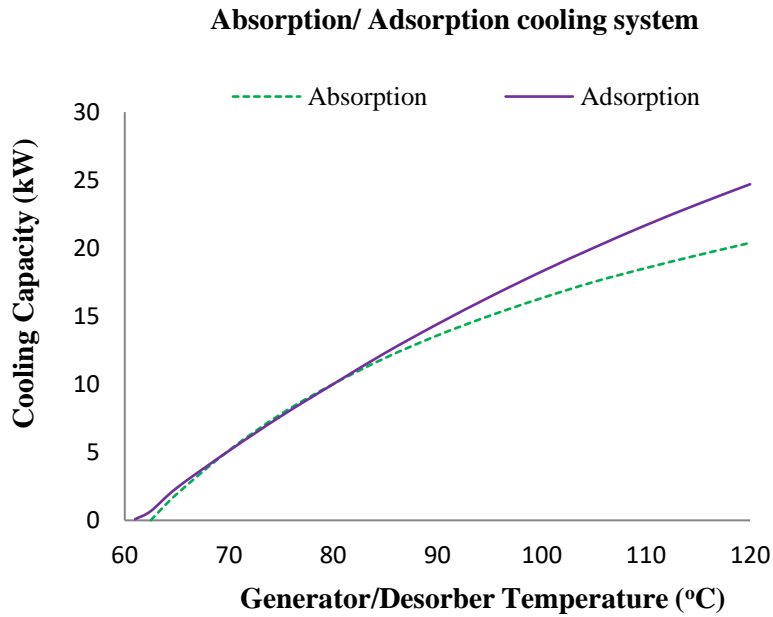


Figure 2.7: Cooling capacity variation with increasing generator or desorber temperature for a constant temperature of 2°C in the evaporator at $T_{cond} = 30^{\circ}\text{C}$, $T_{abs/ads} = 30^{\circ}\text{C}$.

Effect of absorber/adsorber temperature

As cooling of the absorber or adsorber is a major concern for the system performance as well as for the system size and cost of any sorption chiller [Aman *et al.*, 2014; Cacciola & Restuccia, 1995], the dependency of the system performance on the absorber/adsorber temperature is shown in Figure 2.8.

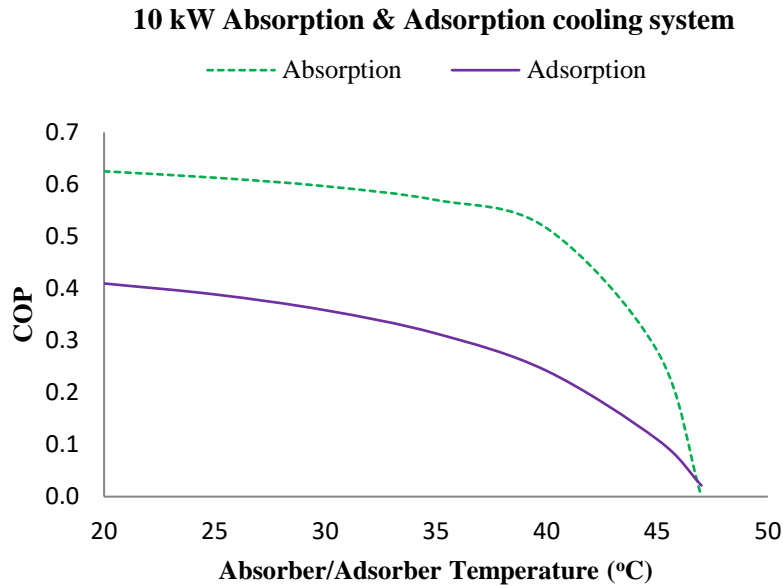


Figure 2.8: Effect of absorber or adsorber temperature on the COP for 10kW Absorption & Adsorption cooling system at $T_{cond} = 30^{\circ}\text{C}$, $T_{eva} = 2^{\circ}\text{C}$, $T_{gen/des} = 80^{\circ}\text{C}$.

In the absorption system, the weak solution in the absorber increases its absorption efficiency as the absorber temperature is lowered. This decreases the amount of energy required in the generator to provide a constant cooling effect. As a result, the COP increases. Similarly, in the adsorption system, the adsorption capacity of the carbon bed increases at lower adsorber temperatures during the adsorption process. Consequently, with a constant amount of carbon, the amount of ammonia desorbed also increases. Therefore, more ammonia vapor would be created during the desorption process. As a result, for a constant cooling load, the desorber thermal load decreases, therefore COP increases. It can be seen that, for both systems, COP decreases with increasing absorber/adsorber temperature. But for the absorption system, the COP decreases sharply above 40°C , whereas for the adsorption system, the decrease of COP is moderate along the adsorber

temperature increase. In both systems, the refrigeration effect essentially ceases at an absorber/adsorber temperature above 47°C. Increasing absorber/adsorber temperature decreases the ammonia concentration in the absorber solution and in the adsorption bed. So, the ammonia absorbed/adsorbed above 47°C is not enough to provide 10 kW cooling in the evaporator at an 80°C generator/desorber temperature. It is also noted that the COP decrease is 8% if the absorber temperature rises from 20°C to 35°C; whereas, it is 24% for an adsorption system with the same temperature difference. Hence, cooling of the adsorption bed has a higher impact on the performance of the adsorption system than the absorption system.

2.5. Conclusions

The objective of this study was to select the sorption cooling system that can provide air-conditioning in a residential building by using a low temperature heat source such as that from a solar thermal collector. To optimize the performance of two sorption systems based on operating conditions, thermodynamic analyses have been performed for the 10 kW ammonia-water absorption and activated carbon-ammonia adsorption cooling systems. The result shows that both systems can operate using a low temperature heat source, ranging from 60 to 90°C, which can be supplied by a flat plate solar collector.

The analysis reveals that the absorption chiller gives a higher system performance (COP = 0.60) than the adsorption system (COP = 0.35) under the same operating conditions. To provide this cooling effect, the adsorption system needs almost twice as much heat supplied (29 kW) compared to the heat supplied (17 kW) to the absorption system. The adsorption system also has a higher heat rejection (27 kW) compared to the heat rejection (15 kW) of the absorption system, to meet the same 10 kW cooling load. As a result, the adsorption system must be designed to collect and reject higher amounts of energy. The analysis also shows that the COP increases for both systems with increasing heat source temperature but decreases as absorber/adsorber temperature increases. And it has been revealed that the absorption COP is always higher than the COP for adsorption under all operating conditions simulated here. The result also demonstrates that the adsorption cooling system is highly sensitive to heat source temperature. A higher heat

source temperature can reduce the adsorbent mass as well as the size of the adsorption chiller with a concomitant increasing system performance.

Finally, the models developed in this paper offer a simple and effective method for the energy analysis of absorption and adsorption cooling systems. This leads to identifying the highest performing thermal cooling system for small scale applications, considering different operating conditions. From the comparison of performances analyzed here for the two sorption cooling systems, it appears that the absorption system is the most suitable solar sorption technology to provide air conditioning in a residential home. However, the cost and the size of the chiller are also important considerations for the application. The final selection will be influenced by the performance of the system and the conditions under which it operates.

Acknowledgement

This work is made possible by the Natural Science and Engineering Research Council of Canada.

Nomenclature

| | | | |
|--------------|---|-------------------|------------------|
| COP | coefficient of performance | <i>Subscripts</i> | |
| C_p | specific heat at constant pressure (kJ/kg-K) | <i>abs</i> | absorber |
| CR | circulation ratio | <i>ac</i> | activated carbon |
| GAX | generator absorber exchanger | <i>ads</i> | adsorber |
| h | specific enthalpy (kJ/kg) | <i>cond</i> | condenser |
| HEX | heat Exchanger | <i>des</i> | desorber |
| \dot{m} | mass flow rate (kg/s) | <i>eva</i> | evaporator |
| P | pressure (kPa) | <i>gen</i> | generator |
| \dot{Q} | heat transfer rate (kW) | <i>in</i> | inlet |
| q_{sh} | heat of adsorption/desorption (kJ/kg) | <i>min</i> | minimum |
| R | universal gas constant (J/kg-K) | <i>max</i> | maximum |
| t_{cycle} | cycle time (hr.) | <i>out</i> | outlet |
| T | temperature (K) | <i>p</i> | pump |
| X | mass fraction of ammonia (%) | <i>ref</i> | refrigerant |
| x | ammonia concentration (kg NH ₃ /kg carbon) | <i>sat</i> | saturation |
| \dot{W} | work rate (kW) | <i>sol</i> | solution |
| η_{HEX} | heat exchanger efficiency | | |
| v | pump specific volume (m ³ /kg) | | |

REFERENCES

- Abdulateef J.M., Sopian K., Alghoul M.A., Optimum design for solar absorption refrigeration systems and comparison of the performances using ammonia-water, ammonia-lithium nitrate and ammonia-sodium thiocyanate solutions. *International Journal of Mechanical and Materials Engineering*, 3 (2008) 17-24.
- Adewusi S.A., Zubair S.M., Second law based thermodynamic analysis of ammonia–water absorption systems. *Energy Conversion and Management*, 45 (2004) 2355–2369.
- Kuczyńska A., Szaflik W., Absorption and adsorption chillers applied to air conditioning systems. *Archives of thermodynamics*, 31 (2010) 77–94.
- Aman J., Ting D., S-K, Henshaw P., Residential solar air conditioning: energy and exergy analyses of an ammonia-water absorption cooling system. *Applied Thermal Engineering*, 62 (2014) 424-432.
- Aphornratana S., Eames I.W., Thermodynamic analysis of absorption refrigeration cycles using the second law of thermodynamics method. *International Journal of Refrigeration*, 18 (1995) 244 – 252.
- Askalany A., Salem A., Ismail I.M., Hamza A., Ali H., Morsy M.G., A review on adsorption cooling systems with adsorbent carbon. *Renewable and Sustainable Energy Reviews*, (2012) 493– 500.
- Balaras C.A., Grossman G., Henning H.M., Ferreira C.A.I., Podesser E., Wang L., Solar air conditioning in Europe—an overview. *Renewable and Sustainable Energy Reviews*, 11(2) (2007) 299–314.
- Boudéhenn F., Demasles H., Wytttenbach J., Jobard X., Chèze D., Papillon P., Development of a 5 kW cooling capacity ammonia-water absorption chiller for solar cooling applications. *Energy Procedia*, 30 (2012) 35–43.
- Cacciola G., and Restuccia G., Reversible adsorption heat pump: a thermodynamic mode. *International Journal of Refrigeration*, 18 (1995) 100 – 106.
- Choudhury B., Chatterjee P.K., Sarkar J.P., 2010. Review paper on solar-powered air-conditioning through adsorption route. *Renewable and Sustainable Energy Review*, 14 (2010) 2189–2195

- Choudhury B., Saha B.B., Chatterjee P.K., Sarkar J.P., An overview of developments in adsorption refrigeration systems towards a sustainable way of cooling. *Applied Energy*, 104 (2013) 554–567.
- Critoph R.E., Metcalf S.J., Specific cooling power intensification limits in ammonia–carbon adsorption refrigeration systems. *Applied Thermal Engineering*, 24 (2004) 661–678.
- Critoph R.E., Zhong Y., Review of trends in solid sorption refrigeration and heat pumping technology. *Proceedings of Institute of Mechanical Engineers*, 219 (2005) 285-300.
- Deng J., Wang R.Z., Han G.Y., A review of thermally activated cooling technologies for combined cooling, heating and power systems. *Progress in Energy and Combustion Science*, 37 (2011) 172-203.
- Ghafoor A., Munir A., Worldwide overview of solar thermal cooling technologies. *Renewable and Sustainable Energy Reviews*, 43 (2015) 763–774.
- Hammad M., Habali S., Design and performance study of a solar energy powered vaccine cabinet. *Applied Thermal Engineering*, 20 (2000) 1785–1798.
- Hassan H.Z., Mohamad A.A., Al-Ansary H.A., Development of a continuously operating solar-driven adsorption cooling system: Thermodynamic analysis and parametric study. *Applied Thermal Engineering*, 48 (2012) 332-341.
- Jakob U., Eicker U., Solar cooling with diffusion absorption principle. World Renewable Energy Congress VII, 2002, Cologne, Germany.
- Jakob U., Pink W., Development and investigation of an ammonia/water absorption chiller – chillii_PSC – for a solar cooling system. *Proceedings of the 2nd International Conference Solar Air-Conditioning*, Tarragona, Spain. (2007) 440–445.
- Luo H., Wang R., Dai Y., The effects of operation parameter on the performance of a solar-powered adsorption chiller. *Applied Energy*. 87 (2010) 3018–3022.
- McNeil M.A., Letschert V.E., Future air conditioning energy consumption in developing countries and what can be done about it: The potential of efficiency in the residential sector. In *Saving Energy—Just Do It!*. European Council for an Energy Efficient Economy Summer Study Proceedings, (2007) http://www.eceee.org/conference_proceedings/eceee/2007, (Accessed November 15, 2013).

- Pons M., Meunier F., Cacciola G., Critoph R.E., Groll M., Puigjaner L., Spinner B., Ziegler F., Thermodynamic based comparison of sorption systems for cooling and heat pumping. *International Journal of Refrigeration*, 22 (1999) 5-17.
- Raghuvansh S., Maheshwari G., Analysis of ammonia –water vapor absorption refrigeration system based on First Law of Thermodynamics. *International Journal of Scientific and Engineering Research*, 2 (2011) 2229-5518.
- Restuccia G., Freni A., Vasta S., Aristov Y., Selective water sorbent for solid sorption chiller: experimental results and modelling. *International Journal of Refrigeration*, 27(3) (2004):284–93.
- Rezk A.R.M., Al-Dadah R.K., Physical and operating conditions effects on silica gel/water adsorption chiller performance. *Applied Energy*, 89 (2012) 142–149.
- Ryan W., New developments in gas cooling. *ASHRAE Journal*. 4 (2002) 23-26.
- Saha B.B., Akisawa A., Kashiwagi T., Solar/waste heat driven two-stage adsorption chiller: the prototype. *Renewable Energy*, 23 (2001) 93–101.
- Shahata A.I., Aboelazm M.M., Elsafty A.F., Energy and exergy analysis for single and parallel flow double effect water-lithium bromide vapor absorption systems. *International Journal of Science and Technology*, 2 (2012) 85-94.
- Sozen A., Altiparmak D., Usta H., Development and testing of a prototype of absorption heat pump operated by solar energy. *Applied Thermal Engineering*, 22 (2002) 1847–1859.
- Sun D.W., Comparison of the performances of $\text{NH}_3\text{-H}_2\text{O}$, $\text{NH}_3\text{-LiNO}_3$ and $\text{NH}_3\text{-NaSCN}$ absorption refrigeration systems. *Energy Convers Management*, 39 (1998) 357-368.
- Tamainot-Telto Z., Critoph R.E., Thermophysical properties of monolithic carbon. *International Journal of Heat and Mass Transfer*, 43 (2000)2053-2058.
- Thu K., Kim Y-D., Myat A., Chun W.G., Choon K.N.G., Entropy generation analysis of an adsorption cooling cycle. *International Journal of Heat and Mass Transfer*. 60 (2013) 143–155.
- Treberspurg M., Djalili M., Staller H., New technical solutions for energy efficient buildings, State of the art report: solar heating & cooling. *SCI-Network: Sustainable Construction & Innovation through Procurement*, (2011).

- Wang D.C., Wu J.Y., Xia Z.Z., Wang R.Z., Zhai H., Dou W.D., Study of a novel silica gel–water adsorption chiller. Part II. Experimental study. *International Journal of Refrigeration*, 28 (2005) 1084–91.
- Wang D.C., Xia Z.Z., Wu J.Y., Wang R.Z., Zhai H., Dou W.D., Study of a novel silica gel–water adsorption chiller. Part I. Design and performance prediction. *International Journal of Refrigeration*, 28 (2005):1073–83.
- Wang R.Z., Ge T.S., Chen C.J., Ma Q., Xiong Z.Q., Solar sorption cooling systems for residential applications: Options and guidelines. *International journal of refrigeration*, (2009) 3638–660.
- Wang R.Z., Wu J.Y., Xu Y.X., Wang W., Performance researches and improvements on heat regenerative adsorption refrigerator and heat pump. *Energy Conversion and Management*, 42(2) (2001) 233–49.
- Yong L., Sumathy K., Review of mathematical investigation on the closed adsorption heat pump and cooling systems. *Renewable and Sustainable Energy Reviews*, 6 (2002) 305–337.
- Zhai X.Q., Wang R.Z., A review for absorption and adsorption solar cooling systems in China. *Renewable and Sustainable Energy Reviews*, 13 (2009) 1523–1531.
- Zhai X.Q., Wang R.Z., Wu J.Y., Dai Y.J., Ma Q., Design and performance of a solar-powered air-conditioning system in a green building. *Applied Energy*, 85 (2008) 297–311.

CHAPTER 3

RESIDENTIAL SOLAR AIR CONDITIONING: ENERGY AND EXERGY ANALYSES OF AN AMMONIA-WATER ABSORPTION COOLING SYSTEM

The previous work was published as “Aman, J., Ting, D. S-K., Henshaw, P., Residential solar air conditioning: energy and exergy analyses of an ammonia-water absorption cooling system, Applied Thermal Engineering 62 (2014) 424 to 432”.

3.1. Introduction

In an absorption cycle, a refrigerant and an absorbent are a pair of substances that work together. With evaporation temperatures about 5 to 10°C, the lithium bromide-water pair is widely used for air cooling applications; but when evaporation temperatures below 0°C are required, the ammonia-water pair is mostly used, such as in small size air conditioning and large industrial applications [Abdulateef *et al.*, 2008]. The high concentration of lithium bromide (~50%) is required for the operation of a lithium bromide-water absorption refrigeration cycle, due to its thermophysical properties. Crystallization occurs at ~70%, but at a lower concentration for the low pressures used in operating systems. This crystallization problem limits the lithium bromide-water solution to a narrow concentration and the absorber lower temperature to approximately 40°C [Deng *et al.*, 2011]. The high absorber temperature and high initial cost restrain the use of lithium bromide-water absorption chillers in residential scale applications. Moreover, the lithium bromide-water absorption chiller is difficult to be air cooled, because air cooling increases the risk of crystallization for this chiller [Izquierdo *et al.*, 2004]. Whereas, ammonia has low freezing point (-77.7°C) and does not crystallize at a low evaporating temperature and this helps the condenser and the absorber units of this chiller cool with direct air cooling. In addition, ammonia is a high-pressure refrigerant with a low specific volume which makes the water-ammonia chiller more compact. For residential buildings, the required cooling capacity should be within the range of 3 to 10 kW [Wang *et al.*, 2009].

The direct fired water-ammonia chiller has been available for air conditioning since 1964 [Ryan, 2002]. But due to the lower efficiency, the commercial availability of this

chiller has been eliminated. In the last few years, however, a few water-ammonia chillers with high efficiency have been developed for residential and light commercial applications employing the GAX (generator -absorber exchanger) concept. In GAX absorption cycle, the efficiency is high because the difference of ammonia concentrations in the rich solution and weak solution is large [Wang *et al.*, 2009]. The Robur Company (Italy) first introduced the GAX technology in a water-ammonia absorption chiller with a cooling capacity of 17.7 kW and a COP of 0.71 [Häberle *et al.*, 2007]. But the problem with the GAX cycle is that it only operates with a high driving temperature: 160°C is needed to reach a COP of 0.75 and the COP increases to 1.0 when the driving temperature reaches nearly 200°C [Sabatelli *et al.*, 2007]. For this reason, this kind of chiller was originally designed to use direct-fired gas.

Another commercial water-ammonia absorption system is SolarNext of Germany. They introduced a commercially available solar powered 10 kW single-effect water-ammonia absorption chiller for residential and commercial air conditioning applications that has a driving temperature of 85~78°C, resulting in a 19~16°C chilled water temperature with a COP of 0.63 [Jacob and Pink, 2007]. This system also uses a cooling tower for absorber and condenser cooling.

Many prototypes have been built for ammonia-water absorption chillers but those are either not direct air cooled or not commercially available. Gazi University in Turkey built a prototype of a water-ammonia absorption heat pump operated by solar energy which has an optimum driving temperature of 80°C for the best COP, and an evaporating temperature of 3°C which means that it could be used for air conditioning and preservation of food [Sozen *et al.*, 2002]. The University of Madrid in Spain constructed a 2 kW prototype of a low-power water-ammonia absorption chiller driven by solar energy. This prototype used a transfer tank instead of a solution pump, which did not operate well, and the experimental COP was lower than 0.05 [De Francisco *et al.*, 2002]. The University of Applied Sciences, Stuttgart in Germany built a 2.5 kW prototype solar powered ammonia–water diffusion absorption chiller which is driven by generator temperatures from 150 to 170°C. For this system, the best cooling capacity reached was 1.5 kW, at COP values between 0.2 and 0.3 [Jakob and Eicker, 2002]. A 10 kW cooling capacity water-ammonia absorption chiller prototype was also developed at ITW Stuttgart in Germany. At driving temperature of

90°C, cold water temperatures of 15°C could be achieved with a cooling capacity of 7.2 kW and a COP of 0.66 [Jakob *et al.*, 2008]. The French National Institute for Solar Energy developed a 4.2 kW prototype water-ammonia absorption chiller operating at 80, 27 and 18°C temperatures for the generator, absorber/condenser and evaporator, respectively. It achieved a COP of 0.65 [Boudéhenn *et al.*, 2012].

In short, the lower efficiency of ammonia-water chillers compared with LiBr-H₂O chillers, limits their widespread use for residential and light-commercial air conditioning applications. In this respect, research for the improvement of the thermal performance of the ammonia- water absorption cycle has been increased.

The potential of the ammonia-water absorption cycle for a small scale solar thermal air conditioning application has been investigated in this paper. In order to reduce the size and increase the thermal performance, this system is intended for air cooling instead of water cooling and a low temperature heat driving source like a flat plate solar collector is anticipated. The energy and exergy analyses of the model ammonia-water absorption cycle will identify the components of the system that have the greatest effect on the system thermal performance. The exergy losses of different components will determine the least efficient components of the system. In this study, the potential and the thermal performance of the system and its exergetic efficiency will be compared in different operating conditions.

3.2. Cycle Operation Principles

Solar thermal cooling systems usually consist of solar thermal collectors linked to a sorption chiller. The main components of such a system are: the solar collectors; a heat storage tank; the heat-driven cooling device; the indoor air cooling system and an auxiliary (backup) subsystem. The backup system may be an auxiliary heater connected in parallel to the collector. A single-effect ammonia-water absorption solar thermal cooling system is illustrated in Figure 3.1, where water is the absorbent and ammonia is the refrigerant. The main four parts in a basic absorption cycle are: the generator, the condenser, the evaporator and the absorber. There are other ‘auxiliary’ components: rectifier, expansion valves, heat exchanger and pump.

In this system, as ammonia is the solute, the rich ammonia solution is heated in the generator by the solar collector and ammonia evaporates, leaving a hot weak solution in the generator [Aphornratana & Eames, 1995]. From the generator, the high-pressure ammonia vapor (State 1) is condensed to high pressure liquid ammonia (State 2) in the condenser; see Figure 3.1. The condensed ammonia is then reduced in pressure while passing through the throttle valve (becoming State 3), and evaporates in the evaporator, where the cooling effect occurs. After leaving the evaporator (State 4), the low-pressure ammonia vapor refrigerant enters the absorber, where it's absorbed by the cold weak solution in the absorber and becomes a rich solution of water saturated with ammonia. From the absorber, the rich solution is pumped to the generator (State 5-7) by the solution pump. The weak hot ammonia solution which was left in the generator after evaporation of the ammonia passes through the pressure reducing throttle valve and flows back to the absorber (State 8-10) at low pressure.

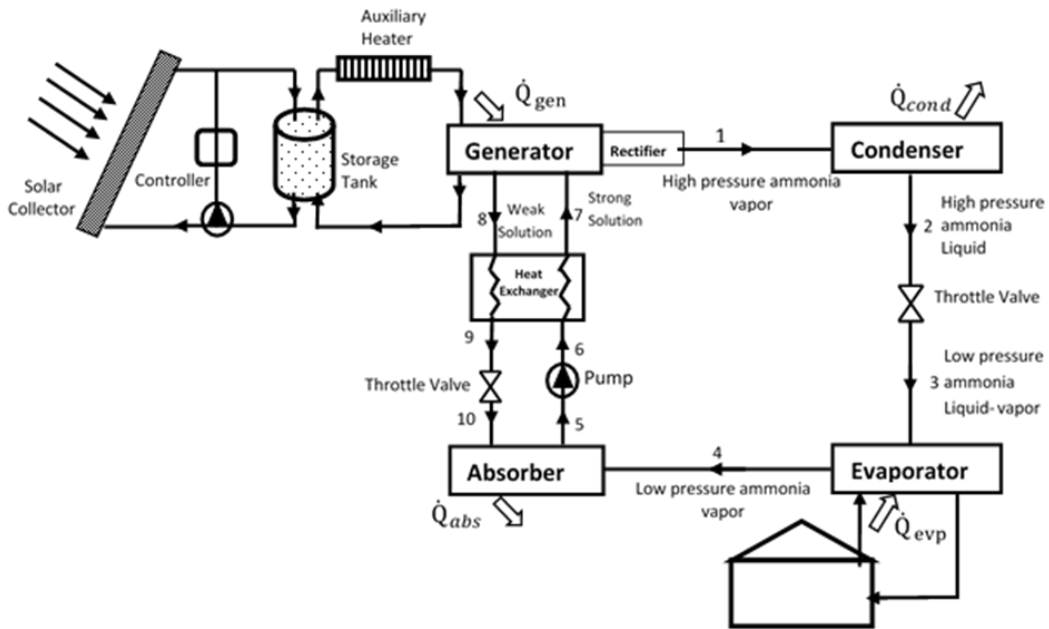


Figure 3.1: Schematic diagram of the solar ammonia-water absorption cooling cycle

The ammonia-water cycle requires a rectifier to purify the ammonia because both water and ammonia are volatile. Without a rectifier, the ammonia vapor from the generator may contain some water vapor which could form ice in the condenser, block the throttling

valve and perhaps freeze in the pipeline [Raghuvansh *et al.*, 2011]. Also, water contaminant entering the evaporator would raise the evaporating temperature and lower the cooling effect of the evaporator [Deng *et al.*, 2011]. A solution heat exchanger, as shown in Figure 3.1, is normally added to the cycle in order to improve the cycle performance [Adewusi & Zubair, 2004]. The solution heat exchanger is important for heat recovery, without which the COP values of the cycle would be much lower [Sun, 1996]. In the absorption refrigeration cycle, the pump is the only part which requires work input. However, this work is very small compared to that used by the compressor in a vapor compression cycle system [Cengel & Boles, 2008].

Figure 3.2 illustrates the heat flow pattern of the ammonia-water absorption cycle. The high temperature heat from the solar collector goes into the generator, and low temperature heat from the air-conditioned area goes into the evaporator. The absorber and the condenser are the components that reject heat, at just above atmospheric temperature, to the environment.

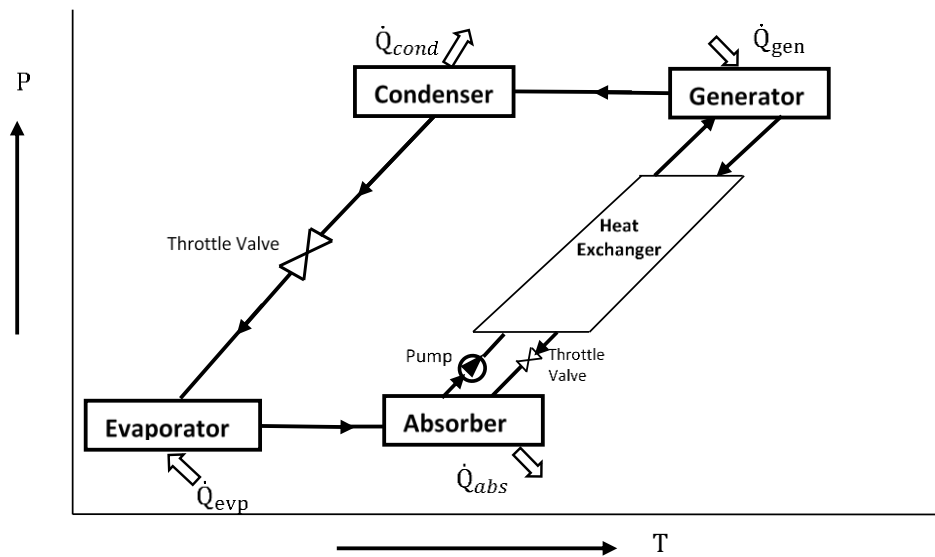


Figure 3.2: Pressure, concentration and temperature diagram of ammonia - water mixture.

The heat can be provided by flat plate, evacuated tube or concentrating solar collectors that are capable of delivering 70-120°C fluid to the generator. A single effect

ammonia-water absorption chiller can be driven by this generator temperature at a COP of 0.3 ~ 0.7 [Wang *et al.*, 2009]. Due to the necessary rectification and lower vaporization heat of ammonia, as opposed to water, the COP of an ammonia-water cycle is lower than that of a lithium bromide-water cycle with the same cooling capacity [Gormi, 2010]. Focusing on exergy destruction or irreversibility is a more direct way to analyze the potential for the improvement of the system performance. In this regard, energy and exergy analyses were performed in order to identify the locations of greatest exergy losses and the components with lower exergy loss in the process.

3.3. Thermodynamic Model

In analyzing this system, the principles of mass and energy conservation, and the second law of thermodynamics have been applied to each component of the refrigeration system. It is assumed that the solar collector loop provides a constant source of thermal energy. This study is limited to the steady flow steady state condition.

3.3.1. First Law Analysis (Energy Method)

In this study, the main components: generator, condenser, evaporator, absorber, solution heat exchanger, and solution pump have been studied. In order to analyze the thermodynamic first law for the absorption system, the following principal equations are used to determine the mass and energy conservation at each component. The condenser temperature determines the condenser pressure which is the pressure of the generator. The evaporator temperature determines the evaporator pressure and the absorber works with this pressure. The energy balances of the generator, the condenser, the absorber and the evaporator were calculated based on the corresponding pressures and temperatures.

$$\text{Mass Conservation: } \sum \dot{m}_{in} - \sum \dot{m}_{out} = 0 \quad (1)$$

$$\text{Energy Conservation: } \sum \dot{Q} = \sum \dot{m}_{out} h_{out} - \sum \dot{m}_{in} h_{in} + \dot{W} \quad (2)$$

where \dot{m} is the mass flow rate (kg/s), h is the specific enthalpy (kJ/kg) and \dot{Q} is the heat transfer rate (kW). The amount of heat transfer to and from each component are determined by the heat balance over each component of the system. The heat transfer for generator,

heat exchanger, pump, absorber, condenser and evaporator are represented by Equations (3) to (15).

For the generator, the mass and energy balances are:

$$\text{Total mass balance:} \quad \dot{m}_7 = \dot{m}_1 + \dot{m}_8 \quad (3)$$

$$\text{NH}_3 \text{ mass balance:} \quad X_7 \dot{m}_7 = \dot{m}_1 + X_8 \dot{m}_8 \quad (4)$$

where X is the NH_3 mass fraction in solution.

$$\text{Energy balance:} \quad \dot{Q}_{\text{gen}} = \dot{m}_1 h_1 + \dot{m}_8 h_8 - \dot{m}_7 h_7 \quad (5)$$

The mass flow rate of the weak and strong solutions can be calculated from Equations (3) and (4),

$$\dot{m}_8 = \frac{1-X_7}{X_7-X_8} \dot{m}_1 \quad (6)$$

$$\dot{m}_7 = \frac{1-X_8}{X_7-X_8} \dot{m}_1 \quad (7)$$

The circulation ratio can be determined from Equation (8) which is the indication of required pumping power. It can be defined as the ratio of the mass flow rate of the strong solution going into the generator and the mass flow rate of the refrigerant [Hammad & Habali, 2000].

$$CR = \frac{\dot{m}_7}{\dot{m}_1} \quad (8)$$

Equations (9) & (10) represent the energy balance for the solution heat exchanger.

$$T_9 = \eta_{HEX} T_6 + (1 - \eta_{HEX}) T_8 \quad (9)$$

where η_{HEX} is the heat exchanger efficiency.

$$h_7 = h_6 + \frac{\dot{m}_8}{\dot{m}_6} (h_8 - h_9) \quad (10)$$

The energy increase by pumping is

$$h_6 = h_5 + (P_6 - P_5) v_6 \quad (11)$$

$$\dot{W}_p = (P_6 - P_5) v_6 \quad (12)$$

Energy balances for the condenser, evaporator and absorber yield:

$$\text{Energy balance for condenser: } \dot{Q}_{\text{cond}} = \dot{m}_1(h_1 - h_2) \quad (13)$$

$$\text{Energy balance for evaporator: } \dot{Q}_{\text{eva}} = \dot{m}_1(h_4 - h_3) \quad (14)$$

$$\text{Energy balance for absorber: } \dot{Q}_{\text{abs}} = \dot{m}_4 h_4 + \dot{m}_{10} h_{10} - \dot{m}_5 h_5 \quad (15)$$

The coefficient of performance (COP) is the ratio of the useful energy gained from the evaporator to the primary energy supply to the generator and mechanical work done by the pump of the system [Shahata *et al.*, 2012].

$$\text{COP} = \frac{\text{useful energy output}}{\text{primary energy input} + \text{work done by pump}} = \frac{\dot{Q}_{\text{eva}}}{\dot{Q}_{\text{gen}} + \dot{W}_p} \quad (16)$$

3.3.2. Second Law Analysis (Exergy Method)

Exergy is defined “as the maximum amount of work potential of a material or an energy stream, in relation to the surrounding environment” [Sencan *et al.*, 2005]. The exergy balance in a control volume during a steady state process is stated as [Shahata, *et al.*, 2012]:

$$\dot{E}_{D,i} = \sum(\dot{m}e)_{in} - \sum(\dot{m}e)_{out} + \sum \dot{Q} \left(1 - \frac{T_o}{T}\right)_{in} - \sum \dot{Q} \left(1 - \frac{T_o}{T}\right)_{out} + \sum \dot{W} \quad (17)$$

where $\dot{E}_{D,i}$ represents the rate of exergy loss (destruction) of each component in the system. On the right-hand side of the equation, the first two terms represent the amount of the exergy entering and leaving the steady flow process in terms of mass transfer. The third and fourth terms are the exergy loss in terms of heat transfer, Q, to/from bodies maintained at constant temperature, T. The last term is the mechanical work transfer to or from the control volume. The exergy is expressed in terms of four types: physical, kinetic, potential and chemical exergy. Kinetic and potential exergy are assumed to be neglected and the chemical exergy is set to zero because there is no loss or gain of chemical substances from the cycle to the environment [Vidal *et al.*, 2006], so the exergy per unit mass of a fluid stream can be defined as [Zhu & Gu, 2010]:

$$e = (h - h_o) - T_o(s - s_o) \quad (18)$$

where e is the specific exergy, h and s are the enthalpy and entropy of the fluid at temperature T , whereas, h_o and s_o are the enthalpy and entropy of the fluid at environmental temperature T_o . In this analysis, T_o was set to 298.15 K. In a process, the principle exergy losses are due to heat transfer under a temperature difference with the surrounding and unrestricted expansion [Shahata *et al.*, 2012]. The reference enthalpy and entropy of the rich $\text{NH}_3\text{-H}_2\text{O}$ solution is considered at reference pressure, $P_0=101.325$ kPa and is assumed to have a NH_3 concentration equal to 55.05%.

The exergy loss in each component and the total exergy loss for the system can be written as:

$$\dot{E}_{D,gen} = \dot{m}_7 e_7 - \dot{m}_8 e_8 - \dot{m}_1 e_1 + \dot{Q}_{gen} \left(1 - \frac{T_o}{T_{gen}}\right) \quad (19)$$

$$\dot{E}_{D,con} = \dot{m}_1 (e_1 - e_2) - \dot{Q}_{con} \left(1 - \frac{T_o}{T_{con}}\right) \quad (20)$$

$$\dot{E}_{D,eva} = \dot{m}_1 (e_3 - e_4) + \dot{Q}_{eva} \left(1 - \frac{T_o}{T_{eva}}\right) \quad (21)$$

$$\dot{E}_{D,abs} = \dot{m}_4 e_4 + \dot{m}_{10} e_{10} - \dot{m}_5 e_5 - \dot{Q}_{abs} \left(1 - \frac{T_o}{T_{abs}}\right) \quad (22)$$

$$\dot{E}_{D,total} = \dot{E}_{D,gen} + \dot{E}_{D,con} + \dot{E}_{D,eva} + \dot{E}_{D,abs} \quad (23)$$

A non-dimensional exergy loss of each component can be defined as the ratio of the exergy loss in each component to the total exergy loss of the system [Zhu & Gu, 2010]. And it is written as follows for each component:

$$\text{Non - dimensional exergy loss} = \frac{\dot{E}_{D,i}}{\dot{E}_{D,total}} \quad (24)$$

The maximum thermal performance of an absorption refrigeration system is determined by assuming that the entire cycle is totally reversible (*i.e.*, the cycle involves no irreversibilities nor any heat transfer through a differential temperature difference) [Cengel & Boles, 2008], in which case the overall maximum thermal performance of an absorption refrigeration system under reversible condition becomes:

$$COP_E = \left(1 - \frac{T_o}{T_{gen}}\right) \left(\frac{T_{eva}}{T_o - T_{eva}}\right) \quad (25)$$

The second law efficiency of the absorption system leads to computing the exergetic efficiency, which is defined as the ratio of the useful exergy gained from a system to that supplied to the system [Ezzine *et al.*, 2004]. The exergetic efficiency can be determined by the ratio of actual coefficient of performance (COP) to the maximum possible coefficient of performance (reversible COP), under the same operating conditions:

$$\eta_{ex} = \frac{COP}{COP_E} \quad (26)$$

3.3.3. *Thermodynamic properties*

In Figure 3.1, States (1) to (4) require the thermodynamic properties for NH₃ and States (5) to (10) are based on NH₃-H₂O mixtures. The two-phase equilibrium pressure and temperature of NH₃, the specific enthalpies of saturated NH₃ liquid and NH₃ vapor in terms of temperature, the relation between saturation equilibrium pressure, concentration and temperature of an ammonia - water mixture and the specific volume of the mixture have been calculated using equations from Sun [1998]. The entropy of an ammonia-water mixture in the saturated liquid phase in terms of temperature, and concentration has been calculated by using a correlation from Alamdari [2007].

3.3.4. *Theoretical Considerations*

In this analysis, the following assumptions have been considered:

1. The system is operating under steady state conditions.
2. Ammonia-water solutions are presumed to be in equilibrium in the generator and in the absorber at their respective pressures and temperatures.
3. Unintentional pressure drops and heat losses in the pipelines and system components are negligible. So, heat transfer to and from the surroundings is negligible, other than at the generator, condenser, evaporator and absorber.
4. All throttle valves are under adiabatic condition, which results in constant enthalpy processes.

5. The circulating pump is isentropic.
6. The vapor leaving the generator/rectifier is 100% ammonia.
7. The refrigerant states leaving the condenser and evaporator are saturated liquid and saturated vapor.
8. The ammonia-water solution at the absorber outlet is a rich solution at the absorber temperature, respectively.
9. The condenser and the absorber are air cooled at atmospheric temperature 25°C.

3.4. Results and analysis

By analyzing the thermodynamic model, the performance of each component of the ammonia-water absorption cycle has been determined. Based on different working conditions, the coefficient of performance (COP), reversible coefficient of performance (COP_E) and exergetic efficiency (η_{ex}) were calculated. The results are presented graphically as a function of varying temperatures for each component of the system.

Imperfect heat and mass transfer in the cycle, mixing losses and circulation losses lead the system to the irreversibilities which reduce COP and exergetic efficiency to a lower value than the ideal reversible cycle in the absorption system. The mixing losses are due to the heat of mixing in the NH_3 - H_2O solution.

Table 3.1 shows the various thermodynamic values in the cycle operation that have been obtained from the analysis at $T_{gen} = 80^\circ C$, $T_{con} = 30^\circ C$, $T_{abs} = 30^\circ C$, $T_{eva} = 2^\circ C$ and a cooling load of 10 kW, and the solution heat exchanger effectiveness of 80% is assumed because, for the single effect ammonia-water absorption refrigeration system, the mass and heat transfer effectiveness is low, approximately 80% [Sun, 1998]. The results of the first law analysis are presented in Table 3.2, which illustrates various energy flows to and from each component of the system. The performance parameters and the exergetic efficiency are also shown in this table. The percentage of exergy losses of different components of the system at the same operating conditions are represented in Figure 3.3. It is noticed that around 63% of the total exergy loss is taking place in the absorption process. The second worst component from the viewpoint of exergy loss is the generator, followed by the condenser. These irreversibilities are mainly due to heat exchange across a large temperature difference in the absorber and mass transfer with a high concentration gradient

and mixing losses in the generator and the absorber [May *et al.*, 2011]. In addition, as the ammonia leaving the generator is superheated, a higher temperature is required under the same pressure, which leads to higher thermodynamic losses in the generator as well as in the absorber. The superheated temperature also drives the extra cooling requirement for the condenser which leads to the exergy losses in the condenser [Barhoumi *et al.*, 2009].

Table 3.1: Thermodynamic properties at different states in ammonia-water absorption cycle at operating conditions $T_{gen} = 80^{\circ}\text{C}$, $T_{cond} = 30^{\circ}\text{C}$, $T_{abs} = 30^{\circ}\text{C}$, $T_{eva} = 2^{\circ}\text{C}$, $\eta_{HEX} = 80\%$ and a cooling load of 10 kW

| Point | Temperature (°C) | Pressure (kPa) | Mass flow (kg/s) | % Concentration | Enthalpy (kJ/kg) | Entropy (kJ/kg.K) | Exergy, e (kJ/kg) |
|--------------------------|------------------|----------------|------------------|-----------------|------------------|-------------------|-------------------|
| Generator ref exit (1) | 80 | 1166.92 | 0.0089 | 100 | 1627.00 | 5.704 | 28.75 |
| Condenser ref exit (2) | 30 | 1166.92 | 0.0089 | 100 | 340.78 | 1.455 | 9.36 |
| Evaporator ref inlet (3) | 2 | 461.67 | 0.0089 | 100 | 340.78 | 1.536 | -14.81 |
| Evaporator ref exit (4) | 2 | 461.67 | 0.0089 | 100 | 1465.82 | 5.595 | -99.94 |
| Absorber sol exit (5) | 30 | 461.67 | 0.0436 | 55.05 | -114.25 | 0.609 | 20.30 |
| Sol HEX inlet (6) | 30 | 1166.92 | 0.0436 | 55.05 | -114.25 | 0.609 | 20.30 |
| Generator sol inlet (7) | 62 | 1166.92 | 0.0436 | 55.05 | 35.42 | 0.663 | 153.67 |
| Generator sol exit (8) | 80 | 1166.92 | 0.0347 | 43.90 | 110.85 | 0.517 | 272.80 |
| Sol HEX exit (9) | 40 | 1166.92 | 0.0347 | 43.90 | -77.13 | 0.459 | 101.95 |
| Absorber sol inlet (10) | 40 | 461.67 | 0.0347 | 43.90 | -77.13 | 0.459 | 101.95 |

Table 3.2: Energy and exergy flow for different components in ammonia-water absorption cycle at operating conditions $T_{gen} = 80^{\circ}\text{C}$, $T_{cond} = 30^{\circ}\text{C}$, $T_{abs} = 30^{\circ}\text{C}$, $T_{eva} = 2^{\circ}\text{C}$, $\eta_{HEX} = 80\%$ and a cooling load of 10 kW

| Components | Energy (kW) | Exergy (kW) |
|---|-----------------------------|---------------------------|
| Generator | $\dot{Q}_{gen} = 16.77$ | $\dot{E}_{D,gen} = 0.42$ |
| Condenser | $\dot{Q}_{cond} = 11.43$ | $\dot{E}_{D,cond} = 0.36$ |
| Evaporator | $\dot{Q}_{eva} = 10.00$ | $\dot{E}_{D,eva} = 0.08$ |
| Absorber | $\dot{Q}_{abs} = 15.33$ | $\dot{E}_{D,abs} = 2.02$ |
| Heat Exchanger | $\dot{Q}_{HEX} = 6.53$ | $\dot{E}_{D,HEX} = 0.12$ |
| Pump W_p | $W_p = 0.89 \times 10^{-3}$ | $\dot{E}_{D,p} = 0$ |
| COP | | 0.60 |
| Reversible COP_E | | 1.86 |
| Exergetic Efficiency, η_{ex} | | 32.01% |
| Circulation Ratio, CR | | 4.91 |

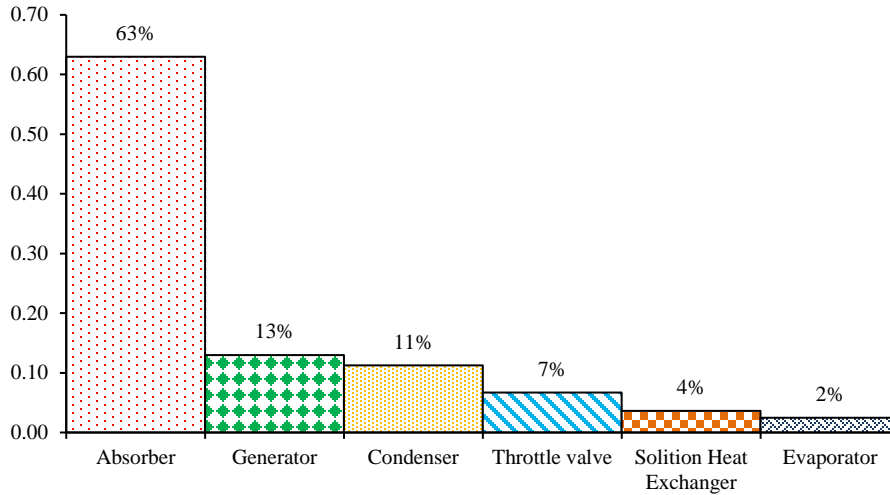


Figure 3.3: Non-dimensional exergy loss of different components of a 10kW system at $T_{gen} = 80^{\circ}\text{C}$, $T_{cond} = 30^{\circ}\text{C}$, $T_{abs} = 30^{\circ}\text{C}$, $T_{eva} = 2^{\circ}\text{C}$, $\eta_{HEX} = 80\%$

The coefficient of performance (COP), reversible coefficient of performance (COP_E) and exergetic efficiency (η_{ex}) of this absorption cycle are plotted in Figure 3.4 as functions of the generator temperature. The reversible COP_E increases with increasing generator temperature. The coefficient of performance (COP) and the exergetic efficiency pass through maxima at 80°C and 70°C respectively. After the maximum point, the gradient of the COP curve becomes almost flat whereas the exergetic efficiency decreases rapidly. This suggests that the exergetic efficiency is more affected by increasing generator temperature than that of the COP. Although the higher generator temperature can produce more ammonia vapor, it also increases the solution temperature in the absorber and the generator which leads to more exergy losses in the absorber and the generator as well as in the condenser. As a result, the total exergy loss of the system is varying with the generator temperature as presented in Figure 3.5. The circulation ratio also decreases with an increase in generator temperature as shown in Figure 3.6. If the generator temperature approaches its low temperature limit, the circulation ratio increases dramatically. Therefore, it is impractical to operate this cycle when the generator temperature is below about 70°C . So, the negative effect of increasing generator temperature can assist in optimizing the driving temperature of this 10 kW absorption cooling system, which lies between $70\text{--}80^{\circ}\text{C}$. This temperature range can be achieved by using flat plate solar collectors which are generally appropriate for temperatures below 90°C [Treberspurg *et al.*, 2011].

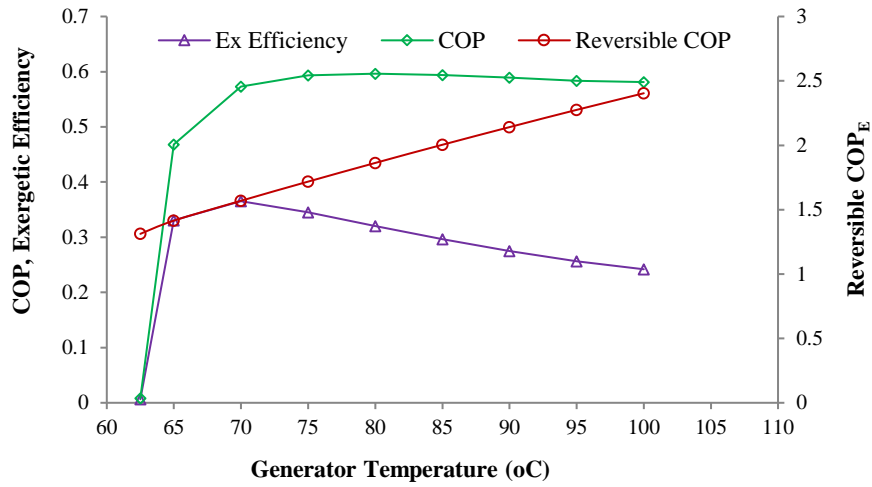


Figure 3.4: Effect of generator temperature on the COP, reversible COPE and exergetic efficiency at $T_{cond} = 30^{\circ}\text{C}$, $T_{abs} = 30^{\circ}\text{C}$, $T_{eva} = 2^{\circ}\text{C}$, $\eta_{HEX} = 80\%$

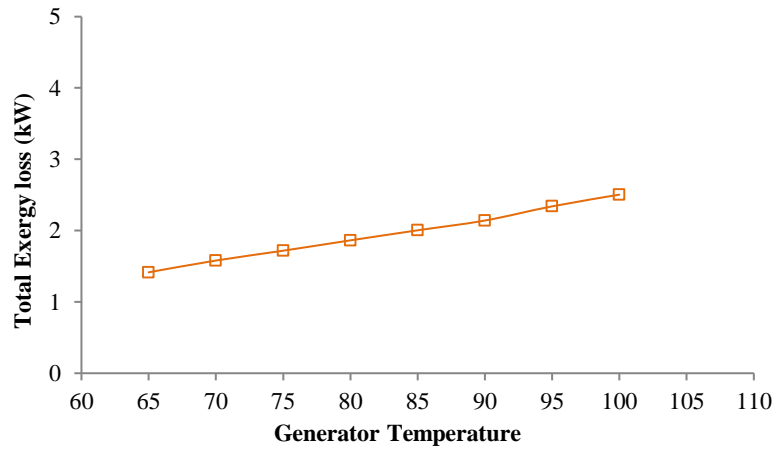


Figure 3.5: Effect of generator temperature on the total exergy loss of the system at $T_{cond} = 30^{\circ}\text{C}$, $T_{abs} = 30^{\circ}\text{C}$, $T_{eva} = 2^{\circ}\text{C}$, $\eta_{HEX} = 80\%$

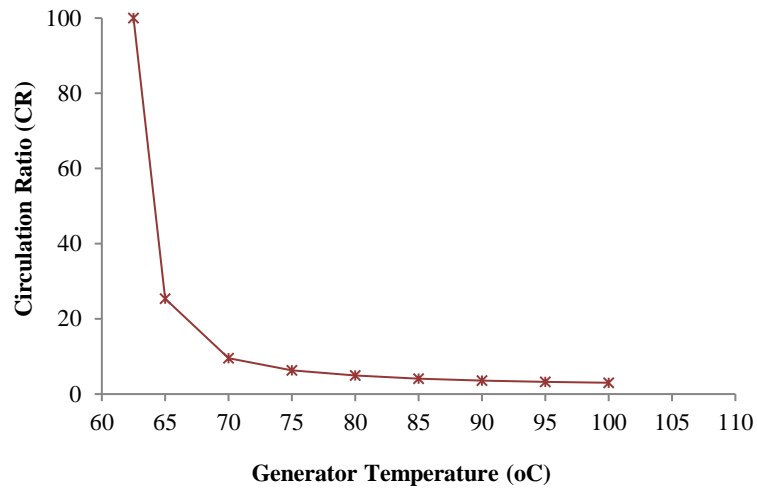


Figure 3.6: Effect of generator temperature on the circulation ratio (CR) at $T_{cond} = 30^{\circ}\text{C}$, $T_{abs} = 30^{\circ}\text{C}$, $T_{eva} = 2^{\circ}\text{C}$, $\eta_{HEX} = 80\%$

The effects of the evaporator temperature are illustrated in Figure 3.7 and Figure 3.8. With varying the evaporator temperature from -4 to 16°C ; both COP and reversible COP_E increase. The higher evaporator temperature causes a higher absorbing pressure which significantly increases the absorption efficiency of the weak solution. With constant cooling load, the absorber and generator thermal loads decrease with increasing evaporator temperature leading to the COP increases. But the increase of COP is almost linear while that of the reversible COP_E is incremental with increasing evaporator temperature. The impact of other variables of the system causes the actual COP to be almost linear. Unlike COP, increasing the evaporator temperature has a negative impact on the exergetic efficiency. It can be seen that the absorption cooling system has higher exergetic efficiency at lower evaporator temperatures. This means that the evaporator has a higher potential for cooling at its lower temperature.

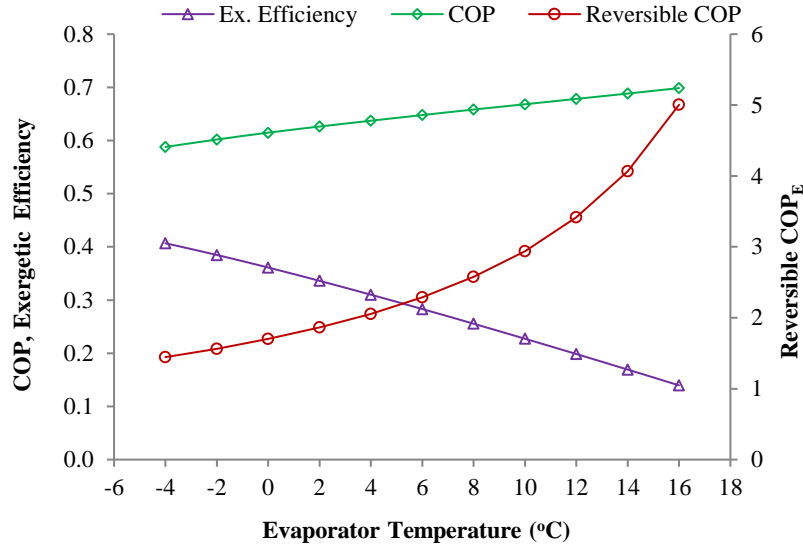


Figure 3.7: Effect of evaporator temperature on the COP, reversible COP_E and exergetic efficiency of 10kW system at $T_{gen} = 80^{\circ}\text{C}$, $T_{cond} = 30^{\circ}\text{C}$, $T_{abs} = 30^{\circ}\text{C}$, $\eta_{HEX} = 80\%$

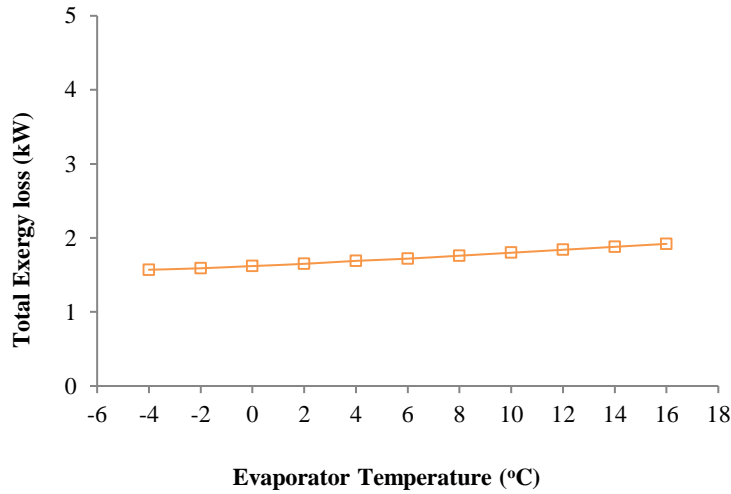


Figure 3.8: Effect of evaporator temperature on the total exergy loss of 10kW system at $T_{gen} = 80^{\circ}\text{C}$, $T_{cond} = 30^{\circ}\text{C}$, $T_{abs} = 30^{\circ}\text{C}$, $\eta_{HEX} = 80\%$

It is also shown in Figure 3.8 that increasing evaporator temperature has very little impact on the total exergy loss of the system as compared to increasing the generator temperature. From the analysis of energy and exergy, it can be explained that the required cooling effect can be achieved by decreasing the evaporator temperature.

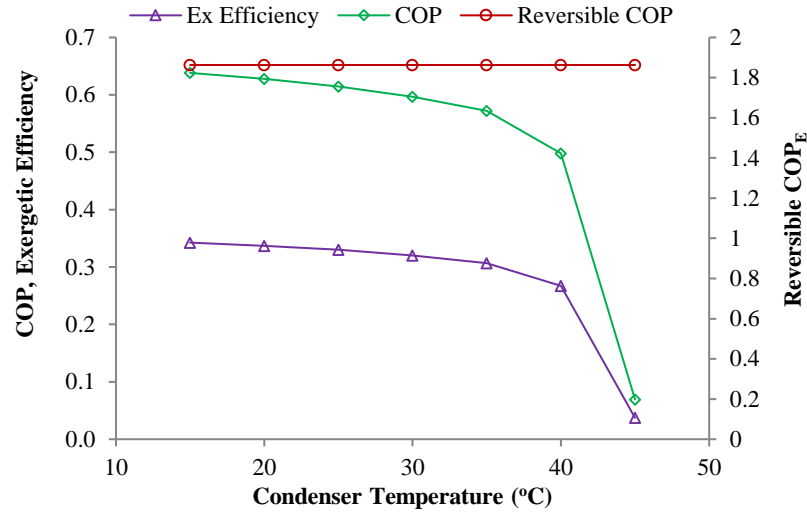


Figure 3.9: Effect of condenser temperature on the COP, reversible COP_E and exergetic efficiency of 10kW system at $T_{gen} = 80^{\circ}\text{C}$, $T_{abs} = 30^{\circ}\text{C}$, $T_{eva} = 2^{\circ}\text{C}$, $\eta_{HEX} = 80\%$

The relationship between the COP, reversible COP_E, exergetic efficiency and condenser temperature are shown in Figure 3.9. A decrease of the system performance and exergetic efficiency occur with increasing condenser temperature. As the system is considered reversible, meaning that the system is a reversible Carnot heat engine and Carnot refrigerator, so the heat transfer between the condenser and the environment occurs across an infinitesimal temperature difference. The overall maximum thermal performance of an absorption refrigeration system under reversible conditions depends on only the heat from the source (generator) and heat removed from the refrigerated space by the evaporator. As the reversible COP_E depends on the generator and the evaporator temperature, there is no condenser temperature impact on the reversible COP_E. With a constant cooling load, increasing the condenser temperature causes a higher pressure in the system, which increases the thermal load on the generator. This results in less ammonia vapor released from the generator, so both COP and exergetic efficiency decrease. This explains why the maximum system performance and exergetic efficiency are attained at lower values of condenser temperature. In order to operate the cycle at a higher condenser temperature, such as in tropical countries, the generator temperature should be higher for a constant cooling load. Therefore, the system must be driven by high temperature flat plate

solar collector or an evacuated tube collector which would result in a higher solar loop temperature. It can also be seen from Figure 3.10 that the total exergy loss also increases rapidly with increasing condenser temperature. The exergy loss in the condenser results from the temperature difference between the environment and the condenser refrigerant. So, the exergy and the system performance benefit from lower condenser temperatures.

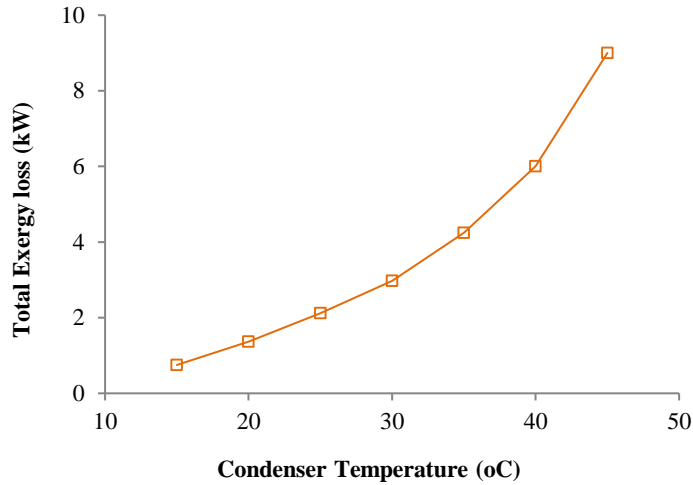


Figure 3.10: Effect of condenser temperature on the total exergy loss of 10kW system at $T_{gen} = 80^{\circ}\text{C}$, $T_{abs} = 30^{\circ}\text{C}$, $T_{eva} = 2^{\circ}\text{C}$, $\eta_{HEX} = 80\%$

The result of the absorber temperature's effect is the same as that of the condenser temperature for both the system performance as well as for the exergy loss. Figure 3.11 shows the variation of the COP, reversible COP_E and exergetic efficiency with the absorber temperature. Increasing absorber temperature decreases the absorption efficiency of the weak solution in the absorber. As a result, with a constant cooling load, absorber and generator thermal loads increase, therefore the COP decreases. The reversible COP_E remains constant as was the case for varying condenser temperature. The higher system performance can be achieved at lower absorber temperature. The increasing absorber temperature increases the solution temperature in the absorber as well as in the generator which leads to greater mixing losses in the absorber and the generator. The increasing solution temperature also affects the heat exchanger. As a result, high temperature solution is entering the absorber. These increase the exergy loss of the heat exchanger as well as of the absorber. This leads to a significant increase in the total exergy loss of the system.

Figure 3.12 illustrates the corresponding effect of the system exergy loss versus absorber temperature.

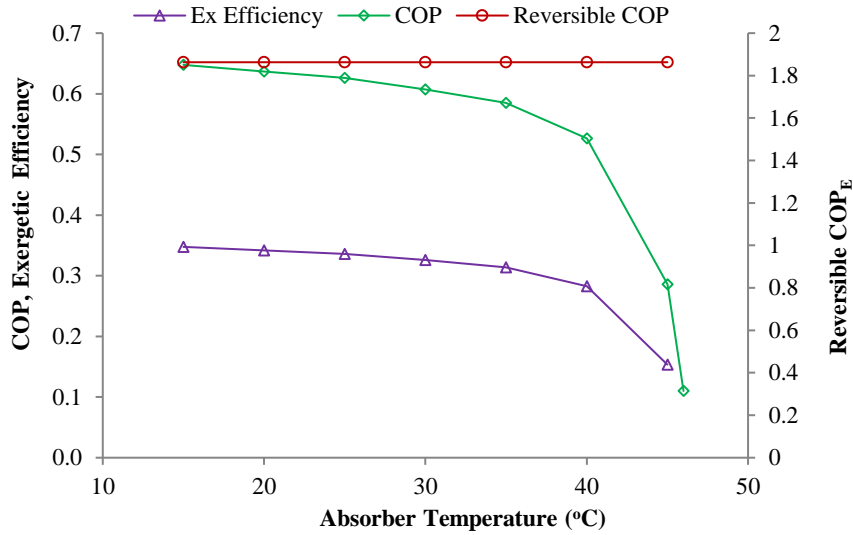


Figure 3.11: Effect of absorber temperature on the COP, reversible COP_E and exergetic efficiency of 10kW system at $T_{gen} = 80^{\circ}\text{C}$, $T_{cond} = 30^{\circ}\text{C}$, $T_{eva} = 2^{\circ}\text{C}$, $\eta_{HEX} = 80\%$

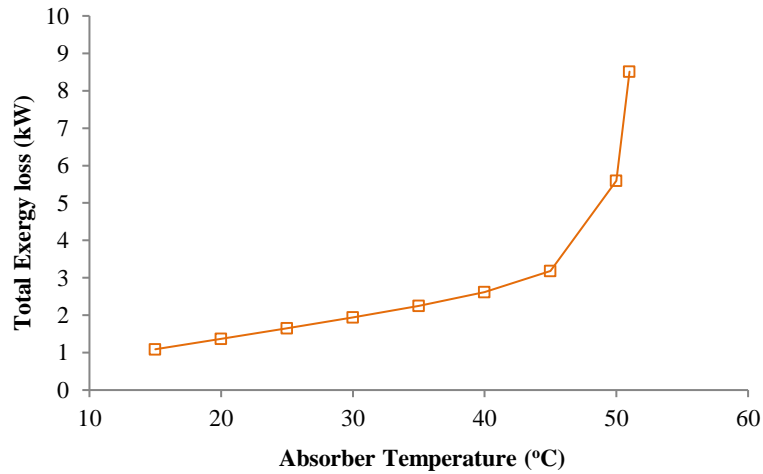


Figure 3.12: Effect of absorber temperature on the total exergy loss of 10kW system at $T_{gen} = 80^{\circ}\text{C}$, $T_{cond} = 30^{\circ}\text{C}$, $T_{eva} = 2^{\circ}\text{C}$, $\eta_{HEX} = 80\%$

Energy and exergy analyses of each component of this small cooling absorption system determine the optimum operation conditions for the best system performance. It also reveals that the absorber, the generator, and the condenser represent the most of the

total exergy losses of the chiller. For an ideal process, the reversible COP_E is 1.86. The potential degradation of all components results in an actual COP of 0.60. The absorber has the greatest potential to improve the system performance. This component needs the maximum design improvement following by the generator and the condenser in order to reduce their exergy loss rate resulting of reducing the irreversibility.

3.5. Conclusions

The goal of this study was to maximize the efficiency of an absorption chiller that can be used for residential air conditioning application with a low temperature driving source such as solar thermal energy. In this regard, energy and exergy analyses of a 10 kW air-cooled ammonia-water absorption chiller have been performed and the system performance, exergetic efficiency and the exergy loss of different components of the system have been calculated.

The first and second law efficiency of the system have been investigated and compared under different system operating conditions. The results show that the COP of the system increases slightly with increasing heat source temperature and the evaporator temperature but decreases as absorber and condenser temperatures increase. However, the exergetic efficiency decreases with the increase of generator, evaporator, condenser and absorber temperatures. The analysis reveals that the cycle is more thermodynamically efficient when the absorption cooling system is operated using low temperature heat sources rather than high temperature heat sources and it has also been noticed that decreasing of the condenser and the absorber temperatures towards the atmospheric temperature does not impact significantly the overall system performance. So, for small scale applications, an ammonia-water absorption chiller can be operated with heat supplied by a flat plate solar collector with ambient air cooling of the absorber and the condenser.

The exergy analysis of this absorption cooling system shows that the highest exergy loss (around 76%) is located in the absorbing process and in the generator. In order to improve cycle efficiency, the highest efforts should be given to improving the absorber while the generator may be considered as the second priority.

Finally, the energy and exergy analyses in this paper offer a simple and effective method to identify where losses are taking place in the small ammonia-water absorption

cooling system and how these affect the system performance. It also offers insight into which component should be modified in design for the best performance of the system. Additionally, the results can also be used in thermoeconomic optimization of absorption systems. The thermoeconomic optimization of the system can take into account “the costs and benefits (or "profitability") of the various mechanisms for utilizing and capturing available energy to do work” [Corning, 2002].

Acknowledgement

This work is made possible by the Natural Science and Engineering Research Council of Canada.

Nomenclature

| | | | |
|------------------|---|-------------------|-------------|
| COP | coefficient of performance | <i>Subscripts</i> | |
| COP _E | coefficient of performance under reversible condition | <i>abs</i> | absorber |
| CR | circulation ratio | <i>cond</i> | condenser |
| e | exergy (kJ/kg) | <i>eva</i> | evaporator |
| E _D | exergy destruction or loss (kW) | <i>gen</i> | generator |
| h | specific enthalpy (kJ/kg) | <i>i</i> | component |
| h _o | specific enthalpy at reference temperature 25°C | <i>in</i> | inlet |
| HEX | Heat Exchanger | <i>out</i> | outlet |
| \dot{m} | mass flow rate (kg/s) | <i>p</i> | pump |
| P | pressure (kPa) | <i>ref</i> | refrigerant |
| P _o | reference pressure 101.325 kPa | <i>sol</i> | solution |
| \dot{Q} | heat transfer rate (kW) | | |
| s | specific entropy (kJ/kg·K) | | |
| s _o | specific entropy at reference temperature 25°C | | |
| T | temperature (K) | | |
| T _o | reference temperature 25°C | | |
| X | mass fraction of ammonia (%) | | |
| \dot{W} | work rate (kW) | | |
| η_{HEX} | heat exchanger efficiency | | |
| η_{ex} | exergetic efficiency | | |
| v | pump specific volume (m ³ /kg) | | |

REFERENCES

- Abdulateef J.M., Sopian K., Alghoul M.A., Optimum design for solar absorption refrigeration systems and comparison of the performances using ammonia-water, ammonia-lithium nitrate and ammonia-sodium thiocyanate solutions. *International Journal of Mechanical and Materials Engineering (IJMME)*, 3 (2008) 17-24.
- Adewusi S.A., Zubair S., M., Second law based thermodynamic analysis of ammonia–water absorption systems. *Energy Conversion and Management*, 45 (2004) 2355–2369.
- Alamdari G. S., Simple equations for predicting entropy of Ammonia-water mixture. *International Journal of Engineering (IJE), Transactions B: Applications*, 20 (2007) 97.
- Aphornratana S., Eames I. W., Thermodynamic analysis of absorption refrigeration cycles using the second law of thermodynamics method. *International Journal of Refrigeration*, 18 (1995) 244 – 252.
- Barhoumi M., Ezzine N. B., Bellagi A., Exergy analysis of an ammonia-water absorption system. *International Journal of Exergy*, 6 (5) (2009).
- Boudéhenn F., Demasles H., Wytttenbach J., Jobard X., Chèze D., Papillon P., Development of a 5 kW cooling capacity ammonia-water absorption chiller for solar cooling applications. *Energy Procedia*, 30 (2012) 35 – 43.
- Cengel Y., Boles M., *Thermodynamics: An Engineering Approach*. McGraw-Hill; 2008.
- Central Electricity Authority (CEA), Ministry of Power, Government of India, June 2013.
- Corning P., A., Thermoeconomics: Beyond the second law. *Journal of Bioeconomics*, 4 (2002) 57-88.
- De Francisco A., Illanes R., Torres J.L., Castillo M., De Blas M., Prieto E., Garcia A., Development and testing of a prototype of low-power water–ammonia absorption equipment for solar energy applications. *Renew. Energy*, 25 (2002) 537–544.
- Deng J., Wang R.Z., Han G.Y., A review of thermally activated cooling technologies for combined cooling, heating and power systems. *Progress in Energy and Combustion Science*, 37 (2011) 172-203.
- Du S., Wang R.Z., Lin P., Xu Z.Z., Pan Q.W., Xu S.C., Experimental studies on an air-cooled two-stage NH₃-H₂O solar absorption air-conditioning prototype. *Energy*, 45 (2012) 581-587.

- Ezzine N., Barhoumi B., Mejbri M., Chemkhi K., Bellagi S., A., Solar cooling with the absorption principle: First and Second Law analysis of an ammonia - water double-generator absorption chiller. *Desalination Strategies in South Mediterranean Countries. Desalination*, 168 (2004) 137-144.
- Gomri R., Investigation of the potential of application of single effect and multiple effect absorption cooling systems. *Energy Conversion and Management*, 51 (2010) 1629–1636.
- Hammad M. , Habali S., Design and performance study of a solar energy powered vaccine cabinet. *Applied Thermal Engineering*, 20 (2000) 1785–1798.
- Henning M., Solar assisted air conditioning of buildings – an overview. *Applied Thermal Engineering*, 27 (2007) 1734–1749.
- Häberle A, Luginsland F, Zahler C, Berger M, Rommel M, Henning HM, et al., A linear concentrating Fresnel collector driving a NH₃-H₂O absorption chiller. *Proceedings of the second international conference solar air-conditioning, Tarragona, Spain; (2007)* 662 -667.
- Izquierdo M, Venegas M, Rodríguez P, Lecuona A., Crystallization as a limit to develop solar air-cooled LiBr-H₂O absorption systems using low-grade heat. *Solar Energy Materials and Solar Cells*, 81 (2004) 205-216.
- Jakob U., Eicker U., Solar cooling with diffusion absorption principle. *World Renewable Energy Congress VII, Cologne, Germany, 29 June–5 July (2002)*.
- Jakob U., Pink W., Development and investigation of an ammonia/water absorption chiller – chillii_ PSC – for a solar cooling system. *Proceedings of the 2nd International Conference Solar Air-Conditioning, Tarragona, Spain, (2007)* 440–445.
- Jakob U., Spiegel K., Pink W., Development and experimental investigation of a novel 10kW ammonia/water absorption chiller for air conditioning and refrigeration systems. *9th International IEA Heat Pump Conference, Zürich, Switzerland, 20 – 22 May (2008)*.
- May S. E. I, Boukholda I., Bellagi A., Energetic and exergetic analysis of a commercial ammonia-water absorption chiller. *International Journal of Exergy*, 8 (1) (2011).
- Raghuvansh S., Maheshwari G., Analysis of Ammonia –Water (NH₃-H₂O) Vapor Absorption Refrigeration System based on First Law of Thermodynamics. *International Journal of Scientific and Engineering Research*, 2 (2011) 2229-5518.

- Ryan W., New developments in gas cooling. *ASHRAE Journal*, 4 (2002) 23-26.
- Sabatelli V., Fiorenza G., Marano D., Technical status report on solar desalination and solar cooling. A technical report of the EU-project “NEGST (New Generation of Thermal Solar Systems)” WP5.D1. <http://www.swt-technologie.de/html/publicdeliverables3.html>, (2007).
- Sencan A., Yakuta K. A., Kalogirou S. A., Exergy analysis of lithium bromide/water absorption systems. *Renewable Energy*, (2005) 645–657.
- Shahata A.I., Aboelazm M. M., Elsafty A. F., Energy and Exergy Analysis for Single and Parallel Flow Double Effect Water-Lithium Bromide Vapor Absorption Systems. *International Journal of Science and Technology*, 2 (2012) 85-94.
- Sozen A., Altiparmak D., Usta H., Development and testing of a prototype of absorption heat pump operated by solar energy. *Applied Thermal Engineering*, 22 (2002) 1847–1859.
- Sun D. W., Comparison of the performances of $\text{NH}_3\text{-H}_2\text{O}$, $\text{NH}_3\text{-LiNO}_3$ and $\text{NH}_3\text{-NaSCN}$ absorption refrigeration systems. *Energy Conversion and Management*, 39 (1998) 357-368.
- Vidal R., Best R., Rivero R., Cerventas J., Analysis of a combined power and refrigeration cycle by the exergy method. *Energy*, 31 (2006) 3401– 3414.
- Wang R.Z., Ge T.S., Chen C.J., Ma Q., Xiong Z.Q., Solar sorption cooling systems for residential applications: Options and guidelines. *International Journal of Refrigeration*, 32 (2009) 638 – 660.
- Zhu L., Gu J., Second law-based thermodynamic analysis of ammonia/sodium thiocyanate absorption system. *Renewable Energy*, 35 (2010) 1940–1946.

CHAPTER 4

MODELLING AND ANALYSIS OF BUBBLE PUMP PARAMETERS FOR VAPOR ABSORPTION REFRIGERATION SYSTEMS

This work was published as “Aman, J., Henshaw, P. Ting, D. S-K., Modelling and Analysis of Bubble Pump Parameters for Vapor Absorption Refrigeration Systems, proceedings of ASHRAE Annual conference 2016, St. Louis, MO, June 25-29, 2016”.

4.1. Introduction

A vapor absorption refrigeration (VAR) cycle for air conditioning applications is of great interest for sustainable development because it can be driven by waste heat or solar thermal energy [Aman *et al.*, 2014]. The VAR system consists of absorber, generator, condenser and evaporator. An electrical/mechanical pump is required in this system to circulate the solution from absorber to generator, exposing the pump to the high temperature corrosive solution. A single pressure VAR cycle such as a diffusion-absorption refrigeration (DAR) system can be driven by solar thermal energy using a bubble pump. In a bubble pump, the vapor created (by using the heat) increases the buoyancy of the fluid, causing it to ascend through a vertical tube under two-phase flow conditions. There are several methods by which vapor or gas can be used for lifting liquids [Abu-Mulaweh *et al.*, 2011]. For example, airlift pumps, where the buoyancy is created by injecting air into the liquid, have been used for decades in the oil industry [White, 2001].

The bubble pump consists of a vertical lift tube connecting the generator and the separator. The generated vapor bubbles rise in the tube carrying the liquid above and around them into the separator as shown in Figure 4.1. Three flow regimes can be observed during bubble pump operation (Figure 4.1). When the temperature is slightly higher than the saturation temperature of the liquid, small vapor bubbles will form in the liquid. This is referred as the bubbly flow regime. With an increase of heat input, the flow of vapor bubbles will increase in the liquid phase, coalesce and generate Taylor bubbles [Reinemann, 1987]. This is termed the slug flow regime. At steady-state, a train of vapor slugs may be observed in the vertical tube, which pushes slugs of liquid upward [Delano, 1998]. The wake developed at the rear of each rising bubble and in a series of bubbles turns

into a turbulent wake [Mayor *et al.*, 2008]. A further increase of heat supply will increase the vapor flow rate, causing the vapor bubbles to become irregular and narrow. This flow is called churn flow. Experimental studies showed that the bubble pump is most efficient in the slug flow regime [Delano, 1998; White, 2001; Benhmidene *et al.*, 2011; Walt, 2012].

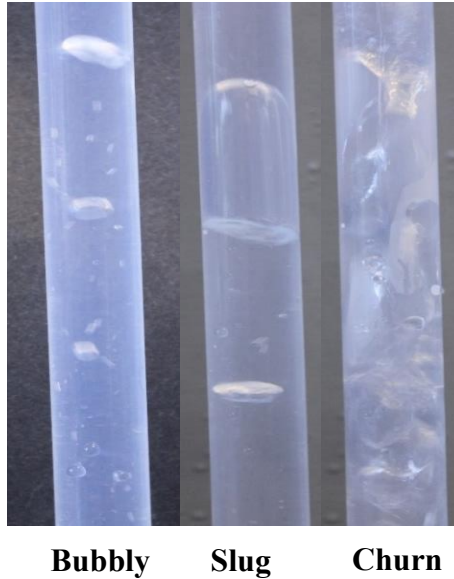


Figure 4.1: Flow regimes in a bubble pump

The Platen-Munters Cycle first introduced the bubble pump for a DAR system in 1920's. The Swedish company Electrolux-Servel Corporation was the first manufacturer to patent this in 1926. Dometic Group is now the manufacturer of this DAR system. Recently there has been lots of interest to use this cycle by changing the generator bubble pump configuration and using different working fluids [Benhmidene *et al.*, 2010]. The experimental performance of a solar driven bubble pump under different operating conditions was obtained by Bourseau *et al.* [1987]. Though the airlift pump has been reported in the literature since 1908, the first theoretical analysis was performed in 1968, using the fundamental principal of two-phase flow [Stenning and Martin, 1968]. A general slug flow equation was provided to design the airlift pump [Clark and Dabolt, 1986]. An analytical model of the bubble pump, based on mass and momentum conservation, was developed by Delano [1998] to fit into the Einstein refrigeration cycle. In his model, all supplied heat was assumed to evaporate the water to generate bubbles, the velocity of the

bubbles was constant, and there was no heat loss. He also used a constant value of slip factor (the ratio of velocities of the vapor and the water), but in reality, the velocities of water and vapor change with the operating regime. As he assumed single-phase flow in his model, he avoided the gas void fraction in his analysis. By using his model, he revealed that the mass flow rate of the liquid varies with heat input and tube diameter.

A bubble pump suitable for the lithium bromide–water vapor absorption cycle was investigated [Pfaff *et al.*, 1998]. A mathematical model was developed based on the manometer principle. Their model focused on the time required to generate a vapor bubble from subcooled liquid for one complete cycle. A test rig was built in glass to visualize the flow behavior and to validate the analytical model. It was found that the pumping action (time required for two consecutive cycles) varied with heat input, lift tube diameter, as well as the lifting height. Recently, an indirectly heated bubble pump for a diffusion absorption refrigeration system was developed [Jakob *et al.*, 2008]. The bubble pump lift tube was surrounded by heat transfer medium and bubbles were generated inside the lift tube under a constant heat supply. They observed a change in the flow pattern, from liquid to vapor, along the vertical tube. Different configurations of a bubble pump were studied by numerical analyses for diffusion absorption refrigeration [Zohar *et al.*, 2008]. The above-mentioned analytical models start with Stenning and Martin’s method, which uses a coefficient to determine the two-phase flow friction factor and the gas void fraction [Stenning and Martin, 1968]. Benhmidene *et al.* [2011] studied and simulated the heat flux into the vertical lift tube of the bubble pump, where the tube was surrounded by the heating element. In their simulation, they used a constant liquid flow rate and determined the optimum heat input without considering the heat loss; and the flow regime was not limited to slug flow. Chan and McCulloch [2013] improved Pfaffs’ model by considering the heat loss to estimate the time required for one cycle operation. They noted that the Taylor bubbles collapsed along the vertical tube in the bubble pump due to heat loss. There is no information provided as to how they estimated the heat loss, and also they ignored the effect of the friction factor.

Although extensive theoretical and experimental work has been performed to make the bubble pump compatible to the DAR system, some analyses were based on air-lift pumps, some did not consider friction factor effects, two-phase flow or the gas void

fraction. Laminar flow was assumed in all of them, and heat loss was not included, except by Chan and McCulloch [2013]. In this work, the bubble pump operation was investigated based on water at atmospheric conditions. Two-phase turbulent flow was considered to find the friction factor; and the surface tension effect was used to find the void fraction. The heat loss was calculated for the reservoir as well as the lift tube. Thermophysical properties of the solution were also considered for the evaluation of bubble pump performance.

4.2. System Analysis

4.2.1. Bubble Pump Modeling

In this analysis, a two-phase flow model is used to determine the flow rate of the liquid in the bubble pump. The following analytical model has been used to describe the bubble pump performance. The actual velocity of the rising vapor bubble relative to a liquid moving slug can be determined by the following equations [Nicklin, 1963]

$$v_g = C_0 v_m + v_b, \quad v_m = \frac{\dot{V}_l + \dot{V}_g}{A}, \quad v_g = \frac{\dot{V}_g}{\alpha_d A} \quad (1)$$

where, v_g is the actual velocity of the rising gas bubble (m/s), C_0 is the liquid slug velocity profile coefficient (ranging from 1.2 for fully developed turbulent flow to 2 for laminar flow), v_b is the velocity of a rising gas bubble in stagnant liquid (m/s), v_m is the mean velocity of the liquid slug (m/s), A is the cross sectional area of the lift tube (m^2), and α_d is the gas void fraction which is defined in Equation (3). The void fraction is one of the important parameters in two-phase flow to determine the flow regime as well as two-phase pressure drop and heat transfer [Walt, 2012].

The volume flow rate of liquid and gas and the gas bubble velocity can be expressed as dimensionless Froude numbers, and written as [Reinemann, 1987]

$$\dot{V}'_l = \frac{\dot{V}_l}{A(gD)^{1/2}}, \quad \dot{V}'_g = \frac{\dot{V}_g}{A(gD)^{1/2}}, \quad v'_b = \frac{v_b}{(gD)^{1/2}} \quad (2)$$

where, \dot{V}'_l = dimensionless liquid volume flow rate, \dot{V}'_g = dimensionless gas volume flow rate, v'_b = dimensionless gas bubble velocity in the liquid, D = inner diameter of the lift tube. Combining Equations (1) & (2), the gas void fraction becomes

$$\alpha_d = \frac{\text{volume of the vapor in the liquid}}{\text{total volume of the liquid vapor mixture}} \quad (3)$$

$$= \frac{\dot{V}'_g}{C_o(\dot{V}'_l + \dot{V}'_g) + v'_b}$$

From theoretical and experimental analysis, Reinemann (1987) showed that the gas bubble velocity Froude number in stagnant liquid can be expressed in terms of the surface tension parameter:

$$v'_b = 0.352(1 - 3.18\Sigma - 14.77\Sigma^2) \quad (4)$$

where, the surface tension parameter, $\Sigma = \frac{\sigma}{\rho g D^2}$ (5)

In bubble pump analysis, the submergence ratio (SR), can be expressed as (see Figure 1)

$$SR = \frac{H}{L} = \frac{\text{Height of the liquid in the lift tube}}{\text{Lift tube length}}$$

The submergence ratio (SR) is related to the pressure due to the weight of the liquid and gas mixture and the friction losses. If the lift tube is partially filled with liquid to height H, the static pressure balance of the lift tube will be

$$\rho g H = \rho g (1 - \alpha_d) L \quad (6)$$

Considering the mean slug velocity, the pressure drop due to frictional losses can be calculated by using the modified single-phase frictional pressure drop

$$P_f = f \frac{L}{2D} \rho v_m^2 (1 - \alpha_d) \quad (7)$$

where, f is the turbulent friction factor for continuous flow slug velocity [Mayor *et al.*, 2008], given by

$$f = \frac{0.316}{Re^{0.25}} \quad (8)$$

Re is the Reynolds number for a mixture of liquid and vapor, and can be expressed as

$$Re = \frac{\rho_{MIX} v_m D}{\mu} \quad (9)$$

So, the total pressure drop along the lift tube is

$$\rho g H = \rho g ((1 - \alpha_d)L + f \frac{L}{2D} \rho v_m^2 (1 - \alpha_d)) \quad (10)$$

Dividing Equation (10) by $\rho g L$ and rearranging with Equations (1) & (2) gives

$$SR = \frac{H}{L} = (1 - \alpha_d) \left(1 + \frac{f}{2} (\dot{V}'_l + \dot{V}'_g)^2\right) \quad (11)$$

The flow rate of vapor depends on the heat supply to the bubble pump. However, the heat loss through the vertical lift tube makes the bubble pump different than an air-lift pump. Due to heat losses, the Taylor bubble may collapse before reaching the top of the vertical tube. The heat loss is equal to the heat release from the two-phase flow inside the tube to the ambient air by free convection and the infrared radiative heat loss of the lift tube.

The best fit equation for the heat loss of two-phase (TP) flow inside the vertical tube has been taken from Katsuharu and Kazama [Sujumnong, 1997]

$$\overline{Nu}_{TP} = 8.7(1 - \alpha_d)^{0.125} (Re)^{0.25} (Pr_{MIX})^{0.4} \quad (12)$$

$$\overline{Nu}_{TP} = \bar{h}_{TP} D / k_{MIX} \quad (13)$$

$$\dot{Q}_{loss} = \frac{T_{TP} - T_{air}}{R_{Total}} + 2\pi r_2 L \epsilon \sigma_{Boltz} (T_{LT}^4 - T^4) \quad (14)$$

$$R_{Total} = \frac{1}{2\pi r_1 L \bar{h}_{TP}} + \frac{\ln(r_2/r_1)}{2\pi L k_{LT}} + \frac{1}{2\pi r_2 L \bar{h}_{air}} \quad (15)$$

The two-phase fluid density (ρ_{MIX}), thermal conductivity (k_{MIX}), and Prandtl number (Pr_{MIX}) have been calculated by using equations from Sujumnong [1997]. The heat loss from the generator can be estimated from Equation (14). The sensible heat loss for the liquid flowing from the reservoir to the generator was also included. After considering heat losses, the vapor and mass flow rates can be calculated by the following equation

$$\dot{Q}_{bubble\ pump} - \dot{Q}_{total\ loss} = \dot{V}_g \rho_g h_{fg} = \dot{m}_g h_{fg} \quad (16)$$

The volume flow rate of the liquid was determined in terms of heat input via Equations (2), (11) & (16). And the mass flow rate of the liquid by the bubble pump was calculated from the following Equation.

$$\dot{m}_l = \dot{V}_l \rho \quad (17)$$

The analytical model was solved by using EES (engineering equation solver) [EES, 2015]. The simulation was performed by assuming initial values of water temperature, pressure, input heat, tube length and diameter, and the SR. After calculating the total heat loss, the volumetric flow rate of vapor was calculated by Equation (16). This lead to an iterative calculation of the volumetric flow rate of liquid by Equations (3) & (11).

4.3. Experimental Set-up and Procedure

Figure 4.2 shows the schematic and experimental set up of the bubble pump. Water was the working fluid for these experiments and the reservoir and separator were open to the atmosphere. This system allows the bubble pump to run intermittently: whenever the water in the generator reaches the boiling point.

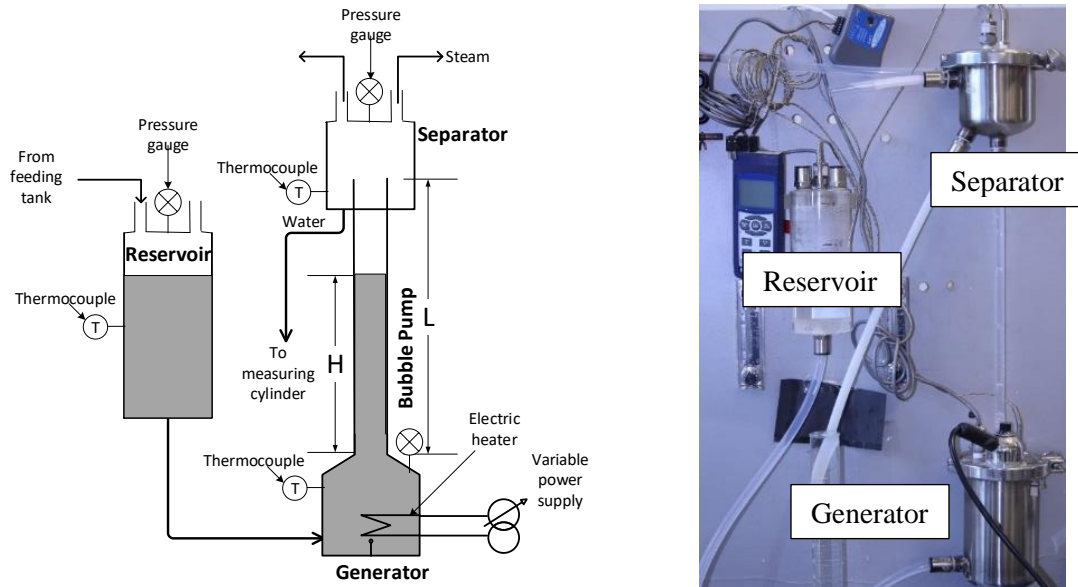


Figure 4.2: Bubble pump schematic and experimental set-up

4.3.1. Measuring Instruments

Temperatures and pressures were measured at three different places in the test set up: (i) at the inlet of the lift tube (generator), (ii) in the liquid-vapor separator, and (iii) in the

reservoir. Type J Grounded Pipe Plug Probe thermocouples were used to measure the temperatures. Temperatures were recorded in a 4 port “Reed SD-947” data logger with an accuracy of $(0.4\% + 1^{\circ}\text{C})$. Type 17-4 PH stainless steel NPT male connection pressure transducers were installed to monitor fluid pressures. The measuring range of the pressure transducer is 0-34 atm with an accuracy of ± 0.2 atm.

4.3.2. Experimental Procedure

Hot water (around 90°C) was fed into the reservoir to establish a certain submergence ratio. An electric heater controlled by a variable power-supply supplied a constant heat flow to the generator. Bubble formation was continuously monitored in the lift tube, and when slug flow was achieved, the system pressures were recorded in the data logger at three points. The two-phases (liquid and vapor) were pumped to the separator by the bubble pump, where the vapor escaped to the room. The liquid from the bottom of the separator was collected over a period of time (determined by stop watch) in a 250 mL graduated cylinder that was scaled in increments of 2 mL to determine the volumetric flow rate of the liquid. The temperature of the collected water was obtained and the mass flow rate was calculated based on the volume of the water and density at the collection water temperature.

The tube diameter and submergence ratio have a direct impact on the bubble pump performance. Clear FEP (fluorinated ethylene propylene) tubing with inner diameters of 10, 8, and 6 mm was used for the lift tube. The tube length was fixed at 0.47 m and the submergence ratio (H/L) was varied from 0.6 to 0.8. The flow behavior of water in the lift tube was observed during the experiment. With increasing heat input, the flow pattern changed from bubbly to slug to churn flow. At each heat input, the experiment was conducted until the temperature of the generator reached steady-state. A longer time was required to reach the steady state temperature at lower heat inputs.

4.4. Results and Discussions

The effects of tube diameter and submergence ratio on lifting liquid in a vertical tube were investigated with varying heat input.

4.4.1. *Effects of Submergence Ratio and Input Heat*

The influence of the submergence ratio and the generator heat input on the mass flow rate of the liquid is shown in Figure 4.3. As the water height of the reservoir was set to a higher level, the submergence ratio increased, which means the relative height for pumping water decreased, so the liquid mass flow rate increased. Figure 4.3 shows that for a tube diameter of 8 mm, the highest mass flow rate of water was achieved at the highest submergence ratio. It was observed and calculated that at low heat input, the mass flow rate of water was low at any submergence ratio. With increasing heat input, the liquid mass flow rate increased and after reaching a maxima, it decreased again. At low heat input, the bubbles were not sufficient to generate a train of gas slugs. These small bubbles did not occupy the full cross-section of the lift tube and the liquid slipped past the rising bubbles. When heat input increased, the gas slugs formed became taller and were large enough to move the water column upward. At higher submergence ratios, the shorter pumping distance decreased the frictional pressure drop and increased the liquid flow rate. From the experimental results, it was found that at 120 watts heat input the maximum mass flow rates were 33, 26 and 18 g/s at submergence ratios of 0.8, 0.7 and 0.6 respectively, which are 6.2%, 4.6% and 13.7% below the theoretical values. At low submergence ratios, the average deviation between the theoretical and experimental results was higher. This might be due to the higher heat loss along the tube in the experiment for lower submergence ratios where the gas slug collapses before reaching at the end of the lift tube. Nonetheless, all the theoretical results are within 14% of the experimental results.

4.4.2. *Effects of Tube Diameter and Input Heat*

Another important parameter effecting the pump performance is the diameter of the lifting tube. Figure 4.4 shows the influence of the tube diameter on the liquid mass flow rate of the bubble pump. With increased tube diameter, the friction factor decreased, which increased the liquid mass flow rate. The surface tension parameter was another factor increasing liquid mass flow rate with increasing tube diameter. According to Equation (5), when this parameter is about 0.2, there is no bubble moving in the liquid. When the tube diameter increased, the surface tension parameter decreased which caused the increased

velocity of the gas bubble in the liquid; and this resulted in the higher liquid flow rate in the pump. Although the liquid flow rate increased with increased tube diameter, the analysis revealed that for the same operating conditions, the maximum liquid flow rate would be achieved at tube diameter of 12 mm. The effect of the increased input heat in Figure 4.4 is same as Figure 4.3, where the increased flow rate went down slowly after reaching a maximum. The flow started almost at the same input heat for all diameter tubes. But for the 6 mm diameter tube, the flow rate was highest when the pumping started and went down with increasing heat input. The maximum liquid flow rate was achieved for a 10 mm diameter tube at 160 W, for 8 mm at 120 W and for 6 mm at 100 W. The theoretical results follow the same trend as the experimental ones for all diameter tubes. At a heat input of 160 W, the measured liquid mass flow rates were 50, 32 and 16 g/s for tube diameters of 10, 8 and 6 mm, respectively. The experimental results for these flows were 0.9%, 4% and 14.4% below theoretical, respectively.

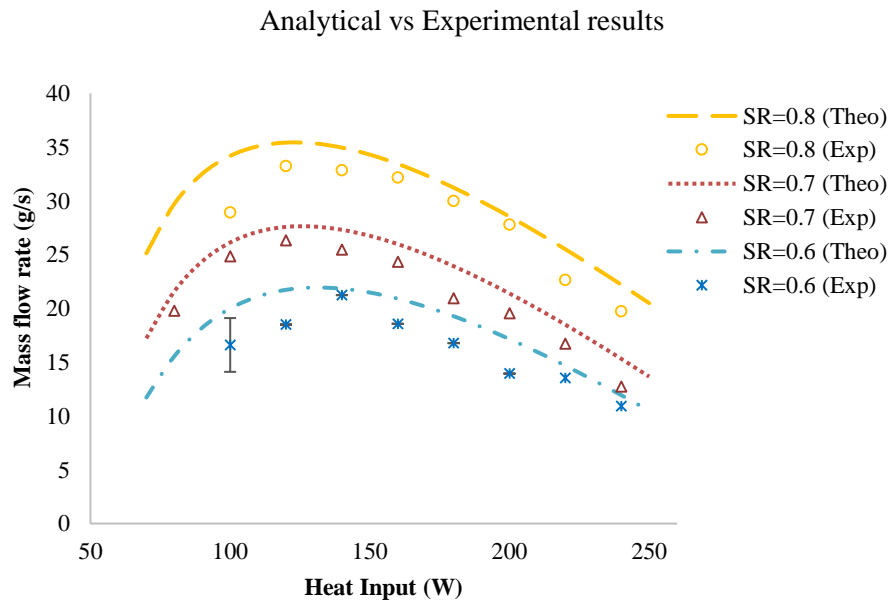


Figure 4.3: Bubble pump performance for different SR ratio at D=8 mm.

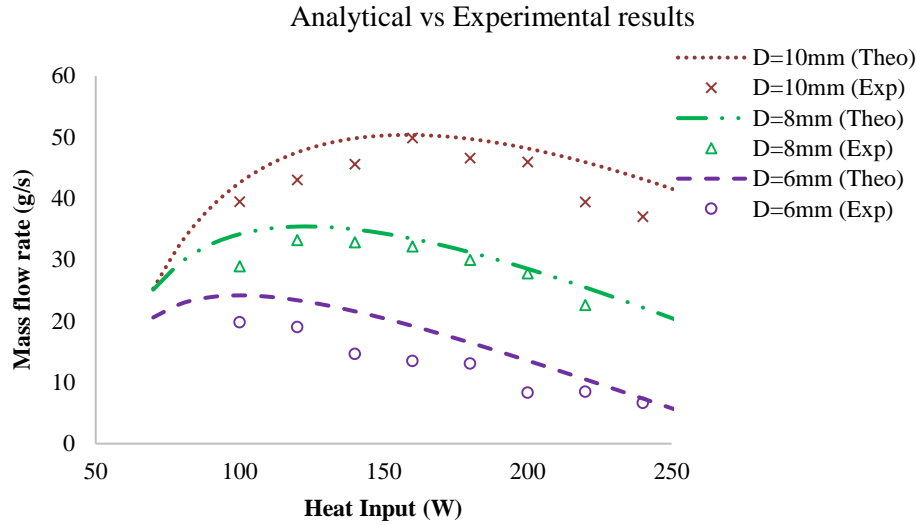


Figure 4.4: Bubble-pump performance for different diameter at submergence ratio, SR=0.8.

A uncertainty analysis was performed for this experiment using the Taylor Series method [Kassab et al., 2009]. Three trials of experiments were performed. The relative uncertainties for mass flow rate, temperature, pressure, time and input heat were calculated by combining random errors by using the standard deviation of experimental data and the bias (instrumentational error), and the values were obtained were 14%, 4%, 19%, 4% and 3%, respectively. This uncertainty is expressed by the error bar in Figure 4.3.

4.5 Conclusions

In this paper, an analytical model was developed to predict the bubble pump performance and was validated with experimental results. The bubble pump performance was measured with variable tube diameters (10, 8 and 6 mm), submergence ratios (0.8, 0.7 and 0.6) and input heat (80 to 250 W) using water as a working fluid at atmospheric conditions. The theoretical model and experimental results showed that the bubble pump liquid mass flow rate varies with all three studied parameters. It was observed that the maximum liquid flow rate of 50 g/s was achieved at a heat input of 160 W, submergence ratio of 0.8, and 10 mm of tube diameter. The analytical results at this condition agreed within 0.9%. The proposed model can be used to accurately predict the bubble pump output. These results may be extended to refrigerants and conditions used in VAR systems.

Acknowledgements

This work is made possible by the Natural Science and Engineering Research Council of Canada.

Nomenclature

| | | <i>Subscripts</i> | |
|------------------|---|-------------------|--------------------------|
| g | Acceleration due to gravity (m/s^2) | | |
| \bar{h} | Heat transfer coefficient (W/m^2-K) | <i>LT</i> | lift tube |
| h_{fg} | Enthalpy of vaporization (kJ/kg) | <i>TP</i> | two-phase |
| \dot{m} | Mass flow rate (kg/s) | <i>MIX</i> | liquid and vapor mixture |
| r_1 | Inner radius of the lift tube (m) | | |
| r_2 | Outer radius of the lift tube (m) | <i>g</i> | gas |
| R_{Total} | Overall heat transfer coefficient (W/m^2-K) | <i>l</i> | liquid |
| \dot{V} | Volumetric flow rate (m^3/s) | | |
| ε | Emissivity of the Lift Tube | | |
| ρ | Density of water (kg/m^3) | | |
| σ | Surface tension (N/m) | | |
| σ_{Boltz} | Sefan-Boltzman constant ($W/m^2- K^4$) | | |

REFERENCES

- Abu-Mulaweh H.I., Mueller D.W., Wegmann B., Speith K., Boehne B., Design of Bubble Pump Cooling System Demonstration Unit. International Journal of Thermal & Environmental Engineering, 2 (2011) 1-8.
- Aman J, Ting D. S-K., Henshaw P., Residential solar air conditioning: energy and exergy analyses of an ammonia-water absorption cooling system. Applied Thermal Engineering, 62 (2014) 424-432.
- Benhmidene A., Chaouachi B., Gabsi S., A Review of Bubble Pump Technologies. Journal of Applied Sciences, 10(16) (2010) 1806-1813.
- Benhmidene A., Chaouachi B., Gabsi S., Bourouis M., Modelling of heat flux received by a bubble pump of absorption-diffusion refrigeration cycle. Heat Mass Transfer, 47 (2011) 1341-1347.

- Bourseau P., Mora J.C., Bugare R., Coupling of an absorption-diffusion refrigeration machine and solar flat-plate collector. *International Journal of Refrigeration*, 9 (1987) 206–214.
- Chan K.W., McCulloch M., Analysis and modelling of water based bubble pump at atmospheric pressure. *International Journal of Refrigeration*, 36 (2013)1521-1528.
- Clark N.N., Dabolt, R.J., A General Design Equation for Air Lift Pumps Operating in Slug Flow. *AIChE Journal*, 32 (1986) 56-64.
- Delano A., Design Analysis of the Einstein Refrigeration Cycle. Ph.D. Thesis, Georgia Institute of Technology, 1998.
- EES (*Engineering Equation Solver*), 2015, F-Chart software, Academic Commercial V9. 941(1992-2015), www.fchart.com
- Herold K.E., Radermacher R., Klein S.A., Absorption Chillers and Heat Pumps.1996. CRC Press, Boca Raton, FL.
- Jakob U., Eicker U., Schneider D., Taki A.H., Cook M.J., 2008. Simulation and experimental investigation into diffusion absorption cooling machines for air conditioning applications. *Applied Thermal Engineering*, 28 (2008) 1138-1150.
- Kassab S.Z., Kandil H.A., Warda H.A., Ahmed W.H., Air-lift pumps characteristics under two-phase flow conditions, *International Journal of Heat and Fluid Flow*, 30 (2009) 88-98.
- Katasuhara T., Kazama T., Heat Transfer in Two-Phase Flow of Mixtures of Air and Water. 2nd Report - Vertical Channel, *Transactions of JSME*, 24 (1958) 552-558.
- Mayor T.S., Pinto A.M.F.R., Campos J.B.L.M., Vertical slug flow in laminar regime in the liquid and turbulent regime in the bubble wake---Comparison with fully turbulent and fully laminar regimes. *Chemical Engineering Science*, 63 (2008) 3614 – 3631.
- Nicklin D.J., The Air-Lift Pump: Theory and Optimization. *Transactions of the Institution of Chemical Engineers*, 41 (1963) 29-39.
- Pfaff M., Saravanan R., Maiya M.P., Srinivasa M., 1998. Studies on bubble pump for a water–lithium bromide vapor absorption refrigeration. *International Journal of Refrigeration*, 21 (1998) 452–462.
- Reinemann D.J., A Theoretical and Experimental study of Airlift Pumping and Aeration with Reference to Aquacultural Applications. PhD Thesis. Cornell University, 1987.

- Stenning A., Martin C., 1968. An analytical and experimental study of air-lift pump performance. ASME Journal of Engineering for Power, (1968) 106-110.
- Sujumnong M., Heat transfer, pressure drop and void fraction in two phase, two component flow in a vertical tube. PhD thesis. Department of Mechanical and Industrial Engineering, University of Manitoba, Winnipeg, Manitoba, Canada, 1997.
- Walt S. van der, The design and optimization of a bubble pump for an aqua-ammonia diffusion absorption heat pump. MSc Thesis. North-West University, University in Potchefstroom, South Africa, 2012.
- White S.J., Bubble Pump Design and Performance. MSc Thesis. Georgia Institute of Technology, Atlanta, USA. Mechanical Engineering, 2001.
- Zohar A., Jelinek M., Levy A., Borde I., The influence of the generator and bubble pump configuration on the performance of diffusion absorption refrigeration (DAR) system. International Journal of Refrigeration, (2008) 962-969.

CHAPTER 5

PERFORMANCE CHARACTERIZATION OF A BUBBLE PUMP FOR VAPOR ABSORPTION REFRIGERATION SYSTEMS

This work was published as “Aman, J., Henshaw, P. Ting, D. S-K., Performance characterization of a bubble pump for vapor absorption refrigeration systems, International Journal of Refrigeration”, <https://doi.org/10.1016/j.ijrefrig.2017.09.011>.

5.1. Introduction

Recently, vapor absorption refrigeration systems (VARs) have acquired significant interest for air-conditioning applications as they use environmental friendly refrigerants and can be driven by waste heat or solar thermal energy [Herold *et al.*, 1996]. LiBr-H₂O and NH₃-H₂O are the most common refrigerant-absorbent working pairs for this VARs. The LiBr-H₂O absorption system has a higher efficiency, but due to its crystallization and corrosion problems, NH₃-H₂O is preferable for small scale commercial or residential applications [Adewusi and Zubair, 2004, Aman *et al.*, 2014]. The main components of the VARs are the generator, condenser, absorber, solution heat exchanger and evaporator as shown in Figure 5.1. In this refrigeration system, the cycle works in dual pressure. An electrical pump is used to convey the solution from the absorber to the generator and to create a pressure difference between the condenser and the evaporator which produces the saturation temperature difference of refrigerant between these two components. This electrical pump is exposed to the high temperature corrosive solution and is the only component that consumes electrical energy in this system. To eliminate the electrical pump and make the VARs completely independent of electricity, a heat driven bubble pump generator can be used to circulate the solution to the system and generate the necessary refrigerant for the required cooling effect. In this application, the VARs will operate as a single pressure refrigeration cycle. For small scale applications like residential air-conditioning, this system will be more reliable and independent of the availability of electricity. For larger scale applications of bubble pump operated VARs, multiple parallel pumps may be explored [Saravanan and Maiya, 2003].

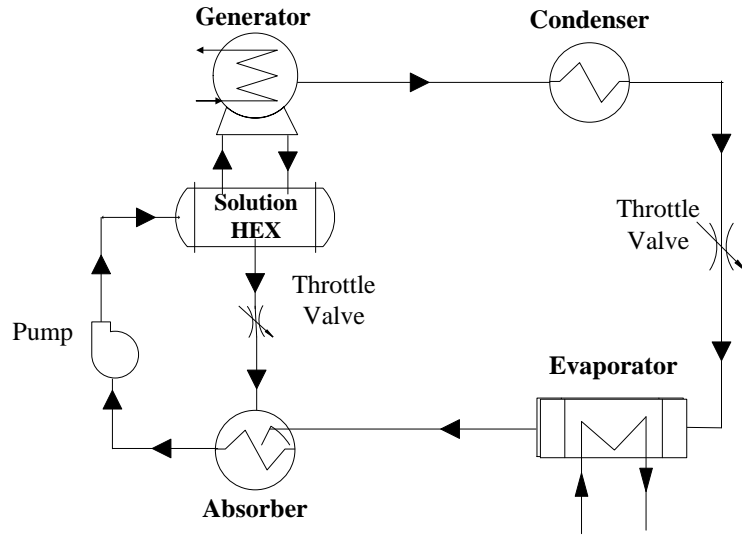


Figure 5.1: Vapor Absorption Refrigeration System

A bubble pump is a thermally driven pump, containing a vertical lift tube connecting with the generator and the separator as shown in Figure 5.2. The heat is supplied to the generator and vapors are formed in the liquid. The vapor bubble is created by the evaporation, increases the buoyancy of the liquid and causes the liquid to ascend through the lift tube under two phase flow conditions.

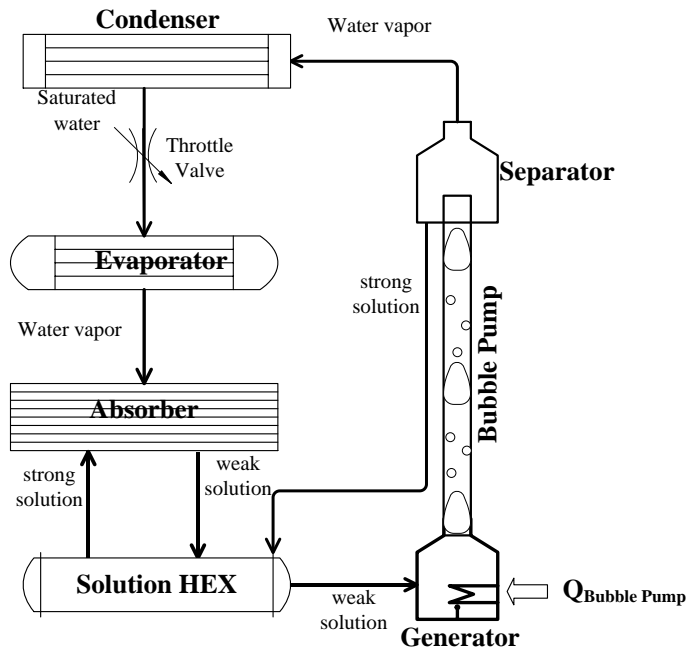


Figure 5.2: Bubble Pump in Vapor Absorption Refrigeration System

With the same principal as a bubble pump, air-lift pumps have been used in the marine and oil industries since the beginning of the twentieth century [Kassab *et al.*, 2009]. The air-lift pump is a device, partially submerged into a liquid, to lift the liquid or solid-liquid mixture through a vertical pipe from a lower to a higher level. In an air-lift pump, compressed air is introduced at the lower end of the pipe. Each air bubble pushes the liquid ahead of it as it discharges from the pipe. The basic difference between an air lift and a bubble pump is the phase change which is associated with the latter. When a bubble pump is used in VARS, the refrigeration cycle is almost a single pressure system as there is a very small pressure difference between the condenser and the evaporator, due to the flow friction and gravity. As an example, in conventional ammonia-water refrigeration system, the pressure difference between the condenser and the evaporator is about 700 kPa, compared to 25 kPa for the bubble-pump-driven cycle. Bubble pumps have been used in VARS for an ammonia-water working fluid since 1928 [White, 2001] by using the Platen and Munters [1928] cycle, known as the diffusion absorption refrigeration (DAR) cycle or by using the Einstein Cycle [1928]. Both systems work on a triple fluid refrigeration cycle where ammonia is the refrigerant, water is the absorbent. Helium or hydrogen is used as an inert gas in the evaporator for the DAR cycle, whereas butane is used as a third working fluid in the evaporator for the Einstein cycle to reduce the partial pressure of the refrigerant for the necessary cooling effect. In the commercial market, a small-scale DAR refrigerator with up to 100W cooling capacity is available and is driven by direct fire heat or an electrical heater [Starace and Pascalis, 2012]. Due to their small size, the efficiency of these cooling systems is very low: in commercially available DAR systems, the coefficient of performance (COP) is 0.2 to 0.3 at cooling capacities of 16 to 60 W and generator temperatures from 160 to 230°C [Starace and Pascalis, 2012, Jacob *et al.*, 2008, Bourseau *et al.*, 1987]. Many extensive studies have been performed to improve the cycle efficiency of DAR systems by using different working fluids [Zohar *et al.*, 2009, Ben Ezzine *et al.*, 2010, Wang *et al.* 2011, Kumar & Das, 2015] or designing different bubble pump configurations [Zohar *et al.*, 2008, Benhmidene *et al.*, 2010, 2011]. The commercial application of the Einstein cycle is very rare. The analysis of recent studies shows that the coefficient of performance of the Einstein cycle is not greater than 0.2 [Chan and McCulloch, 2016]. As ammonia produces high vapor pressure, using a third fluid in the

system can reduce the partial pressure of this refrigerant. In LiBr-H₂O absorption refrigeration systems, water is the refrigerant and lithium-bromide is the absorbent. As water has a low vapor pressure, using a bubble pump in this refrigeration system is not the same as a triple fluid system. This water-based refrigeration system works at vacuum pressure and the pressure difference between the condenser and the evaporator is low enough for the utilization of a bubble pump [Saravanan and Maiya 2003]. But the studies of bubble pump for LiBr-H₂O absorption refrigeration systems are very limited.

In order to use the bubble pump in VAR systems and determine the height of the system, the selection of the working fluid for this refrigeration cycle is crucial [Pfaff *et al.*, 1998]. Specifically, in a bubble pump operated single pressure absorption refrigeration system, the cycle performance totally depends on the refrigerant-absorbent solution properties and the bubble pump parameters. The thermodynamic properties of a solution include viscosity, heat capacity, surface tension, thermal conductivity of single- and two-phase fluids, and the bubble pump parameters include the diameter of the tube, the height of the tube, surface roughness and gas-liquid two-phase flow patterns. When the working fluid is being used to generate the refrigerant, or pump the liquid in a bubble pump operated VARS, each thermodynamic property strongly influences this mechanism. In addition, the geometrical parameters of the bubble pump itself and the flow patterns also influence the bubble pump performance as well as the refrigeration cycle performance. To generalize these variables, it is essential to perform a dimensional analysis that will yield a group of dimensionless numbers describing the influence of important thermodynamic properties and geometric parameters of a bubble pump on the system performance. Dimensional analysis is a powerful and useful technique for representing the multivariable relationships among physical variables and for performing dimensional modeling [Szirtes, 1997, Barenblatt 1996].

The analysis of bubble-pump-operated VAR systems was performed since the 1920s [Platen and Munters, 1928]. Different works have evaluated the performance of a bubble pump based on their parametric studies, but the analytical model of the bubble pump itself were very limited. A solar driven bubble pump has been simulated and tested under different operating conditions [Bourseau *et al.*, 1987]. An analytical model of the bubble pump was developed based on an air lift pump fit into the Einstein refrigeration cycle

[Delano, 1998]. This model, based on the mass and momentum conservation equations, was used to evaluate the performance of the bubble pump with varying parameters. Another design model of a bubble pump and experimental studies was performed in 1998 for a lithium bromide–water vapor absorption cycle [Pfaff *et al.*, 1998]. In this study, a mathematical model was developed based on the manometer principle, focusing on the time required to generate the vapor bubble from the subcooled liquid for one complete cycle. A different configuration of bubble pump has been studied for a diffusion absorption refrigeration system in 2008 [Zohar *et al.*, 2008]. In this numerical analysis, the impact of the bubble pump configuration on the DAR performance was explored. All of these analytical models started with Stenning and Martin’s method which modeled the conventional air-lift pump using continuity and momentum equations, considering fundamental principal of two-phase flow [Stenning and Martin, 1968]. In their analysis, they found that this assumption was a good match for air-lift pump performance analysis. They used a coefficient to determine the two-phase flow friction factor and the gas void fraction. Although a few analytical models have been developed to analyze the bubble pump performance, designing an efficient pump still remains a challenge.

In this paper, a dimensional analysis was performed to represent the performance characteristics of a bubble pump, considering the thermophysical properties of the solution and the geometric parameters of the bubble pump. A mathematical model has been developed using these non-dimensional parameters to determine the bubble pump performance, which can be used in bubble-pump-driven absorption refrigeration systems. The non-dimensional parameters should be valid for all fluids and geometries. As water is a better refrigerant for VARS, especially for air-conditioning applications and considering the limitations of LiBr-H₂O, pure water and LiCl-H₂O have been chosen as the working fluids. In this work, the experimentation was performed by using these two fluids to validate the suggested model for the bubble pump performance evaluation. This paper is a first-time effort to generate and predict bubble pump characteristics and performance using non-dimensional parameters.

5.2. Analytical models

Two-phase flow analysis is used to determine the performance of a bubble pump in this study. The bubble pump is responsible to pump the liquid and generate the required vapor flow for the vapor absorption refrigeration system. Heat is required to generate the bubble which is the key factor to create liquid flow in the bubble pump. The bubble generation depends on the vapor flow rate. The vapor generation and flow rate also depend on the system pressure, which can be set based on the vapor pressure of the liquid and the enthalpy of vaporization, which can be determined from fluid properties. The two-phase flow of liquid and vapor depends on the velocity of the vapor bubble rising in the liquid. The bubble rises as a result of its buoyancy and the inertia of the liquid. The flow rate of liquid in a bubble pump depends on the tube diameter, height of the liquid in the tube, vapor generation, and physical properties of the vapor and liquid such as viscosity, surface tension, and density.

Considering the influence of the physical properties of the bubble pump and the thermophysical properties of the fluid, the bubble pump efficiency can be expressed as

$$\eta_{BP} = f(\dot{Q}, h_{fg}, P, \dot{V}_g, \dot{V}_l, \mu, \sigma, H, \rho, g, D) \quad (1)$$

where, the bubble pump efficiency is the dependent variable and is a function of all independent variables which are shown in Table 5.1.

Table 5.1: Variables used in the bubble pump performance analysis and their dimensions

| Variable | Dimension |
|--|----------------------------------|
| Heat input, \dot{Q} | Watt (W) |
| Enthalpy of vaporization, h_{fg} | kJ kg^{-1} |
| System pressure, P | $\text{Pa (N m}^{-2}\text{)}$ |
| Volume flow rate of vapor, \dot{V}_g | $\text{m}^3 \text{s}^{-1}$ |
| Volume flow rate of liquid, \dot{V}_l | $\text{m}^3 \text{s}^{-1}$ |
| Viscosity, μ | $\text{kg m}^{-1} \text{s}^{-1}$ |
| Surface tension, σ | N m^{-1} |
| Height of the liquid in the lift tube, H | m |
| Density, ρ | kg m^{-3} |
| Gravity, g | m s^{-2} |
| Tube diameter, D | m |

Considering these relevant variables, a dimensional matrix (Table 5.2) was produced. The dimension column and the variable row generate the boundaries for the dimensional matrix. By applying the procedure for the dimensional analysis from Szirtes [1997], a dimensional set of four matrices can be formed as shown in Table 5.3 which consist of A, B, C and D matrices. In this analysis, the number of dimensions is three, so three variables must be used to form the A matrix and, in this case, ρ , g and D were chosen as repeating parameters. It was assumed that ρ , g and D are the most important variables that affect the fluid flow considering the fluid properties and the bubble pump geometry. The variables in the A matrix were chosen in such a way that the determinant of this matrix is not zero, which means the contained variables cannot make a dimensionless number by themselves. In developing the non-dimensional parameters, an analysis was performed using H instead of D as a repeating parameter such that the non-dimensional pressure parameter was the hydrostatic pressure ($P/\rho gh$) as opposed to the non-dimensional pressure (P'). Using the non-dimensional hydrostatic pressure, there was no variation of the efficiency with a change in the heat input parameter and all efficiency curves were very similar for all non-dimensional hydrostatic pressures. So, there was little effect on efficiency for using different liquids. Furthermore, using H , the other non-dimensional numbers do not represent the classical non-dimensional numbers for two phase-flow (Eotvos number, Galileo number, etc.). The classical non-dimensional numbers of two phase flow in a vertical tube are mostly related to the tube diameter. When the bubble forms in a bubble pump lift tube, the shape of the bubbles, the surface tension effects and the fluid flow depend on the fluid properties and the bubble pump geometry, especially the tube diameter. The flow patterns also vary by the tube diameter. The non-dimensional numbers in which ρ , g and D were assumed as repeated parameters also have physical meaning for explaining the two-phase flow in a vertical tube. By producing the matrix with these variables, the calculated determinant is 2, which is not zero. The B matrix was formed from the remaining variables of the dimensional matrix in Table 5.2.

Table 5.2: Dimensional matrix with all independent variables for bubble pump performance

| Variable Dimension | \dot{Q} | h_{fg} | P | \dot{V}_g | \dot{V}_l | σ | μ | H | ρ_l | g | D |
|-----------------------|-----------|----------|-----|-------------|-------------|----------|-------|-----|----------|-----|-----|
| kg | 1 | 0 | 1 | 0 | 0 | 1 | 1 | 0 | 1 | 0 | 0 |
| m | 2 | 2 | -1 | 3 | 3 | 0 | -1 | 1 | -3 | 1 | 1 |
| s | -3 | -2 | -2 | -1 | -1 | -2 | -1 | 0 | 0 | -2 | 0 |

Table 5.3: Dimensional set for possible dimensional variables for bubble pump performance

| | | \dot{Q} | h_{fg} | P | \dot{V}_g | \dot{V}_l | σ | μ | H | ρ_l | g | D |
|-----------------|---------|-----------|----------|-----|-------------|-------------|----------|-------|-----|----------|------|------|
| B matrix | kg | 1 | 0 | 1 | 0 | 0 | 1 | 1 | 0 | 1 | 0 | 0 |
| | m | 2 | 2 | -1 | 3 | 3 | 0 | -1 | 1 | -3 | 1 | 1 |
| | s | -3 | -2 | -2 | -1 | -1 | -2 | -1 | 0 | 0 | -2 | 0 |
| D matrix | π_1 | 1 | 0 | 0 | 0 | 0 | 0 | 0 | 0 | -1 | -1.5 | -3.5 |
| | π_2 | 0 | 1 | 0 | 0 | 0 | 0 | 0 | 0 | 0 | -1 | -1 |
| | π_3 | 0 | 0 | 1 | 0 | 0 | 0 | 0 | 0 | -1 | -1 | -1 |
| | π_4 | 0 | 0 | 0 | 1 | 0 | 0 | 0 | 0 | 0 | -0.5 | -2.5 |
| | π_5 | 0 | 0 | 0 | 0 | 1 | 0 | 0 | 0 | 0 | -0.5 | -2.5 |
| | π_6 | 0 | 0 | 0 | 0 | 0 | 1 | 0 | 0 | -1 | -1 | -2 |
| | π_7 | 0 | 0 | 0 | 0 | 0 | 0 | 1 | 0 | -1 | -0.5 | -1.5 |
| | π_8 | 0 | 0 | 0 | 0 | 0 | 0 | 0 | 1 | 0 | 0 | -1 |

The C matrix is the transpose product of A^{-1} (inverse of A matrix) and B ($C = -[A^{-1} * B]^T$). D is the identity matrix. From the above matrices, it can be seen that there are eleven variables and three dimensions. Buckingham's Theorem states that the number of independent dimensional variables is the difference between the number of variables and the number of dimensions. Following this theorem, eight dimensionless groups can represent the parameters of the bubble pump. The dimensionless numbers that have been formed by this analysis and their physical interpretations are shown in Table 5.4.

Table 5.4: Dimensionless numbers and their physical interpretations

| Non-dimensional variable | Dimensionless number | Physical interpretation (ratio of forces) |
|---|--|---|
| $\pi_1 = \frac{\dot{Q}}{\rho_l g D^3 \sqrt{gD}}$ | | Heat required to generate the bubble: thermal force/gravitational force |
| $\pi_2 = \frac{h_{fg}}{gD}$ | | Internal Energy/buoyancy force |
| $\pi_3 = \frac{P}{\rho_l g D} = P'$ | $P' = \text{Nondimensional Pressure}$ | System pressure/buoyancy force |
| $\pi_4 = \frac{\dot{V}_g}{D^2 \sqrt{gD}} = Fr_g$ | $Fr_g = \text{Froude Number of gas}$ | Inertia force of the vapor/gravitational force. |
| $\pi_5 = \frac{\dot{V}_l}{D^2 \sqrt{gD}} = Fr_l$ | $Fr_l = \text{Froude Number of liquid}$ | Inertia force of the liquid/gravitational force. |
| $\pi_6 = \frac{\rho_l g D^2}{\sigma} = Eo$ | $Eo = \text{Eotvos Number}$ | Buoyancy (gravitational) force /surface tension force |
| $\pi_7 = \frac{\rho_l^2 g D^3}{\mu^2} = Ga$ | $Ga = \text{Galileo Number}$ | Gravitational force/viscous force |
| $\pi_8 = \frac{H}{D}$ | Aspect ratio | |
| $Mo = \frac{Eo^3}{Ga^4} = \frac{g\mu^4}{\rho_l \sigma^3}$ | $Mo = \text{Morton Number}$ | Viscous force/surface tension force |
| $Q' = \frac{\pi_1}{\pi_2}$ $= \frac{\dot{Q}}{h_{fg} \rho_l D^2 \sqrt{gD}}$ | $Q' = \text{Nondimensional Heat Input}$ | Thermal force/buoyancy force |
| $h'_{fg} = \frac{\pi_2}{\pi_8} = \frac{h_{fg}}{gH}$ | $h'_{fg} = \text{Nondimensional Energy}$ | Internal Energy/buoyancy force |

So, the efficiency of a bubble pump, Equation (1), can be written as a function of six dimensionless numbers as follows:

$$\eta_{BP} = f(Q', h'_{fg}, P', Fr_g, Fr_l, Mo) \quad (2)$$

The mass flow rate of pumped liquid strongly depends on the bubble pump parameters, heat input to the bubble pump generator and the properties of the pumped fluid. Three different flow regimes are observed when a bubble pump is being used for vapor absorption refrigeration systems. The characteristic feature and structure of these flow regimes are highly related to the gas-liquid two phase flow patterns existing in the upright flow in a vertical tube [Tudose, 1997]. At a certain heat input, when the temperature of the fluid exceeds the saturation temperature of the fluid, small vapor bubbles are generated. This is referred as a bubbly flow regime. In this regime, the gas phase is homogeneously distributed in the liquid phase as small, discrete bubbles [Taitel *et al.*, 1980]. With an increased heat supply, the vapor bubble generation increases, which leads to the coalescence of the small bubbles, forming bullet shaped bubbles. This is known as a vapor slug or Taylor bubble [Reinemann, 1987]. The shape of this bubble occupies most of the cross-sectional area of the inside of the tube and the Taylor bubble will rise upward due to buoyancy of the liquid. A small thin liquid film will be generated along the side of this bubble. A liquid slug with some small bubbles is entrained between two consecutive Taylor bubbles. At steady state, a series of Taylor bubbles is observed which pushes the liquid slugs upward in the vertical tube. This termed as a slug flow regime. The wake developed at the rear of each Taylor bubble and in a series of bubbles turns into a turbulent wake [Mayor *et al.*, 2008]. A further increase of heat supply will increase the vapor flow rate, causing the vapor bubbles to become irregular and narrower in shape. As a result, the liquid slugs are not continuous and create a disorderly flow regime. This is known as a churn flow regime and the liquid flow becomes oscillatory in the vertical tube. Experimental studies showed that the bubble pump is most efficient while moving liquid in the slug flow regime [Delano, 1998; White, 2001; Benhmidene *et al.* 2011; Walt, 2012].

To determine the bubble pump performance, an analytical model has been developed in which bubble pump parameters are defined as non-dimensional numbers and the characteristics of a bubble pump are described with these numbers. Figure 5.3 shows the schematic diagram of a bubble pump.

The following equations have been established to determine the flow rate of pumping liquid by the bubble pump. The flow rate of the liquid and the vapor depends on the heat supply to the bubble pump generator. The volume flow rate of vapor can be determined by

$$\dot{Q} = \dot{V}_g \rho_g (h_g - h_{sol}) = \dot{V}_g \rho_g h_{fg} \quad (3)$$

where, \dot{Q} (W) is the heat input for the generating vapor, \dot{V}_g is the volume flow rate of the vapor (m^3/s), h_g is the enthalpy of the gas/vapor (kJ/kg), h_{sol} is the enthalpy of the solution (kJ/kg), h_{fg} is the enthalpy of vaporization of the fluid (kJ/kg). These parameters can be expressed as dimensionless numbers: non-dimensional heat input (Q'), Froude numbers of gas (Fr_g) and liquid (Fr_l), and non-dimensional energy (h'_{fg}), which have been found by dimensional analysis as summarized in Table 5.4.

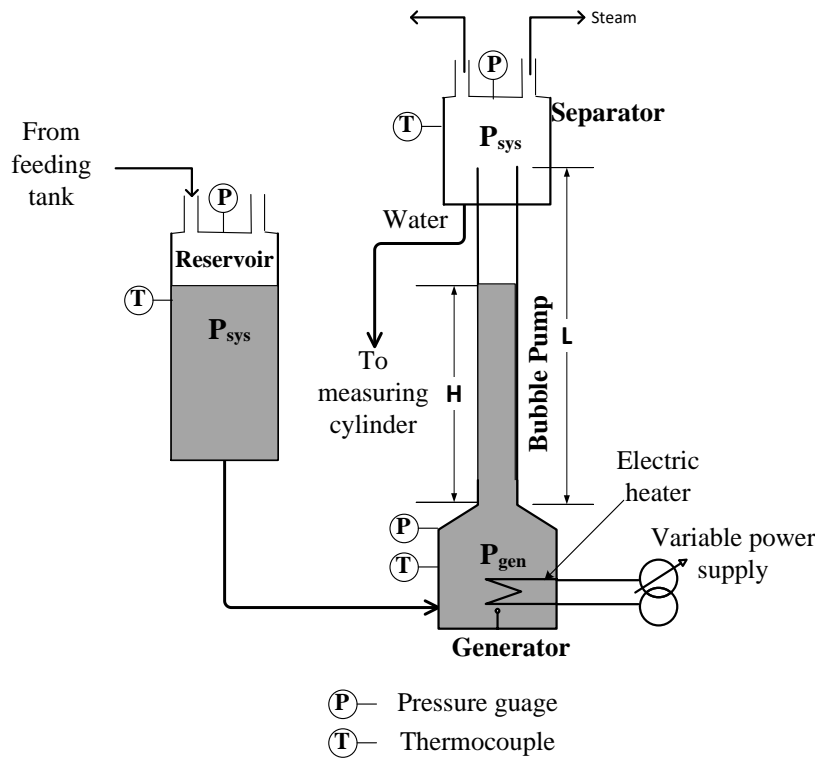


Figure 5.3: Bubble Pump Apparatus used.

The liquid flow rate depends on the vapor flow rate, which in turn depends on the heat supplied to the generator. After generating the Taylor bubble in the liquid slug, it rises upward with a certain velocity. In an air-lift pump, many researchers have determined the actual velocity of the Taylor bubble relative to a moving liquid slug as [Reinemann *et al.*, 1990; Reinemann, 1987; Nicklin, 1962]

$$v_g = C_0 v_m + v_b, \quad v_m = \frac{\dot{V}_l + \dot{V}_g}{A} \quad (5)$$

Nicklin (1963) described that the velocity of the Taylor bubble as a linear function of the average gas velocity in the lift tube.

$$v_g = \frac{\dot{V}_g}{\alpha_d A} \quad (6)$$

where, v_g is the actual velocity of the rising gas bubble (m/s), C_0 is the velocity profile coefficient of gas-liquid mixture (ranging from 1.2 for fully developed turbulent flow to 2 for laminar flow; Nicklin, 1963), v_b is the velocity of a Taylor bubble in stagnant liquid (m/s), v_m is the mean velocity of the liquid slug (m/s), \dot{V}_l is the volumetric flow rate of liquid (m³/s), \dot{V}_g is the volumetric flow rate of gas (m³/s), A is the cross sectional area of the lift tube (m²), and α_d is the gas void fraction.

Different analyses have shown that turbulent flow is achieved in an air-lift pump when the Reynolds number (as defined by Reinemann, 1987) of the liquid slug of an air/water system is higher than 8000 and this can only be achieved for air/water system when the tube diameter is greater than 20 mm [Nicklin *et al.*, 1963; Reinemann, 1987; Kassab *et al.*, 2009]. In an air/water system, Reinemann [1987] experimentally found a turbulence velocity profile of the liquid slug at Reynolds numbers as low as 800 and he argued that the erratic behavior of the small bubbles in the liquid slug confirmed his results. In an air/water system, the size and the frequency of the bubble depend on the air flow rate and the pressure of the air entering the tube. The size of the bubble is constant along the length of the tube of an air/water system. In contrast, in a bubble pump system, the formation of a vapor slug in the liquid depends on the heat input, the system pressure, and the flow is treated as a homogenous two-phase flow system. However, the heat loss through the vertical lift tube makes the bubble pump different than an air-lift pump. Due to heat losses, the Taylor bubble may become smaller in size and may collapse before reaching at the top of the vertical tube.

The gas void fraction is one of the important parameters in two-phase flow to determine the flow regime as well as the two-phase pressure drop and heat transfer (Walt, 2012) and defined as:

$$\alpha_d = \text{gas void fraction} = \frac{\text{volume of the gas(vapor) in the liquid}}{\text{total volume of the liquid gas mixture}}$$

The velocity of the gas(vapor) bubble can be expressed by a dimensionless number (Froude number) as [Reinemann, 1987]:

$$v'_b = \frac{v_b}{(gD)^{1/2}} \quad (7)$$

where v'_b is the non-dimensional vapor (Taylor) bubble velocity in the liquid, D = inner diameter of the lift tube.

Furthermore, Taylor vapor bubble generation and its velocity in the liquid depends on the liquid properties. The velocity of the Taylor bubble is the effect of the resultant forces acting on it which are its buoyancy force as well as the liquid inertia, gravitational, surface tension and viscosity forces. As a result, the Taylor bubble velocity can also be stated in terms of Morton, Eotvos and Reynolds numbers as [Brennen, 2005]

$$v'_b = \left[\frac{MoRe^4}{Eo^3} \right]^{1/4} \quad (8)$$

where, Re is the Reynolds number based on the mean velocity [Reinemann, 1987], modified by using the two-phase liquid and vapor mixture [Katasuhara & Kazama, 1958]

$$Re = \frac{\rho_{MIX} v_m D}{\mu_{MIX}} \quad (9)$$

where, $\mu_{MIX} = x\mu_g + (1 - x)\mu_l$, x is the quality. (10)

White and Beardmore [1962] experimentally found that the viscosity does not affect the Taylor bubble velocity when the Morton number is below 10^{-8} . When $Ga > 10^{10}$, viscous effects are not important [Nickens & Yannitell, 1987]. In this condition, Nickens & Yannitell correlate the gas bubble velocity in stagnant liquid with the Eotvos number as

$$v'_b = 0.352 \left(1 - \frac{3.18}{Eo} - \frac{14.77}{Eo^2} \right) \quad (11)$$

The Eotvos number determines the deformation of the vapor bubble based on its gravitational and surface tension forces. With increasing Eo , the gravitational force dominates over the surface tension force. When the Eotvos number is less than one ($Eo < 1$), the bubble cannot rise as the surface tension force is the dominant force, but when it is much greater than one ($Eo \gg 1$), the flow is weakly dependent on surface tension forces [Montoya *et al.*, 2016]. The Eotvos number increases as the tube diameter increases.

Combining Equations (4) to (9), the gas void fraction can be represented by dimensionless numbers as

$$\alpha_d = \frac{Fr_g}{C_o(Fr_l + Fr_g) + v'_b} \quad (12)$$

An important parameter to consider in bubble pump analysis is the pressure drop along the lift tube of the bubble pump. In an air-lift pump, the lift tube is considered as an adiabatic vertical tube where the pump works at atmospheric pressure while the compressed air is injected from external sources [White, 2001]. It is assumed that the liquid flow rate into the tube is the same as the liquid flow rate out of the tube [Shelton and White-Stewart, 2002]. Different correlations have been developed based on these assumptions in air-lift pump analytical model. But in bubble pump operation, the vapor flow depends on the heat input in the generator, enthalpy of vaporization and the system pressure. Also, the velocity of the vapor bubble in the liquid of the lift tube is associated with the temperature of the bubble and the surrounding as heat loss occurs through the tube wall. As a result, the flow rate of the liquid out of the lift tube is not the same as the flow rate into the tube. Hence, the terminal mean velocity of liquid and vapor mixture is considered in this analysis.

The total pressure drop along the lift tube is the summation of the static pressure loss due to the weight of the liquid and gas mixture and the friction pressure loss due to the mixture moving along the tube. If the reservoir is at the height of H which determines the liquid head into the lift tube, the system pressure is P_{sys} , and the generator pressure is P_{gen} in Figure 5.3, then the total pressure drop is

$$P_{gen} - P_{sys} = \rho_{MIX}gH = \rho_{MIX}gL + f \frac{L}{2D} \rho_{MIX}v_m^2 \quad (13)$$

where, ρ_{MIX} is the density of liquid and vapor mixture and is defined as

$$\rho_{MIX} = \alpha_d \rho_g + (1 - \alpha_d)\rho_l \quad (14)$$

f is the friction factor and can be assumed to be [Giles, 1962],

$$f = \frac{0.316}{Re^{0.25}} \quad (15)$$

It is assumed that the weight of the vapor is negligible compared to the liquid weight. Rearranging Equations (4) to (12), it yields

$$\frac{H}{L} = (1 - \alpha_d) \left(1 + \frac{f}{2} (Fr_l + Fr_g)^2 \right) \quad (16)$$

Thus, the volumetric flow rate can be calculated by using Equation (3) which gives the gas Froude number for a given set of fluid properties, heat input and geometry of the bubble pump. Then the liquid Froude number as well as the liquid flow rate by the pump can be determined by an iterative calculation by using Equations (3) to (16).

Efficiency is normally defined as the useful output per input energy. Nicklin [1963] defined the efficiency of the air-lift pump as the net work done in lifting the liquid divided by the isothermal expansion of the air. But in a bubble pump, the input parameter is “heat input”. Hence, the efficiency of a bubble pump can be defined as the ratio of net work done in lifting the liquid to the heat input.

$$\eta_{BP} = \frac{\text{Net work done in lifting liquid}}{\text{Input heat}} = \frac{\dot{V}_l \rho g (L - H)}{\dot{Q}_{BP}} \quad (17)$$

Neglecting the friction in the bubble pump analysis, the bubble pump efficiency can be expressed in a non-dimensional form by using Equations (7), (12), (16) & (17) and Table 5.3 as

$$\eta_{BP} = \frac{1}{Q'} \times \frac{1}{h'_{fg}} \left[\frac{Fr_l Fr_g}{C_o (Fr_l + Fr_g) + v'_b - Fr_g} \right] \quad (18)$$

Bubble pump efficiency can be determined by Equation (18) for any non-dimensional pressure (P') value. The equation shows that the efficiency will decrease with increasing non-dimensional heat input (Q') at a fixed geometry of a bubble pump. However, increasing the tube diameter (within a certain range, determined by Equation (19)) will decrease Q' and will increase the surface tension effect (EO number), which in turn will decrease the non-dimensional bubble velocity (v'_b). As a result, the bubble pump efficiency will increase. The efficiency will also be affected by the fluid properties as the energy (enthalpy) varies by the fluid and pressure values. An experiment has been performed considering two working fluids to determine the relative effect of these parameters on bubble pump performance.

For the operation of the bubble pump, a stable Taylor bubble diameter in a two-phase flow will be the maximum diameter of the lift tube. The formation of the Taylor bubble is due to the interaction of the bubbles and the surrounding fluid, which depends on the fluid properties, flow conditions as well as the geometry of the flow channel [Montoya et al., 2016]. For many years, the reason for the coalescence of Taylor bubbles and their effects on the energy, mass and momentum transport processes in two-phase gas-liquid flow have been studied. Different researchers have found that when the Taylor bubbles coalesce, the bubble diameter is equal to the tube diameter and the maximum limit of this bubble size is determined based on the Kelvin-Helmholtz and Rayleigh-Taylor instabilities [Issii and Zuber, 1979]. Accordingly, the maximum size of the Taylor bubble is D_{max} [Issii and Kim, 2004]:

$$D_{max} = 4 \sqrt{\frac{\sigma}{(\rho_l - \rho_g)g}} \quad (19)$$

5.3. Theoretical Results

The numerical solution of above equations was performed in EES (engineering equation solver) [2015] to describe the characteristic performance of a bubble pump. The thermo-physical properties (density, viscosity, surface tension) of the working fluid were determined in EES with given input parameters. By using data produced from EES, the Cubic Spline method in Microsoft Office EXCEL was used to create the non-dimensional

characteristic curves of the bubble pump. The input parameters were tube length (L) and diameter (D) of the lift tube, height of the reservoir (H), system pressure (P), and bubble pump heat input (\dot{Q}). All non-dimensional numbers were calculated in EES with varying input parameters and the bubble pump efficiency was determined for each.

The bubble pump performance characteristic curves are shown using non-dimensional numbers in Figure 5.4. The liquid Froude number is shown with varying non-dimensional heat input (Q') at different non-dimensional pressure (P'). In this analysis, the bubble pump parametric study was performed based on LiCl-H₂O solution at different pressures (40 kPa to 101 kPa) and different tube diameters (6 mm to 16 mm). It was found that the gas Froude number (Fr_g) was constant at the corresponding non-dimensional heat input (Q') for different pressure levels at a certain tube diameter of the bubble pump. So, the non-dimensional pressure is calculated considering different tube diameters. Also, it is noted that the log of the Morton number is between -13 to -11. Bhaga and Weber [1981] showed that within this range of Mo , the bubble starts forming with a spherical shape at low Eotvos number which turns into a Taylor bubble with a bullet shaped nose and flat tail as Eotvos number increases.

The correlation of pump efficiency with liquid and gas Froude numbers and non-dimensional heat input at variable non-dimensional pressure is shown in Figure 5.4. From this figure, it can be seen that for all P' numbers, Fr_l increased very rapidly with Q' and after maxima they dropped steadily, whereas Fr_g increases as Fr_l drops. This behavior can be better explained in Figure 5.5 where the flow regime is described. At low $Q' (< 10^{-3})$, when $Fr_g < 1$, the gas void fraction is low ($\alpha_d < 25\%$), small gas bubbles are generated as this region is dominated by surface tension forces. When $Fr_g > 1$, the gas volume fraction increases with increasing Q' : larger gas bubbles (Taylor bubbles) form by coalescing small bubbles. Hence, the buoyancy increases which produces a high flow rate of liquid. At higher Q' , the increasing thermal force (input heat) increases the gas volume fraction in the vapor-liquid flow which leads to a high liquid flow as the buoyancy of the vapor slug increases. At higher gas void fraction ($\alpha_d > 60\%$), when $Fr_g > 9$, the Fr_l starts to decrease as the gravitational force becomes stronger than the inertia force of the liquid. Churn flow is achieved in this region.

Figure 5.4 also shows that at high P' number, the pumping started at high Fr_1 number ($Fr_1 > 4$), at which point the inertia forces of the liquid should be comparatively higher than the gravitational forces to start the bubble pump. It is noticed that the highest efficiency is attained at the starting point of slug flow (Figure 5.5) and at low P' , the slug flow started earlier than at higher P' . At this low Q' point, the Froude number of the vapor is low. As P' increases, more heat is required to form the Taylor bubble that produces the slug flow. As a result, the efficiency is shifting to the lower range. Hence, at high P' , Q' has to increase to operate the bubble pump at its highest efficiency. This indicates that higher thermal forces are required to dominate the gravitational forces and to increase the inertia forces of the liquid and vapor flows.

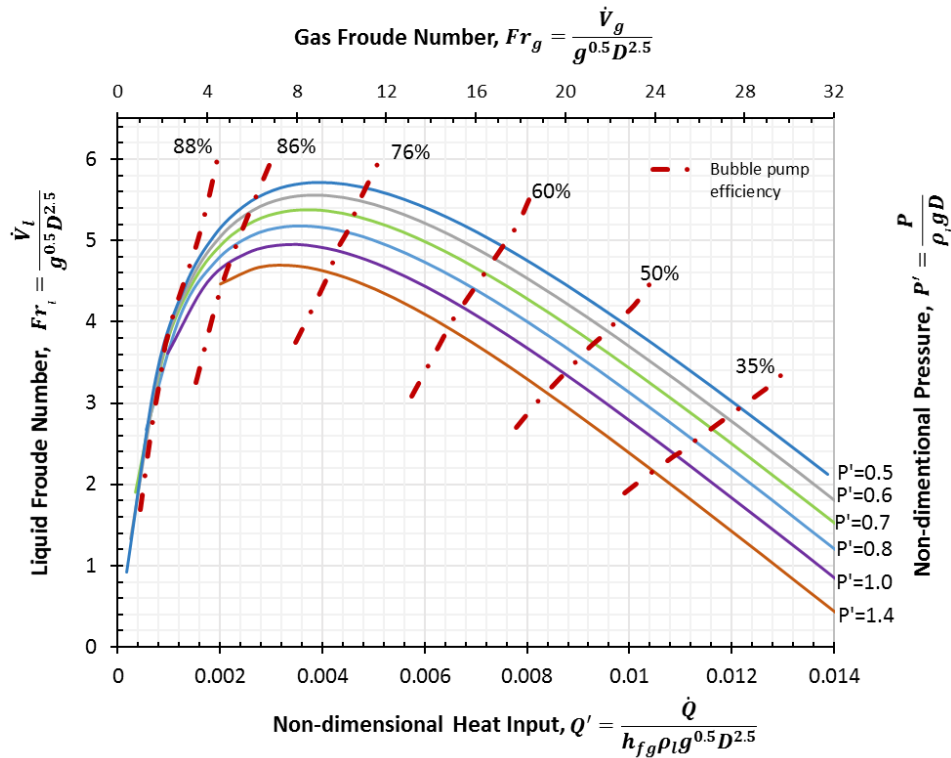


Figure 5.4: Performance characteristics of a bubble pump at $v'_b=0.145$.

Figure 5.5 shows the dependency of gas and liquid slug flow rate, in terms of Froude number of gas and liquid at different P' . The two mixed flow Reynolds numbers (Re) that are found at different P' are also shown in this figure. In the bubble pump analysis, it is revealed that the Reynolds number is always greater than 10^4 for all P' numbers, unlike an air/water system. The Reynolds number in this analysis is calculated based on the two-

phase flow homogenous mixture model. In a bubble pump, vapor generation (phase change) occurs via evaporation when the liquid is heated. Then the coalescence occurs due to the random collision of the vapor bubbles induced by the turbulent conditions and a long length Taylor bubble is formed. As this bubble, along with the fluid in its vicinity, is progressing upward through the tube, the generated Taylor bubble losses heat and becomes smaller. Therefore, the end velocity of the Taylor bubble is reduced and its buoyancy decreased. So, the train of Taylor bubbles in the liquid column of a bubble pump do not have the same size and same velocity. Hence, collisions occur due to the different sizes and different velocities, which produces the two-phase turbulent flow conditions along the tube [Montoya at al., 2016]. As a result, the Reynolds number is higher than the air lift pump. In Figure 5.5, the liquid Froude number (Fr_l) increased sharply but after reaching the maxima, it decreased at moderate rate with increasing gas Froude number (Fr_g). At low heat input, the vapor flow was low, hence, the volume fraction of the vapor in the liquid was low due to the surface tension forces. Beyond a gas volume fraction (α_d) of 25% [Kleinstreuer, 2003], small bubbles started to coalesce to form larger bubbles where the buoyancy is the dominant force and this is the slug flow regime. In the slug flow regime, if the generation of vapor bubbles increases, but $\alpha_d < 65\%$ [Kleinstreuer, 2003], with the increase of heat, the Taylor bubbles lose their regularity and stability, which causes the breakup of large cap bubbles and produces a chaotic flow pattern. This is known as churn flow, where the gravitational force dominates the surface tension force. This flow regime can be characterized by intense coalescence and breakup where a wider range of bubbles and liquid occupies the lift tube alternately with an oscillatory motion.

5.4. Experimental Technique

To compare the analytical results produced by this model, experiments were performed in a bubble pump test rig (Figure 5.3). The experiment was conducted at atmospheric conditions using LiCl-H₂O solution (41% of weight/weight concentration) and also with pure water to evaluate the bubble pump characteristics in VAR systems. The separator and the reservoir in Figure 5.3 were open to the atmosphere. The first experiment was started with 50% w/w concentrated LiCl-H₂O solution. But at high heat input, the crystallization of salt occurred very quickly and deposited on the immersion heater and tip

of the thermocouple which turned the heater off. After thermodynamic analysis of the VAR systems with LiCl-H₂O solution, it was determined that a 41% w/w LiCl-H₂O solution is required at atmospheric pressure for absorbing the refrigerant vapor by the solution.

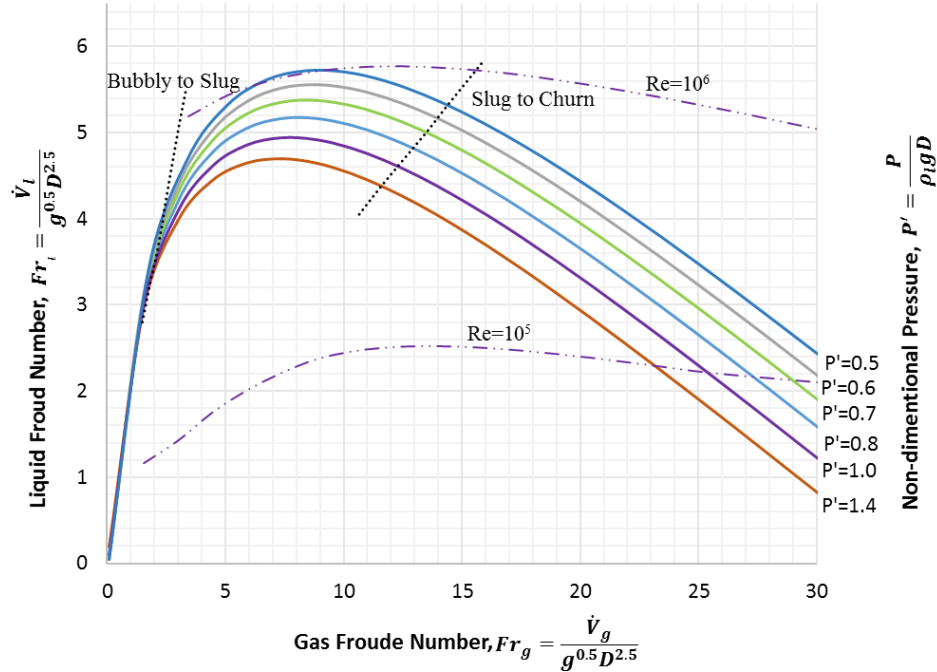


Figure 5.5: Flow regime of a bubble pump.

5.3. Measuring Instrument

In the test set up, pressures and temperatures were measured at three different places: (i) in the generator, (ii) in the separator, and (iii) in the reservoir, as shown in Figure 5.3. Temperatures were measured by using Type J Grounded Pipe Plug Probe thermocouples (Omega, Canada) and pressures were measured by stainless steel Type 17-4 PH pressure transducers (Omega, Canada). A “Reed SD-947” data logger (DMM, Canada) (accuracy, 0.4%+1°C) was used to record the temperature data and a LOGiTpc Interface data logger (Omega, Canada) with an accuracy of ±0.2 atm was employed to record the pressure.

5.4.1. Experimental procedure

In every experiment, the reservoir was filled with preheated solution to a predetermined height (H). An immersion electric heater was used to supply heat to the

generator. The heat input was controlled by a 500 Watts variable power supply. A 47 cm long clear FEP (fluorinated ethylene propylene) tube was used as the lift tube, enabling easy visualization of the flow pattern. At each heat input, when the temperature reached a steady state, the flow pattern was monitored through the lift tube and the temperature and pressure were recorded. It was observed that at low heat input, a longer time was required to reach the steady state temperature. The two-phase flow mixture (liquid and vapor) pumped into the separator. A 250 mL graduated cylinder, scaled in increments of 2 mL, was used to collect the liquid from the bottom of the separator over a period of time. Then the volume flow rate of the liquid was estimated. The vapor from the separator escaped to the atmosphere. Three different diameters of tube (12, 10, and 6 mm) were utilized at three different heights of the reservoir ($H= 37$ mm, 32 mm, and 27 mm).

5.4.2. *Experimental Results and Model Validation*

Different non-dimensional pressure variables (P') were achieved by changing the diameter of the lift tube while keeping the pressure constant at atmospheric pressure. The effect of the tube diameter was observed in bubble pump system performance. Different flow regimes were also observed in the experiments when the tube diameter was changed from 6 mm to 12 mm.

A graph of liquid Froude number (Fr_l) has been plotted against the non-dimensional heat input in Figure 5.6. The theoretical liquid Froude number (Fr_l) has been calculated considering both the Reynolds number of two-phase homogenous (mixed slug) flow that has been assumed in this bubble pump theory, and the Reynolds number of a liquid slug as used for an air-lift pump. This figure shows that the experimental results for both liquids agree well with the theoretical results when the Reynolds number was based on a two-phase flow mixture (mixed slug). When the Reynolds number was calculated considering only the liquid slug based on the air/water lift pump theory, a deviation was observed between these theoretical results and the experimental results. Although the trend of liquid Froude number for both cases is the same, at low Q' both results are very close. This is because the volume fraction of vapor is low at low heat input, so the calculated Reynolds numbers using the liquid slug and the mixed slug are close. In a bubble pump, the gas void fraction is dominated by the phase change of the liquid rather than by compression of the

gas as is the case in an air/water lift pump. The gas void fraction increases as the heat supply increases in a bubble pump, resulting in the increasing frequency of Taylor bubbles with entrained small bubbles in their wake. Therefore, the inertia forces are accounted for in the mixed slug analysis, unlike the liquid slug only. This is the reason for the deviation of experimental results when comparing with analytical results of an air/water lift pump.

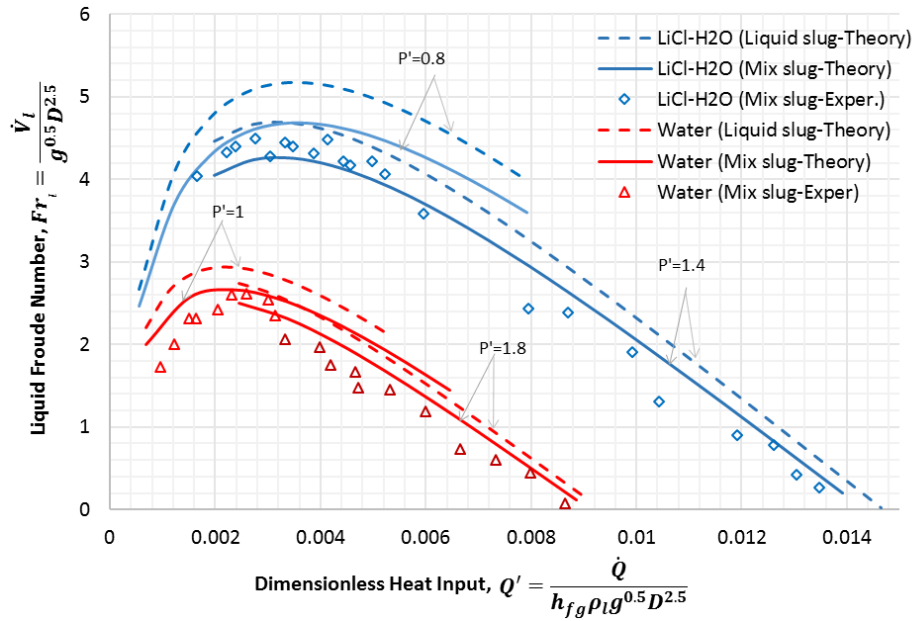


Figure 5.6: Comparison between theoretical and experimental results of a bubble pump at different P' for LiCl-H₂O ($v'_b=0.145$) and pure water ($v'_b=0.038$) working fluids.

In this analysis, two different diameter tubes (10 mm and 6 mm) were used for both the water and LiCl-H₂O solution. The results at $P'=0.8$ & 1.4 are for the LiCl-H₂O solution, and those at $P'=1$ & 1.8 are for water. The root mean square deviation between the theoretical (bubble pump theory) and experimental results is about 12%. This suggests that the mixed flow Reynolds number should be used for the case of bubble pump.

5.4. Conclusions

A thermally driven bubble pump can be used in a vapor absorption refrigeration (VAR) system to replace the electrical pump for lifting the liquid from the absorber to the generator. The goal of this study was to characterize a bubble pump that can be used in

VAR systems regardless of the type of working fluid or the physical parameters of the pump itself. In this regard, a dimensional analysis was performed to describe the operation of the bubble pump considering the thermophysical properties of the working fluid and the physical parameters of the bubble pump. A proper analytical method is essential for determining the bubble pump performance when it is used in VAR systems as it is the driving force for refrigeration. A theory was developed and the analyses were conducted to determine the bubble pump efficiency at various operating parameters. An experimental work was performed to validate the analytical results.

Non-dimensional parameters such as non-dimensional heat input, non-dimensional pressure variable, Froude number (liquid and gas), and Reynolds number were found that characterize the efficiency of the bubble pump. The non-dimensional parameters were related with input heat, system pressure, fluid properties and the geometry of the bubble pump. The highest efficiency was obtained at lower non-dimensional pressure when the flow structure was at the starting of slug flow regime. At this flow regime, the highest liquid Froude number was found but it decreased with increasing gas (vapor) Froude number (at higher heat supply) and the flow became churn flow. From this analysis, it was revealed that the bubble pump always operates in a two-phase flow turbulent condition where the Reynolds number is always higher than 10^4 and the Morton number is between (10^{-13} to 10^{-11}). The analytical results of proposed model and the experimental results agreed within 12% with water or LiCl-H₂O solution as the working fluid.

The characteristic curves produced by the analyses of this study will provide a standard map concurring the bubble pump usage in any vapor absorption refrigeration system for any kind of working fluid and geometric structure.

Acknowledgements

This work is made possible by the Natural Science and Engineering Research Council of Canada.

Nomenclature

| | | |
|-----------------|---|-------------------------------------|
| A | Area of the tube (m ²) | <i>Subscripts</i> |
| C _o | Velocity profile coefficient | <i>BP</i> bubble pump |
| D | Diameter (m) | <i>b</i> bubble |
| Fr | Froude number | <i>g</i> gas (vapor) |
| g | Acceleration due to gravity (m/s ²) | <i>gen</i> generator |
| H | Height of the reservoir (m) | <i>l</i> liquid |
| h _{fg} | Enthalpy of vaporization [kJ/kg] | <i>LT</i> lift tube |
| L | Length of the lift tube (m) | <i>MIX</i> liquid and vapor mixture |
| Mo | Morton number, $Mo = \frac{g\mu^4}{\rho\sigma^3}$ | <i>m</i> mean |
| P | Pressure (kPa) | <i>sol</i> solution |
| P' | Non-dimensional pressure variable, $P' = \frac{P}{\rho g D}$ | <i>sys</i> system |
| Q̇ | Input heat (W) | |
| Q' | Non-dimensional heat input, $Q' = \frac{\dot{Q}}{h_{fg}\rho_l g^{0.5} D^{2.5}}$ | |
| Re | Reynolds number | |
| Ṁ | Volumetric flow rate (m ³ /s) | |
| v | Velocity (m/s) | |
| x | Quality | |
| ρ | Density (kg/m) | |
| σ | Surface tension (N/m) | |
| α _d | Gas void fraction | |
| μ | Viscosity (Pa-s) | |

REFERENCES

- Adewusi, S.A., Zubair, S.M., 2004. Second law based thermodynamic analysis of ammonia-water absorption systems. *Energy Convers. Manage.* 45, 2355-2369.
- Aman, J. Ting, D.S-K. Henshaw, P. 2014. Residential solar air conditioning: Energy and exergy analyses of an ammonia-water absorption cooling system. *Applied Thermal Engineering.* 62, 424-432.
- Aman, J., Henshaw, P. Ting, D. S-K., 2016. Modelling and Analysis of Bubble Pump Parameters for Vapor Absorption Refrigeration Systems. proceedings of ASHRAE Annual Conference. St.-Louis, MO, USA, June 25 to 29.
- Barenblatt, G. I., 1996. *Dimensional Analysis and Intermediate Asymptotics.* Cambridge University Press, Cambridge.
- Ben-Ezzine N, Garma R, Bellagi A., 2010. A Numerical Investigation of a Diffusion-Absorption Refrigeration Cycle Based on R124- DMAC Mixture for Solar Cooling. *International Journal of Energy.* 35, 1874-1883.
- Benhmidene, A., Chaouachi, B. Gabsi, S. Bourouis, M., 2011. Modelling of heat flux received by a bubble pump of absorption-diffusion refrigeration cycle. *Heat Mass Transfer.* 47, 1341-1347.
- Benhmidene, A., Chaouachi, B. Gabsi, S., 2010. A Review of Bubble Pump Technologies. *Journal of Applied Sciences.* 10(16), 1806-1813.
- Bhaga, D. Weber, M.E., 1981. Bubbles in viscous liquid: shapes, wakes and velocities. *Journal of Fluid Mechanics.* 150, 61–85.
- Bourseau P, Mora J.C., Bugare, R. 1987. Coupling of an absorption-diffusion refrigeration machine and solar flat-plate collector. *International Journal of Refrigeration.* 9, 206–214.
- Bourseau P., Mora J.C., Bugare R., 1987. Coupling of an absorption-diffusion refrigeration machine and solar flat-plate collector. *International Journal of Refrigeration.* 9, 206–214.
- Brennen, C. E., 2005. *Fundamentals of Multiphase Flow.* Cambridge University Press publisher, New York, NY 10011-4211, USA, P-61.
- Chan, K.W., Malcolm, M., 2016, The Einstein-Szilard refrigerator: an experimental exploration. *American Society of Heating, Refrigerating, and Air-Conditioning*

- Engineers. 2016 ASHRAE transection. <https://www.thefreelibrary.com/The+Einstein-Szilard+refrigerator%3a+an+experimental+exploration.-a0462045170>
- Clement Kleinstreuer, Two Phase Flow, Taylor & Francis publisher, 2003, New York, pp-69-75
- Delano A., 1998. Design Analysis of the Einstein Refrigeration Cycle, Ph.D. Thesis, Georgia Institute of Technology.
- EES (Engineering Equation Solver), 2015. F-Chart software, Academic Commercial V9. 941(1992-2015), www.fchart.com
- Einstein, A. Szilard, L. 1928. Improvements Relating to Refrigerating Apparatus. (Appl. U.K. Patent: 16 Dec. 1927; Priority: Germany, 16 Dec. 1926).
- Giles, R.V., 1962. Schaum's Outline of Theory and Problems of Fluid Mechanics and Hydraulics, McGrawHill Book Company, New York.
- Herold, K.E., Radermacher, R., Klein, S.A., 1996. Absorption Chillers and Heat Pumps. CRC Press, New York.
- Ishii, M. Kim, S., 2004. Development of one-group and two-group interfacial area transport equation. Nuclear Science Engineering Journal. 146(3), 257–273.
- Ishii, M. Zuber, N., 1979. Drag coefficient and relative velocity in bubbly, droplet or particle flows. AIChE Journal. 25, 843–855.
- Jakob U, Eicker U, Schneider D, Taki A.H., Cook M.J., 2008. Simulation and experimental investigation into diffusion absorption cooling machines for air conditioning applications. Applied Thermal Engineering. 28, 1138-1150.
- Kassab, S.Z., Kandil, H.A., Warda, H.A., Ahmed, W.H., 2009. Air-lift pumps characteristics under two-phase flow conditions. International Journal of Heat and Fluid Flow. 30, 88-98.
- Katasuhara, T., Kazama, T., 1958. Heat Transfer in Two-Phase Flow of Mixtures of Air and Water. 2nd Report - Vertical Channel, Transection of JSME. 24, 552-558.
- Kumar, M., Das, R.K., 2015. Thermodynamic study of diffusion absorption refrigeration system with organic fluid. Int. J. Mech. Eng. & Rob. Res. 4(1), 473-484.
- Mayor, T.S., Pinto, A.M.F.R., Campos, J.B.L.M., 2008. Vertical slug flow in laminar regime in the liquid and turbulent regime in the bubble wake---Comparison with fully turbulent and fully laminar regimes. Chemical Engineering Science. 63, 3614 – 3631.

- Montoya, G. Lucas, D. Baglietto, E. Liao, Y., 2016. A review on mechanisms and models for churn-turbulent flow regime. *Chemical Engineering Science*. 141, 86-103.
- Nickens, H.V., Yannitell, D.W., 1987. The effects of surface tension and viscosity on the rise velocity of a large gas bubble in a closed vertical liquid filled tube. *International Journal of Multiphase flow*. 13, 57-69.
- Nicklin, D.J., 1963. *The Air-Lift Pump: Theory and Optimization*. Transactions of the Institution of Chemical Engineers. 41, 29-39.
- Pfaff M., Saravanan R., Maiya M.P., Srinivasa M., 1998. Studies on bubble pump for a water–lithium bromide vapor absorption refrigeration. *International Journal of Refrigeration*. 21, 452–462.
- Platen, B.C. Munters, C.G., 1928. Refrigerator. U.S. Patent 1,685,764.
- Reinemann, D.J., 1987. A Theoretical and Experimental study of Airlift Pumping and Aeration with Reference to Aquacultural Applications. PhD Thesis. Cornell University.
- Reinemann, D.J., Parlange, J.Y., Timmons, M.B., 1990. Theory of small-diameter airlift pump. *Int. J. Multiphase Flow*. 16, 113-122.
- Saravanan R., Maiya M.P., 2003. Experimental analysis of a bubble pump operated H₂O–LiBr vapor absorption cooler. *Applied Thermal Engineering*. 23, 2383–2397.
- Shelton, S.V. and white-stewart, S.J., 2002. Bubble pump design for single pressure absorption refrigeration cycles. *ASHRAE Transactions*, 108.
- Starace, G., Pascalis, L. D., 2012. An advanced analytical model of the diffusion absorption refrigerator cycle. *International Journal of Refrigeration*. 35, 605-612.
- Stenning, A. Martin, C., 1968. An analytical and experimental study of air-lift pump performance. *ASME Journal of Engineering for Power* 106-110.
- Szirtes, T., 1997. *Applied Dimensional Analysis and Modeling*. McGraw-Hill, New York.
- Taitel, Y., Bamea, D., Dukler, A.E., 1980, Modelling Flow Pattern Transitions for Steady Upward Gas-Liquid Flow in Vertical Tubes. *AIChE J.* 26, 345-354.
- Tudose, E-T., 1997, Experimental investigation of Taylor bubble acceleration mechanism in slug flow. Masters' thesis, Department of Chemical Engineering and Applied Chemistry, University of Toronto, Toronto, Ontario, Canada.

- Walt, S., 2012. The design and optimization of a bubble pump for an aqua-ammonia diffusion absorption heat pump. MSc Thesis, North-West University, University in Potchefstroom, South Africa.
- Wang, Q., Gong, L., Wang, J.P., Sun, T.F., Cui, K., Chen, G.M., 2011. A Numerical Investigation of a Diffusion Absorption Refrigerator Operating with the Binary Refrigerant for Low Temperature Applications. *Applied Thermal Engineering*. 31, 1763-1769.
- White, S.J., 2001. Bubble Pump Design and Performance. MSc Thesis. Georgia Institute of Technology, Atlanta, USA. Mechanical Engineering.
- White, E.T., Beardmore, R.H., 1962, The Velocity of Rise of Single cylindrical Air Bubbles Through Liquids Contained in vertical Tubes. *Chemical Engineering science*. 17, 351-361.
- Zohar, A., Jelinek, M., Levy, A. Borde, I., 2009. Performance of Diffusion Absorption Refrigeration Cycle with Organic Working Fluids. *International Journal of Refrigeration*. 32, 1241-1246.
- Zohar, A., Jelinek, M., Levy, A., Borde, I., 2008. The influence of the generator and bubble pump configuration on the performance of diffusion absorption refrigeration (DAR) system. *International Journal of Refrigeration*. 962-969.

CHAPTER 6

BUBBLE-PUMP-DRIVEN LiBr-H₂O AND LiCl-H₂O ABSORPTION AIR-CONDITIONING SYSTEMS

This work was published as “Aman, J., Henshaw, P. Ting, D. S-K., Bubble-pump-driven LiBr-H₂O and LiCl-H₂O absorption air-conditioning systems, Thermal Science and Engineering Progress”, <https://doi.org/10.1016/j.tsep.2017.10.022>.

6.1. Introduction

A vapor absorption refrigeration system (VARs) can be driven by waste heat or solar thermal energy. LiBr-H₂O and NH₃-H₂O are the most common refrigerant-absorbent working pairs for this VARs. The LiBr-H₂O absorption system has the advantage of higher efficiency, but due to its crystallization and corrosion problems, NH₃-H₂O is more preferable for small scale commercial or residential applications [Aman *et al.*, 2014]. The core components of absorption cooling systems are the absorber, generator, condenser and evaporator. A pump is a critical component of the absorption system to circulate the refrigerant-absorbent solution from the low-pressure absorber to the high-pressure generator. High quality mechanical/electrical energy is used to run this pump. Furthermore, the pump must handle high temperature corrosive solutions. A thermally-driven bubble pump, which can be powered by waste heat or solar thermal energy, can be employed to circulate the liquid solution and generate the necessary refrigerant for the required cooling effects [Aman *et al.*, 2016]. In the diffusion-absorption refrigeration cycle, a bubble pump or vapor-lift pump can be used to circulate the solution from the generator to the absorber without electrical work input. In a bubble pump, the vapor created (via heating) increases the buoyancy of the fluid, causing it to ascend through a vertical tube under two-phase flow conditions. For small scale applications like residential air-conditioning, this system will be more reliable and independent of the availability of electricity. But for larger scale applications of a bubble-pump-operated VARs, multiple parallel pumps may be explored [Saravanan & Maiya, 2003].

The conventional absorption refrigeration cycle works at two pressure levels to achieve the saturation temperature difference between the condenser and the evaporator.

But in a diffusion absorption refrigeration system, the circulation of the solution is carried out by the bubble pump, maintaining essentially a single pressure throughout the entire cycle. This concept was first introduced by Platen and Munters in 1920 [Platen & Munters, 1928]. Although it is called a 'single pressure' system, there are still minor pressure variations due to the flow friction and gravity. A heat-driven bubble pump is a mechanism to move the fluid through the cycle against this flow friction and gravity. As a result, this thermally-driven absorption cycle does not require any electricity to create the pressure difference. Bubble pumps are portable, operate silently, have high reliability and are inexpensive to build [White, 2001]. These advantages make this system ideal for remote locations and to where electricity is not available. However, their widespread application is somewhat hindered because of their low COP compared to a conventional absorption system.

The single pressure absorption system cycle works on two thermodynamic cycles: the ammonia-water-hydrogen cycle and the Einstein cycle. The most familiar is the ammonia-water-hydrogen cycle which is known as the diffusion absorption refrigeration (DAR) cycle patented by Swedish engineers Platen and Munter in 1920 [Platen & Munters, 1928]. This cycle uses at least three working fluids to achieve a low evaporation temperature and high condensation temperature at a single pressure level. The third, an inert fluid is introduced to the working fluid to lower the partial pressure of the refrigerant in the evaporator and maintaining pressure equalization throughout the system. Thus, the refrigerant can evaporate at a lower temperature in the evaporator. The most common working fluids for this cycle are ammonia-water-hydrogen/helium where ammonia is the refrigerant, water is the absorbent and hydrogen or helium is the inert gas which provides the pressure equalization of the system. In the Platen and Munter cycle, the refrigerant ammonia is absorbed by the water and its partial pressure is lowered by the inert gas hydrogen or helium. The water separates the ammonia from the inert gas. In 1930, Albert Einstein and Szilard Leo disclosed another single pressure refrigeration cycle which uses butane, ammonia, and water [Delano, 1998]. Unlike the Platen and Munter cycle, the Einstein cycle utilizes absorbate fluid for pressure equalization instead of an inert gas. In this cycle, butane works as the refrigerant, ammonia is used to lower the partial pressure of the refrigerant, and water is used to absorb the ammonia and separate the butane. The

Platen and Munter refrigeration cycle has been used for refrigerators in homes, RV's and hotel rooms since the 1920's. The COP of this cycle is 0.15 to 0.2 [White, 2001]. Because of the lower efficiency of this cycle compared to a conventional absorption cycle, research has been conducted to improve the efficiency, and with the variation of the evaporator temperature, the best published COP is approximately 0.3 [Jacob *et al.*, 2008, Starace & Pascalis, 2012]. Though the Einstein cycle was patented in 1930, the first detailed study of the cycle was by George Alefeld in 1980. With many simplifying assumptions, he found the cycle COP to be 0.25 [Shelton *et al.*, 1999]. In 1997, Delano analyzed this cycle performance in detail based on Stenning and Martin's analysis and improved the cycle performance by adding two regenerative heat exchangers. The best COP was 0.4 [Delano, 1998].

Water-based refrigerant VARSs like LiBr-H₂O work on low (vacuum) pressure, whereas NH₃-H₂O is a high-pressure refrigeration system. As a result, when a bubble pump is used for a water-based refrigerant VARS, the refrigeration cycle does not work as in DAR systems. Pfaff *et al.* [1998] were the first to study the bubble pump for use in a LiBr-H₂O refrigeration system and the bubble pump was modelled based on intermittent slug flow using the manometer principal. The performance of the bubble pump was evaluated experimentally in a glass tube test rig to visualize the flow behavior. Saravanan and Maiya [2003] designed and built a 50 W bubble pump operated LiBr-H₂O VARS and tested it with different operation conditions [Saravanan & Maiya, 2003]. In their design, they restricted the refrigerator height to 1.5 m to operate the system with a low-pressure difference between the condenser and the evaporator. They used a parallel flow path and a combination of 'U' tube and capillary tubes to reduce the pressure drop between the condenser and the evaporator.

The pressure difference between the evaporator and the condenser should be low to operate the bubble pump in water-based refrigeration systems [Saravanan & Maiya, 2003]. The water vapor pressure difference between the condenser and the evaporator of a water-salt refrigeration system is low enough to employ the bubble pump to circulate the solution and refrigerant in the system. The pressure drop in the connecting tubes and in the system components is a major concern for this system because it operates under a vacuumed pressure. For a conventional LiBr-H₂O VARS, equal-pressure components are used to

minimize the pressure loss, but the pressure drop could be high in small scale applications [Saravanan & Maiya, 2003]. Hence, little research has been carried out to use bubble pumps in LiBr-H₂O VARS and commercial applications are not yet practicable.

The performance of VARSs strongly depends on the thermophysical properties of the refrigerant-absorbent working fluids [Perez, 1984]. Saravanan and Maiya studied water based refrigerant working fluids for VARS and found that LiCl-H₂O has advantages over LiBr-H₂O in terms of the system performance as well as for low energy consumption. They suggested that the lower circulation ratio (ratio of the mass flow rate of salt solution and refrigerant) in LiCl-H₂O systems is the cause of higher performance [Saravanan & Maiya, 1998]. Grover et al. [1988] analyzed the thermodynamic properties of LiCl-H₂O for VARS and found that this solution can operate at lower generator temperature. A thermophysical properties analysis of different working fluids for VARS was performed by Flores et al. [2014] and it was found that LiCl-H₂O has a higher COP over a LiBr-H₂O VARS at lower heat input because of their low C_p (heat capacity) values. Gogoi and Konwar [2016] performed exergy analysis of LiCl-H₂O VARS and observed that at the same operating conditions, LiCl-H₂O systems had higher COP and exergetic efficiency values than LiBr-H₂O systems. They suggested that the thermodynamic properties of LiCl-H₂O solution account for this higher efficiency. Recently, She et al. [2015] proposed a low-grade heat-driven double-effect VARS where LiCl-H₂O was used on the high-pressure side and LiBr-H₂O was utilized on the low-pressure side because LiCl-H₂O has a larger vapor pressure than LiBr-H₂O. Bellos et al. [2017] investigated the LiCl-H₂O working pair for a double-effect absorption chiller driven by a solar thermal collector and found that it can achieve 8% more cooling compared to a LiBr-H₂O system.

Since low efficiency is the main downside of bubble-pump-operated absorption refrigeration systems, a complete thermodynamic analysis of each component is necessary. As the cycle efficiency depends on the amount of refrigerant desorbed from the generator, so the detailed analysis of the bubble pump generator is needed before one can improve the system efficiency. Since water is the better refrigerant for VARS, especially for air-conditioning applications, and also because of the limitation of LiBr-H₂O use in bubble-pump-operated absorption systems due to its low vapor pressure, the present research has incorporated the thermophysical properties of LiBr-H₂O and LiCl-H₂O in the bubble pump

modelling. This study has also focused on the development of a mathematical simulation model for the bubble pump generator by using a two-phase flow model that will determine the cooling effect of the refrigeration cycle and a thermodynamic model of every component of this cycle in order to achieve the maximum system efficiency.

6.2. System Description

A schematic of a bubble-pump-operated water-based refrigerant vapor absorption refrigeration system which can be driven by solar thermal energy is shown in Figure 6.1. In order to make the system completely independent of the grid electricity, the solar collector is also operated by a solar bubble pump in this figure. The air-cooler with the solar collector is used only for cooling the vapor that may be produced from the collector. For the thermodynamic performance analysis of the absorption air-conditioning system, only the refrigeration cycle (absorption air-conditioning cycle in Figure 6.1) operation is described and analyzed in this study. In an absorption air-conditioning system, the pure water vapor flows to the condenser (State 1) from the separator, and is condensed by releasing ' \dot{Q}_{cond} ' heat to the atmosphere by air cooling. Then the condensed, saturated water (State 2) flows to the evaporator through the throttle valve where its pressure is reduced for the necessary cooling effect (\dot{Q}_{eva}) in the evaporator (State 3). The water vapor from the evaporator (State 4) is absorbed in the absorber by the high-concentration (strong) salt solution, which comes back from the bubble pump generator, and becomes a low-concentration (weak) salt solution. The weak solution from the absorber (State 5) flows to the bubble pump generator through the heat exchanger (State 6) by gravity. In the bubble pump generator, the solution is heated by solar heat input ($\dot{Q}_{bubble\ pump}$). When the temperature of water in the solution is higher than the saturation temperature, bubbles of water vapor start to form. Many small vapor bubbles coalesce into a big bubble and rise in the bubble pump tube, carrying the solution above it into the separator. Water vapor separates from the solution in the separator and the solution becomes strong (State 7) and drains back to the absorber through the solution heat exchanger. The strong solution in the absorber rejects heat (\dot{Q}_{abs}) to the atmosphere and absorbs the water vapor from the evaporator.

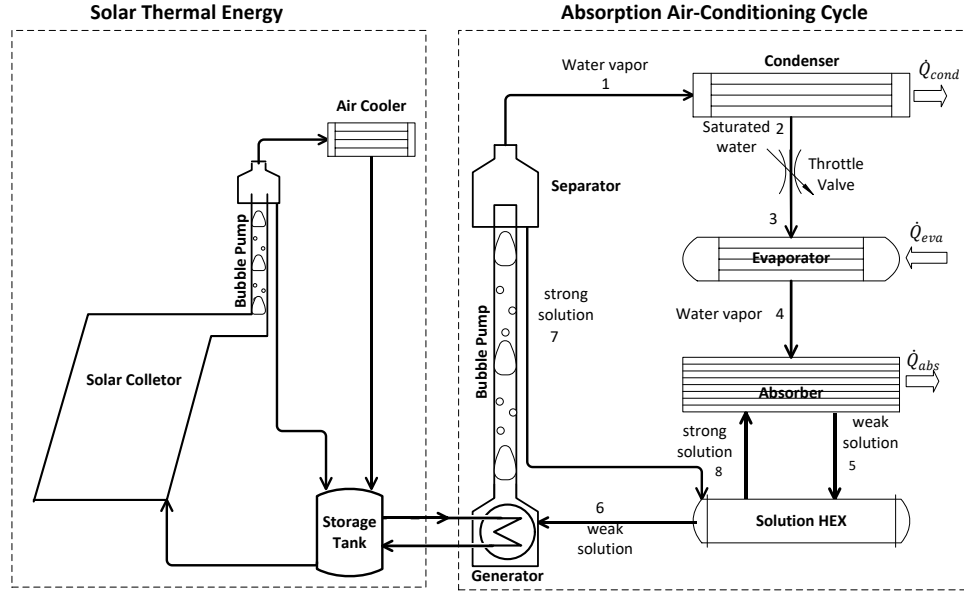


Figure 6.1: Flow diagram of solar absorption air-conditioning system

6.3. Thermodynamic and Simulation Model

For a thermodynamic model of the bubble pump operated refrigeration cycle, the principles of mass and energy conservation have been applied for each component of the system. In this study, the main components: generator and bubble pump, condenser, evaporator, gas heat exchanger, absorber, and solution heat exchanger have been studied. To analyze the thermodynamic cycle, a control volume is applied to each component. The system is sized to use a bubble pump for which experimental data is available [Aman *et al.*, 2016].

Generator and the bubble pump

The bubble pump heat input to the generator evaporates the water vapor and separates it from the solution as shown in Figure 2. The strong solution is pumped back to the solution heat exchanger through the bubble pump and separator. The mass and energy balance of the generator and the bubble pump control volume yields:

$$\dot{m}_6 = \dot{m}_1 + \dot{m}_7 \quad (1)$$

Energy balance:
$$\dot{Q}_{gen} = \dot{m}_1 h_1 + \dot{m}_7 h_7 - \dot{m}_6 h_6 \quad (2)$$

The species conservation equation for salt solution in the generator is:

$$X_6 \dot{m}_6 = X_7 \dot{m}_7 \quad (3)$$

where X is the LiBr or LiCl mass fraction in solution.

Bubble pump modeling

The mass flow rate of refrigerant strongly depends on the bubble pump parameters (such as lift tube diameter (D), lift tube length (L), height (H) of the liquid in the lift tube) and the heat input to the bubble pump ($\dot{Q}_{bubble\ pump}$). The bubble pump consists of a lift tube connecting the generator and separator. The generated vapor bubbles rise in the tube lifting the solution ahead of it into the separator.

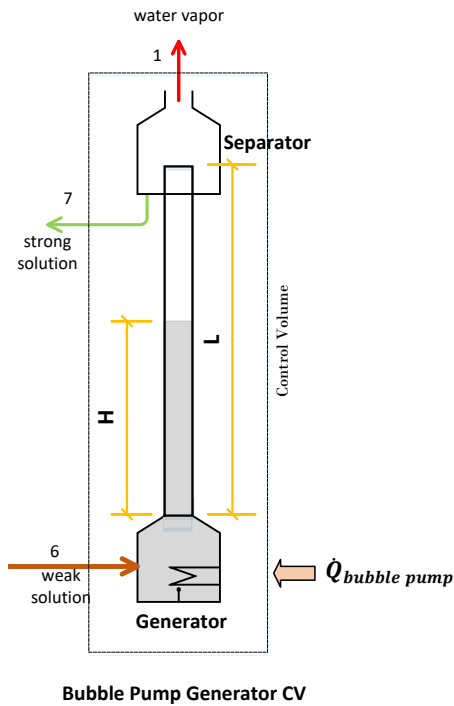


Figure 6.2: Bubble Pump Generator Control Volume

In this analysis, a two-phase flow model is used to determine the flow rate of the weak solution in the bubble pump. The following analytical model, taken from Aman et al. has been used to describe the bubble pump performance [Aman *et al.*, 2016].

The void fraction is the ratio of volume of the gas in the liquid over total volume of the liquid gas mixture, an important parameter in two-phase flow to determine the flow regime as well as two-phase pressure drop and heat transfer [Aman *et al.*, 2016]. It can be determined as

$$\alpha_d = \frac{\text{volume of the gas in the liquid}}{\text{total volume of the liquid gas mixture}} = \frac{\dot{V}'_g}{C_o(\dot{V}'_l + \dot{V}'_g) + v'_b} \quad (4)$$

where,

$$\dot{V}'_l = \frac{\dot{V}_l}{A(gD)^{1/2}}, \quad \dot{V}'_g = \frac{\dot{V}_g}{A(gD)^{1/2}}, \quad v'_b = \frac{v_b}{(gD)^{1/2}} \quad (5)$$

C_o is the velocity profile coefficient of gas-liquid mixture (ranging from 1.2 for fully-developed turbulent flow to 2 for laminar flow [Reinemann *et al.*, 1990], v'_b is the non-dimensional vapor bubble velocity, v_b is the velocity of a vapor bubble in stagnant liquid (m/s), \dot{V}'_l is the non-dimensional volume flow rate of liquid, \dot{V}_l is the volumetric flow rate of liquid (m³/s), \dot{V}'_g is the non-dimensional volume flow rate of vapor, \dot{V}_g is the volumetric flow rate of gas (m³/s), A is the cross sectional area of the lift tube (m²), and D is the inner diameter of the lift tube.

From theoretical and experimental analysis, Reinemann *et al.* [1990] showed that non-dimensional vapor bubble velocity can be expressed as the surface tension parameter:

$$V'_b = 0.352(1 - 3.18\Sigma - 14.77\Sigma^2) \quad (6)$$

$$\text{where, surface tension parameter, } \Sigma = \frac{\sigma}{\rho g D^2} \quad (7)$$

If the lift tube length is L and it is partially filled with the liquid solution with height H , which is the height of the absorber, the total pressure drop along the lift tube is the sum of the static pressure drop and the frictional losses, and can be calculated by [Aman *et al.*, 2016]

$$\rho g H = \rho g ((1 - \alpha_d)L + f \frac{L}{2D} \rho v_m^2 (1 - \alpha_d)) \quad (8)$$

where, f is the friction factor for continuous flow [Bellos *et al.*, 2017] given by

$$f = \frac{0.316}{Re^{0.25}} \quad (9)$$

Re is the Reynolds number for a solution in liquid and vapor phase and expressed as

$$Re = \frac{\rho_{sol} v_m D}{\mu} \quad (10)$$

The following equation can be established by rearranging Equation (8),

$$\frac{H}{L} = (1 - \alpha_d) \left(1 + \frac{f}{2} (\dot{V}'_l + \dot{V}'_g)^2 \right) \quad (11)$$

The flow rate of vapor depends on the heat addition to the generator which is the required heat for the bubble pump. Assuming that there is no heat loss through the lift tube of the bubble pump and the generator (so, $\dot{Q}_{bubble\ pump} = \dot{Q}_{gen}$), the required heat input will be used to determine the volumetric flow rate of vapor by the following equation

$$\dot{Q}_{bubble\ pump} = \dot{V}_g \rho_g h_{fg} \quad (12)$$

And the mass flow rate of vapor refrigerant by the bubble pump is calculated by

$$\dot{m}_1 = \dot{V}_g \rho_g \quad (13)$$

The volume flow rate of the strong solution will be determined by using Equations 11 and 12. And the mass flow rate of the strong solution is

$$\dot{m}_7 = \dot{V}_l \rho_{sol} \quad (14)$$

To quantify the bubble pump generator performance, the lifting ratio is an important parameter that is determined by the volumetric flow rate of strong solution per volumetric flow rate of vapor and can be expressed as

$$b = \frac{\dot{V}_l}{\dot{V}_g} = \frac{\dot{m}_7}{\dot{m}_1} \quad (15)$$

Solution Heat Exchanger (SHX) (Figure 6.3):

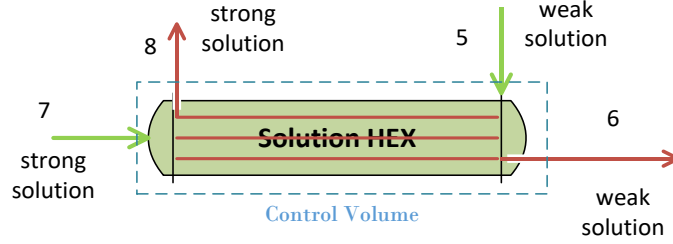


Figure 6.3: Solution Heat Exchanger Control Volume

Equations 16 and 17 represent the energy balance for the solution heat exchanger [Aman *et al.*, 2014].

$$T_6 = \frac{\dot{m}_7}{\dot{m}_5} \eta_{\text{HEX}} T_7 + \left(1 - \frac{\dot{m}_7}{\dot{m}_5} \eta_{\text{HEX}}\right) T_5 \quad (16)$$

where η_{HEX} is the heat exchanger efficiency.

$$h_8 = h_7 - \frac{\dot{m}_5}{\dot{m}_7} (h_6 - h_5) \quad (17)$$

Absorber (Figure 6.4):

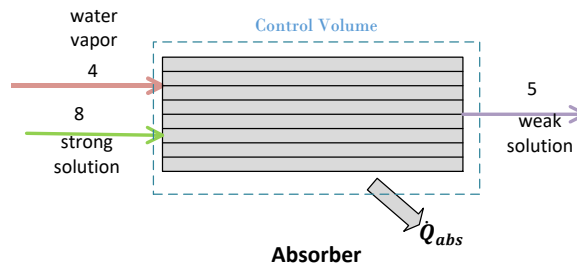


Figure 6.4: Absorber Control Volume

Energy balance of the absorber: $\dot{Q}_{abs} = \dot{m}_8 h_8 + \dot{m}_4 h_4 - \dot{m}_5 h_5 \quad (18)$

Evaporator (Figure 6.5):

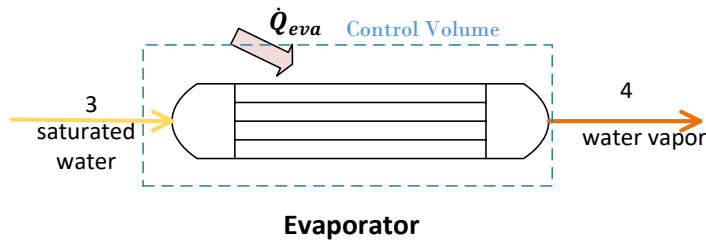


Figure 6.5: Evaporator Control Volume

$$\text{Energy balance of the evaporator: } \dot{Q}_{eva} = \dot{m}_4 h_4 - \dot{m}_3 h_3 \quad (19)$$

Condenser (Figure 6.6):

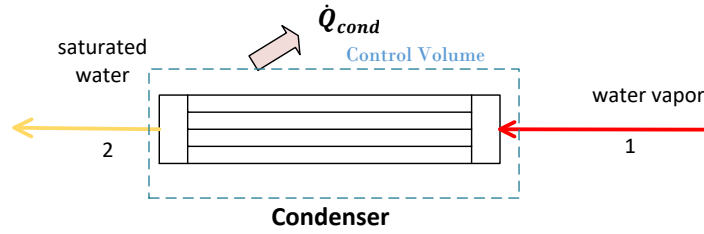


Figure 6.6: Condenser Control Volume

$$\text{Energy balance of the condenser: } \dot{Q}_{con} = \dot{m}_1 (h_1 - h_2) \quad (20)$$

Cycle performance:

In a bubble pump operated VARS, the bubble pump solar heat input is the only primary energy input to the generator. The coefficient of performance of this system is defined as:

$$COP = \frac{\text{useful energy output}}{\text{primary energy input}} = \frac{\dot{Q}_{eva}}{\dot{Q}_{bubble\ pump}}$$

6.3.1. Thermodynamic properties

For the absorption air-conditioning cycle analysis, the thermodynamic properties and the concentration of the salt (LiBr/LiCl) in water are determined by using the Engineering Equation Solver (EES) software [EES, 2015] at the equilibrium pressure and temperature for each state. The analysis is performed considering the fluid flow is steady and the system is in a steady-state condition.

6.4. Results and Analysis

The performance of each component of the bubble pump operated VARS has been predicted by the thermodynamic analysis and the bubble pump performance has been analyzed under two-phase fluid flow conditions. The coefficient of performance (COP) of the air-conditioning cycle has been calculated by using two working fluids (LiBr-H₂O and LiCl-H₂O).

In order to validate the proposed thermodynamic model in this study, the analysis of a LiBr-H₂O absorption system was compared with the experimental results of Saravanan & Maiya [2003] in Figure 6.7. Saravanan & Maiya [2003] reported that the temperature of generator fluctuated, which would result in lower performance of the system, compared to this steady-state analytical model. The COP was calculated at different generator heat inputs for 50 W of cooling capacity at the evaporator temperature of 7°C. It was clearly shown that the agreement between the analytical and the experimental results are very good; the average variation is within 3.2%.

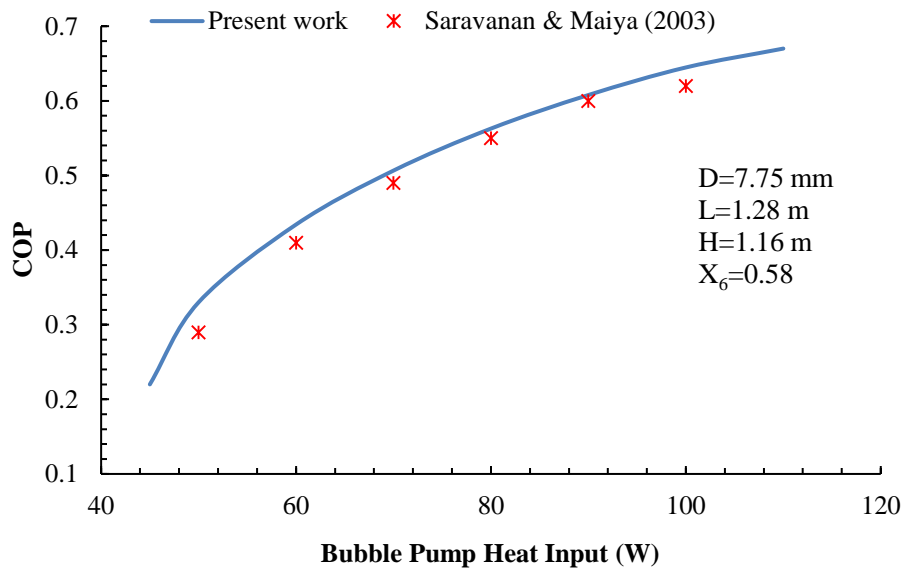


Figure 6.7: Performance comparison of a bubble pump operated LiBr-H₂O VARS between the proposed model and the experimental results of Saravanan & Maiya [2003].

Various thermodynamic properties at different stages in the cycle operation of LiBr-H₂O and LiCl-H₂O absorption air-conditioning systems driven by bubble pump are shown in Table 6.1. The properties have been obtained from the cycle analysis at the operating condition of $T_{BP\ gen} = 70^\circ\text{C}$, $T_{cond} = 35^\circ\text{C}$, $T_{abs} = 35^\circ\text{C}$, $T_{eva} = 7^\circ\text{C}$, the heat exchanger efficiency = 80%, and the bubble pump parameters: $D=10\text{ m}$, $L= 0.47\text{ m}$ and $H= 0.28\text{ m}$. The results of the thermodynamic model analysis of two systems are presented in Table 6.2 which illustrates the strong and weak solution concentrations, system pressures and

various energy flows to and from the systems. The lifting ratio and the cycle performance is also listed in the table.

Table 6.1: Thermodynamic properties at different states in LiBr-H₂O and LiCl-H₂O absorption cycles at operating conditions $T_{gen} = 70^{\circ}\text{C}$, $T_{cond} = 35^{\circ}\text{C}$, $T_{abs} = 35^{\circ}\text{C}$, $T_{eva} = 7^{\circ}\text{C}$, $\eta_{HEX} = 80$, $D=10$ mm, $H=0.28$ m, and $L=0.47$ m.

| State | Temperature (°C) | Pressure (kPa) | Mass flow (g/s) | | % Concentration | | Enthalpy (kJ/kg) | |
|------------------------------------|------------------|----------------|-----------------------|-----------------------|-----------------------|-----------------------|-----------------------|-----------------------|
| | | | LiBr-H ₂ O | LiCl-H ₂ O | LiBr-H ₂ O | LiCl-H ₂ O | LiBr-H ₂ O | LiCl-H ₂ O |
| Bubble pump generator ref exit (1) | 70 | 5.627 | 0.014 | 0.021 | 100 | 100 | 2630 | 2630 |
| Condenser ref exit (2) | 35 | 5.627 | 0.014 | 0.021 | 100 | 100 | 147 | 147 |
| Evaporator ref inlet (3) | 7 | 1.002 | 0.014 | 0.021 | 100 | 100 | 147 | 147 |
| Evaporator ref exit (4) | 7 | 1.002 | 0.014 | 0.021 | 100 | 100 | 2513 | 2513 |
| Absorber sol exit (5) | 35 | 1.002 | 0.672 | 0.413 | 54.08 | 41.07 | 81 | 155 |
| Sol HEX exit (6) | 63 | 1.002 | 0.672 | 0.413 | 54.08 | 41.07 | 139 | 229 |
| Sol HEX inlet (7) | 70 | 1.002 | 0.518 | 0.335 | 55.60 | 43.77 | 157 | 265 |
| Absorber sol inlet (8) | 44 | 1.002 | 0.518 | 0.335 | 55.60 | 43.77 | 113 | 186 |

ref = refrigerant;
sol = solution

Table 6.2: Thermodynamic analysis of bubble pump operated LiBr-H₂O and LiCl-H₂O absorption air-conditioning systems

| | LiBr-H ₂ O | LiCl-H ₂ O |
|--|-----------------------|-----------------------|
| Generator Temp (°C) | 70 | 70 |
| Mass fract. weak sol (X ₆) | 54.08% | 41.07% |
| Mass fract. strong sol (X ₇) | 55.6% | 43.77% |
| Vapor Pressure (kPa) | 6.5 | 6.8 |
| Bubble pump, $\dot{Q}_{bubble\ pump}$ | 73 W | 87 W |
| Generator, \dot{Q}_{gen} | 73 W | 87 W |
| Evaporator, \dot{Q}_{eva} | 34 W | 49 W |
| Absorber, \dot{Q}_{abs} | 70 W | 78 W |
| Condenser, \dot{Q}_{cond} | 37 W | 58 W |
| COP | 0.46 | 0.56 |
| Lifting ratio, b | 58.85 | 31.48 |

For the steady-state operation of a bubble-pump-driven VARS, the strong solution flow rate is determined based on the solution flow rate required to absorb the refrigerant vapor generated by the bubble pump. Therefore, the highest liquid (strong solution) flow rate by the pump is not desired as proportionally less vapor (refrigerant) is generated at this stage. Figure 6.8 shows that the lifting ratio increases sharply as the bubble pump heat input decreases. The lower (lifting ratio) limit of these curves was determined by the conditions

in Table 6.2. Lower heat inputs give excess liquid flow (strong solution), compared to vapor (refrigerant) flow. This is reflected in Figure 6.9. It shows that the strong solution mass flow is low at low heat input whereas the refrigerant flow rate is very low. Under these conditions, the refrigeration cycle cannot operate efficiently. As the heat input increases, the strong solution flow rate increases and after reaching a maximum it decreases sharply; whereas the refrigerant flow rate increases steadily as heat input increases. Therefore, it is impractical for this refrigeration cycle to operate at low heat input at these operating conditions. Comparing the LiBr-H₂O system and the LiCl-H₂O system, it is shown that the LiCl-H₂O can operate at higher heat input values. This results in higher vapor (refrigerant) generation which effects the system performance. According to the p-T-X (pressure, temperature and concentration) relationship, the salt concentration in the LiBr-H₂O system needs to be higher to acquire the required system pressure to operate the system. The minimum required pressure can be achieved for this system at the temperature of 70°C. At the operating condition described in Table 6.1, the minimum concentration of LiBr-H₂O in solution is 54%. The corresponding strong solution concentration is 56%. At a constant heat input, the required concentration becomes stronger/higher as the temperature increases, which would result in crystallization in the bubble pump generator as well as in the absorber. In contrast, with the same operating conditions as the LiBr-H₂O system, the LiCl-H₂O requires a lower concentration of salt (41%) in the absorber and this system can operate up to a concentration of 51% before crystallization occurs. Hence, the LiCl-H₂O system can operate from 70 to 75°C, although there is little change in the COP (0.459 to 0.460) over this temperature range. As a result of the higher system pressure in the LiCl-H₂O system, a higher amount of refrigerant vapor will be produced as the heat input increases, resulting in a higher COP.

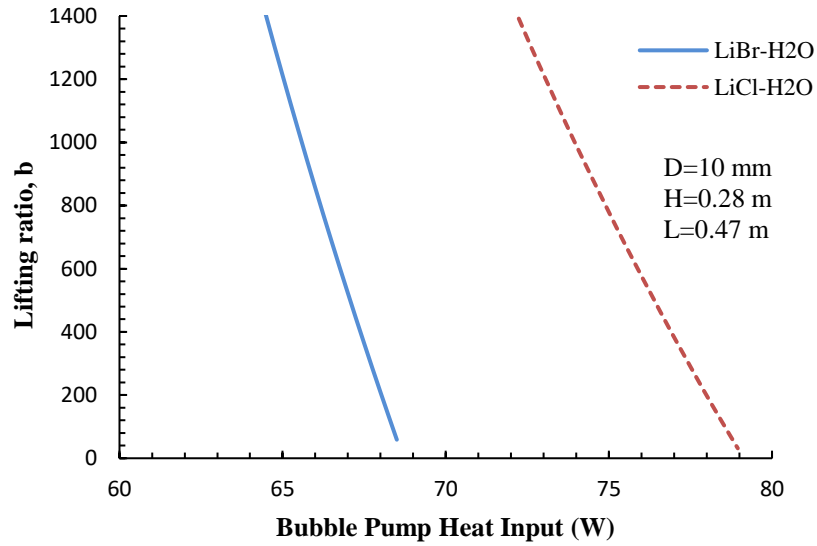


Figure 6.8: Lifting ratio of LiBr-H₂O and LiCl-H₂O VARS at different bubble pump heat input at $T_{gen} = 70^{\circ}\text{C}$.

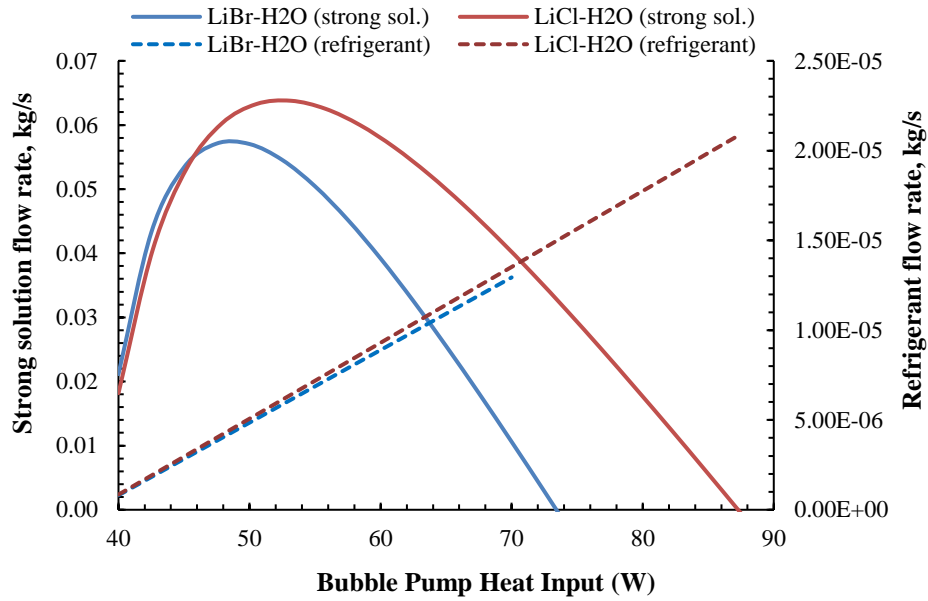


Figure 6.9: Strong solution and refrigerant flow rate by the bubble pump at different heat input at $T_{gen} = 70^{\circ}\text{C}$ for LiBr-H₂O and LiCl-H₂O.

The coefficient of performance of LiBr-H₂O and LiCl-H₂O systems is compared at different bubble pump heat inputs in Figure 6.10. The COP increases for both systems with increasing heat input but suddenly drops down at certain heat input. This is because the

refrigerant vapor generation increases in the bubble pump generator as the heat input increases and this causes the lifting of liquid solution (strong solution) by the pump. The increasing vapor flow increases the gas void fraction in the two-phase flow mixture of the bubble pump lift tube. When the gas void fraction exceeds 80%, there is a liquid film around the tube wall and the core of the tube fills with vapor [Delano, 1998]. This is called annular flow, and as a result, there is no more liquid flow. This situation is reached at heat inputs of 73.2 W and 87.3 W for LiBr-H₂O and LiCl-H₂O systems, respectively, at the operating conditions mentioned in Table 6.1. This negative effect of increasing heat input causes the COP to drop down at a certain heat input and allows for the prediction of the highest COP of the system. In order to achieve a higher COP of the system, the heat input needs to be controlled to allow the system to operate nearly at the maximum value of heat input for the churn flow regime, without exceeding it. In Figure 6.10, it is clearly seen that the COP is higher in a LiCl-H₂O system and it provides its highest performance at higher heat input compared to a LiBr-H₂O system. The highest performances for LiBr-H₂O and LiCl-H₂O systems were 0.46 at 73.2 W and 0.56 at 84.7 W, respectively.

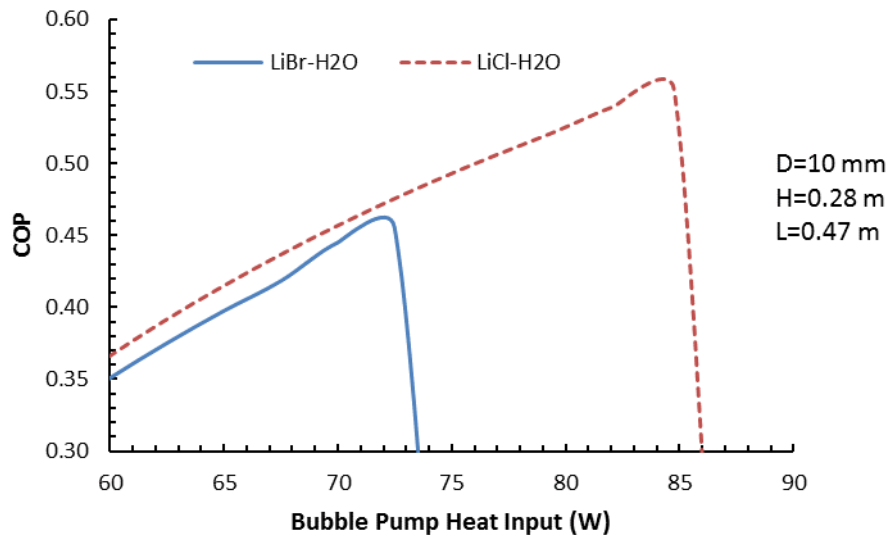


Figure 6.10: Coefficient of performance of LiBr-H₂O and LiCl-H₂O VARS at different bubble pump heat input at $T_{gen} = 70^{\circ}\text{C}$, $T_{cond} = 35^{\circ}\text{C}$, $T_{abs} = 35^{\circ}\text{C}$, $T_{eva} = 7^{\circ}\text{C}$, $\eta_{HEX} = 80$.

In this analysis, the cooling capacity of the system was determined based on the refrigerant generated by the bubble pump using a lift tube of 10 mm diameter and 0.47 m

height. In order to compare the analytical model with the experimental results, the bubble pump experimental set-up was constructed with these dimensions. For scale-up to the cooling capacity required for residential applications, such as 10 kW, a bubble-pump with multiple tubes must be incorporated. The height of the tube and the submergence ratio will be determined based on the required mass flow rate for this cooling capacity.

6.5. Conclusions

A water-based refrigerant vapor absorption refrigeration system (VARs), that can operate by a solar thermally-driven bubble pump, was analyzed in this study. In this refrigeration cycle, the pump is the key component for driving an air-conditioning system by generating the refrigerant vapor, as well as by pumping the liquid solution to absorb this refrigerant in the absorber. Therefore, the physical properties of the bubble pump were incorporated in this refrigeration cycle in order to analyze the whole cycle performance. A component-by-component thermodynamic model was developed to analyze the energy performance of the system, which lead to improving the system efficiency. The analysis was performed using two different working fluids in the bubble-pump-driven VARs. The LiCl-H₂O system operates at high efficiency due to its higher system pressure and thermophysical properties compared to the low pressure LiBr-H₂O system. The crystallization problem constrains the LiBr-H₂O system to operate at lower heat input with lower performance.

Overall, the model in this study will provide an effective tool to analyze water-based refrigerant VARs systems that can be driven by a bubble pump with solar heat input, and simulate the effect of bubble pump operation on steady-state system performance.

Acknowledgements

This work is made possible by the Natural Science and Engineering Research Council of Canada.

Nomenclature

| | | | |
|------------------|---|-------------------|---------------------------------------|
| A | area (m ²) | X | mass fraction of salt in the solution |
| b | lifting ratio | η_{HEX} | heat exchanger efficiency |
| COP | coefficient of performance | <i>Subscripts</i> | |
| D | lift tube diameter (m) | <i>abs</i> | absorber |
| g | acceleration due to gravity (m/s ²) | <i>b</i> | vapor bubble |
| h | specific enthalpy (kJ/kg) | <i>cond</i> | condenser |
| HEX | heat exchanger | <i>eva</i> | evaporator |
| H ₂ O | water | <i>g</i> | gas |
| LiBr | lithium-bromide | <i>gen</i> | generator |
| LiCl | lithium-chloride | <i>l</i> | liquid |
| \dot{m} | mass flow rate (kg/s) | <i>sol</i> | solution |
| P | pressure (kPa) | | |
| \dot{Q} | heat transfer rate (Watts) | | |
| ref | refrigerant | | |
| sol | solution | | |
| T | temperature (°C) | | |

REFERENCES

- Aman J, Ting DS-K, Henshaw P. Residential solar air conditioning: energy and exergy analyses of an ammonia-water absorption cooling system. *Applied Thermal Engineering* 62 (2014) 424-432.
- Aman, J., Henshaw, P. Ting, D. S-K., 2016, Modelling and Analysis of Bubble Pump Parameters for Vapor Absorption Refrigeration Systems, proceedings of ASHRAE Annual Conference, St. Louis, MO, USA, June 25 to 29.
- Bellos E., Tzivanidis C., Pavlovic S., Stefanovic V., Thermodynamic investigation of LiCl-H₂O working pair in a double effect absorption chiller driven by parabolic trough collectors. *Thermal Science and Engineering Progress* 3 (2017) 75–87.
- Delano A. Design Analysis of the Einstein Refrigeration Cycle, Ph.D. Thesis, Georgia Institute of Technology, 1998, http://www.me.gatech.edu/energy/andy_phd.
- EES (Engineering Equation Solver), 2015. F-Chart software, Academic Commercial V9. 941(1992-2015), www.fchart.com

- Flores V H F, Román JC, Alpírez GM, Performance analysis of different working fluids for an absorption refrigeration cycle, *American Journal of Environmental Engineering* 4(4A) (2014) 1-10, DOI: 10.5923/s.ajee.201401.01.
- Gogoi TK., Konwar D., Exergy analysis of a H₂O–LiCl absorption refrigeration system with operating temperatures estimated through inverse analysis, *Energy Conversion and Management* 110 (2016) 436–447.
- Grover GS, Eisa MAR, Holland FA. Thermodynamic design data for absorption heat pump systems operating on water-Lithium Chloride–Part one. Cooling. *Heat Recovery Syst CHP* 8 (1988) 33-41.
- Jakob U, Eicker U, Schneider D, Taki AH, Cook MJ. Simulation and experimental investigation into diffusion absorption cooling machines for air conditioning applications. *Applied Thermal Engineering* 28(2008) 1138-1150.
- Perez BH., Absorption heat pump performance for different types of solution. *Int. J. Refrigeration* 7 (1984) 115-122.
- Pfaff M., Saravanan R., Maiya MP, Srinivasa M. 1998. Studies on bubble pump for a water–lithium bromide vapor absorption refrigeration. *International Journal of Refrigeration* 21 (1998) 452–462.
- Platen, B.C. Munters, C.G., 1928. Refrigerator. U.S. Patent 1,685,764.
- Reinemann, D.J., Parlange, J.Y., Timmons, M.B., 1990. Theory of small-diameter airlift pump. *Int. J. Multiphase Flow*. 16, 113-122.
- Saravanan R., Maiya MP., Experimental analysis of a bubble pump operated H₂O–LiBr vapor absorption cooler. *Applied Thermal Engineering* 23 (2003) 2383–2397.
- Saravanan R., Maiya MP., Thermodynamic comparison of water-based working fluid combinations for a vapour absorption refrigeration system, *Applied Thermal Engineering* 18(7) (1998) 553-568.
- She X., Yin Y., Mengfei Xu M., Zhang, X., A novel low-grade heat-driven absorption refrigeration system with LiCl-H₂O and LiBr-H₂O working pairs, *International Journal of Refrigeration* 58 (2015) 219-234.
- Shelton S., Delano A., Schaefer L., Second Law Study of the Einstein Refrigeration Cycle, *Proceedings of the Renewable and Advanced Energy Systems for the 21st Century*, April 1999.

Starace G., Pascalis LD., 2012. An advanced analytical model of the diffusion absorption refrigerator cycle. *International Journal of Refrigeration*. 35, 605-612.

White, S.J. Bubble Pump Design and Performance. MSc Thesis. Georgia Institute of Technology, Atlanta, USA. Mechanical Engineering. 2001.

CHAPTER 7

ADVANCED EXERGY ANALYSIS OF A BUBBLE-PUMP-DRIVEN LiCl-H₂O ABSORPTION AIR-CONDITIONING SYSTEM

7.1. Introduction

In thermodynamic analysis, to quantify the potential of useful energy in any system, exergy analysis identifies the irreversibilities of the system component through the exergy destruction and losses. This process determines the true inefficiencies in the system and where the losses are taking place. Exergy analysis measures the actual potential of the system to improve. This analysis has been employed for many different energy conversion systems [Brjan *et al.*, 1996, Kotas, 1985, Szargut & Morris, 1988, Tsatsaronis, 1999, Aman *et al.*, 2014, Esfahani *et al.*, 2015, Fallah *et al.*, 2016].

Irreversibilities occur in all real processes due to heat transfer to the environment, caused by the finite temperature difference, chemical reaction, mass transfer from mixing substances of different composition and/or at different states, unrestrained expansion, and friction [Kelly, 2009]. The highest exergy destruction of any component of the system, and the process that causes it, can be identified by conventional exergy analysis. Based on this, the exergy destruction can be reduced by improving the efficiency within the component. However, part of the exergy destruction is due to the technical limitation of the component or design structure, which might be unavoidable. Part of it is due to the irreversibilities of the other components of the energy conversion system [Tsatsaronis *et al.*, 1999]. Therefore, the best location for improvement can be identified, not simply the component with the highest exergy destruction. This analysis can be performed through advanced exergy analysis, first introduced by Tsatsaronis *et al.* [1999]. In advanced exergy analysis, the total exergy destruction of each component is split into unavoidable and avoidable parts and also into endogenous and exogenous parts. By splitting the component's exergy destruction, this analysis provides detailed insight for thermodynamic, economic and environment system improvement [Kelly *et al.*, 2009]. Tsatsaronis *et al.* applied their advanced exergy analysis methods for analysing the vapor absorption refrigeration machine [Morosuk & Tsatsaronis, 2008], vapor compression refrigeration machine and gas-turbine power system compression [Kelly *et al.*, 2009], natural gas based co-generation

system [Morosuk & Tsatsaronis, 2011], regasification and electricity generation system [Morosuk & Tsatsaronis, 2012], and combustion process [Tsatsaronis et al., 2013]. In their analysis, they discovered the potential of each component of the system and the interactions between the components for optimizing the overall system performance. Recently, many other researchers have applied this new concept of exergy destruction analysis in order to identify real components' inefficiencies that will have the most impact on system performance [Hepbasli & Kecebas, 2013, Gungor et al., 2013, Tan & Kecebas, 2014, Anvari *et al.*, 2015, Esfahani *et al.*, 2015, Fallah *et al.*, 2016].

The authors analyzed a LiCl-H₂O vapor absorption refrigeration cycle that can be driven by solar bubble pump as described in the previous publications [Aman *et al.*, 2017]. Conventional exergy and advanced exergy analyses were applied to identifying the magnitude, location, and the source of thermodynamic inefficiencies in a bubble-pump-driven LiCl-H₂O vapor absorption refrigeration system. The conventional exergy analysis was performed for each component and the total exergy destruction of each component was divided into endogenous, exogenous, unavoidable, and avoidable exergies. A comparison of conventional and advanced exergy analysis will be performed in this present study. This information will be a useful tool for the designer to identify the component(s) that need to be improved for exergy losses.

7.2. System Description

A schematic of a bubble-pump-operated LiCl-H₂O vapor absorption refrigeration system is shown in Figure 7.1. In this absorption air-conditioning system, pure water vapor flows to the condenser (State 1) from the separator, and is condensed by releasing heat at a rate of ' \dot{Q}_{cond} ' to the atmosphere by air cooling. Then the condensed, saturated water (State 2) flows to the evaporator through the throttle valve where its pressure is reduced. The necessary cooling effect takes place in the evaporator where the refrigerant absorbs heat at a rate of ' \dot{Q}_{eva} ' (State 3). The water vapor from the evaporator (State 4) is absorbed in the absorber by the high-concentration (strong) LiCl-H₂O solution, which has returned from the bubble pump generator, and dilutes it to a low-concentration (weak) LiCl-H₂O solution. The weak solution from the absorber (State 5) flows to the bubble pump generator through the heat exchanger by gravity. In the bubble pump generator, the solution (State 6)

is heated by solar heat ($\dot{Q}_{bubble\ pump}$). When the temperature of water in the solution is higher than the saturation temperature, bubbles of water vapor start to form. Many small vapor bubbles coalesce into a big bubble and rise in the bubble pump tube, carrying the solution above it into the separator. Water vapor separates from the strong solution (State 7) in the separator and drains back to the absorber through the solution heat exchanger. The strong solution in the absorber rejects heat (\dot{Q}_{abs}) to the atmosphere and absorbs the water vapor from the evaporator.

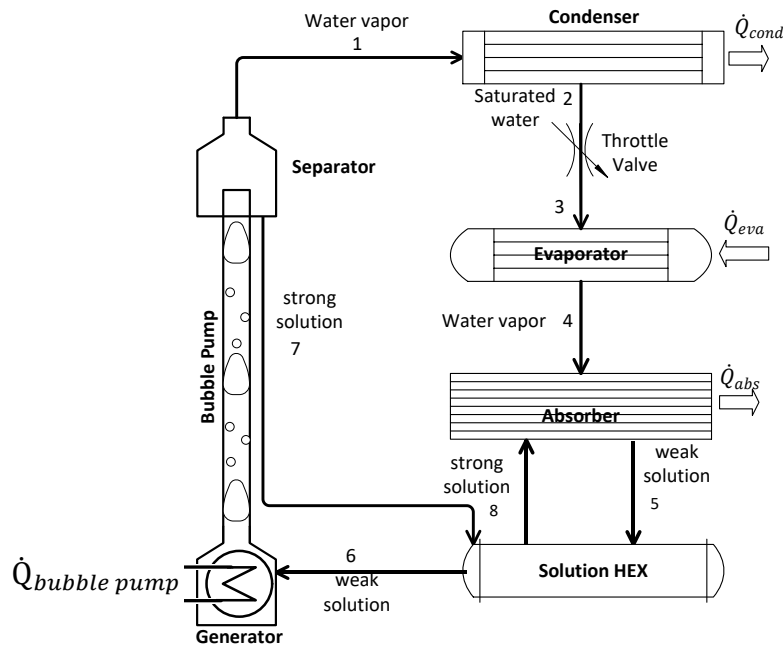


Figure 7.1: Flow diagram of a bubble pump operated vapor absorption air-conditioning system

7.3. Thermodynamic Analysis

For a thermodynamic model of a bubble-pump-operated refrigeration cycle, the principles of mass and energy conservation, and exergy balances have been applied for each component of the system. In this study, the main components: generator and bubble pump, condenser, evaporator, absorber, and solution heat exchanger have been studied. To analyze the thermodynamic cycle, a control volume was applied to each component. In this study, all analyses were performed, considering the system under steady-state conditions.

The mass flow rate of refrigerant strongly depends on the bubble pump parameters (such as lift tube diameter (D), lift tube length (L), and height (H) of the liquid in the lift tube) and the heat input rate to the bubble pump ($\dot{Q}_{bubble\ pump}$). The bubble pump consists of a lift tube connecting the generator and separator. The generated vapor bubbles rise in the tube lifting the solution ahead of it into the separator. In this analysis, the flow rate of refrigerant, the weak solution, and the strong solution of the LiCl-H₂O refrigeration cycle (as shown in Figure 7.1) are determined by using the Equations from (1) to (14) taken from Chapter 6.

7.3.1. Conventional Exergy Analysis

The mass and the energy balance of each component of the LiCl-H₂O refrigeration cycle in a control volume can be written as

$$\text{Mass Conservation:} \quad \sum \dot{m}_{in} - \sum \dot{m}_{out} = 0 \quad (1)$$

$$\text{Energy Conservation:} \quad \sum \dot{Q} = \sum \dot{m}_{out} h_{out} - \sum \dot{m}_{in} h_{in} + \dot{W} \quad (2)$$

where \dot{m} is the mass flow rate (kg/s), \dot{Q} is the rate of heat transfer rate (kW), h is the specific enthalpy (kJ/kg) and \dot{W} is the rate of work leaving the control volume (kW).

Exergy determines the maximum work potential of a system that can be produced when the system proceeds from initial state to final state in relation to the surrounding environment. The exergy balance in a control volume can be determined by [Fallah, *et al.*, 2016]

$$\dot{E}_D = \sum (\dot{m}e)_{in} - \sum (\dot{m}e)_{out} + \sum \dot{E}_{Q_{in}} - \sum \dot{E}_{Q_{out}} + \sum \dot{W} \quad (3)$$

where \dot{E}_D represents the rate of exergy destruction (loss) in the system. $(\dot{m}e)_{in}$ is the exergy entering to the control volume, $(\dot{m}e)_{out}$ is the exergy leaving the control volume, \dot{E}_Q represents the exergy destruction in terms of heat transfer, to/from the component, and \dot{W} is the mechanical work done to and from the control volume.

At any constant temperature (T),

$$\dot{E}_Q = \dot{Q} \left(1 - \frac{T_o}{T}\right) \quad (4)$$

The overall exergy can be expressed by the thermomechanical exergy and the chemical exergy. The thermomechanical exergy represents the system that can produce maximum amount of work when the system is thermally and mechanically in equilibrium with the surrounding environment. When the system temperature and pressure change with the environmental temperature and pressure, the thermomechanical exergy can be attained [Esfahani *et al.*, 2015]. In this analysis, the chemical exergy is assumed to be zero as the chemical composition of the cycle is not changing with the environmental conditions [Vidal *et al.*, 2006]. Therefore, the overall exergy per unit mass of a fluid stream can be calculated by [Zhu & Gu, 2010]

$$e = (h - h_o) - T_o(s - s_o) \quad (5)$$

where e is the specific exergy, h is the enthalpy and s is the entropy at a given temperature T , and h_o is the enthalpy and s_o is the entropy at the environmental temperature T_o . In this analysis, the reference temperature and pressure are considered $T_o = 273.15$ K and $P_o = 101.325$ kPa, respectively. The specific exergy, specific enthalpy and entropy of LiCl-H₂O solution at a given temperature and pressure are calculated by using EES software [EES, 2017].

In conventional exergy analysis, the exergy destruction [Aman *et al.*, 2014] and the exergy destruction ratio [Morosuk & Tsatsaronis, 2011] can be written as

$$\dot{E}_{D,k} = (\dot{E}_k)_{in} - (\dot{E}_k)_{out} \quad (6)$$

$$y_k = \frac{\dot{E}_{D,k}}{\dot{E}_{D,total}} \quad (7)$$

In Equation (6) & (7), $\dot{E}_{D,k}$ is the exergy destruction rate of k component, $(\dot{E}_k)_{in}$ and $(\dot{E}_k)_{out}$ are the exergy entering/leaving to/from the k component, y_k is the exergy destruction ratio of the k component over the total exergy destruction of the system. The exergy destruction ratio is a useful parameter to compare the efficiency of each component

of the system. It provides the thermodynamic inefficiency of each component of the system [Anvari *et al.*, 2015].

The energy and the exergy balance of each component of the LiCl-H₂O absorption refrigeration system is shown in Table 7.1.

Table 7.1: Energy and the exergy balance equations of the LiCl-H₂O absorption refrigeration cycle

| Cycle Components | Energy balance equation | Exergy balance equation |
|------------------|---|--|
| Generator | $\dot{Q}_{gen} = \dot{m}_1 h_1 + \dot{m}_7 h_7 - \dot{m}_6 h_6$ $X_6 \dot{m}_6 = X_7 \dot{m}_7$ | $\dot{E}_{D,gen} = \dot{m}_6 e_6 - \dot{m}_1 e_1 - \dot{m}_7 e_7 + \dot{Q}_{gen} \left(1 - \frac{T_o}{T_{gen}}\right)$ |
| Condenser | $\dot{Q}_{con} = \dot{m}_1 (h_1 - h_2)$ | $\dot{E}_{D,con} = \dot{m}_1 (e_1 - e_2) - \dot{Q}_{con} \left(1 - \frac{T_o}{T_{con}}\right)$ |
| Evaporator | $\dot{Q}_{eva} = \dot{m}_4 h_4 - \dot{m}_3 h_3$ | $\dot{E}_{D,eva} = \dot{m}_1 (e_3 - e_4) + \dot{Q}_{eva} \left(1 - \frac{T_o}{T_{eva}}\right)$ |
| Absorber | $\dot{Q}_{abs} = \dot{m}_8 h_8 + \dot{m}_4 h_4 - \dot{m}_5 h_5$ | $\dot{E}_{D,abs} = \dot{m}_4 e_4 + \dot{m}_8 e_8 - \dot{m}_5 e_5 - \dot{Q}_{abs} \left(1 - \frac{T_o}{T_{abs}}\right)$ |
| Solution HEX | $T_6 = \frac{\dot{m}_7}{\dot{m}_5} \eta_{HEX} T_7 + \left(1 - \frac{\dot{m}_7}{\dot{m}_5} \eta_{HEX}\right) T_5$ $h_8 = h_7 - \frac{\dot{m}_5}{\dot{m}_7} (h_6 - h_5)$ | $\dot{E}_{D,HEX} = \dot{m}_7 e_7 + \dot{m}_5 e_5 - \dot{m}_8 e_8 - \dot{m}_6 e_6$ |
| | | $\dot{E}_{D,total} = \dot{E}_{D,gen} + \dot{E}_{D,con} + \dot{E}_{D,eva} + \dot{E}_{D,abs}$ |

X is the LiCl mass fraction in solution
 η_{HEX} is the heat exchanger efficiency

7.3.2. Advanced Exergy Analysis

Advanced exergy analysis offers more detailed information than the conventional exergy analysis. The exergy destruction of each component can be split into endogenous/exogenous and unavoidable/avoidable exergy destruction parts [Morosuk & Tsatsaronis, 2008]. Dividing exergy destruction of a component into endogenous and exogenous parts provides the actual exergy destruction caused by the component itself and the exergy destruction of that component caused by the remaining components of the system. As a result, it will provide the information as to whether the focus to improve the system performance should be in the component itself or on the remaining components of the system. Alternatively, when the component operates at actual (real) and theoretical conditions, dividing the exergy destruction into unavoidable and avoidable parts

determines the difference of the exergy destruction. Table 7.2 shows the different operating conditions that were applied for this advanced exergy analysis. This will provide the realistic potential of each component in order to improve the thermodynamic efficiency. Furthermore, the endogenous and exogeneous exergies can be subdivided into unavoidable and avoidable subdivisions. Combining these exergy destruction calculations helps to identify the component that has greatest possible influence on the system performance and the amount of improvement that can be made on the component [Kecebas & Hepbasli, 2014, Petrakopoulou *et al.*, 2012].

Table 7.2: The algorithm and the assumption of parameters considering for different operating conditions of a LiCl-H₂O absorption refrigeration cycle

| Cycle Components | Algorithm* | Ideal cycle | Real cycle* | Unavoidable cycle* |
|------------------------|--|--|--|--|
| Generator | $P_{gen} = P_{cond}(1 - \Delta P_{gen})$ $T_{gen} = (T_{gen} - \Delta T_{gen})$ | $\Delta P_{gen} = 0$ $\Delta T_{gen} = 0$ | $\Delta P_{gen} = 2\%$ $\Delta T_{gen} = 5\text{ }^\circ\text{C}$ | $\Delta P_{gen} = 0.2\%$ $\Delta T_{gen} = 0.5\text{ }^\circ\text{C}$ |
| Condenser | $T_{cond} = (T_{cond} + \Delta T_{cond})$ $T_{cond} \rightarrow P_{cond}$ | $\Delta T_{cond} = 0$ | $\Delta T_{cond} = 5\text{ }^\circ\text{C}$ | $\Delta T_{cond} = 0.5\text{ }^\circ\text{C}$ |
| Evaporator | $T_{eva} = T_{eva} + \Delta T_{eva}$ $T_{eva} \rightarrow P_{eva}$ | $\Delta T_{eva} = 0$ | $\Delta T_{eva} = 2\text{ }^\circ\text{C}$ | $\Delta T_{eva} = 0.2\text{ }^\circ\text{C}$ |
| Absorber | $T_{abs} = T_{abs} + \Delta T_{abs}$ $P_{abs} = P_{eva}(1 - \Delta P_{abs})$ | $\Delta T_{abs} = 0$ $\Delta P_{abs} = 0$ | $\Delta T_{abs} = 5\text{ }^\circ\text{C}$ $\Delta P_{abs} = 2\%$ | $\Delta T_{abs} = 0.5\text{ }^\circ\text{C}$ $\Delta P_{abs} = 0.2\%$ |
| Solution HEX | $\Delta T_{HEX} = T_7 - T_6$ | $\Delta T_{HEX} = 0$ $\eta_{HEX} = 90\%$ | $\Delta T_{HEX} = 5\text{ }^\circ\text{C}$ $\eta_{HEX} = 80\%$ | $\Delta T_{HEX} = 0.5\text{ }^\circ\text{C}$ $\eta_{HEX} = 88\%$ |
| Solution concentration | $X_{strong} = \varphi(T_{gen}, P_{gen})$ | | | |

*[Morosuk & Tsatsaronis, 2008]

Endogenous/Exogenous Exergy Destruction

The total exergy destruction ($E_{D,k}^{real}$) of a component (k) can be divided into endogenous ($E_{D,k}^{EN}$) and exogenous ($E_{D,k}^{EX}$) parts and can be written as [Kelly *et al.*, 2009].

$$\dot{E}_{D,k}^{real} = \dot{E}_{D,k}^{EN} + \dot{E}_{D,k}^{EX} \quad (8)$$

The endogenous exergy destruction of a component is associated with the internal irreversibilities of that component only when the other components are without

irreversibilities. This can be determined by considering the case where this component will work on real operating conditions while the other components of the system will work in an ideal (theoretical) operating conditions. Therefore, the exogenous exergy destruction is only due to the inefficiency of the k component. The remaining exergy destruction is the endogenous exergy destruction in that component. This exergy destruction represents the inefficiency of the k component and the inefficiencies of the remaining components of the system.

Unavoidable/Avoidable Exergy Destruction

In real operating conditions, every component of a system works with some limitations such as technical and design limitations including material availability or cost of the materials etc. Therefore, some part of the total exergy destruction of a component cannot be reduced. This is called the unavoidable exergy destruction ($E_{D,k}^{UN}$). The rest of the total exergy destruction of the component is avoidable ($E_{D,k}^{AV}$) which is represented by Equation (9). The unavoidable exergy destruction of a component is calculated assuming that the component is isolated from the system. The most reasonable operating conditions for calculating the unavoidable exergy destruction are the lowest temperature difference and the pressure losses [Morosuk & Tsatsaronis, 2008, Petrakopoulou *et al.*, 2012]. The unavoidable conditions are determined based on the maximum improvement that can be achieved for the component.

$$\dot{E}_{D,k}^{real} = \dot{E}_{D,k}^{UN} + \dot{E}_{D,k}^{AV} \quad (9)$$

Combination of two Dimension of Exergy Destruction

The unavoidable exergy destruction of a component can be split again into endogenous unavoidable exergy destruction and exogenous unavoidable exergy destruction of that component. The endogenous unavoidable parts of a component cannot be reduced any further due to the technical limitations of that component. The endogenous unavoidable exergy destruction of a component can be determined by considering only that component working under unavoidable operating conditions while the remaining components of the system work in ideal conditions without irreversibilities.

The exogenous unavoidable parts of a component cannot be reduced any more due to the technical limitations of the other components of the system for a given design and structure [Morosuk & Tsatsaronis, 2008]. For a component, it can be determined by subtracting the endogenous unavoidable exergy destruction from the total unavoidable exergy destruction of that component and is defined by

$$\dot{E}_{D,k}^{UN} = \dot{E}_{D,k}^{EN-UN} + \dot{E}_{D,k}^{EX-UN} \quad (10)$$

The endogenous avoidable part of the exergy destruction of a component can be reduced by improving the efficiency of that component. It can be calculated by subtracting the endogenous unavoidable exergy destruction from the total endogenous exergy destruction of the component and can be determined by

$$\dot{E}_{D,k}^{EN} = \dot{E}_{D,k}^{EN-UN} + \dot{E}_{D,k}^{EN-AV} \quad (11)$$

Likewise, the exogenous avoidable exergy destruction of a component can be reduced by the improving the design and structure of the overall system and also by improving the efficiency the remaining components of the system. It can be determined by subtracting the unavoidable exergy destruction from the total exogenous exergy destruction of the component and is defined by

$$\dot{E}_{D,k}^{EX} = \dot{E}_{D,k}^{EX-UN} + \dot{E}_{D,k}^{EX-AV} \quad (12)$$

Therefore, the effect of the exergy destruction of each component on the overall system performance can be determined through this advanced exergy analysis. The total exergy destruction of a component is

$$\dot{E}_{D,k}^{real} = \dot{E}_{D,k}^{EN-UN} + \dot{E}_{D,k}^{EN-AV} + \dot{E}_{D,k}^{EX-UN} + \dot{E}_{D,k}^{EX-AV} \quad (13)$$

7.4. Theoretical Considerations

The following assumption have been used for analyzing the thermodynamic cycle in this study:

1. The system is operating under steady state conditions.

2. LiCl-H₂O solutions are assumed to be in equilibrium in the bubble pump generator and in the absorber at their corresponding pressures and temperatures.
3. The throttle valve is a constant enthalpy process under adiabatic condition.
4. The vapor leaving the bubble pump generator is 100% water vapor.
5. The refrigerant leaving the condenser is saturated water and leaving the evaporator is water vapor.
6. The air cooling is considered for cooling of the condenser and the absorber at an atmospheric temperature of 25°C.

7.5. Results and Analysis

In this analysis, the system was considered using a bubble-pump with a 0.47 m long lift tube of 10 mm of diameter. The cooling effect was determined by the refrigerant flow rate by the bubble pump with a heat input of 85 W in ideal operating conditions, to correspond to bubble pump data from Chapters 5 and 6. However, a residential air-conditioning system needs to absorb about 10 kW in its evaporator. To scale-up the system for residential applications, a bubble-pump with multiple tubes is required for the necessary cooling effect.

The thermodynamic values of different states of a bubble-pump-driven LiCl-H₂O refrigeration cycle obtained from conventional exergy analysis under ideal (theoretical), real and unavoidable operating conditions have been shown in Table 7.3 – 7.5. The exergy destruction ($E_{D,k}$) and exergy destruction ratio ($y_{D,k}$) of each component under these operating conditions is shown in Table 7.6. Table 7.6 shows that the highest exergy destruction is in the absorber followed by the generator and the condenser. The evaporator and the solution heat exchange have lower values under all operating conditions. These losses are due to high irreversibilities occurring in the absorber and the generator. This is because of the high temperature difference across the heat exchanger in the absorber, mass transfer between the two differently concentrated solutions and the mixing losses in the absorber and the generator [May *et al.*, 2011]. Furthermore, the refrigerant (water) vapor is superheated when it leaves from the generator/separator. As a result, a higher temperature is required under the same operating conditions, and this leads to higher

thermodynamic losses in the generator. In addition, the condenser requires more cooling in order to cool the superheated water vapor that comes from the generator and this generates more exergy destruction in the condenser. This conventional exergy analysis suggests that the exergy loss in the absorber needs to be reduced first to improve the overall system efficiency. In fact, the irreversibilities of the other components in the system are partly responsible for the generator and condenser exergy destructions, and the extent of responsibility can be determined by advanced exergy analysis.

Table 7.3: Thermodynamic properties at different states in LiCl-H₂O absorption cycles under ideal operating conditions $T_{gen} = 75^{\circ}\text{C}$, $T_{cond} = 35^{\circ}\text{C}$, $T_{abs} = 35^{\circ}\text{C}$, $T_{eva} = 7^{\circ}\text{C}$, $\eta_{HEX} = 90$, $D=10$ mm, $H=0.3$ m, $L=0.5$ m and $\dot{Q}_{BP}= 85$ W.

| State | Temperature (°C) | Pressure (kPa) | Mass flow (g/s) | % Concentration | Enthalpy (kJ/kg) | Entropy (kJ/kg.K) | Exergy, e (kJ/kg) |
|---------------------------------------|---------------------|-------------------|--------------------|--------------------|---------------------|----------------------|----------------------|
| Bubble pump generator ref exit (1) | 75 | 5.627 | 0.02 | 100 | 2640 | 8.5 | 111.7 |
| Condenser ref exit (2) | 35 | 5.627 | 0.02 | 100 | 147 | 0.51 | 0.59 |
| Evaporator ref inlet (3) | 7 | 1.002 | 0.02 | 100 | 147 | 0.51 | 0.59 |
| Evaporator ref exit (4) | 7 | 1.002 | 0.02 | 100 | 2513 | 8.97 | -157.3 |
| Absorber sol exit (5) | 35 | 1.002 | 0.152 | 41.07 | 156 | 0.31 | -51.58 |
| Sol HEX exit (6) | 71 | 1.002 | 0.152 | 41.07 | 250 | 0.60 | 75.42 |
| Sol HEX inlet (7) | 75 | 1.002 | 0.133 | 47.23 | 301 | 0.21 | 128.3 |
| Absorber sol inlet (8) | 47 | 1.002 | 0.133 | 47.23 | 241 | 0.41 | 77.46 |

ref = refrigerant;
sol = solution

Table 7.4: Thermodynamic properties at different states in LiCl-H₂O absorption cycles under real operating conditions $T_{gen} = 70^{\circ}\text{C}$, $T_{cond} = 40^{\circ}\text{C}$, $T_{abs} = 40^{\circ}\text{C}$, $T_{eva} = 9^{\circ}\text{C}$, $\eta_{HEX} = 80\%$, $D=10$ mm, $H=0.3$ m, $L=0.5$ m and $\dot{Q}_{BP}= 80$ W.

| State | Temperature (°C) | Pressure (kPa) | Mass flow (g/s) | % Concentration | Enthalpy (kJ/kg) | Entropy (kJ/kg.K) | Exergy, e (kJ/kg) |
|---------------------------------------|---------------------|-------------------|--------------------|--------------------|---------------------|----------------------|----------------------|
| Bubble pump generator ref exit (1) | 70 | 6.5 | 0.023 | 100 | 2630 | 8.5 | 104.4 |
| Condenser ref exit (2) | 40 | 7.38 | 0.023 | 100 | 167.5 | 0.57 | 1.43 |
| Evaporator ref inlet (3) | 9 | 1.17 | 0.023 | 100 | 167.5 | 0.57 | 1.43 |
| Evaporator ref exit (4) | 9 | 1.17 | 0.023 | 100 | 2517 | 8.92 | -138.8 |
| Absorber sol exit (5) | 40 | 1.17 | 0.32 | 39.86 | 181.6 | 0.35 | -24.8 |
| Sol HEX exit (6) | 64 | 1.17 | 0.32 | 39.86 | 243.8 | 0.54 | 87.87 |
| Sol HEX inlet (7) | 70 | 1.17 | 0.297 | 42.95 | 240 | 0.60 | 66.16 |
| Absorber sol inlet (8) | 44 | 1.17 | 0.297 | 42.95 | 301.5 | 0.79 | 28.09 |

ref = refrigerant;
sol = solution

In advanced exergy analysis, the exergy destruction of each component is split into four parts. The results of this analysis are shown in Table 7.7. The detailed calculations for this analysis are described below.

Generator:

For calculating endogenous exergy destruction for the generator ($E_{D,gen}^{EN}$), it was assumed that the generator works with irreversibilities (under real operating conditions) while other components operates without irreversibilities (under ideal operating conditions). The operating conditions were $T_{gen} = 70^{\circ}\text{C}$, $P_{gen} = 6.5 \text{ kPa}$, $T_{cond} = 35^{\circ}\text{C}$, $T_{abs} = 35^{\circ}\text{C}$, $T_{eva} = 7^{\circ}\text{C}$, $\eta_{HEX} = 90$, $D=10 \text{ mm}$, $H=0.3 \text{ m}$, $L=0.5 \text{ m}$ and $\dot{Q}_{BP} = 85 \text{ W}$. For calculating the unavoidable exergy destruction for the generator ($E_{D,gen}^{EN-UN}$), the operating conditions were $T_{gen} = 74.5^{\circ}\text{C}$, $P_{gen} = 6.77 \text{ kPa}$, $T_{cond} = 35^{\circ}\text{C}$, $T_{abs} = 35^{\circ}\text{C}$, $T_{eva} = 7^{\circ}\text{C}$, $\eta_{HEX} = 90$, $D=10 \text{ mm}$, $H=0.3 \text{ m}$, $L=0.5 \text{ m}$ and $\dot{Q}_{BP} = 85 \text{ W}$. Equations (9) to (12) were used to calculate other parts of the exergy destructions and the results are shown in Table 7.7.

Table 7.5: Thermodynamic properties at different states in LiCl-H₂O absorption cycles under unavoidable operating conditions $T_{gen} = 74.5^{\circ}\text{C}$, $T_{cond} = 35.5^{\circ}\text{C}$, $T_{abs} = 35.5^{\circ}\text{C}$, $T_{eva} = 7.2^{\circ}\text{C}$, $\eta_{HEX} = 88\%$, $D=10 \text{ mm}$, $H=0.3 \text{ m}$, $L=0.5 \text{ m}$ and $\dot{Q}_{BP} = 84 \text{ W}$.

| State | Temperature (°C) | Pressure (kPa) | Mass flow (g/s) | % Concentration | Enthalpy (kJ/kg) | Entropy (kJ/kg.K) | Exergy, e (kJ/kg) |
|--------------------------|---------------------|-------------------|--------------------|--------------------|---------------------|----------------------|----------------------|
| Bubble pump generator | | | | | | | |
| ref exit (1) | 74.5 | 6.77 | 0.02 | 100 | 2639 | 8.5 | 11.1 |
| Condenser ref exit (2) | 35.5 | 5.78 | 0.02 | 100 | 148.7 | 0.512 | 0.66 |
| Evaporator ref inlet (3) | 7.2 | 1.02 | 0.02 | 100 | 148.7 | 0.512 | 0.66 |
| Evaporator ref exit (4) | 7.2 | 1.02 | 0.02 | 100 | 2514 | 8.97 | -155.5 |
| Absorber sol exit (5) | 35.5 | 1.02 | 0.177 | 41.25 | 157.5 | 0.31 | -43.41 |
| Sol HEX exit (6) | 69.82 | 1.02 | 0.177 | 41.25 | 247.8 | 0.59 | 76.45 |
| Sol HEX inlet (7) | 74.5 | 1.02 | 0.157 | 46.50 | 295.8 | 0.60 | 121.5 |
| Absorber sol inlet (8) | 45 | 1.02 | 0.157 | 46.50 | 236.5 | 0.42 | 71.09 |

ref = refrigerant;
sol = solution

Table 7.6: Results of conventional exergy analysis of a LiCl-H₂O absorption refrigeration cycle under different operating conditions

| Cycle Components | Ideal | | Real | | Unavoidable | |
|------------------|------------------|------------------|------------------|------------------|------------------|------------------|
| | $E_{D,k}$ (W) | $y_{D,k}$ (%) | $E_{D,k}$ (W) | $y_{D,k}$ (%) | $E_{D,k}$ (W) | $y_{D,k}$ (%) |
| Generator | 36 | 19.5 | 84 | 27.2 | 38.2 | 19.9 |
| Condenser | 35 | 19.07 | 39 | 12.6 | 35.4 | 18.4 |
| Evaporator | 28 | 15.27 | 32 | 10.4 | 28.3 | 14.7 |
| Absorber | 78 | 42.13 | 143 | 46.3 | 83 | 43.3 |
| Solution HEX | 7 | 4 | 11 | 3.6 | 7 | 3.6 |

Condenser:

For calculating endogenous ($\dot{E}_{D,cond}^{EN}$), and endogenous unavoidable ($\dot{E}_{D,cond}^{EN-UN}$) exergy destruction for the condenser, it was assumed that only the condenser works with irreversibilities (under real operating conditions) while other components are without irreversibilities (under ideal operating conditions). The operating conditions were $T_{cond} = 40^{\circ}\text{C}$ and $T_{cond} = 35.5^{\circ}\text{C}$ and $T_{cond} = P_{cond}$, respectively while the other components worked under theoretical conditions.

Evaporator:

The evaporator was assumed to operate under real conditions, while the other components of the absorption system operate under theoretical conditions. The operating conditions for the evaporator endogenous ($\dot{E}_{D,eva}^{EN}$) and endogenous unavoidable ($\dot{E}_{D,eva}^{EN-UN}$) exergy destructions were $T_{eva} = 9^{\circ}\text{C}$ and $T_{eva} = 7.2^{\circ}\text{C}$ and $T_{eva} = P_{eva}$, respectively.

Absorber:

The endogenous ($\dot{E}_{D,abs}^{EN}$) exergy destruction was calculated when the absorber operates at $T_{abs} = 40^{\circ}\text{C}$ and $P_{abs} = 1.022$ kPa, while other components were at the theoretical condition. The absorber endogenous unavoidable ($\dot{E}_{D,abs}^{EN-UN}$) operating conditions were $T_{abs} = 35.5^{\circ}\text{C}$ and $P_{abs} = 1.004$ kPa.

Table 7.7: Results of advanced exergy analysis of a LiCl-H₂O absorption refrigeration cycle

| Components | $E_{D,k}^{real}$ (W) | $E_{D,k}^{EN}$ (W) | $E_{D,k}^{EX}$ (W) | $E_{D,k}^{UN}$ (W) | $E_{D,k}^{AV}$ (W) | UN | | AV | |
|--------------|-------------------------|-----------------------|-----------------------|-----------------------|-----------------------|--------------------------|--------------------------|--------------------------|--------------------------|
| | | | | | | $E_{D,k}^{EN-UN}$ (W) | $E_{D,k}^{EX-UN}$ (W) | $E_{D,k}^{EN-AV}$ (W) | $E_{D,k}^{EX-AV}$ (W) |
| Generator | 84 | 66 | 18 | 38 | 46 | 37 | 1 | 29 | 17 |
| | | 79% | 21% | 45% | 55% | 44% | 1% | 35% | 20% |
| Condenser | 39 | 37 | 2 | 35.4 | 3.6 | 34 | 1.4 | 3 | 0.6 |
| | | 95% | 5% | 91% | 9% | 87% | 4% | 8% | 2% |
| Evaporator | 32 | 29 | 3 | 28.3 | 3.7 | 27 | 1.3 | 2 | 1.7 |
| | | 91% | 9% | 88% | 12% | 84% | 4% | 6% | 5% |
| Absorber | 143 | 109 | 34 | 83 | 60 | 81 | 2 | 28 | 32 |
| | | 76% | 24% | 58% | 42% | 57% | 1% | 20% | 22% |
| Solution HEX | 11 | 7.5 | 3.5 | 7 | 4 | 6.8 | 0.2 | 0.7 | 3.3 |
| | | 68% | 32% | 64% | 36% | 62% | 2% | 6% | 30% |
| Total | 309 | 249 | 61 | 192 | 117 | 186 | 6 | 63 | 55 |
| | | 80% | 20% | 62% | 38% | 60% | 2% | 20% | 18% |

Solution Heat Exchanger:

The operating conditions for solution heat exchanger (HEX) were considered as $T_7 - T_6 = 5^\circ\text{C}$ and $\eta_{HEX} = 80\%$ for the endogenous ($\dot{E}_{D,HEX}^{EN}$) exergy destruction and $T_7 - T_6 = 0.5^\circ\text{C}$ and $\eta_{HEX} = 88\%$ for endogenous unavoidable ($\dot{E}_{D,HEX}^{EN-UN}$) exergy destruction. All other components were at theoretical conditions.

It can be found from Table 7.7 that in a bubble-pump-driven LiCl-H₂O absorption refrigeration system, the endogenous exergy destruction ($\dot{E}_{D,k}^{EN}$) for all components were higher than the exogenous exergy destruction ($\dot{E}_{D,k}^{EX}$). This demonstrates that the internal irreversibility of the component itself need to be reduced. Therefore, in order to improve the overall system efficiency, the components themselves should be examined on for their design and performance improvement. It is comparable that the percentage of exogenous exergy destruction rate of the solution heat exchanger (32%), the generator (21%) and the absorber (24%) are comparatively higher that of the condenser (5%) and the evaporator

(9%). Therefore, the other components' efficiency improvement will impact to reduce the exergy destruction rate of the solution heat exchanger, the generator, and the absorber.

It is also noted from Table 7.7 that the total unavoidable exergy destruction ($\dot{E}_{D,total}^{UN}$) of the system is 192 W which is 62% of the total exergy destruction rate. While $\dot{E}_{D,total}^{UN} = 186$ W (60%) is due to the components themselves. Therefore, the minimum exergy destruction rate of the system is 192 W and cannot be reduced furthermore. In practice, only the avoidable part of the total exergy destruction can be reduced. It is noticed that the avoidable part of the exergy destruction is lower than the unavoidable part and only 38% (117 W) of the total exergy destruction rate ($\dot{E}_{D,total}^{real} = 309$ W) can be reduced by improving the components efficiencies. Referring to the Table 7.7, it is observed that for improvement of the system performance, the first priority should be to the generator among all other components as it has $\dot{E}_{D,gen}^{EN-AV} > \dot{E}_{D,gen}^{EX-AV}$. It indicates that the improvement of the generator efficiency is more important than improving the other component efficiencies in order to reduce the overall exergy destruction. It also provides the insight that improving the generator efficiency will have impact on other component's exergy destruction reduction for components which have the exogenous avoidable is higher than the endogenous avoidable exergy destruction such as the absorber and solution heat exchanger.

The value of $\dot{E}_{D,abs}^{EN-AV}$ in Table 7.7 indicates that after the generator, the second most inefficient component is the absorber. The endogenous avoidable exergy destruction (28 W) in the absorber is lower than the exogenous exergy destruction (32 W). This indicates that the exergy destruction of the absorber can be reduced by improving the other components' efficiencies. From the table, it can be seen that the potential of improvement of the condenser is low as most of the exergy destruction (34 W or 87%) is unavoidable because of the condenser's own internal irreversibilities. Only 8% of the total exergy destruction of the condenser can be reduced by using the technological improvement. Other components' irreversibility affects on the condenser are very little, since only a 2% improvement can be achieved by reducing the exergy destruction of the other components. For the evaporator, it is observed that the exogenous is much smaller than endogenous exergy destruction, $\dot{E}_{D,eva}^{EN} \gg \dot{E}_{D,eva}^{EX}$. However, 84% of the total endogenous exergy destruction is unavoidable, only 6% of the exergy destruction can be reduced by improving the evaporator performance and 5% will be improved by improving the other components.

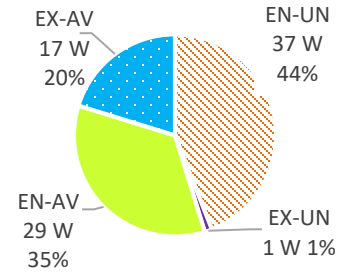
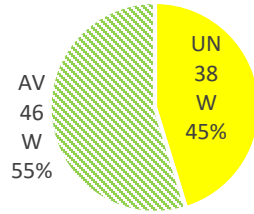
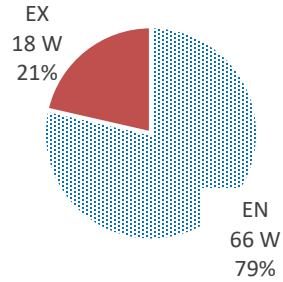
It also can be seen from Table 7.7 that the exogenous avoidable is higher than the endogenous avoidable exergy destruction ($\dot{E}_{D,HEX}^{EX-AV} > \dot{E}_{D,HEX}^{EN-AV}$) in the solution heat exchanger. Therefore, the improvement of the efficiencies of other components plays a significant role in enhancing the efficiency of the solution heat exchanger.

In advanced exergy analysis, the division of the exergy destruction of each component into the endogenous, exogenous, unavoidable, avoidable, endogenous-unavoidable, exogenous-unavoidable, endogenous-avoidable, exogenous-avoidable exergy destruction of each component of a bubble-pump-driven LiCl-H₂O absorption refrigeration system are illustrated in Figure 7.2. In order to evaluate the overall system performance, the available exergy destruction is the focus as this has the potential for improvement. The endogenous exergy destruction of the overall system is 80% with 20% avoidable and 18% is the exogenous avoidable, as shown in Figure 7.3. These results show the interaction between the components and determines the influence of reducing the internal irreversibilities of each component. In this analysis, the higher unavoidable exergy destruction governs the necessity of the improvement of the component for optimizing the system efficiency.

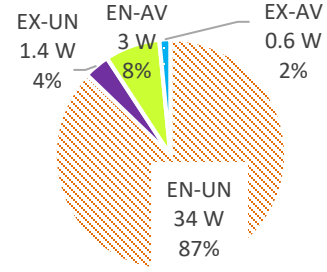
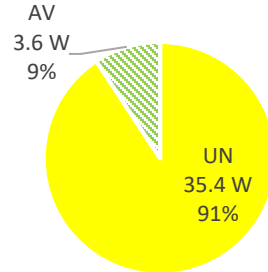
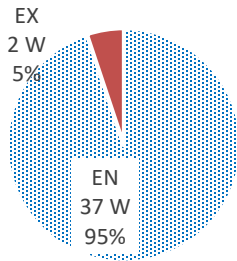
Furthermore, based on the conventional and advanced exergy analysis, the influence of each component on the overall exergy destruction is demonstrated in Figure 7.4. Conventional exergy analysis concludes that the highest potential for improvement is in the absorber, prior to the generator, in order to improve the overall system performance. However, the advanced exergy analysis suggests that while 58% (83 W) of the total exergy destruction in the absorber is unavoidable, the generator is the most influential component on the overall system performance. 35% (29 W) of the generator total exergy destruction can be reduced by technical modification or technological improvement where as 22% (32 W) of the absorber exergy destruction will be reduced by improving the other components. The advanced exergy analysis also proposes that the condenser, evaporator and the solution heat exchanger does not require any improvement while the conventional exergy analysis shows a considerable amount of exergy destruction rate in these components. Actually, among these components, 38% of the exergy destruction rate can be reduced through improving the efficiency of the components and most of the remaining parts are

unavoidable and a portion (20%) are designated to improve in the overall system performance.

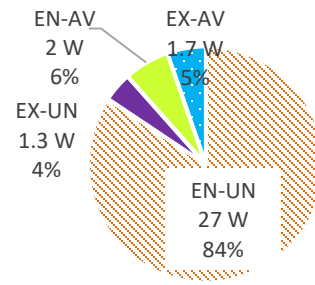
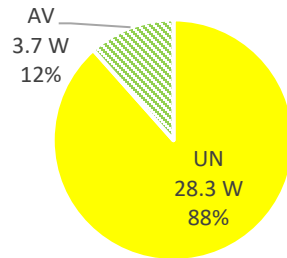
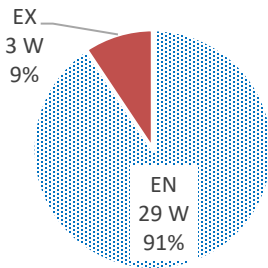
Generator



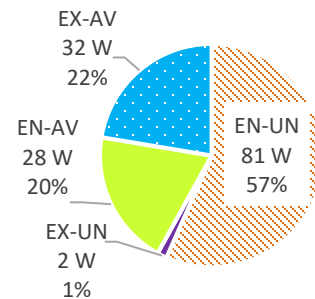
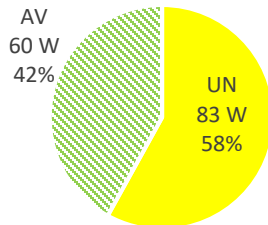
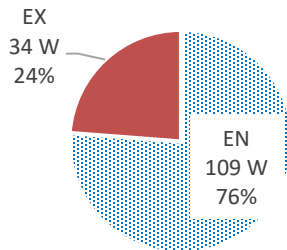
Condenser



Evaporator



Absorber



Solution Heat Exchanger

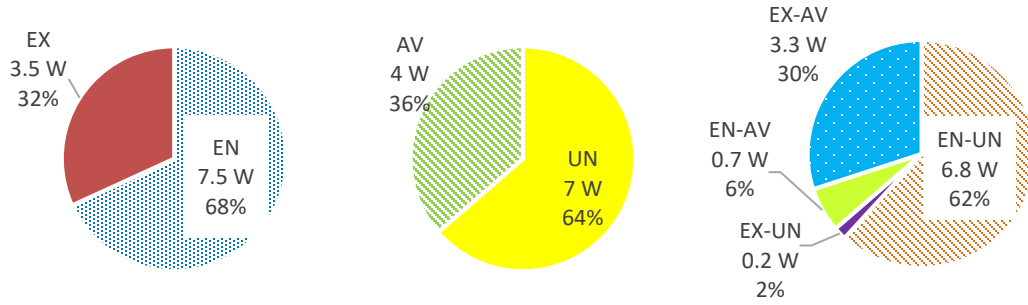


Figure 7.2: The total exergy destruction split into the endogenous, exogenous, unavoidable, avoidable, endogenous-unavoidable, exogenous-unavoidable, endogenous-avoidable, and exogenous-avoidable divisions for each component.

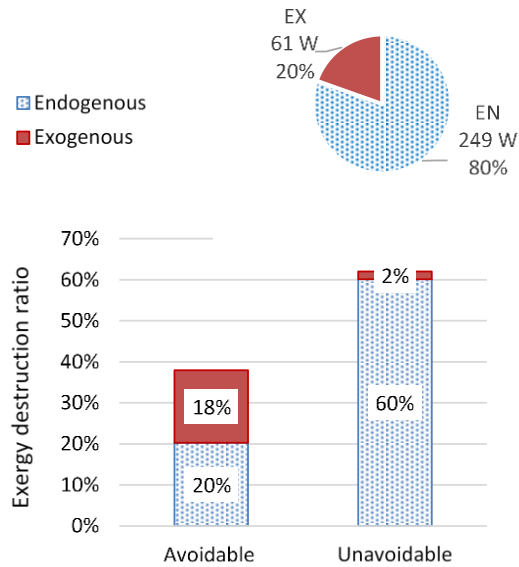


Figure 7.3: Exergy destruction ratio of the overall system based on advanced exergy analysis.

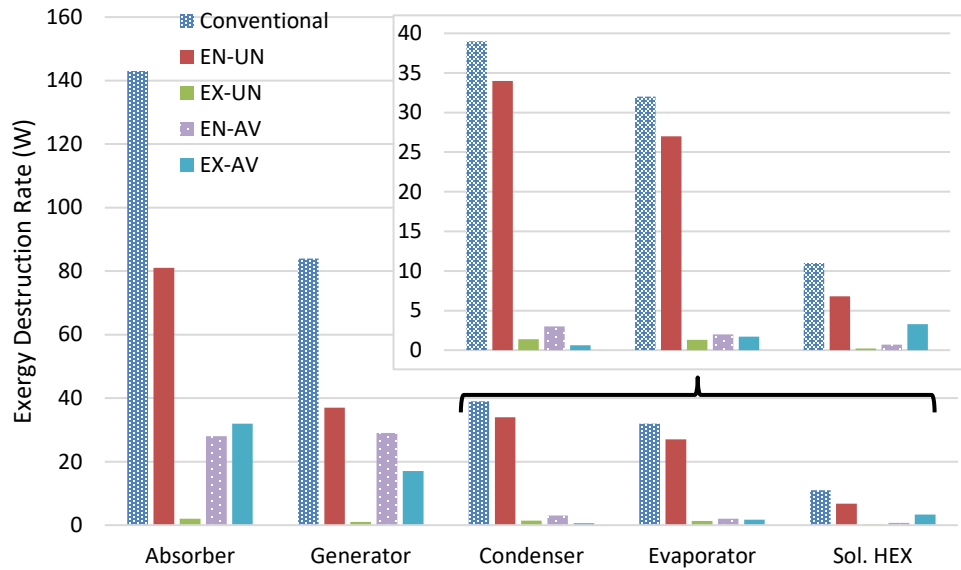


Figure 7.4: Exergy destruction rate of each component of a bubble-pump-driven LiCl-H₂O absorption refrigeration cycle based on conventional exergy and advanced exergy analyses.

7.6. Conclusions

The advanced exergy analysis of a bubble-pump-driven LiCl-H₂O absorption air-conditioning system offers useful information in order to identify the component that has the most potential for the overall system improvement. This information cannot be provided by the conventional exergy analysis. The avoidable exergy destruction identifies the potential of each component that can be improved by technological improvement. The endogenous avoidable and exogenous avoidable exergy destruction correlate the interactions between the components' irreversibilities and quantify the importance of the relative improvement of each component and the overall system structure.

The evaluation of the analyses in this study shows that 80% of the total exergy destruction is due to the component's own internal irreversibilities whereas the remaining is through the interaction of the components in the system. The conventional exergy analysis demonstrates that the highest exergy losses were found in the absorber which is 46% of the total exergy destruction, however, the advanced exergy analysis suggests that

the first priority for the improvement should be the generator. In the absorber, 58% of the exergy destruction is unavoidable. Of the avoidable part, 22% can be reduced by improving the other components of the system and 20% (28W) can be reduced in the absorber itself. Whereas, a 35% (29W) of the generator exergy destruction can be reduced by internal efficiency improvement could result in a significant improvement of the overall system performance. The analyses reveal that the necessity for the improvement of the condenser, the evaporator and the solution heat exchanger is very low as most of the exergy losses are unavoidable and the remaining can be improved by improving the efficiency of the other component of the system.

Finally, the analyses in this study could be helpful for the exergoeconomic optimization of energy conversion systems [Tsatsaronis, 1999, Tsatsaronis & Park, 2002, Cziesla *et al.*, 2006]. It will provide the useful information to the designer for the investment in order to reduce the endogenous avoidable and exogenous avoidable parts of exergy destruction and to measure the potential improvement of the overall system structure.

Nomenclature

| | | <i>Superscripts</i> | |
|--------------|--|---------------------|---------------------------|
| e | exergy (kJ/kg) | | |
| \dot{E}_D | exergy destruction rate or loss (kW) | <i>AV</i> | avoidable |
| \dot{E}_Q | exergy destruction rate in terms of heat transfer (kW) | <i>EN</i> | endogenous |
| h | specific enthalpy (kJ/kg) | <i>EN-AV</i> | endogenous avoidable |
| h_o | specific enthalpy at reference temperature 25°C | <i>EN-UN</i> | endogenous unavoidable |
| HEX | Heat Exchanger | <i>EX</i> | exogenous |
| \dot{m} | mass flow rate (kg/s) | <i>EX-AV</i> | exogenous avoidable |
| P | pressure (kPa) | <i>EX-UN</i> | exogenous unavoidable |
| P_o | reference pressure 101.325 kPa | | |
| \dot{Q} | heat transfer rate (kW) | <i>Subscripts</i> | |
| s | specific entropy (kJ/kg·K) | <i>abs</i> | absorber |
| s_o | specific entropy at reference temperature 25°C | <i>cond</i> | condenser |
| T | temperature (K) | <i>eva</i> | evaporator |
| T_o | reference temperature 25°C | <i>gen</i> | generator |
| X | mass fraction of ammonia (%) | <i>i</i> | component |
| \dot{W} | work rate (kW) | <i>in</i> | inlet |
| η_{HEX} | heat exchanger efficiency | <i>k</i> | component |
| | | <i>out</i> | outlet |
| | | <i>p</i> | pump |
| | | <i>ref</i> | refrigerant |
| | | <i>sol</i> | solution |

REFERENCES

- Aman J, Ting D.S-K., Henshaw P., Residential solar air conditioning: energy and exergy analyses of an ammonia-water absorption cooling system. *Applied Thermal Engineering*, 62 (2014) 424-432.
- Aman J., Henshaw P., Ting D. S-K., Bubble-pump-driven LiBr-H₂O and LiCl-H₂O absorption air-conditioning systems. *Thermal Science and Engineering*, 2017 <https://doi.org/10.1016/j.tsep.2017.10.022>.

- Bejan A., Tsatsaronis G., Moran M., Thermal design and optimization. New York: Wiley; 1996.
- Cziesla F., Tsatsaronis G., Gao Z., Avoidable thermodynamic inefficiencies and costs in an externally fired combined cycle power plant. *Energy International Journal*, 31(10-11) (2006) 1472-89.
- EES (Engineering Equation Solver). F-Chart software, Academic Commercial V9. (2015), 941(1992-2017), www.fchart.com
- Esfahani I.J., Lee S.C., Yoo C.K., Evaluation and optimization of a multi-effect evaporation-absorption heat pump desalination based conventional and advanced exergy and exergoeconomic analyses. *Desalination*, 359 (2015) 92–107.
- Fallah M., Mohammad S., Mahmoudi S., Yari M., Akbarpour Ghiasi R., Advanced exergy analysis of the Kalina cycle applied for low temperature enhanced geothermal system. *Energy Conversion and Management*, 108 (2016) 190–201.
- Gungor A., Erbay Z., Hepbasli A., Gunerhan H., Splitting the exergy destruction into avoidable and unavoidable parts of a gas engine heat pump (GEHP) for food drying processes based on experimental values. *Energy Conversion and Management*, 73 (2013) 309–16.
- Hepbasli A., Keçebas A., A comparative study on conventional and advanced exergetic analyses of geothermal district heating systems based on actual operational data. *Energy Buildings*, 61 (2013) 193–201.
- Kecebas A., Hepbasli A., Conventional and advanced exergoeconomic analysis of geothermal district heating systems. *Energy and Buildings*, 69 (2014) 434–441.
- Kelly S., Tsatsaronis G., Morosuk T., Advanced exergetic analysis: approaches for splitting the exergy destruction into endogenous and exogenous parts. *Energy*, 34(3) (2009) 384–91.
- Kotas T.J., The exergy method of thermal plant analysis. FL, USA: Krieger Publishing Company; 1985.

- May S., E.I., Boukholda I., Bellagi A., Energetic and exergetic analysis of a commercial ammonia-water absorption chiller. *International Journal of Exergy*, 8 (1) (2011) 33-50.
- Morosuk T., Tsatsaronis G., Boyano A., Gantiva C., Advanced exergy-based analyses applied to a system including LNG regasification and electricity generation. *Int J Energy and Environmental Engineering*, 3(1) (2012) 1–9.
- Morosuk T., Tsatsaronis G., Comparative evaluation of LNG-based cogeneration systems using advanced exergetic analysis. *Energy*, 36(6) (2011) 3771–8.
- Morosuka T., Tsatsaronis G., A new approach to the exergy analysis of absorption refrigeration machines, *Energy*, 33 (2008) 890–907.
- Petrakopoulou F., Tsatsaronis G., Morosuk T., Carassai A., Conventional and advanced exergetic analysis applied to a combined cycle power plant. *Energy*, 41 (2012) 146–152.
- Szargut J., Morris D.R., Steward F.R., Exergy analysis of thermal, chemical, and metallurgical processes. Berlin: Springer; 1988.
- Tan M., Keçebas A., Thermodynamic and economic evaluations of a geothermal district heating system using advanced exergy-based methods. *Energy Conversion and Management*, 77 (2014) 504–13.
- Tsatsaronis G., Morosuk T., Koch D., Sorgenfrei M., Understanding the thermodynamic inefficiencies in combustion processes. *Energy*, 62 (2013) 3–11.
- Tsatsaronis G., Park M.H., On avoidable and unavoidable exergy destructions and investment costs in thermal systems. *Energy Conversion and Management*, 43 (2002) 1259-70.
- Tsatsaronis G., Design optimization using exergoeconomics. In: Bejan A., Mamut E., editors. *Thermodynamic optimization of complex energy systems*. Dordrecht: Kluwer Academic Publishers; (1999) 101-15.
- Tsatsaronis G., Strengths and limitations of exergy analysis. In: Bejan A., Mamut E., editors. *Thermodynamic optimization of complex energy systems*. Dordrecht: Kluwer Academic Publishers; (1999) 93–100.

Vidal R., Best R., Rivero R., Cervetas J., Analysis of a combined power and refrigeration cycle by the exergy method. *Energy*, 31 (2006) 3401– 3414.

Zhu L., Gu J., Second law-based thermodynamic analysis of ammonia/sodium thiocyanate absorption system. *Renewable Energy*, 35 (2010) 1940-1946.

CHAPTER 8

DISCUSSION AND CONCLUSIONS

8.1. Research Outcomes

Small scale absorption cooling technologies that can be driven by solar thermal energy are still emerging. The development of these technologies requires more research focusing on low temperature heat driven machines with a higher coefficient of performance (COP) for small scale air conditioning application. This research contributes through analyzing an efficient cooling system for providing air conditioning in residential communities, driven by solar thermal energy using an environmental friendly refrigerant. The following research has been accomplished in this regard.

The ability of two sorption cooling technologies (absorption and adsorption), which can be operated by using a low temperature heat source such as the heat from a solar thermal collector, were compared. To optimize the performance of these two systems based on operating conditions, thermodynamic analyses were performed for the 10 kW ammonia-water absorption and activated carbon-ammonia adsorption cooling systems. The result shows that both systems can operate using a low temperature heat source, ranging from 60 to 90°C, which can be supplied by a flat plate solar collector. The analysis reveals that the absorption chiller gives a higher system performance (COP = 0.60) than the adsorption system (COP = 0.35) under the same operating conditions. To provide this cooling effect, the adsorption system needs almost twice as much heat supplied (29 kW) compared to the heat supplied (17 kW) to the absorption system. The adsorption system also has a higher heat rejection (27 kW) compared to the heat rejection (15 kW) of the absorption system, to meet the same 10 kW cooling load. As a result, the adsorption system must be designed to collect and reject higher amounts of energy. The analysis also shows that the COP increases for both systems with increasing heat source temperature but decreases as absorber/adsorber temperature increases. And it has been revealed that the absorption COP is always higher than the COP for adsorption under all operating conditions simulated here. The result also demonstrates that the adsorption cooling system is highly sensitive to heat source temperature. A higher heat source temperature can reduce the adsorbent mass as well as the size of the adsorption chiller with a concomitant increasing system performance.

From the comparison of performances analyzed here for the two sorption cooling systems considering different operating conditions, it appears that the absorption system is the most suitable solar sorption technology to provide air conditioning in a residential home.

The high temperature requirement in the generator, crystallization problem and cooling tower requirement for the absorber restrains the most widely used LiBr-H₂O absorption cooling systems in small scale applications. High pressure and the low freezing point (-77.7°C) properties of ammonia have advantages for residential scale applications within the range of 3 to 10 kW. However, the lower efficiency of ammonia-water chillers compared to LiBr-H₂O chillers, limits their widespread use. In this respect, the potential of the NH₃-H₂O absorption cycle for a small scale solar thermal air conditioning application was investigated in Chapter 3. In order to reduce the size and increase the thermal performance, this system was intended for air cooling instead of water cooling and a low temperature heat driving source like a flat plate solar collector was anticipated. In order to maximize the cycle efficiency, energy and exergy analyses of a 10 kW air-cooled ammonia-water absorption chiller were performed and the system performance, exergetic efficiency and the exergy loss of each component of the system were calculated. The first and second law efficiency of the system were investigated and compared under different system operating conditions. The results show that increasing the heat source temperature increases the coefficient of performance (COP) and the exergetic efficiency of the system. After reaching the maximum, the COP is almost steady, whereas the exergetic efficiency decreases with increasing heat source temperature. Moreover, the COP increases with increasing the evaporator temperature but decreases as absorber and condenser temperatures increase. However, the exergetic efficiency decreases with an increase in evaporator, condenser and absorber temperatures. The analysis revealed that the highest energy conversion of the cycle occurs when the absorption cooling system is operated using low temperature heat sources rather than high temperature heat sources and it was also found that decreasing the condenser and the absorber temperatures towards the atmospheric temperature does not impact significantly the overall system performance. So, for small scale applications, an ammonia-water absorption chiller can be operated with heat supplied by a flat plate solar collector with ambient air cooling of the absorber and the condenser. The exergy analysis of this absorption cooling system shows that the highest exergy loss

(around 63%) is located in the absorbing process followed by the generator (13%), condenser (11%), throttle valve (7%), solution heat exchanger (4%), and evaporator (2%). In order to improve cycle efficiency, the highest focus of the improvement should be the absorber while the generator may be considered as the second priority.

The core components of vapor absorption refrigeration systems (VARs) are the absorber, generator, condenser and evaporator. An electrical pump is a critical component of a VAR for circulating the refrigerant-absorbent solution from the low-pressure absorber to the high-pressure generator. In order to provide air-conditioning independent of grid electricity, a thermally-driven bubble pump, which can be powered by waste heat or solar thermal energy, offers a simple and efficient technique for lifting a liquid from lower to higher levels, after which it can fall by gravity. Thus, it can replace the electrically driven pump by thermally driven one. This thermally-driven bubble pump is a more desirable option compared to a conventional (electrical) pump driven by small PV panel due to its simple construction and lack of moving parts. Furthermore, the efficiency of the heat-driven-bubble-pump in absorption refrigeration cycle is almost 48% compared to the PV module (efficiency is around 15%) for harnessing the sun. A battery is another component required for a PV-operated pump. As a result, a heat-driven -bubble-pump provides an efficient technique for circulation the solution in an absorption refrigeration cycle in order to achieve a higher overall system performance. A detailed analysis of a bubble pump was carried out in order to make it compatible with VAR systems. However, the performance of the bubble pump itself and the VAR performance strongly depend on the working fluid properties and the geometry of the bubble pump.

In order to use this pump in a VAR, an analytical model of a bubble pump was developed and experimental work was conducted. In the simulation model, two-phase turbulent flow with heat loss, friction, surface tension effects and other thermophysical properties was considered. The model was validated by operating a bubble pump with water at atmospheric conditions. The bubble pump performance was investigated with tube diameters of 6 to 10 mm and lifting ratios (the ratio of the height of the liquid in the tube to the tube length) of 0.6 to 0.8, and at different heat inputs (80 to 250 W). The theoretical model and experimental results showed that the bubble pump liquid mass flow rate varied with all three studied parameters. The maximum liquid flow rate was obtained during slug

flow at 160 Watts heat input, a lifting ratio of 0.8, and a tube diameter of 10 mm. The analytical calculation at this condition agreed within 0.9% of the experimental results. The proposed model can be used to accurately predict the bubble pump output.

With the aim of characterizing a bubble pump that can be used in VAR systems regardless of the type of working fluid or the physical parameters of the pump itself, a dimensional analysis was performed. A theory was developed based on the non-dimensional parameters to describe the operation of the bubble pump while considering the thermophysical properties of the working fluid and the physical parameters of the bubble pump. Experiments were performed using water to validate the analytical results. Non-dimensional parameters such as non-dimensional heat input, non-dimensional pressure, Froude number (liquid and gas), Eotvos number, Galileo number, Morton number, non-dimensional energy and Reynolds number were found to characterize the efficiency of the bubble pump. The non-dimensional parameters were related to experimental measures of input heat, system pressure, fluid properties and the geometry of the bubble pump. The highest efficiency was obtained at lower non-dimensional pressure when the flow pattern was at the starting of slug flow regime. In this flow regime, the highest liquid Froude number was found but it decreased with increasing gas (vapor) Froude number (at higher heat supply) and the flow became churn flow. From this analysis, it was revealed that the bubble pump always operates in a two-phase flow turbulent condition where the Reynolds number is always higher than 10^4 and the Morton number is between 10^{-13} and 10^{-11} . The analytical results of the proposed model and the experimental results agreed within 12% with water or LiCl-H₂O solution as the working fluid.

The operation of bubble-pump-driven NH₃-H₂O VARS, known as diffusion absorption refrigeration (DAR), and LiBr-H₂O VARS are completely different due to the physical properties of ammonia (a high-pressure refrigerant) and water (a low-pressure refrigerant). Although much research has been performed for the improvement of DAR systems, the research on bubble pump operated LiBr-H₂O VARS is very limited. The crystallization challenge, low pressure, and low efficiency of LiBr-H₂O confines its use in a bubble pump in this refrigeration cycle. Therefore, a LiCl-H₂O refrigerant vapor absorption refrigeration system (VARS) that can operate by a solar thermally-driven bubble pump was analyzed. A thermodynamic model was developed that includes the

bubble pump parameters in the refrigerant cycle operation. The results were compared for bubble-pump-driven LiBr-H₂O and LiCl-H₂O VARS. The thermodynamic properties were calculated for each component and each state in this new refrigeration cycle. As the pump is the key component for driving an air conditioning system, by generating the refrigerant vapor as well as by pumping the liquid solution to absorb this refrigerant in the absorber, the COP was calculated at various bubble pump heat inputs. The result shows the LiCl-H₂O system can achieve a higher system performance over the LiBr-H₂O system at high heat input due to its thermophysical properties. Due to the crystallization problem, the LiBr-H₂O system must be operated at lower heat input with lower performance. At the same operating condition, the lower lifting ratio (31) of the LiCl-H₂O system resulted in a higher COP (0.56) compared to a LiBr-H₂O system with a COP of 0.46 at a lifting ratio of 59. The analysis also revealed that the highest liquid flow rate by the pump does not provide the highest COP of the refrigeration cycle as proportionally less vapor (refrigerant) is generated at this stage. The liquid (strong solution) flow rate is tied to the solution flow rate required to absorb the refrigerant vapor generated by the bubble pump.

The advanced exergy analysis of a bubble-pump-driven LiCl-H₂O absorption air-conditioning system offers useful information in order to identify the component that has the most potential for the overall system improvement. This information cannot be provided by conventional exergy analysis. The avoidable exergy destruction identifies the potential of each component that can be improved through the technological improvement. The endogenous avoidable and exogenous avoidable exergy destruction describe the interactions between the components' irreversibilities and those of the overall system. The scale of simulation was tied to the experimental bubble pump tested in Chapters 5 and 6. 80% of the total exergy destruction is due to each component's own internal irreversibilities, whereas the remaining is through the interaction of the components in the system. The conventional exergy analysis determined that the highest exergy losses were found in the absorber, which is 46% of the total exergy destruction. However, the advanced exergy analysis suggests that the first priority for the improvement should be given to the generator. In the total absorber exergy destruction, 58% is unavoidable. Of the avoidable parts, 22% can be reduced by improving the performance of other components in the system, and 20% (28 W) can be reduced in the absorber itself. Whereas, 35% (29 W) of

the generator exergy destruction can be reduced by improving its internal efficiency, which could result in a significant improvement of the overall system performance. The analyses revealed that the necessity for the improvement of the condenser, the evaporator and the solution heat exchanger is very low as most of the exergy losses in those components are unavoidable and the remaining can be improved by improving the efficiency of the other components of the system.

Finally, this study shows that the absorption refrigeration cycle dominates the adsorption cycle in order to provide an efficient cooling system for residential air conditioning applications that can be driven by low temperature heat source such as a flat plate solar collector. The integration of a bubble pump provides a promising technology in the refrigeration cycle that can operate by solar thermal energy as well, delivering the air-conditioning system independent of grid electricity. A dimensional analysis in this study determined the bubble pump performance in non-dimensional numbers regardless of the working fluid and the geometry of the pump. The analysis also revealed that the highest efficiency of the pump does not provide the highest performance of the bubble pump operated refrigeration cycle. High vapor generation and the high-pressure property of the LiCl-H₂O working solution shows the advantages of the bubble pump of the absorption refrigeration cycle for residential air conditioning applications. Furthermore, the energy, exergy and advanced exergy analyses in this research can provide a useful tool for the exergoeconomic optimization of energy conversion of this bubble-pump-driven absorption cooling system. It will provide the useful information to the designer for the investment in order to reduce the avoidable parts of exergy destruction and to measure the potential improvement of the overall system.

8.2. Recommendations for Future Research

The aim of this research was to develop analysis methods for an efficient air-conditioning system in a residential home that can be powered by solar thermal energy independent of grid electricity. The thermodynamic cycle of this absorption system was analyzed and examined in order to operate from a low temperature heat source, such as a flat plate solar thermal collector. The meteorological data of solar thermal energy was not analyzed in this research. In future, solar intensity, collector efficiency, or different type of

solar collectors as well as an energy storage system can be customized for providing the required temperature in the generator of this cooling system. Numerical transient simulation with an automatic control strategy will assist in practical system design. Furthermore, the energy and exergy analyses can be performed for the overall system efficiency improvement.

An analytical model was developed in Chapter 5 to characterize the bubble pump in the form of non-dimensional numbers and was validated with experimental results by using two liquids (pure water and LiCl-H₂O). Experiments with the working fluid of NH₃-H₂O are recommended for further validation of this model for DAR systems.

In the bubble pump experiments, the flow behavior in the lift tube of a bubble pump was observed. The flow patterns were limited to bubbly, slug, slug-churn and churn turbulent flow. Two phase turbulent flow was considered in the analytical model which showed good agreement with the experimental results. However, the turbulent condition throughout the tube is not the same which affects the heat loss through the tube. In this research, the steady-state condition was applied for all analysis. The turbulence structure and the phase distribution in two phase flow modelling are always limited due to the complex nature of the interface which is time dependent. A properly formulated two fluid multiphase flow model can provide a wide range of steady and transient multiphase flow phenomena. In order to improve the bubble pump efficiency, a multidimensional multiphase flow and heat transfer analysis can be performed by using computational fluid dynamics (CFD) methods for a wide range of adiabatic flows in a vertical tube by applying different boundary conditions.

In the present analysis, the mean velocity of the bubble in the liquid slug was calculated based on the average liquid and gas flow rate. However, the behavior of the Taylor bubble in the liquid slug is very complex. The highly distorted bubble and the highly aerated liquid slug should account for in the theoretical prediction. The hydrodynamics of the Taylor bubble in the liquid slug needs to be investigated for the development of predictive algorithms that can provide the information about different flow regimes. In the experiment, the hydrodynamics of different flow patterns can be observed by using an appropriate non-intrusive image acquisition system in order to acquire more accurate experimental data (such as bubble and slug length distribution, bubble velocity distribution,

flow pattern in the wake region, coalescence and the length of established flow patterns) to improve the accuracy of the predictive model.

In this research, the experimentation was limited to analyzing the bubble pump characteristics at atmospheric conditions. In order to use this bubble pump in water-based refrigerant absorption air-conditioning systems, the experiments can be performed at vacuum pressure as this refrigeration cycle works at low pressure (negative atmospheric pressure) in practice. A complete prototype of a bubble-pump-driven absorption cooling system will then be the next step for further investigation.

APPENDICES

Appendix A

ENERGY EFFICIENCY AND ECONOMIC FEASIBILITY OF AN ABSORPTION AIR-CONDITIONING SYSTEM USING WET, DRY AND HYBRID HEAT REJECTION METHODS

This work was published as “Aman, J., Henshaw, P. Ting, D. S-K., Energy efficiency and economic feasibility of an absorption air-conditioning system using wet, dry and hybrid heat rejection methods, International Journal of Environmental Studies”
<https://doi.org/10.1080/00207233.2017.1396073>.

A.1. Introduction

In tropical and sub-tropical regions, modern cities are the main consumers of electricity and most of this energy is for air-conditioning systems in buildings. In the United Arab Emirates, 60% of the total electrical energy is consumed by building air-conditioning systems during summer [Mokhtar, *et al.*, 2010]. Improving the efficiency of existing energy usage and using renewable energy resources are key to protect the environment. Renewable energy integration either alone or in hybrid systems can meet the growing energy demand and provide sustainable energies for the future [Shafiullah, 2016]. For air-conditioning applications, conventional vapor compression systems are commonly used, which are driven by electrical energy. This causes stress in the generation and distribution systems during the peak load period in the summer. Thermally driven cooling systems are a sustainable energy technology that provides cooling by replacing electrically driven compressor chillers with thermally driven chillers, and they have already proven their technical feasibility [Zhai & Wang, 2009]. Solar thermal energy is a suitable option for providing this cooling comfort. For example, Australia, with the highest annual solar radiation in the world, can meet its total energy demand by solar thermal energy using an area approximately equal to its existing rooftops [Lovegrove & Dennis, 2006].

Thermal absorption cooling systems can be driven by waste heat or solar thermal energy. Such a system consists of a heat driven generator, a condenser, an evaporator, a

solution heat exchanger and an absorber. While providing cooling, the condenser and the absorber of the absorption chiller produce heat that must be rejected, the same as the condenser of a traditional vapor compression chiller. The performance of the absorption chiller strongly depends on the heat rejection of the absorber as well as the condenser. Hence, it is crucial to consider efficient heat rejection methods and energy consumption of auxiliaries for the overall primary energy balance of this cooling system [Eicker *et al.*, 2012].

There are various heat rejection methods that can be applied for condenser and absorber cooling in absorption cooling systems. These include evaporative or wet (water) cooling towers, air or dry cooling, hybrid cooling (with both wet and dry cooling), geothermal heat sinks, and night radiative cooling [Eicker & Dalibard, 2011]. Kummert *et al.*, [2007] compared the system performance and energy cost for a geothermal absorption chiller and a vapor compression chiller for providing space heating and cooling in three different cities in Canada. The system coefficient of performance (COP) is always higher for compression heat pump systems, but where electricity prices are relatively low (Vancouver and Montreal) the life cycle cost is higher for natural gas-driven absorption heat pump systems. Although wet cooling is preferable for better system performance for the heat rejection of the absorber and condenser in an absorption chiller, water consumption is dominant in this method. The statistics of water usage at the California Institute of Technology show that 40% of the water consumption is for the central air-conditioning system in the campus [Kim, 2008]. In most of the arid Southwest USA and subtropical regions where policy and cost oppose water usage, an air-cooled condenser and absorber are required. In cities like Hong Kong, the building density is very high and, due to the climate, cooling is needed year-round [Gang *et al.*, 2015]. The government in Hong Kong does not give permission to use fresh water for heat rejection in building/central air-conditioning applications [Yik *et al.*, 2001]. However, in hot weather where water is available, both wet and dry cooling methods can be used in parallel in a hybrid system. When a cooling tower is used as a heat rejection method for absorption air-conditioning, the energy needed is accounted in the primary energy balance. The effectiveness of dry-cooling and wet-cooling methods are distinguished by the minimum temperature that each heat rejection method can provide. The wet cooling methods use the evaporation process

to reject the heat, based on the wet bulb temperature, whereas dry cooling depends on the ambient dry-bulb temperature [Turchi *et al.*, 2010].

An absorption air-conditioning system can be driven by a single-effect absorption chiller with a generator temperature varying from 60°C to 120°C [Aman *et al.* 2014]. The heat rejection for this system can be air-cooled or wet-cooled. As the performance of the absorption chiller strongly depends on the absorber heat rejection, different studies of heat and mass transfer have been performed to improve the absorber efficiency, considering the expected high ambient temperature at the time of air conditioning use [Izquierdo *et al.*, 2008]. A wet-cooled single effect LiBr-H₂O absorption chiller has been studied and the efficiency was found to be higher at a higher dry bulb temperature due to the lower relative humidity at the high dry bulb temperature [Syed *et al.*, 2005]. An experiment using a single effect LiBr-H₂O absorption was performed by Asdrubali and Grignaffini [2005], and the highest performance was found at a 70°C generator temperature when wet-cooled heat rejection was applied. A 34 kW LiBr-H₂O absorption chiller integrated with membrane distillation was simulated based on United Arab Emirates weather conditions and the highest COP was 0.7 during the peak period of summer [Mohan *et al.*, 2016]. Different studies have been carried out for the performance of air-cooled LiBr-H₂O absorption chillers [Izquierdo *et al.*, 2008, Kim & Infante Ferreira, 2009, Palaci'n, Monne' & Alonso, 2011]. However, an ammonia-water absorption chiller is suitable for small-scale applications [Aman *et al.*, 2014]. The SolarNext company in Germany introduced a 10 kW water cooled NH₃-H₂O absorption system for commercial air-conditioning applications that has a thermal coefficient of performance (COP_{th}) of 0.63 at a 16°C chilled water temperature [Jacob & Pink, 2007]. Many prototypes have been built for air-cooled NH₃-H₂O absorption chillers in order to analyze them experimentally. Du *et al.* [2012] performed an experiment on a two-stage 2 kW air-cooled chiller and reported a COP_{th} of 0.21 and an electrical coefficient of performance (COP_{el}) of 5.1 with 8°C and 29°C evaporator and air temperatures, respectively. Aprile *et al.* [2015] found that a 2.5 kW double-effect air-cooled NH₃-H₂O chiller performed at a COP_{th} of 0.3 and COP_{el} of 10, at an air temperature of 30°C, to provide 7°C chilled water.

In short, many research and experimental studies are striving to improve of the system performance of absorption chillers with different heat rejection systems. However,

with depleting clean water, the optimization of primary energy and water consumption, correlated with system performance and economic index is crucial. To the authors' knowledge, no analyses have been conducted for the comparison of different cooling methods in absorption air-conditioning systems with respect to energy and economic analysis. In this present work, a dynamic simulation model has been developed in TRNSYS 17 in order to evaluate the primary energy consumption as well as water usage for different cooling systems in a 15 kW absorption chiller at different operating conditions. Much research has been carried out for the simulation of LiBr-H₂O absorption chillers by TRNSYS 17 software [Shirazi *et al.*, 2016, Januševičius *et al.*, 2015, Molero-Villa *et al.*, 2012, Monfet & Zmeureanu, 2009, González-Gil *et al.*, 2011, Eicker *et al.*, 2015]. However, this software is restricted only to the LiBr-H₂O absorption chiller [TRNSYS] and the simulation is independent of thermodynamic properties of the absorbent-refrigerant solution and the internal thermodynamic cycle performance. To overcome these limitations of TRNSYS, a detailed thermodynamic analysis has been performed of a 15 kW NH₃-H₂O absorption solar air-conditioning system within Engineering Equation Solver (EES) [2015] and coupled with the simulation model of heat rejection systems in TRNSYS 17. As a result, the model describes the energy consumption by different auxiliaries, and their effects on the overall system performance based on thermodynamic analyses of this air-conditioning system. Additionally, an economic analysis has been developed, considering the capital investment and operating cost, and the penalty cost of CO₂ emissions. Finally, energetic and economic analyses have been compared for different heat rejection methods.

A.2. System Analysis

A model was developed for a 15 kW single effect NH₃-H₂O absorption chiller driven by solar thermal energy for the evaluation of primary energy consumption and the energy efficiency of the cooling system. This system was analyzed with different heat rejection methods at different operating conditions. Figures A.1 and A.2 represent the schematics of single-effect absorption refrigeration systems with different heat rejection methods: Figure A.1 for wet or dry cooling and Figure A.2 for hybrid cooling. The model describes the thermodynamic process of the absorption cooling system in order to calculate the primary energy consumption of the absorption chiller and auxiliaries at different heat rejection

systems. The system performance and primary energy efficiency are analyzed in this model.

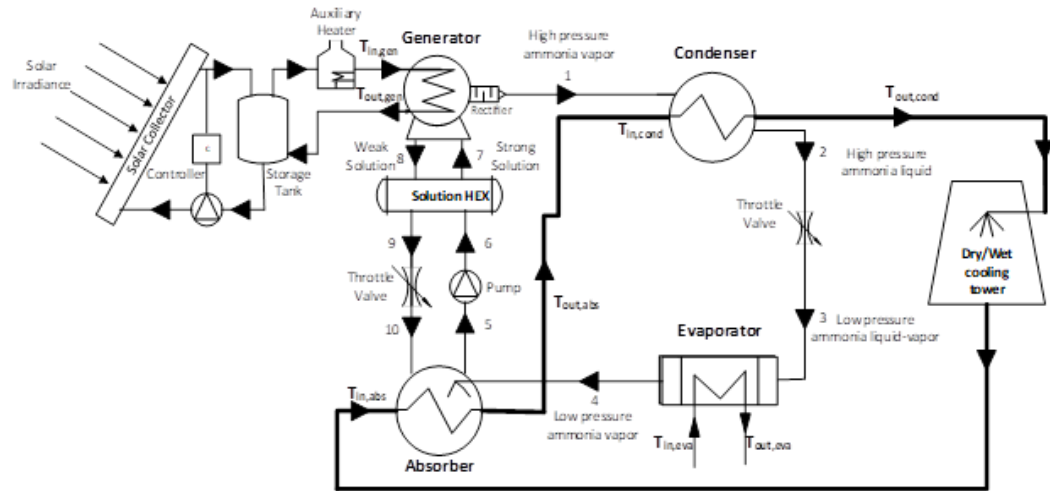


Figure A.1: Schematic of a wet/dry cooled single-effect NH₃-H₂O absorption cooling system.

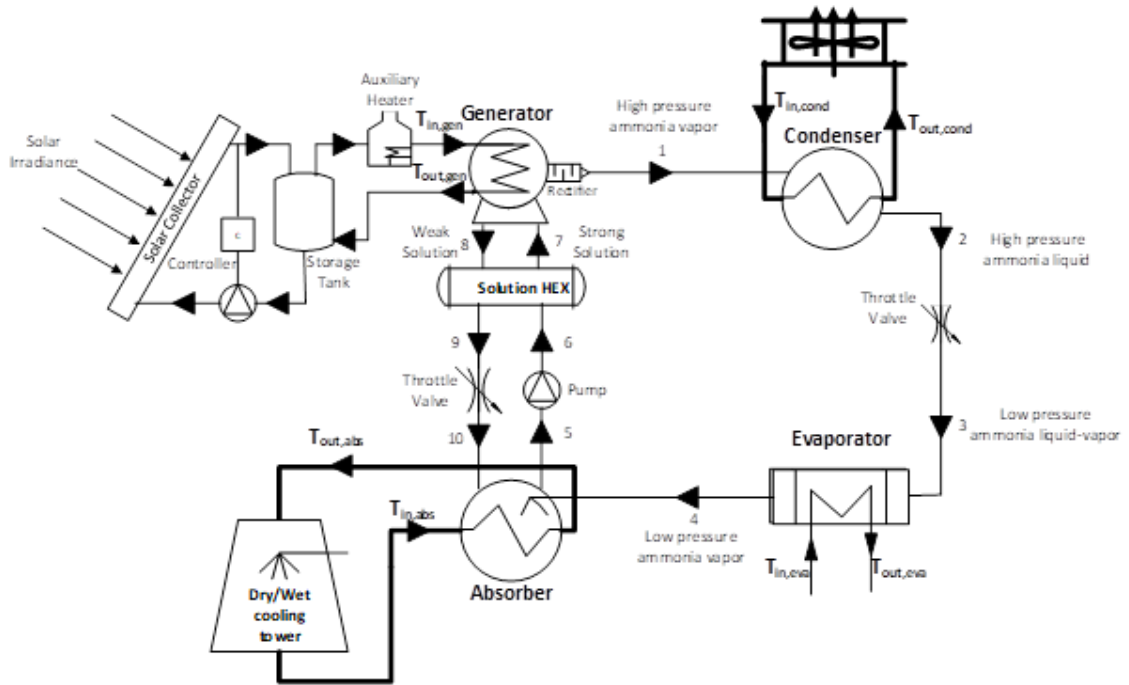


Figure A.2: Schematic of a hybrid-cooled single-effect NH₃-H₂O absorption cooling system.

A.2.1. Thermodynamic analysis

Assuming that there are no heat losses, the rated energy supplied to the generator is:

$$\dot{Q}_{gen} = \dot{m}_{w.gen} C_{p,w} (T_{in,gen} - T_{out,gen}) \quad (1)$$

The cooling load of the evaporator, which was set to a constant 15 kW in this study, is:

$$\dot{Q}_{eva} = \dot{m}_{w.eva} C_{p,w} (T_{in,eva} - T_{out,eva}) \quad (2)$$

The temperature of the absorber and the condenser depends on the different heat rejection methods. The following equation yields the energy required for the absorber:

$$\dot{Q}_{abs} = \dot{m}_{w.abs} C_{p,w} (T_{out,abs} - T_{in,abs}) \quad (3)$$

The total energy balance of the absorption chiller can be calculated from the total heat gained by the system and the total heat rejected from the system, assuming no heat losses to the surroundings, and can be written as:

$$\dot{Q}_{abs} + \dot{Q}_{cond} = \dot{Q}_{gen} + \dot{Q}_{eva} \quad (4)$$

By using Equations (1) to (4), the energy required by the condenser can be deduced.

The solution heat exchanger effectiveness can be evaluated by the following equation:

$$\varepsilon_{HEX} = \frac{T_8 - T_9}{T_8 - T_6} \quad (5)$$

For pumping the solution from the absorber to the generator, the energy required by the pump of the absorption chiller can be defined by:

$$\dot{W}_{solp} = (P_6 - P_5) v_6 \quad (6)$$

The coefficient of performance of an absorption cooling system can be defined in three different ways:

- a) The *thermal* coefficient of performance (COP_{th}) is the ratio of the cooling load to the heat input to the generator:

$$COP_{th} = \frac{\dot{Q}_{eva}}{\dot{Q}_{gen}} \quad (7)$$

- b) Considering the electrical energy consumption by the absorption chiller and auxiliaries including all pumps, fans and cooling tower, the *electrical* coefficient of performance is:

$$COP_{el} = \frac{\dot{Q}_{eva}}{\sum \dot{W}_{aux}} \quad (8)$$

- c) It is important to consider primary energy consumption by auxiliaries and the cooling tower when analyzing the total performance of an absorption refrigeration system. In this context, the performance of the absorption cooling system can be defined as a primary energy ratio (PER) [Eicker *et al.*, 2015], which is the ratio of useful energy output to the primary energy (electrical and thermal energy) input. The primary energy input is considered as the total energy input to the system, which includes the total electrical energy consumption and the thermal energy supplied to the system and it is defined as:

$$PER = \frac{\dot{Q}_{eva}}{\dot{Q}_{gen} + \sum \dot{W}_{aux} \cdot PEF_{el}} \quad (9)$$

where PEF_{el} is the primary energy factor for electricity, equal to 3.36 [Deru & Torcellini, 2007].

A.2.2. Economic analysis

In order to evaluate the economic feasibility of different cooling methods in an absorption chiller, a simple cost analysis which includes capital and operating costs of the total cooling system was performed. As the operating cost is different in different regions due to different electricity or water prices, two different countries - Canada and the United Arab Emirates (UAE) - were chosen for comparison in this cost analysis because of their differences in cooling demand, electricity and water costs. It was assumed that the air-conditioning period for Canada and the UAE are 4 months and 12 months in a year,

respectively. Since the cooling tower dominates the primary energy consumption and water usage, the cost of its energy usage is the primary factor for economic analysis. The investment costs of an absorption chiller and cooling tower are the major costs, so these were the only items considered for the capital cost investment (CI), other component costs were not reflected in this study. The specific capital costs of wet cooling, dry cooling and hybrid cooling were considered to be 110 USD/kW, 134 USD/kW and 146 USD/kW, respectively; values which were taken from regression analysis of different manufacturing data [Absorption Chiller suppliers, 2016]. Hence, the major investment cost of an absorption cooling system was determined as:

$$CI_{Total} = CI_{CH} + CI_{CT} \quad (10)$$

The operating cost (C_{op}) of this cooling system includes the consumption of electrical energy (C_{el}), water (C_w) and can be calculated by the following equation:

$$C_{op} = C_{el} \times c_e + C_w \times c_w \quad (11)$$

where, c_e and c_w are the unit costs of electricity and water (including waste water) and were assumed to be 0.10 USD/kWh and 2.86 USD/m³ for Canada [Ontario Energy Board, 2016] and 0.044 USD/kWh and 2.95 USD/m³ for the UAE [RSB, 2016]. In a wet cooling tower, another major cost is the water treatment. In this analysis, the treatment is considered to occur every two weeks for the sump water and the water treatment cost was assumed 7.13 USD/m³ [Timothy, 2008].

Although the wet cooling absorption chiller is thermodynamically more energy efficient than the dry cooling system, it may not be in terms of the combined energy and water cost. It is necessary to put in perspective the total cost (capital and operating) of different cooling systems for absorption chillers. Therefore, a simple payback period (SPBP) was calculated as an economic index of dry and hybrid cooling systems compared to a wet cooling system. In terms of environmental factors, CO₂ emission is important and its cost was also included in this analysis. So, the simple payback period of different cooling methods was assessed as follows:

$$SPBP = \frac{(CI_{total})_{dry/hybrid} - (CI_{total})_{wet}}{(C_{op,wet} - C_{op,dry/hybrid}) + (C_{CO_2,wet} - C_{CO_2,dry/hybrid})} \quad (12)$$

where,

$$C_{CO_2} = C_{el} \times EF_{CO_2} \times c_{CO_2} \quad (13)$$

In Equation (13), EF_{CO_2} is the CO_2 emission factor for electricity production, and was assumed to be 0.856 kg of CO_2 / kWh [NRCan, 2017] in Canada and 0.739 kg of CO_2 / kWh [Environment agency, 2012] in the UAE. c_{CO_2} is the CO_2 emission penalty cost of 0.01 USD per kg in both Canada and the UAE [ECCC, 2017, IREA, 2016].

A.3. *Simulation Procedure*

If the heat supply to the absorption chiller is constant, the thermal performance of the chiller strongly depends on the outdoor temperature and the heat rejection temperature [Palaci'n, & Alonso, 2011]. In this analysis, three variants of the absorption cooling system have been developed with different heat rejection methods: a wet cooling system, a dry cooling system or a hybrid cooling system. The thermodynamic properties of the absorbent-refrigerant solution of a 15 kW absorption chiller were determined using equations in Ref. [Aman *et al.*, 2014] and calculated in EES [2015]. A dynamic simulation model for different cooling towers was developed by using the energy simulation tool TRNSYS 17 [2016]. Based on the required outlet temperature of the cooling tower, which was the inlet temperature of the absorber cooling water in the chiller, the amount of heat rejection and energy consumption by variant cooling towers were determined using this software. The primary energy balance and the performance of the absorption chiller were then calculated by solving Equations (1) to (9) in EES. Figure A.3 shows the simulation procedure of this analysis. The simulation started with the input of the required refrigerant absorber temperature (T_{abs}) in EES which determined the $T_{in,abs}$, $T_{out,cond}$ and refrigerant temperature in the condenser (T_{cond}) by using an internal heat exchanger efficiency of 80%. The T_{cond} determined the chiller system pressure which was used to calculate the refrigerant concentration at the absorber temperature in the absorber. Then the energy balance of the chiller was calculated. In TRNSYS, $T_{in,abs}$ was input as the target temperature. To achieve the target $T_{in,abs}$, the flow rate of water in wet cooling or the fan power in dry cooling were varied. When the targeted $T_{in,abs}$ was reached, the auxiliary energy consumption, fan power,

water loss due to evaporation in wet cooling and heat rejection were calculated. These results from TRNSYS were used in EES to calculate the efficiency of the system.

In TRNSYS, in order to simulate the wet cooling tower and dry cooling tower, type51b and type511 were used, respectively. Each cooling method was used separately for the heat rejection of the absorber and condenser loop. For hybrid cooling, type51b was used for absorber cooling and type511 was used for condenser cooling to optimize the absorption system performance with minimum water usage. The water flow rate of the wet cooling tower and the electrical energy consumption rates by the fan of different cooling modes were determined by TRNSYS. Other electrical energy consuming devices of the absorption chiller are shown in Table A.1.

Table A.1: Electrical energy consumption by pumps of a 15 kW absorption cooling system [Shafiullah, 2016].

| Components | Nominal volume flow (m³/h) | Required electrical energy (W) |
|-------------------------------------|--|---------------------------------------|
| Solution pump of absorption chiller | 5.0 | 300 |
| Absorption/Condenser Auxiliary Pump | 10.0 | 1100 |
| Generator Auxiliary Pump | 2.0 | 56 |
| Evaporator Auxiliary Pump | 1.9 | 52 |

As the weather data was not used in this analysis, the assumptions of the dry-bulb and wet-bulb temperatures with respect to absorber temperature are shown in Table A.2.

Table A.2: Variation of dry-bulb and wet-bulb temperature with respect to absorber temperature

| Absorber temperature, °C | Wet-bulb temperature, °C | Dry-bulb temperature, °C | Relative humidity |
|---------------------------------|---------------------------------|---------------------------------|--------------------------|
| 20 | 17 | 18 | 91 |
| 25 | 18 | 20 | 83 |
| 30 | 21 | 25 | 71 |
| 35 | 23 | 30 | 56 |
| 40 | 25 | 35 | 45 |

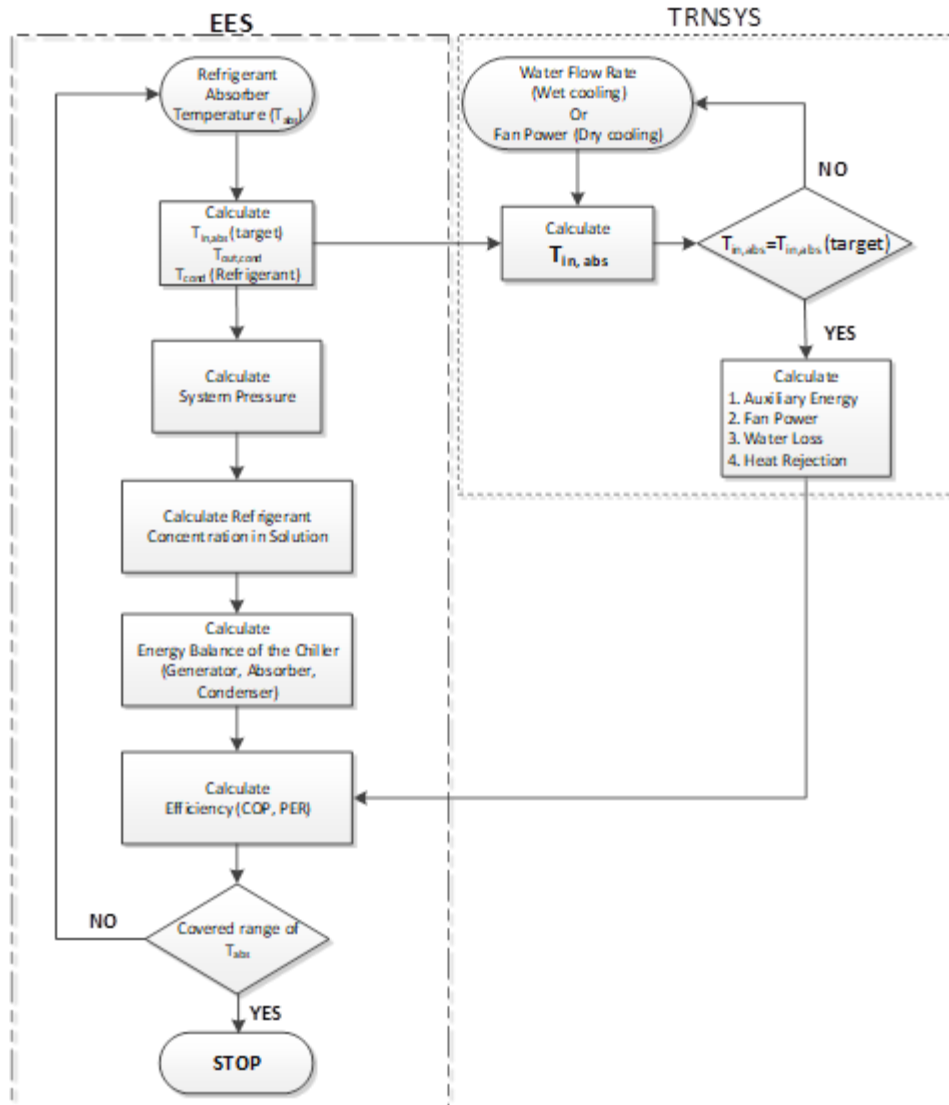


Figure A.3: Simulation procedure for the analysis of a 15 kW NH₃-H₂O absorption cooling system with different heat rejection methods

Wet Cooling Tower (Type51b)

Two input parameters need to be defined in this cooling tower: the mass transfer constant and the mass transfer exponent. The mass transfer constant is the ratio of water mass flow rate to air mass flow rate in the cooling tower and was set at 1.2 [Januševičius *et al.*, 2015]. The mass transfer exponent was set at -0.65 according to an ASHRAE guideline [2004]. The input parameters of this cooling system are shown in Table A.3.

Table A.3: Type51b: Input variables for cooling tower

| Parameters | Input |
|------------------------------|---------------------|
| Water inlet temperature | $T_{out,cond}$, °C |
| Inlet water flow rate, kg/s | 0.33 to 3.63 |
| Dry-bulb temperature, °C | 20 to 35 |
| Wet-bulb temperature, °C | 18 to 25 |
| Sump make-up temperature, °C | 25 |
| Relative fan speed for cell | 1 |

The outlet temperature of the cooling tower, which is the inlet water temperature of the absorber ($T_{in,abs}$) (shown in Figure A.1), was adjusted by varying the water flow rate while running the fan at constant speed until the target $T_{in,abs}$ was achieved. The water flow rate, the heat rejection and water consumption due to evaporation were determined from the simulation results of the cooling tower. The electrical energy consumption by this cooling tower was calculated by the power consumption of the fan and the auxiliary pump.

Dry Cooling Tower (Type511)

The TRNSYS fluid cooler dry cooling device was used to simulate a dry cooling system for this absorption chiller. Water was used as the heat exchanging fluid between the absorber/condenser and the dry cooler. In order to achieve the required absorber/condenser temperature, the fan speed of the cooler was controlled by varying the fan power. The input parameters for this cooling tower are shown in Table A.4.

Table A.4: Type511: Input variables for cooling tower

| Parameters | Input |
|-----------------------------|--------------|
| Inlet fluid temperature, °C | 30 to 45 |
| Inlet fluid flow rate, kg/s | 0.5 |
| Set point temperature, °C | T_{abs} |
| Surrounding temperature, °C | 19 to 35 |
| Rated fan capacity | variable |

Hybrid Cooling

A hybrid cooling system was considered in order to conserve water and to achieve the optimum performance of this absorption cooling system. The performance of the chiller

depends more on the absorber temperature than the condenser temperature when other parameters are constant. This is because the absorbent-refrigerant concentration ratio in the absorber strongly depends on the absorber temperature. Targeting this fact, in hybrid cooling, a wet cooling tower (type51b) was used for rejection of heat from the absorber by varying the fan speed while the water flow was kept at 0.8 kg/s. Unlike the case where only wet or dry cooling was used, the condenser temperature was fixed at 40°C by air-cooling, as shown in Figure A.2, but the absorber temperature was varied. In this condition, the refrigerant was directly cooled by the fin tube heat exchanger in type511 with forced air, so no external water was needed for this cooling. As a result, in hot weather conditions, the maximum system performance can be achieved by lowering the absorber temperature with minimum water usage.

A.4. Results and Analysis

A.4.1. Thermodynamic performance

The energy flows in each component of a 15 kW absorption air-conditioning system operating at 80°C generator, 40°C condenser, 35°C absorber and 6°C evaporator temperatures to provide 10°C chilled water ($T_{out,eva}$) with an 80% heat exchanger effectiveness are presented in Table A.5.

Table A.5: Energy flow rate of each component of 15 kW NH₃-H₂O absorption air-conditioning system.

| Parameters | |
|-------------------------|----------|
| Generator, Q_{gen} | 29.57 kW |
| Condenser, Q_{cond} | 17.02 kW |
| Evaporator, Q_{eva} | 15.00 kW |
| Absorber, Q_{abs} | 27.55 kW |
| Cooling Tower, Q_{CT} | 44.84 kW |

As electrical energy consumption is one criterion to evaluate the advantages of absorption chillers, Figure A.4 shows the electrical coefficient of performance of the 15 kW absorption chiller with different modes of heat rejection. Here, the analysis revealed that this 15 kW ammonia-water cooling system can operate only up to 40°C absorber temperature, at which temperature the absorber absorbs barely sufficient absorbent

(assuming at 45°C condenser temperature) to provide 15 kW cooling in the evaporator under the operating conditions of 80°C generator and 6°C evaporator temperatures, respectively. Figure A.4 shows that the COP_{el} increased with increasing absorber/condenser temperature for all modes of operation. At higher absorber/condenser temperatures, the relative humidity was less, so less fan power was required for the heat rejection by the cooling tower for cooling the absorber/condenser at increased temperature. Note that the COP_{el} reached 8.05 in the wet cooling mode versus 5.2 for the dry cooling mode at 40°C absorber temperature. In the wet cooling tower, the heat rejection occurred by the combination of heat and mass transfer. For this simulation with a wet cooling tower, the fan speed was constant but the *water flow rate* was controlled to achieve the required outlet temperature from the tower. Increasing the water flow rate increases the water surface area exposed to the air, which increases the evaporation of water, which in turn increases the cooling rate of water in the tower. Therefore, the heat rejection depends on the water flow rate. In this cooling tower, the evaporation of water was the main mode of heat removal. Hence, less electrical energy was needed for the same amount of heat rejection compared to other cooling methods. As a result, a high COP_{el} was obtained by this cooling tower. In contrast, the *fan speed* was controlled for the convection heat rejection in the dry cooling tower, which required a high volume of air to be moved to create the necessary heat transfer. This accounted for the high electrical energy consumption by the fan. As a result, the COP_{el} of the dry cooling mode was the lowest compared to the other two modes of operation. In the hybrid cooling system, the wet and dry cooling tower were in parallel. Therefore, the electrical energy consumption was intermediate between those of the other two cooling systems.

The primary energy ratio (PER) and thermal coefficient of performance (COP_{th}) of different modes of heat rejection are compared in Figure A.5. The absorber system thermal performance decreased as the absorber/condenser temperature increased for all modes of operation. Increasing the absorber temperature adversely affected the refrigerant vapor absorption in the absorber. Therefore, to supply a constant cooling load in the evaporator, the thermal load of the generator had to increase. At the same time, increasing the condenser temperature increased the system pressure, which increased the thermal load in the generator as well. These two effects were responsible for lowering the COP_{th} .

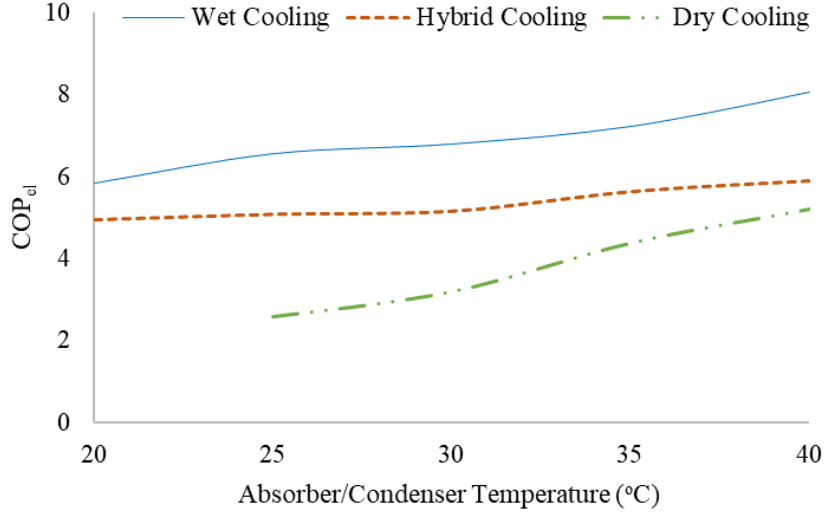


Figure A.4: Electrical COP of 15kW NH₃-H₂O absorption cooling system with different heat rejection methods at $T_{gen}=80^{\circ}\text{C}$, $T_{eva}=6^{\circ}\text{C}$.

In wet or dry cooling modes, the condenser temperature depended on the absorber temperature as the outlet temperature of the absorber cooling water ($T_{out,abs}$) is the inlet temperature of the condenser coolant ($T_{in,cond}$) for heat rejection as shown in Figure A.1. So, the condenser temperature was always higher than the absorber temperature. However, the absorption chiller itself operated through the same cycle and at the same absorber/condenser temperatures for the wet cooling mode or the dry cooling mode. As a result, there was no variation of the thermal performance (COP_{th}) by wet and dry cooling methods with respect to absorber/condenser temperatures. In the wet cooling mode, the primary energy consumption, including thermal and electrical, was lower than all other cooling modes and it increased as the absorber temperature rose, therefore the PER decreased. In contrast, a slight increase of PER was observed for the dry cooling mode as the absorber temperature rose from 25 to 35°C. At higher absorber temperature, less heat rejection was observed that required less fan power which meant a higher PER. Although the thermal load was the same as that for the wet cooling system, the electrical energy consumption by the fan for the dry cooling tower was higher, so the total primary energy consumption was much greater compared to the wet cooling mode. As a result, the overall PER of dry cooling was lower than that in the wet cooling mode. As the generator thermal

load increased above 35°C absorber temperature for all cooling modes, so the PER dropped for all.

For the hybrid cooling mode, it was observed that the COP_{th} was lower than the wet/dry cooling mode. In this cooling method, the condenser was cooled by dry cooling and kept at a constant 40°C, and the absorber temperature was controlled by wet cooling. Therefore, increasing the absorber temperature decreased the refrigerant absorption in the absorber at a high constant condenser temperature that resulted in an increased system pressure. As a result, the thermal load of the absorber and the generator increased, hence lowering the COP_{th} for this cooling method compared to the other two modes. As a dry cooling tower was used for the condenser to maintain a high temperature, so the electrical energy consumption by the fan was less than that of the dry cooling mode, therefore, the PER was intermediate for this cooling method. Over the range of temperatures simulated, the average PER of the hybrid system was 13% lower than for wet cooling and 20% higher than the dry cooling mode of operation, which compensated for the 8% lower COP_{th} compared to the other two cooling systems.

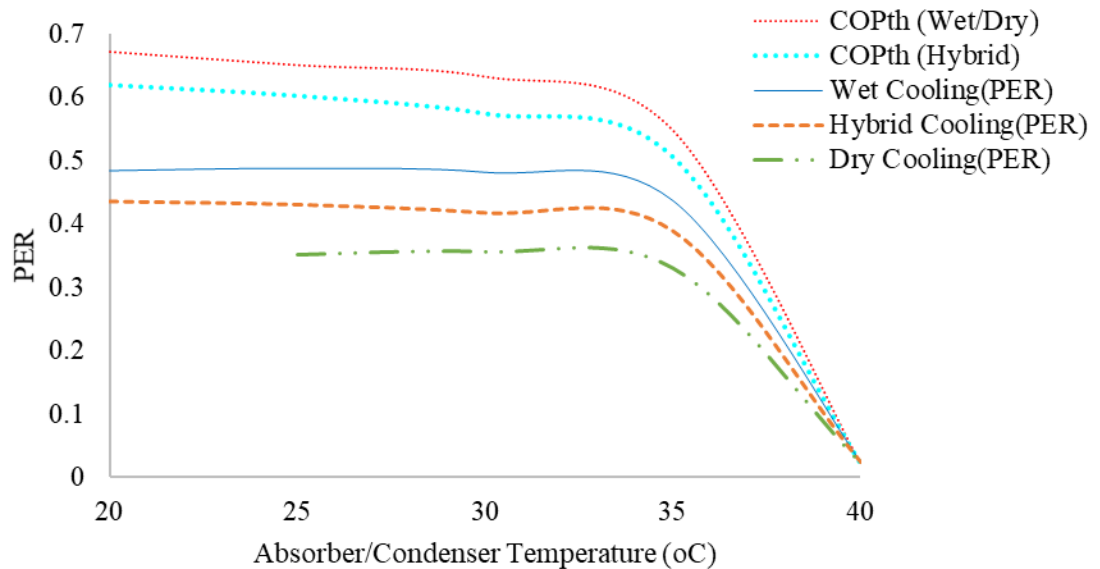


Figure A.5: Primary Energy Ratio (PER) of 15 kW NH_3-H_2O absorption cooling system with different heat rejection methods at $T_{gen}=80^{\circ}C$, $T_{eva}=6^{\circ}C$.

A.4.2. Energy and Economic Performance

The electrical energy and water consumption rates of the three different cooling methods are shown in Figure A.6. The highest electrical energy consumption was observed in the dry cooling mode, which decreased rapidly as the absorber/condenser temperature increased, but it was on average 54% higher than that for the wet cooling mode. The required electrical energy of the wet cooling system was the lowest of all cooling modes and was almost constant as the temperature rose. In contrast, the water consumption was highest in this mode of cooling. The hybrid cooling system demonstrated a trade-off between electrical energy and water consumption. In this cooling method, the water flow rate was kept constant while the fan speed was controlled to circulate the atmospheric air for the evaporation of water in the wet cooling tower for the absorber cooling. This was done to keep the water consumption low, while providing the same heat rejection as the wet cooling tower. A dry cooling tower was used for the condenser cooling in the hybrid cooling method. As a result, the average electrical energy consumption of the hybrid cooling method was 22% higher than the wet cooling mode but 41% lower than the dry cooling mode. This hybrid cooling used 49% less water than that of the wet cooling mode of operation.

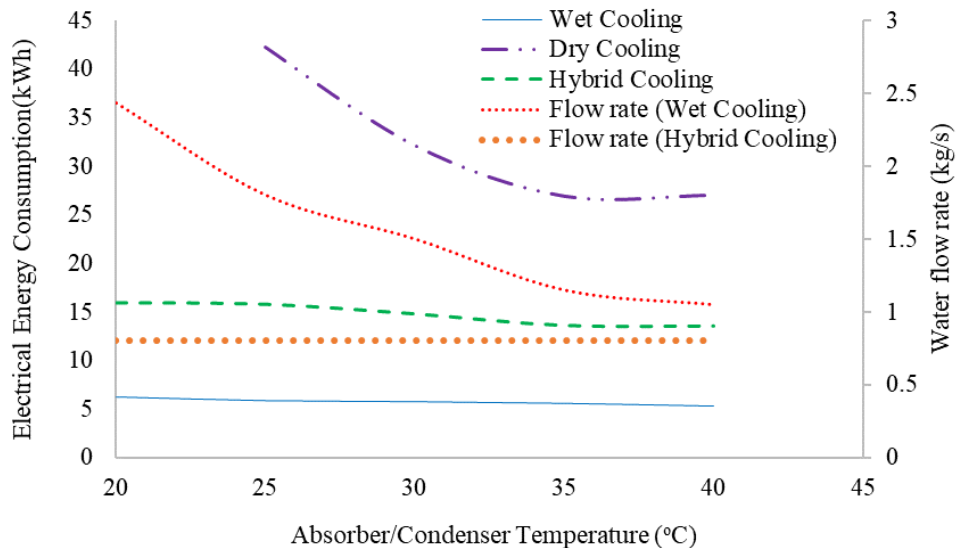


Figure A.6: Electrical energy consumption and water flow rate of 15 kW NH₃-H₂O absorption cooling system with different heat rejection methods at $T_{\text{gen}}=80^{\circ}\text{C}$, $T_{\text{eva}}=6^{\circ}\text{C}$.

The electricity and water consumption per year using different cooling methods, to provide 15 kW cooling in Canada and the UAE are presented in Figure A.7 and Figure A.8. The thermal performance, primary energy ratio and economic performance of these cooling systems are summarized in Table A.6. When comparing the electricity and water consumption and their costs between these two countries, it can be seen that the electricity and water consumption in the UAE are higher than Canada by 3 times and 1.95 times, respectively. Due to the weather in the UAE, air-conditioning is required all the year round; whereas in Canada, the air-conditioning needs to run only four months. In contrast, the total cost of this electricity in the UAE is only 1.3 times higher as the unit price of electricity in the UAE is 2.7 times less than Canada. In terms of water cost, the UAE pays 2.02 times more compared to Canada.

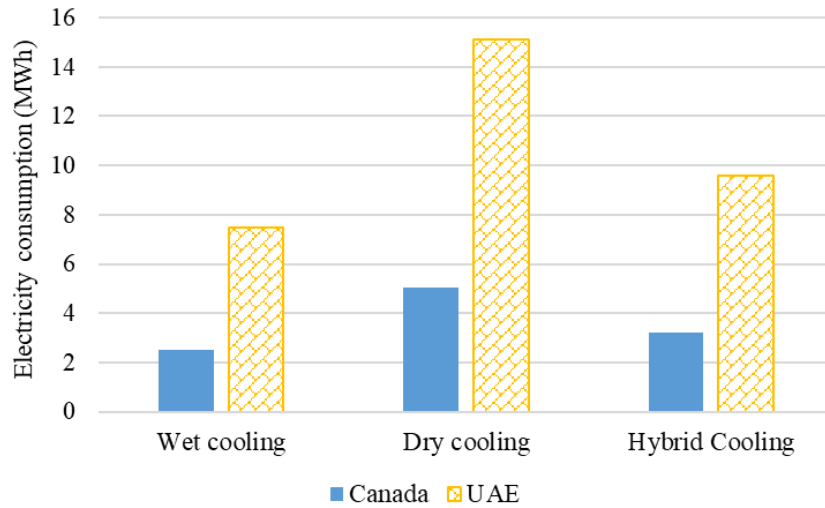


Figure A.7: Electricity consumption per year in Canada and UAE for 15 kW NH₃-H₂O absorption cooling system with different heat rejection methods.

The simple payback period in Table A.6 was calculated to compare the economic benefit of dry and hybrid cooling over wet cooling methods. The capital cost of the wet cooling system was less than the other two methods and the thermal performance and primary energy ratio were also higher for the wet cooling system. Whereas, the operating cost of a wet cooling system is higher than the dry cooling system due to the high water cost and water treatment cost. The analysis reveals that although the dry cooling system had a lower PER and a higher capital cost, from an economic point of view, the cost can be paid back within 1 year over the wet cooling system. Therefore, the dry cooling tower

can replace the wet cooling tower where the water cost is high and the use of fresh water is forbidden for air-conditioning applications. However, due to the high dry bulb temperatures in some locations like southern California and Nevada, dry cooling is not feasible [Kim, 2008]. In this respect, the hybrid cooling system can be used to trade-off between water consumption and primary energy consumption. The total cost of hybrid cooling in this situation can be recovered within 2.9 years as a result of less water consumption compared to wet cooling. In contrast, in the UAE, the payback periods for dry and hybrid cooling systems over wet cooling are lower than Canada as the electricity price is fairly low compared to the water price.

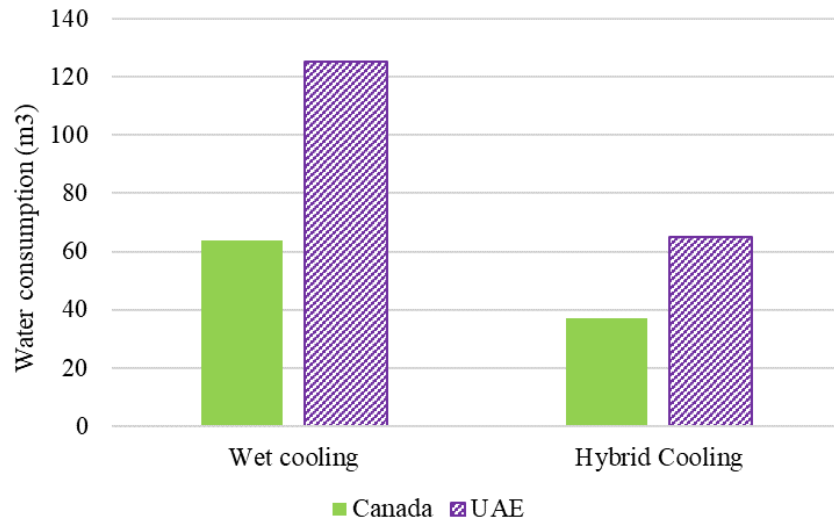


Figure A.8: Water consumption per year in Canada and UAE for 15 kW NH₃-H₂O absorption cooling system with wet and hybrid heat rejection methods.

Table A.6: Energy and economic performance of different cooling methods of absorption chiller at operating condition of at T_{gen}=80°C, T_{eva}=6°C, T_{abs}=35°C, T_{cond}=40°C

| Configuration | Capacity (kW) | COP _{th} | PER | Electricity Cost (USD/year) | Water Cost (USD/year) | Water Treatment Cost (USD/year) | Operating Cost (USD/year) | SPBP (years) | |
|----------------|---------------|-------------------|------|-----------------------------|-----------------------|---------------------------------|---------------------------|--------------|-------------|
| | | | | | | | | Canada/ UAE | Canada/ UAE |
| Wet cooling | 15 | 0.57 | 0.44 | 250/330 | 183/370 | 455/893 | 888/1593 | 0 | 0 |
| Dry cooling | 15 | 0.57 | 0.36 | 504/665 | 0 | | 504/665 | 1 | 0.4 |
| Hybrid cooling | 15 | 0.51 | 0.39 | 320/422 | 106/192 | 264/464 | 690/1079 | 2.9 | 1.1 |

A.5. Conclusion

The aim of this study was to show how water usage and primary energy consumption of a 15kW NH₃-H₂O absorption cooling system could be reduced with different heat rejection methods. The primary energy and water usage for the best performance of the chiller, then the thermal, electrical and primary energy efficiency as well as cost effectiveness of wet cooling, dry cooling and hybrid cooling heat rejection methods of this absorption chiller have been investigated. A dynamic simulation model of different cooling methods was developed in TRNSYS software to estimate their electrical energy and water consumption. The thermodynamic properties of the refrigerant-absorbent solution and energy balance of the absorption chiller were calculated in EES to determine the efficiencies of this absorption cooling system.

The analysis reveals that the dry cooling method offers the highest potential for reducing the water consumption and best economic index for its operation. In contrast, the wet cooling method has the lowest primary energy consumption but a higher amount of water consumption and a higher operating cost. The hybrid cooling method uses the wet and dry cooling methods in parallel. With an average 8% lower thermal efficiency, this hybrid system can reduce water consumption by 49% and primary energy consumption by 41% compared to wet and dry cooling methods, respectively. The efficiency of this cooling method can return its cost within 2.9 years compared to the wet cooling method.

Finally, the analysis in this paper indicates that a wet cooling absorption system can be replaced by a dry cooling system at the same thermal efficiency where there is scarcity of water or the cost of water is high. However, hybrid cooling comprises the best trade-off between primary energy and water usage in hot weather conditions. Overall, the analytical methods of this study provide a clear thermo-economic guidance for choosing a suitable cooling method for the application of absorption air-conditioning systems.

Acknowledgements

This work is made possible by the Natural Science and Engineering Research Council of Canada.

Nomenclature

| | | | |
|-------------------------|--|-------------------|----------------------|
| CI | capital investment cost (USD) | <i>Subscripts</i> | |
| COP _{th} | thermal coefficient of performance | <i>abs</i> | absorber |
| COP _{el} | electrical coefficient of performance | <i>cond</i> | condenser |
| C _p | specific heat at constant pressure (kJ/kg.K) | <i>CH</i> | chiller |
| c | cost (USD/unit) | <i>CT</i> | cooling tower |
| C | consumption | <i>DCT</i> | dry cooling tower |
| \dot{m} | mass flow rate (kg/s) | <i>el</i> | electrical |
| P | Pressure (kPa) | <i>eva</i> | evaporator |
| PER | primary energy ratio | <i>gen</i> | generator |
| \dot{Q} | heat load (kW) | <i>HCT</i> | Hybrid cooling tower |
| SPBP | simple payback period (year) | <i>i</i> | component |
| T | temperature (K) | <i>in</i> | inlet |
| USD | USA dollars | <i>l</i> | liquid |
| \dot{W} | work done (kW) | <i>out</i> | outlet |
| ϵ_{HEX} | heat exchanger effectiveness | <i>p</i> | pump |
| v | refrigerant specific volume (m ³ /kg) | <i>ref</i> | reference |
| | | <i>sol</i> | solution |
| | | <i>th</i> | thermal |
| | | <i>w</i> | water |
| | | <i>WCT</i> | wet cooling tower |
| | | <i>WT</i> | water treatment |

REFERENCES

- Absorption Chiller suppliers, 2016. Available at <http://www.alibaba.com/showroom/absorption-chiller.html> (accessed April 2016).
- Aman, J., Henshaw, P., Ting, D.S-K., 2014, Residential solar air conditioning: Energy and exergy analyses of an ammonia-water absorption cooling system. *Appl. Therm. Eng.* 62, 424-432.
- Aprile, M., Toppi, T., Guerra, M., Motta, M., 2015, Experimental and numerical analysis of an air-cooled double-lift NH₃-H₂O absorption refrigeration system. *Int. J. Refrigeration* 50, 57-68.
- Asdrubali, F., Gignaffini, S., 2005, Evaluation of the performances of a H₂O-LiBr absorption refrigerator under different service conditions. *Int. J. Refrigeration* 28, 489-497.

- ASHRAE, HVAC system and equipment-Cooling Tower (Chapter-9), American Society of Heating, Refrigeration and air-conditioning Engineers, Inc, Atlanta, Ca, (2004), <http://thermairsystems.com/wp-content/uploads/2011/10/ASHRAE-Systems-and-Equipment-Cooling-Towers.pdf>
- NRCan, CO₂ emission factor, Natural Resources Canada, Government of Canada, retrieved September 2017 from <http://www.nrcan.gc.ca/energy/efficiency/industry/technical-info/benchmarking/canadian-steel-industry/5193>
- Deru, M., Torcellini, P., 2007, Source Energy and Emission Factors for Energy Use in Buildings, Technical Report, NREL/TP-550-38617, June.
- Du, S., Wang, R.Z., Lin, P., Xu, Z.Z., Pan, Q.W., Xu, S.C., 2012, Experimental studies on an air-cooled two-stage NH₃-H₂O solar absorption air-conditioning prototype. *Energy* 45, 581–587.
- ECCC, 2017, Technical paper on federal carbon pricing backstop, Ministry of Environment and Climate Change Canada, retrieved on September 2017 from <https://www.canada.ca/content/dam/eccc/documents/pdf/20170518-2-en.pdf>
- EES (Engineering Equation Solver), 2015, F-Chart software, Academic Commercial V9.941(1992-2015), www.fchart.com
- Eicker, U., Dalibard, A., 2011, Photovoltaic-thermal collectors for night radiative cooling of buildings. *Solar Energy* 85, 1322-1335.
- Eicker, U., Dalibard, A., Pesch, R., 2012, Heat rejection and primary energy efficiency of solar driven absorption cooling systems. *Int. J. Refrigeration* 35 729-738.
- Eicker, U., Pietruschka, D., Haag, M., Schmitt, A., 2015, Systematic design and analysis of solar thermal cooling systems in different climates. *Renewable Energy* 80, 827-836.
- Environment agency – Abu Dhabi: Greenhouse gas inventory, Inventory results, Executive summary, December 2012, retrieved on September 2017 from <https://www.ead.ae/Documents/PDF-Files/AD-Greenhouse-gas-inventory-Eng.pdf>
- Gang, W., Wang, S., Gao, D., Xiao, F., 2015, Performance assessment of district cooling systems for a new development district at planning stage. *Applied Energy* 1140, 33-43.
- González-Gil, A., Izquierdo, M., Marcos, J.D., Palacios, E., 2011, Experimental evaluation of a direct air-cooled lithium bromide-water absorption prototype for solar air conditioning. *Appl. Therm. Eng.* 1, 1-11.

- IREA, 2016, The true cost of fossil fuels: Externality cost assessment methodology, International Renewable Energy Agency, retrieved on September 2017 from http://www.irena.org/DocumentDownloads/Publications/IRENA_REmap_externality_methodology_2016.pdf
- Izquierdo, M., Lizarte, R., Marcos, J.D., Gutie´ rrez, G., 2008, Air conditioning using an air-cooled single effect lithium bromide absorption chiller: results of a trial conducted in Madrid in August 2005. *Appl. Therm. Eng.* 28, 1074-1081.
- Jakob, U., Pink, W., 2007, Development and investigation of an ammonia/water absorption chiller - chillii_ PSC - for a solar cooling system, in: Proceedings of the 2nd International Conference Solar Air-conditioning, Tarragona, Spain, pp. 440-445.
- Januševičius, K., Streckienė, G., Misevičiūtė, V., 2015, Simulation and Analysis of Small-Scale Solar Adsorption Cooling System for Cold Climate. *Int. J. of Enviro. Sci. Development* 6(1), 561.
- Kim, C., S., 2008, Increasing Cooling Tower Water Efficiency, California Institute of Technology. Available online at: https://www.sustainability.caltech.edu/documents/33-chang_sub_final_paper.pdf (accessed April 2016).
- Kim, D.S., Infante Ferreira, C.A., 2009, Air-cooled LiBr-water absorption chillers for solar air conditioning in extremely hot weathers. *Energy Convers. Manage.* 50, 1018-1025.
- Kummert, M., Bernier, M., Costa, A., Paris, J., 2007, A comparison between geothermal absorption and compression heat pumps for space conditioning. *Int. J. Environmental Studies* 64 (4), August, 467–487.
- Lovegrove, K., Dennis, M., 2006, Solar thermal energy systems in Australia. *Int. J. Environmental Studies* 63 (6), December, 791–802.
- Mohan, G., Kumar, N.T. U., Pokhrel, M. K., Martin, A., 2016, A novel solar thermal polygeneration system for sustainable production of cooling, clean water and domestic hot water in United Arab Emirates: Dynamic simulation and economic evaluation. *Applied Energy* 167, 173-188.

- Mokhtar, M., Ali, M.T., Brauniger, S., Afshari, A., Sgouridis, S., Armstrong, P., Chiesa, M., 2010, Systemetic comprehensive techno-economic assessment of solar cooling technologies using location-specific climate data. *Applied Energy* 87, 3766-3778.
- Molero-Villar, N., Cejudo-Lo´pez, J.M., Dom´ınguez-Mun˜oz, J.M., Carrillo-Andre´s A., 2012, A comparison of solar absorption system configurations. *Solar Energy* 86, 242–252.
- Monfet, D., Zmeureanu, R., 2009, Simulation of a large central cooling and heating plant using TRNSYS and calibration with monitored data. Eleventh International IBPSA Conference, Glasgow, Scotland, July 27-30.
- Ontario Energy Board, 2016 Available at <http://www.ontarioenergyboard.ca/oeb/Consumers/Electricity/Electricity%20Prices> (accessed April 2016)
- Palaci´n, Monne´, F., Alonso, S., 2011, Improvement of an existing solar powered absorption cooling system by means of dynamic simulation and experimental diagnosis. *Energy* 36, 4109-4118.
- RSB, 2016, New Water and Electricity Tariffs Structure Regulation & Supervision Bureau, <http://rsb.gov.ae/en/sector/new-water-and-electricity-tariffs-structure> (accessed May 2016).
- Shafiullah, G.M., 2016, Hybrid renewable energy integration (HREI) system for subtropical climate in Central Queensland, Australia. *Renewable Energy* 96, 1034-1053.
- Shirazi, A., Taylor, R.A., White, S.D., Morrison, G.L., 2016, A systematic parametric study and feasibility assessment of solar-assisted single-effect, double-effect, and triple-effect absorption chillers for heating and cooling applications. *Energy Convers. Manage* 114, 258–277.
- Syed, A., Izquierdo, M., Rodr´ıguez, P., Maidment, Missenden, J., Lecuona, A., Tozer, R., 2005, A novel experimental investigation of a solar cooling system in Madrid. *Int. J. Refrigeration* 28, 859-871.
- Timothy K., 2008, Cooling Water Management: Basic Principles and Technology, Technical report, ProChemTech International, Inc. Apache Junction, AZ, and Brockway, Pennsylvania. Available at

http://www.prochemtech.com/Literature/Technical/Basic_Cooling_Water_Management_II.pdf

TRNSYS 17: A Transient Simulation Program, 2016, Solar Energy Lab. University of Wisconsin, Madison, WI.

Turchi, C.S., Wagner, M.J., Kutscher, C.F., 2010, Water Use in Parabolic Trough Power Plants: Summary Results from WorleyParsons' Analyses, NREL (National laboratory of the U.S. Department of Energy, Technical Report NREL/TP-5500-49468, December 2010).

Yik, F.W.H., Burnett, J., Prescott, I., 2001, Predicting air-conditioning energy consumption of a group of buildings using different heat rejection methods. *Energy Building* 33, 151-166.

Zhai, X.Q., Wang, R.Z., 2009, A review for absorption and adsorption solar cooling systems in China. *Renewable and Sustainable Energy Reviews* 13, 1523–1531.

Appendix B

AIR LIFT PUMP AND TWO-PHASE FLOW

A typical air-lift pump configuration is illustrated in Figure B.1. A gas, usually air, is injected at the base of a submerged vertical pipe. As a result, the gas bubbles suspended in the fluid, the average density of the two-phase mixture in the tube is less than that of the surrounding fluid. The resulting buoyant force causes a pumping action. In Figure B.1, a pipe is submersed in water in a depth H , so the water level in the pipe is same as the tank. The air-injector is located close to the submerged pipe at the bottom. If the ambient pressure is P_a , the pressure at this location is

$$P_o - P_a = \rho_L g H$$

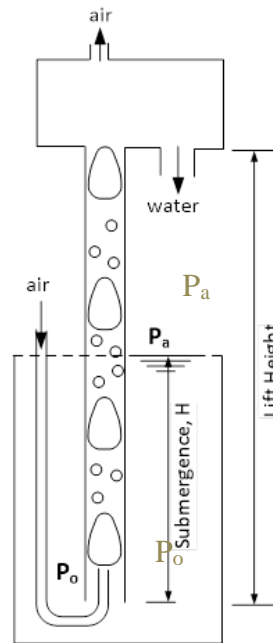


Figure B.1: Schematic of Air-Lift pump

B.1. Two-Phase Flow





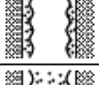
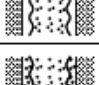
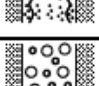
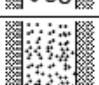
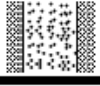

A two-phase flow is the flow involving two of the three phases (solid, liquid and gas). There are a variety of two-phase flows depending on combinations of two phases as well as on interface structures. Two-phase mixtures are characterized by the existence of one or several interfaces and discontinuities at the interface. It is easy to classify two-phase

mixtures according to the combinations of two phases, since in standard conditions there are only three states of matters, namely, solid, liquid, and gas phases. Therefore, the two-phase can be combination of

1. Gas-solid mixture;
2. Gas-liquid mixture;
3. Liquid-solid mixture;

Single-phase flow can be classified according to the structure of flow into laminar, transitional and turbulent flow. In contrast, two-phase flow can be classified according to the structure of interface into several major groups which can be called flow regimes or patterns such as separated flow, transitional or mixed flow and dispersed flow as shown in as shown in Table B.1.

Table B.1: Classification of two-phase flow [Ishii & Hibiki, 2013]

| Class | Typical regimes | Geometry | Configuration | Examples |
|-----------------------------|-----------------------------------|---|---|-------------------------------------|
| Separated flows | Film flow |  | Liquid film in gas Gas film in liquid | Film condensation Film boiling |
| | Annular flow |  | Liquid core and gas film Gas core and liquid film | Film boiling Boilers |
| | Jet flow |  | Liquid jet in gas Gas jet in liquid | Atomization Jet condenser |
| Mixed or Transitional flows | Cap, Slug or Churn-turbulent flow |  | Gas pocket in liquid | Sodium boiling in forced convection |
| | Bubbly annular flow |  | Gas bubbles in liquid film with gas core | Evaporators with wall nucleation |
| | Droplet annular flow |  | Gas core with droplets and liquid film | Steam generator |
| | Bubbly droplet annular flow |  | Gas core with droplets and liquid film with gas bubbles | Boiling nuclear reactor channel |
| Dispersed flows | Bubbly flow |  | Gas bubbles in liquid | Chemical reactors |
| | Droplet flow |  | Liquid droplets in gas | Spray cooling |
| | Particulate flow |  | Solid particles in gas or liquid | Transportation of powder |

The typical air-water flow regimes can be observed in vertical are bubbly, cap-bubbly, slug, churn-turbulent, and annular flows.

In any two-phase flow, some commonly used terms are:

Dryness fraction (quality): It is defined as a ratio of mass flow of gas to the total mass flow.

$$x = \frac{\dot{m}_G}{\dot{m}_L + \dot{m}_G}$$

Void fraction: The void fraction is one of the important parameters in two-phase flow to determine the flow regime as well as two-phase pressure drop and heat transfer [Walt, 2012]

Cross sectional void fraction: The void fraction is the ratio of the gas flow cross-sectional area to the total flow cross-sectional area.

$$\alpha_d = \frac{A_G}{A} = \frac{A_G}{A_L + A_G}$$

Volumetric void fraction: The volumetric void fraction is usually determined on a volumetric basis.

$$\alpha_d = \text{gas void fraction} = \frac{\text{volume of the gas(vapor) in the liquid}}{\text{total volume of the liquid gas mixture}} = \frac{V_G}{V_L + V_G}$$

The void fraction can be predicted by methods such as the homogeneous model and empirical models. The most widely used method is the basic empirical model developed by Zuber and Findlay in 1965 which has been modified numerous times. The basic model of Zuber and Findlay is as follows [White, 2001]:

$$\alpha_d = \frac{J_G}{C_o(J_L + J_G) + U_b}$$

where, J_G and J_L are the superficial velocities of the gas phases and liquid phases, defined as $J_G = \frac{\dot{V}_G}{A}$ and $J_L = \frac{\dot{V}_L}{A}$ (m/s), with \dot{V}_G and \dot{V}_L the volumetric flow rate of the vapour phase and liquid phase, and A total the total cross-sectional area of the pipe, C_o is the velocity

profile coefficient of gas-liquid mixture (ranging from 1.2 for fully developed turbulent flow to 2 for laminar flow) and J_b is the velocity of a gas bubble in still liquid (m/s) which is defined by $U_b = 0.35\sqrt{gD}$, g =gravity and D = diameter of the tube [Nicklin, 1963].

Mass velocity: In two-phase flow literature, mass velocity is extensively used. It is the ratio of mass flow rate to the total flow cross-section area of the mixture.

$$G = \frac{\dot{m}_G}{A}$$

B.2. Methods of Analysis for Gas-Liquid Flow

The methods used for analyzing a two-phase flow are extensions of those already well tried for single-phase flows. The procedure always is to write down the basic equations governing the conservation of mass, momentum, and energy, often in a one-dimensional form and to solve these equations by the use of various simplifying assumptions. Vapour-liquid mixtures, where the vapour and liquid are phases of the same fluid are referred to as two-phase single fluid mixtures (e. g. vapour-liquid mixture in a bubble pump) while gas-liquid mixtures where the vapour and liquid are different fluids are referred to as two-phase two fluid systems (e.g. air-liquid mixture in an air-lift pump). Three main types of flow analysis can be made,

1. **The homogenous flow model:** In this analysis, the two-phase flow is assumed to be a single-phase flow. This requires assuming (1) zero slip between the phases, (2) uniform flow and (3) thermal equilibrium between the phases. In air-water system, phase changes are not occurring, quality (x) does not vary along the tube. Whereas in a bubble pump, vaporization can occur in the fluid (steam-water), so x can vary.

The density of the homogenous mixture is the ratio of the mass flow to the volume flow:

$$\rho_H = \frac{GA}{AxGv_G + (1-x)GAv_L} \quad (1)$$

G = Mass velocity, A = cross sectional area, x = quality, v_G =specific volume of gas, v_L = specific volume of liquid

$$v_G = \frac{1}{\rho_G} \quad \text{and} \quad v_L = \frac{1}{\rho_L} \quad (2)$$

Thus

$$\frac{1}{\rho_H} = xv_G + (1-x)v_L = \frac{x}{\rho_G} + \frac{(1-x)}{\rho_L} \quad (3)$$

A mixture velocity defined as

$$u_H = \frac{G}{\rho_H} \quad (4)$$

where, u_H is the velocity of homogeneous mixture and if u_L and u_G are the velocities of liquid and gas,

$$\alpha_d = \frac{\dot{V}_G}{\dot{V}_G + \dot{V}_L} = \frac{xGAv_G}{xGAv_G + (1-x)GAv_L} = x \frac{v_G}{v_H} = x \frac{\rho_H}{\rho_G} \quad (5)$$

Also,

$$\frac{\alpha_d}{1-\alpha_d} = \frac{x}{(1-x)} \frac{\rho_L}{\rho_G} \quad (6)$$

2. The separated flow model: The separated flow model differs from homogenous model by recognizing that the velocities are usually different. It is a special one-dimensional two fluid model where the phases are considered as two separate streams.

A slip ratio between the two phases is defined as the ratio of the velocity of gas and liquid,

$$S = \frac{u_G}{u_L} \quad (7)$$

If the volumetric flows of gas and liquid are $\dot{V}_G = Gxv_G$ and $\dot{V}_L = G(1-x)v_L$, then

$$u_G = \frac{GAx}{\rho_G A \alpha} \quad (8)$$

$$u_L = \frac{GA(1-x)}{\rho_L A (1-\alpha_d)} \quad (9)$$

where α and $(1 - \alpha)$ are the fractions of cross section, A, occupied by gas and the liquid. So, the slip ratio becomes

$$S = \frac{x}{(1-x)} \frac{(1-\alpha_d) \rho_L}{\alpha_d \rho_G} \quad (10)$$

3. The flow pattern model: This is a more sophisticated analysis where the two phases are considered in one of three or four definite prescribed geometries. These geometries are based on the various configurations or flow patterns found when a gas and a liquid flow together in a channel. The basic equations are solved for each flow pattern. In order to apply these models, it is necessary to know when each should be used and to be able to predict the transition from one pattern to another.

B.3. Flow Pattern in Upward Vertical Two-Phase Flow

The flow distribution of a gas-liquid two phase flow in a vertical pipe depends on the flow rate, physical properties of the fluid, and also on the geometry of the pipe. The different distributions of two phase flow are known as flow pattern [Chen & Brill,1997]. Many design parameters of two phase flow systems, such as pressure drop, heat and mass transfer, system stability are strongly dependent on flow patterns. Hence, the prediction of flow pattern is one of the most fundamental and important problems associated with two phase flows.

Several investigations of patterns for upward flow of air and water have been reported in the literature. A number of techniques have been used to determine the transition [Dukler & Taitel, 1986, Delhaya, 1981, Hewitt & Hall-Taylor, 1970]. For a fixed liquid flow, the following regimes appear with increasing gas velocity.

Bubbly flow: At low gas flow, a bubbly pattern is observed when the liquid flow rate is low. At this flow regime, the liquid phase is continuous and the gas is broken into bubbles by inertia forces. The bubbles can have different sizes. The largest, called cap bubbles, have a hemispherical shape. The bubbles are not distributed uniformly over the pipe cross section so the void fraction can vary with location.

Slug flow: At higher gas velocities, a slug can appear. It consists of the progression of bullet shaped bubbles (called Taylor bubbles) that have a diameter almost equal to the pipe diameter and move uniformly upward. The front resembles cap bubbles and the backs are almost flat. Taylor bubbles are separated by slugs of continuous liquid phase and the liquid slug between the Taylor bubbles can be aerated. Between the Taylor bubbles and the pipe wall, liquid flow downward in the form of a thin falling film.

Churn flow: With an increase in gas velocity, the ratio of Taylor bubbles and the liquid slug length decreases and the liquid slug becomes more aerated. When a critical gas flow rate is reached, a transition from slug to churn flow will take place. In churn flow, the Taylor bubbles which appeared in slug are distorted. The continuity of the liquid phase in the slug between successive Taylor bubbles is frequently destroyed by the gas phase, and as this appears a liquid slug falls. The falling liquid accumulates, forms a bridge, and is again lifted by the gas. The unique feature of the churn flow is an oscillatory up and down motion of the liquid as well as the liquid film on the pipe wall.

B.4. Mechanism for the breakdown of the bubbly flow pattern

Hewitt and Hall-Taylor [1970] and Govier and Aziz [1972] described in their books that if the inlet mixing process creates bubbles, the appearance of the Taylor bubble depends on the coalescence of the bubbles and on the stability of the Taylor bubbles that are formed. Griffith and Snyder [1964] suggested that bubbly flow cannot be sustained for the void fraction greater than 35%. This observation has been supported by Hewitt and Hall-Taylor [1970], which shows that the number of collisions increases rapidly with void fraction in the range of $\alpha = 0.30$. Dukler and Taitel [1986] assumed that the bubbly to slug transition will occur at $\alpha = 0.25$.

B.5. Mechanism for the slug to churn flow transition

The main reason on the transition from a slug flow to churn flow is the consideration of the stability of the Taylor bubbles which is a breakdown of the film between gas (Taylor) bubbles and the wall, where it changes from downward and upward flow. From the experimental results for the phase distribution in upward vertical slug flow, Brauner and Barnea [1986] and Barnea [1987] suggested that instability arises from excessive aeration in the liquid slugs between the Taylor bubbles and the slug to churn transition take place when the gas void fraction in the liquid slug reaches the maximum possible cubic packing of the spherical bubbles, i.e $\alpha = 0.52$, Experiments suggest that this transition indeed occurs when the void fraction in the liquid slug $\alpha = 0.50$ to 0.60 [Barnea & Shemer, 1989].

B.6. Air Lift Pump

Figure B.1 show a schematic of an air-lift pump with water. When air is injected at a small rate, the gas-liquid flow looks like a bubble column which involves the passage of gas bubbles in a stationary liquid. In this regime, the mass transfer of gas occurs between the gas and liquid. The rate of transfer is strongly related to the interfacial area per unit volume, which increases with the increase of volume fraction, α , and decreases in the bubble diameter. The expansion of the column, α , depends on the velocity of the bubble relative to the surrounding liquid. As the air rate increases, the height of this column (and gas void fraction) increases. The liquid flow rate increases with increasing air flow.

If the lift tube length is L , the total pressure drop (static head and friction loss) along the lift tube is

$$\rho g H = \rho g ((1 - \alpha_d)L + f \frac{L}{2D} \rho v_m^2 (1 - \alpha_d)) \quad (11)$$

where,

$$v_m = \frac{\dot{V}_L + \dot{V}_G}{A} \quad (12)$$

Equation (11) can be written as

$$\frac{H}{L} = (1 - \alpha_d) \left(1 + \frac{f}{2Dg} \left(\frac{\dot{V}_L + \dot{V}_G}{A} \right)^2 \right) \quad (13)$$

For a given air(gas) flow, the liquid flow increases with increase of submergence ratio (H/L). So, the prediction of liquid flow for a given gas flow, tube diameter and submergence ratio depends on the void fraction and the frictional pressure losses.

Nicklin (1963) defined the efficiency of the air-lift pump as the net work done in lifting the liquid divided by the isothermal expansion of the air.

$$\eta = \frac{\rho g \dot{V}_L (L - H)}{\dot{V}_g \left[P_a \ln \frac{P_o}{P_a} \right]} \quad (14)$$

The top part of Equation (14) is the work done per time to lift a volume of liquid (\dot{V}_L) to a height L above the submergence H. the bottom part is the work needed to compress an ideal gas with a volume (\dot{V}_G) (isothermally), from a pressure P_a to a pressure P_o shown in Figure B.1.

Neglecting the friction factor, Reinmann [1987] defined the air-lift pump efficiency as

$$\eta = \frac{\dot{V}_L \alpha_d}{\dot{V}_g (1 - \alpha_d)} = \frac{\dot{V}_L}{C_o (\dot{V}_L + \dot{V}_G) + U_b A - \dot{V}_G} \quad (15)$$

To analysis the air-lift pump, the homogenous flow model is not adequate, the separation flow model is needed. The working curves for the operation of the air-lift are plots of the liquid flow and the efficiency as a function of a gas flow for a given submergence ratio (Figure B.2). These curves show the increase of liquid flow as well as the efficiency as the gas flow increased where the flow pattern is slug flow in a smaller tube diameter. The efficiency in the operating graph is reached its maximum value before the liquid flow rate reaches it maximum. Thus, the location of the maximum efficiency in the graph is at low gas flow than required to reach a maximum flow. The flow pattern will change in a churn flow which depends on the frictional losses and the void fraction in the column.

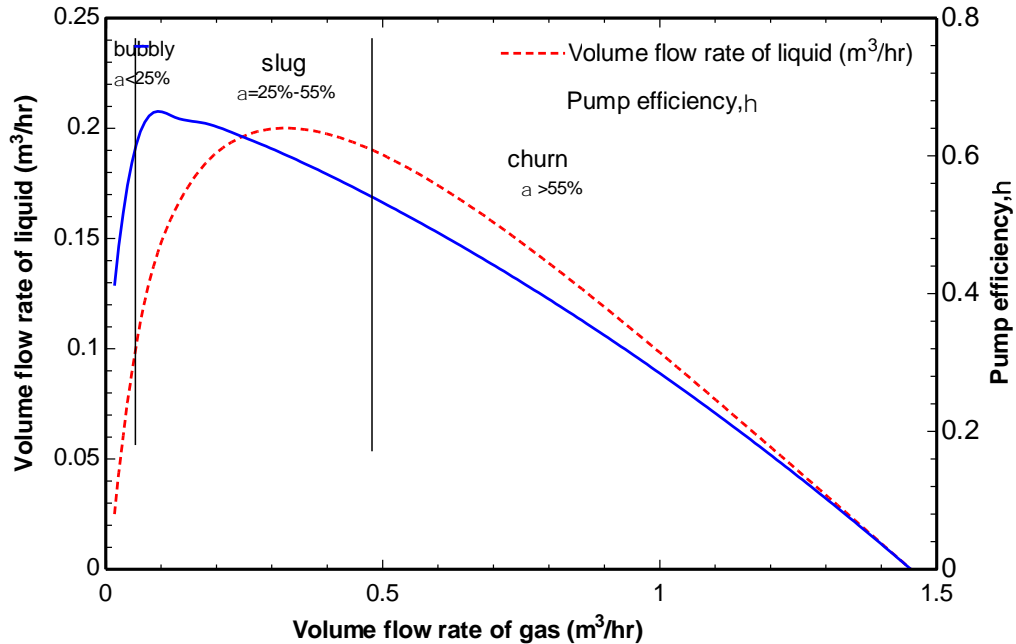


Figure B.2: Operation curve for a 9.53 mm in diameter air-water lift pump at $H/L=0.8$.

REFERENCES

- Barnea D, Shemer L., Void fraction measurements in vertical slug flow: applications to slug characteristics and transition. *International journal of Multiphase Flow*, 15 (1989) 495-504.
- Barnea D., A unified model for predicting flow-pattern transitions for the whole range of pipe inclinations. *International journal of Multiphase Flow*, 13 (1987) 1-12.
- Brauner N., Barnea D., Slug/churn transition in vertical upward flow. *Chemical Engineering Science*, 41 (1986) 159-163.
- Chen X.T., Brill J.P., Slug to churn transition in upward vertical two-phase flow. *Chemical Engineering Science*, 52 (23) (1997) 4269-4272.
- Delhaye J. M., Two-phase flow pattern, In *Two-Phase Flow and Heat Transfer in the Power and Process Industries*. Washington DC: Hemisphere, (1981).
- Dukler A.E., Hubbard M.G., A model for gas-liquid slug flow in horizontal tube. *Industrial Engineering & Chemistry Fundamentals*, 14 (1975) 337-347.
- Dukler A.E., Taitel Y., 1986, Flow pattern transitions in gas-liquid systems: Measurements and modelling. *Multiphase Science Technology*, 2 (1986) 1-94.

- Govier G.W., Aziz K., *The Flow of Complex Mixture in Pipes*. New York: Van Nostrand Reinhold, 1972.
- Griffith P., Snyder P.A., *The bubbly-slug transition in a high velocity two-phase flow*. (1964), MIT report 5003-29 (TID-20947).
- Hewitt G.F., Hall-Taylor N.S., *Annular Two-Phase Flow*, Oxford: Pergamon Press, (1970).
- Ishii M., Hibiki T., *Thermo-Fluid Dynamics of Two-Phase Flow*, Second edition, Springer, (2013).
- Reinemann D.J., *A Theoretical and Experimental study of Airlift Pumping and Aeration with Reference to Aquacultural Applications*. PhD Thesis, Cornell University, (1987).
- Nicklin D.J., *The Air-Lift Pump: Theory and Optimization*. *Transactions of the Institution of Chemical Engineers*. 41 (1963) 29-39.

Appendix C

PERMISSIONS FOR PREVIOUSLY PUBLISHED WORKS

Chapter 2: Solar sorption cooling for residential air-conditioning applications, International Journal of Renewable Energy Technologies, in press.

It is specified by the Inderscience in Author Rights [Inderscience, 2017] that the author of the publication retains significant rights to include the article in a thesis or dissertation which provided the acknowledgement to journal publication is made explicit.

Chapter 3: Residential solar air conditioning: energy and exergy analyses of an ammonia-water absorption cooling system

It is specified by the Elsevier's Author Rights [Elsevier, 2017] that the author of the publication retains significant rights to include the article in a thesis or dissertation which provided the acknowledgement to journal publication is made explicit.

Chapter 4: Modelling and Analysis of Bubble Pump Parameters for Vapor Absorption Refrigeration Systems

It is specified in ASHRAE [2016] copyright policies, authors retain the right for certain specific uses of their paper without requesting ASHRAE's permission. This provided the acknowledgement to journal publication is made explicit.

Chapter 5: Performance characterization of a bubble pump for vapor absorption refrigeration systems

It is specified by the Elsevier's Author Rights [Elsevier, 2017] that the author of the publication retains significant rights to include the article in a thesis or dissertation which provided the acknowledgement to journal publication is made explicit.

Chapter 6: Bubble-pump-driven LiBr-H₂O and LiCl-H₂O absorption air-conditioning systems

It is specified by the Elsevier's Author Rights [Elsevier, 2017] that the author of the publication retains significant rights to include the article in a thesis or dissertation which provided the acknowledgement to journal publication is made explicit.

Appendix A: Energy efficiency and economic feasibility of an absorption air-conditioning system using wet, dry and hybrid heat rejection methods.

It is specified by Taylor & Francis [2017] Right policy that authors retain many rights (such as to include the article in a thesis or dissertation), which provided the acknowledgement to journal publication is made explicit.

References

ASHRAE, ASHRAE Author's Manual: Copyright, 2016

Elsevier, <https://www.elsevier.com/about/our-business/policies/copyright>, Accessed on November 30, 2017.

Inderscience, http://www.inderscience.com/info/inauthors/author_copyright.php, Accessed on November 30, 2017.

Taylor & Francis, <http://journalauthors.tandf.co.uk/preparation/copyright.asp>, Accessed on November 30, 2017.

VITA AUCTORIS

NAME: Julia Aman

PLACE OF BIRTH: Jhenidah, Bangladesh

YEAR OF BIRTH: 1975

EDUCATION: Jhenidah K.C College, High School, 1992

Rajshahi University of Engineering and
Technology, Bangladesh, B.Sc., 1998.

University of Oldenburg, Germany, M.Sc., 2004.